Feasibility of Optical Gyroscopic Sensors in Silicon-On-Insulator Technology

by

Miguel Ángel Guillén-Torres

B.Sc., National Autonomous University of Mexico, 2004
M.Phil., The University of Cambridge, 2007

A THESIS SUBMITTED IN PARTIAL FULFILLMENT OF
THE REQUIREMENTS FOR THE DEGREE OF

DOCTOR OF PHILOSOPHY

in

The Faculty of Graduate and Postdoctoral Studies

(Electrical and Computer Engineering)

THE UNIVERSITY OF BRITISH COLUMBIA

(Vancouver)

August 2015

Abstract

In the last decade, silicon photonics has become a strategic technology for the development of telecommunications and sensors. Due to its compatibility with well-developed complementary metal oxide semiconductor (CMOS) fabrication processes, silicon on insulator (SOI) wafers can be processed to create thousands of devices per die in a fast and inexpensive way. Being solid state devices with no movable parts, optical gyroscopes have longer life expectancies and shock resistance compared to micro-electro-mechanical gyroscopes. Thus, the implementation of SOI-based gyroscopes is desirable for large-scale, low-cost production.

This thesis presents a study of the feasibility of implementing optical gyroscopes in SOI technology. A comprehensive theoretical study has been carried out to develop a device-level optimization and robustness analysis, showing that the most crucial resonator parameter is the propagation loss, followed by length and coupling. For a given propagation loss, there is an optimal resonator size, beyond which the angular speed resolution is severely degraded. On the system level, the impact of signal-to-noise ratio and insertion loss on the resolution are described.

Given that the propagation loss is the most important parameter, strategies were proposed to reduce it as much as possible while still using CMOS-compatible processes. The quality factor, Q, was chosen as the figure of merit to be maximized during the design iterations. As a result, the largest Q factors reported to date on SOI, using standard CMOS-compatible processes, were achieved. These Q factors are comparable to, or exceed, those of optical resonators intended for gyroscopic applications that are fabricated in materials such as indium phosphide (InP). Innovative approaches to compensate for fabrication variations are proposed, such as thermally-tuneable

coupling and reference rings for differential measurements.

Complex mechano-opto-electrical measurement setups were designed and implemented to characterize SOI gyroscopes, both at rest and under rotation. As a result, the Microsystem Integration Platform for Silicon-Photonics (Si-P MIP) was created. This characterization platform is now being commercialized by CMC Microsystems for academic and industrial applications.

The main practical and theoretical challenges regarding the implementation of optical ring gyroscopes on SOI have been identified. Schemes to address them and suggestions for future work are proposed.

Preface

This thesis work is partially based on the publications listed below, some of which resulted from collaborations with other researchers. Note that only the publications directly linked to this thesis work are shown below. It should also be noted that some numerical simulations and experiments have been re-made since their first publication, to yield more insightful results and comparisons, and may not necessarily be identical to those previously published. An additional list of publications, not directly related to this work, is given in Appendix A.

Journal Publications

1. M. A. Guillen-Torres, E. Cretu, N. A. F. Jaeger, and L. Chrostowski, "Ring Resonator Optical Gyroscopes - Parameter Optimization and Robustness Analysis," *J. Lightw. Technol.*, vol. 30, no. 12, pp. 1802-1817, 2012

   I conceived the idea of a theoretical study about the robustness of ring resonator gyroscopes to variations in their design parameters. I carried out the analytical and numerical modelling, and wrote the manuscript. L. Chrostowski provided deep insight into how ring resonators work and how to model them. N. A. F. Jaeger provided invaluable insights throughout the course of numerous discussions to further understand the principles of the Sagnac Effect, as well as the effect of waveguide coupling on resonance depth and quality factor. E. Cretu suggested valuable analytical and numerical approaches, such as parameter normalization, in order to find generalized optimal parameters. L. Chrostowski, N. A. F. Jaeger, and E. Cretu supervised the work, provided

feedback and advice regarding visualization and interpretation of numerical simulation results, and contributed to editing the manuscript. Chapter 2 is mostly based on this publication.

Conference Proceedings

1. M. A. Guillen-Torres, M. Almarghalani, E. H. Sarraf, M. Caverley, N. A. F. Jaeger, E. Cretu, and L. Chrostowski, "Silicon photonics characterization platform for gyroscopic devices," in *SPIE Photonics North*, Proc. SPIE, vol. 9288, Montréal, Canada, pp. 1-8, May 2014

   I conceived the idea of a rotational setup for gyroscope device characterization, built up the optomechanical setup, coordinated the software development, performed the measurements, post-processed the data, and wrote the manuscript. N. A. F. Jaeger suggested using special coupler designs for splitting and combining of optical signals, and provided the optical instruments and opto-mechanics required for creating the apparatus. L Chrostowski suggested the use of straight multimode waveguides for resonator roundtrip loss reduction and quality factor improvement. I implemented these ideas, and created scripts for semi-automatic device layout generation with optimum coupling values, as per the findings of our previous journal publication. L. Chrostowski and N. A. F. Jaeger provided advice regarding various optical device test procedures. E. Cretu provided special equipment and guidance for the creation of the platform computerized control, and contributed to the conception of tests for apparatus characterization. M. Almarghalani created hardware and software interfaces for motor control, as well as codes for rotational patterns. E. H. Sarraf created interfaces for data acquisition and instrument communication. M. Caverley contributed to post-processing and data analysis. L. Chrostowski, N. A. F. Jaeger, and E. Cretu supervised the work. All authors commented and assisted in editing the manuscript. Part of Chapter 3 is based on this publication.

2. M. A. Guillen-Torres, M. Caverley, E. Cretu, N. A. F. Jaeger, and

L. Chrostowski, "Large-area, high-Q SOI ring resonators", in *IEEE Photonics Conference*, San Diego, California, USA, pp. 1-2, Oct. 2014

L. Chrostowski, N. A. F. Jaeger, and I conceived the idea. L Chrostowski suggested the use of Bézier bends for the resonator corners for further improvement of the resonator quality factor values, as well as the creation of robust test structures for multimode waveguide propagation loss characterization. N. A. F. Jaeger provided valuable insight into the interplay of key parameters that influence the value of the Q factor. I implemented the idea and conducted the device layout design and performed the measurements. M. Caverley contributed to device designs, assisted with measurements. M. Caverley and I wrote the manuscript. L. Chrostowski, N. A. F. Jaeger, and E. Cretu supervised the work and assisted in editing the manuscript. All authors commented on the manuscript. Part of Chapter 3 is also based on this publication.

3. M. A. Guillen-Torres, L. Chrostowski, E. Cretu, and N. A. F. Jaeger, "Ring Resonator Gyroscope: System Level Analysis and Parameter Optimization," *Canadian Semiconductor Science and Tech. Conf.*, MPA, p. 1, Vancouver, Canada, 2011

   I conceived the idea of a theoretical study about the obtention of optimal ring resonator gyroscope design parameters. I carried out the analytical and numerical modelling, and wrote the manuscript. L. Chrostowski provided insight into the main figures of merit of ring resonators. N. A. F. Jaeger provided insights into the Sagnac effect and concepts related to waveguide coupling. E. Cretu helped develop generalized analytical equations for modelling double-bus-waveguide ring resonators, and suggested numerical approaches and tools for parameter optimization. L. Chrostowski, N. A. F. Jaeger, and E. Cretu supervised the work, provided feedback and advice regarding the interpretation of results, and contributed to editing the manuscript. Chapter 2 is partially based on this publication.

The following work, currently unpublished, was the result of collaborations with various members of the UBC Micro- and Nano-technology group:

1. L. Chrostowski conceived the idea of resonators with thermally-tuneable couplers. M. Caverley and I created the device layout designs. K. Murray and I created the theoretical device models. M. Caverley and I performed the device measurements. Part of Chapter 3 is based on this work.

2. Theoretical models were created in collaboration with K. Murray to describe the behaviour of various device designs, as well as to analyze the effect of backscattering in them. Part of Chapter 3 is also based on this work.

Table of Contents

Appendix

List of Tables

List of Figures

Glossary

Acronym	Meaning
AOM(s)	Acusto-Optic Modulator(s)
AP	All-Pass
AR	Aspect Ratio
AWG	Arbitrary Waveform Generator
BOX	Burried OXide layer
CC	Critical Coupling
CMC	Canadian Microsystems Corporation
CMOS	Complementary Metal Oxide Semiconductor
CPU	Central Processing Unit
CSS	Continuous Spectral Sweep
CCW	Counter-clock-wise
CW	Clock-wise
DMA FIFO	Direct Memory Access - First Input/First Output
DRC	Design Rule Checking
DUT	Device Under Test
DUV	Deep Ultra-Violet
ER	Extinction Ratio
FFT	Fast Fourier Transform
FOG(s)	Fiber-Optic Gyroscope(s)
FPGA	Field-Programmable Gate Array
FSIL COM	Fast Spectral Insertion Loss COM port drivers
FSR	Free Spectral Range
FWHM	Full Width at Half Maximum

Continued in next page...

Acronym	Meaning
GC	Grating Coupler
GCC	Globally-optimized Critical Coupling
GOC	Global Optimal Coupling
GPIB	General Purpose Interface Bus
GUI	Graphical User Interface
I/O GC	Input/Output Grating Coupler
IFOG(s)	Interferometric Fiber-Optic Gyroscope(s)
IL(s)	Insertion Loss(es)
IME	Institute of Micro Electronics
IMEC	Interuniversity Microelectronics Centre
IMOG(s)	Interferometric Micro-Optic Gyroscope(s)
InP	Indium Phosphide
IOG	Integrated Optic Gyroscope
LIA(s)	Lock-In Amplifier(s)
LOC	Locally-Optimized, under-Coupled ring
LPF	Low-Pass Filter
MEMS	Micro Electro-Mechanical System
MIG	MEMS Interferometric Gyroscope
LCC	Locally-optimized, Critical Coupling
LOC	Locally-optimized, Optimal under-Coupling
MM	Multi-Mode
MMWG	Multi-Mode Waveguide
MZI	Mach-Zehnder Interferometer
OC	Optimal under-Coupling
PCI	Peripheral Component Interconnect
PD	Photo-Detector
PM	Polarization-Maintaining
PSD	power spectral density
PWM	Pulse-Width Modulation
PXI	PCI eXtensions for Instrumentation
RF	Radio Frequency

Continued in next page...

Acronym	Meaning
SiN	Silicon Nitride
Si-P MIP	Microsystem Integration Platform for Si-Photonics
SM	Single-Mode
SMWG	Single-Mode Waveguide
SNR	Signal-to-Noise Ratio
SOI	Silicon On Insulator
SSE	Spontaneous Source Emission
TE	Transverse Electric
TM	Transverse Magnetic
TS	Test Structure
T-MZI	Tuneable Mach-Zehnder Interferometer
TEC	Thermo-Electric Peltier Cooler
TLS	Tuneable Laser Source
UW	University of Washington
VI	Virtual Instrument
WDC	Waveguide Directional Coupler
ZRO	Zero-Rate Output

Acknowledgements

To my three co-supervisors, Dr. Lukas Chrostowski, Dr. Nicolas A. F. Jaeger, and Dr. Edmond Cretu, for all their guidance, knowledgeable advice, early-morning and late-night brainstorming sessions, invaluable support, patience, kind mentoring, encouragement, and friendship during my graduate years at UBC. A very special mention to Dr. Nicolas Jaeger for the countless hours invested on the detail-oriented read-through sessions during the editing of this thesis document.

Thanks to CMC Microsystems through Dr. Robert Mallard, for providing me with the equipment to create the Microsystem Integration Platform for Si-Photonics (Si-P MIP), which constitutes our current device characterization platform. Thanks to the Natural Science and Engineering Research Council of Canada, as well as the National Science and Technology Council of Mexico.

To each and every one of the members and collaborators of the three outstanding research labs where I have done my theoretical and experimental work, for all their help, fruitful discussions, and support, as well as many faculty and staff members from Electrical and Computer Engineering and AMPEL Laboratories, who contributed to this work with either discussions, tools, or suggestions:

I thank Dr. B. Faraji, Dr. W. Shi, Dr. R. Vafaei, and Dr. S. Talebi-Fard, for our fruitful discussions regarding the initial modelling of ring resonators. I thank R. Boeck for insightful discussions regarding the state of the art. Thanks to A. Sharkia, M. Finnis, Dr. M. Beaudoin, Dr. M. Greenberg, and D. Dawson, for their help and advice during the design and fabrication of custom parts for various characterization setups. Many thanks to E. Hernández, M. Almarghalani, Dr. E. Sarraf, and C. Gerardo for their

collaboration, brainstorming, and feedback during the implementation of the time-domain interfaces in LabVIEW^{TM}. Thanks to Dr. R. Rosales for various discussions regarding signal processing.

A very special mention to K. Murray for his collaboration, feedback, and invaluable help during the creation and verification of theoretical device models, as well as during experimental data processing and interpretation. I thank H. Yun for discussions regarding the behaviour of his adiabatic splitting coupler, and for facilitating its layout design, used as a subcomponent in some of my devices. I appreciate the contributions of H. Jayatilleka and M. Caverley with ideas and collaboration during measurements, as well as insightful discussions and suggestions to increase efficiency during experiments and data processing. Last, but not least, I thank K. Khondoker for his help and feedback during the creation and de-bugging of MATLAB^{TM} scripts for data post-processing.

Dedication

To God, my wife, my family, and my friends, for their love and support throughout this journey.

Chapter 1

Introduction

For decades, gyroscopes have been mounted on both military and civilian vehicles such as airplanes, submarines, satellites, and missiles, to name a few. Depending on its specific purpose, each vehicle has different requirements for angular speed resolution, bias drift (i.e., the variation of its output over time), and its scale factor (defined as the variation of the output signal per unit change in rotation speed [143]), form factor (i.e., size and weight), and power consumption. For instance, inertial grade applications such as satellite orbit control and submarine navigation require very stringent performance, whereas automotive and consumer electronics applications allow for more relaxed specifications [35, 143].

Figure 1.1 shows a comparison between the bias stability and resolution requirements in the early 2000s and the present, based on information available in [11, 35, 110]. From this figure, one can see the growth in gyro applications, as well as the advent of MEMS gyroscopic devices. In the early 2000s the aerospace and defence applications were dominant, requiring primarily inertial- and tactical-grade gyroscopes [110]. Now, the availability of smaller, inexpensive MEMS devices has made them the sensor of choice for rate-grade applications such as robotics, automotive safety systems, medical instrumentation, and even general consumer products [35].

The high-end gyroscope applications belong to aerospace and defence sectors, where considerable efforts have been made to create optical gyroscopes since the mid 1970s. See, for instance, the pioneering fibre optic interferometer experiments of Vali and Shorthill in 1976 [130] and the free-space experiments to create a passive ring resonator gyroscope by Ezekiel and Balsamo in 1977 [45]. Thanks to the low propagation loss levels achieved in optical fibres and glass waveguides, glass became the material of choice

for passive resonator optical gyroscopes.

Efforts to integrate micro electro-mechanical system (MEMS) with optical technology, in order to create micro opto-electro-mechanical system (MOEMS) gyroscopes, started in the late 1970s. According to Liu et al. [81], Northrop started its silicon waveguide investigations in 1978, leading to the development in 1991 of a MOEMS gyroscope with a resolution of 10 deg/h.

The use of silicon (Si) and silicon nitride (SiN) waveguide resonators for sensing and telecommunication applications has been extensively investigated in the past two decades [4, 18, 80]. Special attention has been devoted to silicon-on-insulator (SOI) and silicon-nitride-on-silica (SiN) technologies, in which a waveguide (made of Si or SiN, respectively) is on top of a silica (SiO_2) layer. These particular materials exhibit relatively low losses in the C-band, with single-mode waveguide losses ranging from 0.27 dB/cm [15] to 3 dB/cm [38] for SOI, and ranging from 0.7 dB/m [12] to 6 dB/m [91] for SiN waveguides. In particular, SOI technology shows good optical confinement due to its high refractive index contrast (cf. $n_{Si} = 3.48$ vs. $n_{SiO_2} = 1.45$; $n_{Si_3N_4} = 2$), as well as CMOS fabrication technology compatibility [4, 85, 106, 111].

As shown in Fig. 1.2, Interferometric Fiber-Optic Gyroscopes (IFOGs) and Ring Laser Gyroscopes (RLGs) are by far the most sensitive rotation sensors to date, with sensitivities in the range of 1 to 100 $\frac{\mu\text{deg/s}}{\sqrt{\text{Hz}}}$ for high-end systems [20, 37, 108]. However, the optical path length required to achieve such high sensitivities (e.g. $\sim 10^2$ to $\sim 10^3$ m) require complicated fibre spool winding and thermal control schemes [32, 64, 74, 88], which prevent their further miniaturization and cost reduction. On the other hand, MEMS-based vibratory gyroscopes allow for small size designs, but at the expense of resolution, usually 2 to 4 orders of magnitude worse than those of IFOGs and RLGs, and with proof-masses driven very close to their resonance frequency, which impacts the expected lifespan of the device.

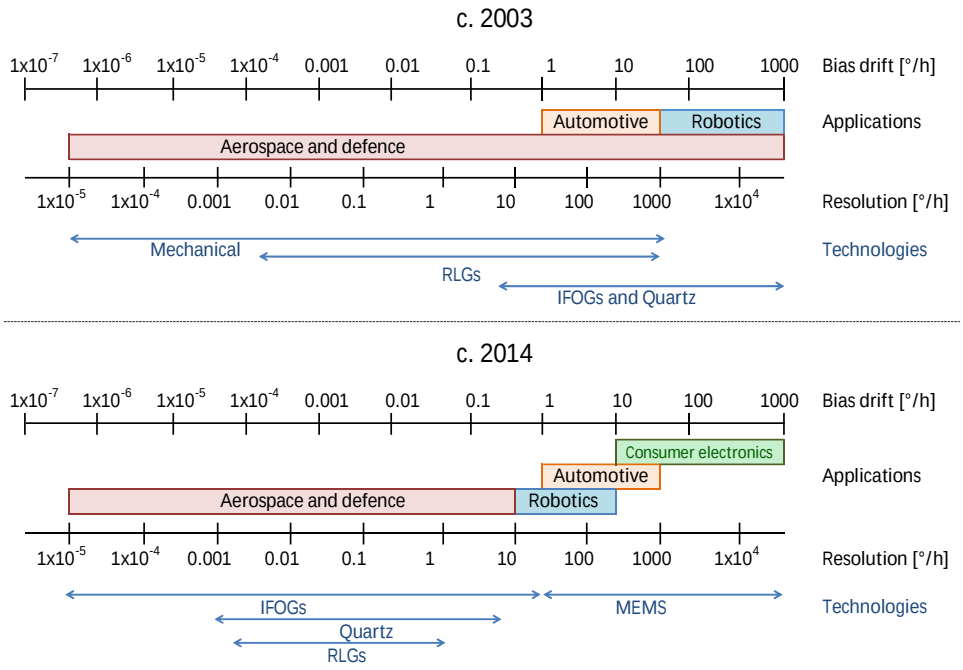

Figure 1.1: Gyro technology requirement by application, based on [11, 35, 110].

The most important performance figures for a gyroscope are its resolution, scale factor, zero-rate output (ZRO), and bias drift. Resolution is the minimum detectable angular rate. Scale factor is the amount of change in the output signal per unit change of angular speed. Since optical gyroscopes usually have voltage outputs, this is usually expressed in V/(deg/s) [143]. The ZRO is the random output of the sensor in the absence of rotation, and is the sum of white noise and a slowly varying random function. The noise defines the resolution of the sensor, expressed in units of angular speed per square root of bandwidth, e.g., $\frac{deg/s}{\sqrt{Hz}}$. The slow varying function defines the drift of the gyroscope, usually expressed in units of deg/s or deg/h, depending on the gyroscope grade [81, 143]. Table 1.1 shows the performance requirements of different gyroscope grades [143].

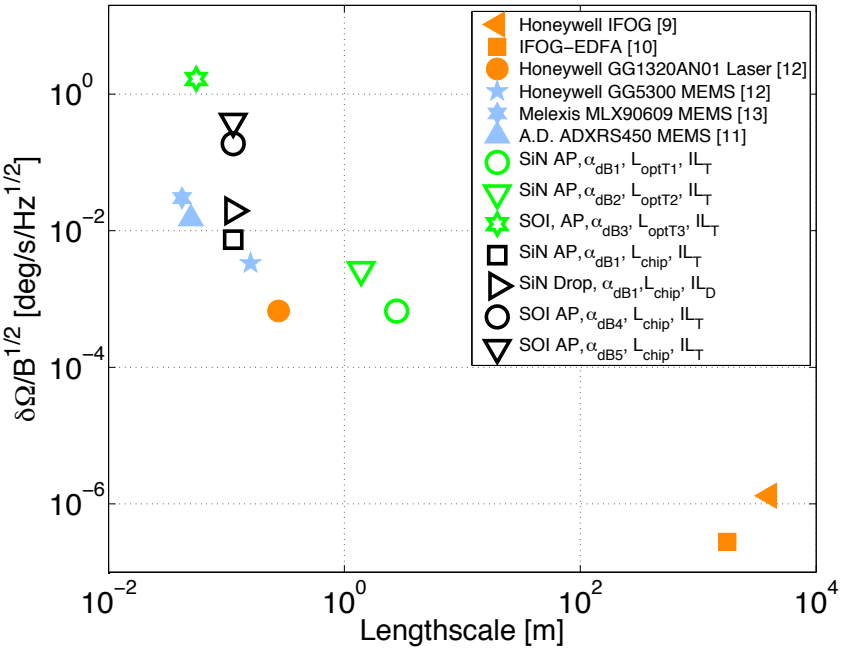

Figure 1.2: Resolution vs. lengthscale for selected optical and MEMS-based gyroscopes, either reported in the literature, [20, 108], or commercially available, [1, 2, 37], and theoretical resolution estimations (hollow markers) for ring resonator gyroscopes fabricated in different materials and port configurations. For silicon nitride (SiN), $\alpha_{\mathrm{dB1}} = 0.06$ dB/cm [91], and $\alpha_{\mathrm{dB2}} = 0.12$ dB/cm [53]. For silicon on insulator (SOI), $\alpha_{\mathrm{dB3}} = 3$ dB/cm [13]. For SOI resonators with different waveguide widths for different segments, the projected propagation loss estimations are between $\alpha_{\mathrm{dB4}} = 1$ dB/cm and $\alpha_{\mathrm{dB5}} = 1.46$ dB/cm. $L_{\mathrm{optT1}} = 2.77$ m; $L_{\mathrm{optT2}} = 1.39$ m; $L_{\mathrm{optT3}} = 55.5$ mm; and the perimeter of a chip is $L_{chip} = 114$ mm. The insertion losses (ILs) for the All-Pass (AP) and the Drop-Port rings are assumed to be $IL_T = 7$ dB and $IL_D = 3$ dB, respectively.

Table 1.1: Performance requirements of different gyroscope grades [143].

Parameter	Rate grade	Tactical grade	Inertial grade
Angle Random Walk [°/$\sqrt{\text{h}}$]	> 0.5	0.5 - 0.05	< 0.001
Bias Drift [°/h]	10 - 1000	0.1 - 10	< 0.01
Scale Factor Accuracy [%]	0.1 - 1	0.01 - 0.1	< 0.001
Full Scale Range [°/s]	50 - 1000	> 500	> 400
Max. Shock in 1 ms [g]	10^3	10^3 - 10^4	10^3
Bandwidth [Hz]	> 70	100	100

1.1 State of the Art

Compared with ring laser gyroscopes (RLGs) and fiber-optic gyroscopes (FOGs), MOEMS gyroscopes replace the long fibre coils with optical devices or cavities, offering the advantages of small size and lighter weight. MOEMS gyroscopes can be categorized into interferometric micro-optic gyroscopes (IMOGs) and resonant micro-optic gyroscopes (RMOGs).

IMOGs can be fabricated with waveguides, mirror arrays, proof-masses, or a combination thereof, on silicon substrates [81]. Design and simulation efforts to implement optical gyroscopic devices using micro-mirrors started in the early 2000s. For instance, in 2000, the Air Force Institute of Technology of the United States of America proposed a MEMS interferometric gyroscope (MIG), in which mirrors were placed on a silicon die to create two spiral paths with an increased path length [119]. Also in 2000, the University of Alabama proposed a 3-axis, monolithic, all-reflective gyroscope based on simulation of parabolic reflectors to create long multi-turn helical paths in free space, with the objective of enhancing the Sagnac effect [25]. The simulation results predicted a resolution of 0.001 deg/h for a structure of approximately 7 cm in diameter, with a 1-W input power at a wavelength of 0.5 µm. However, there is no evidence in the literature of any fabrication efforts to create such a device.

Obstacles such as high mirror losses, fragility, stringent misalignment tolerances, and fabrication complexity [94], preclude any significant ad-

vancement of micro-mirror-based devices for gyroscopic applications. Other IMOG designs rely on interferometric techniques to determine the displacement of a movable proof-mass, usually fabricated in SOI technology. This has allowed for interferometric techniques to determine the spectral response of the proofmasses, [5, 6], and experimental angular rate sensitivities as low as 27 deg/h/$\sqrt{\text{Hz}}$ have been reported [95].

RMOGs principle of operation is an optical micro-resonator, which inherently has the advantage of not requiring movable masses. RMOGs can be fabricated with optical waveguide resonators on various materials, silica being the most commonly used [48, 57, 82, 84, 120, 121]. Recent efforts focused on the design and fabrication of optical resonators using silica [48] and alternative materials such as InP [22] have lead to a decrease in propagation loss values and improvement in resonator quality factor (Q). Several design proposals compatible with fabrication technologies in materials such as silicon nitride, silicon oxynitride, and SOI exist in the literature, for instance, see [58, 109, 113], but to the best of my knowledge, there has not been a study of the feasibility, nor a fully demonstrated device of such kind, in SOI.

As mentioned earlier, after an early start, Northrop developed a MOEMS gyroscope in 1991. Honeywell and the University of Minnesota also developed special components for RMOGs in 2000, such as alumina (Al_2O_3) and zirconia (ZrO_2) low-loss (0.1 dB/cm) trench waveguides, ion-beam deposited to form a 2-cm diameter cavity on an ultra-low-expansion substrate. Rare-earth doping was used to allow for optical cavity gain. A theoretical resolution range between 0.1 and 1 deg/h was predicted [50].

In 2003, an integrated optic gyroscope was presented by the University of Arizona [19]. It was fabricated in Schott IOG-10 glass [129], using a $Ag^+ - Na^+$ ion exchange process [135]. It had a 28-mm diameter resonator, designed with single-mode waveguides for an operating wavelength of 1550 nm. Based on spectral characterization at rest and geometrical parameters, a shot-noise limited resolution of 170 deg/h was predicted. However, to the best of my knowledge, there are no reports in the literature regarding any dynamic tests of this particular device.

In 2003, Litton systems proposed and patented an integrated optic gyroscope (IOG) using a multi-layer waveguide coil instead of a fiber coil [52], which can in principle reduce the cost of waveguide coils, although it would increase their fabrication complexity. Another possible approach consists of utilizing waveguide crossings (such as those investigated by our team [112]), to create multi-turn planar coils. However, the integration of such crossings is, to the best of my knowledge, still at the theoretical design stage, e.g., see [116], and could require stringent fabrication restrictions.

1.1.1 Motivation and Potential Applications

The main objective of this thesis is to explore the feasibility of using SOI for fabricating rate-grade gyroscopes. If tactical- and rate-grade optical gyroscopes can be implemented in SOI technology, these sensors could be used in high-volume applications such as automotive or consumer electronics. This thesis provides insight into theoretical limitations as well as specific practical challenges regarding the design, fabrication, and interrogation of SOI gyroscopic devices.

1.2 Structure of the Thesis

The remainder of this thesis is organized in three chapters. Chapter 2 focuses on the theoretical analysis of optical gyroscopic devices, their working principles, the key optical resonator parameters and their interdependence to achieve optimal angular resolution, the impact of parameter variations in the device performance, and the requirements to implement frequency tracking using phase modulation.

Chapter 3 guides the reader through the iterative process carried out for the design, fabrication, and characterization of devices, as well as the construction and improvement of the characterization setups, which has been divided in five design cycles. Thus, Chapter 3 is divided in five sections, stating for each cycle the initial objectives, describing device designs, the device characterization. A critical evaluation of the results is conducted at

the end of each iteration, in order to identify problems, plan approaches to solve them, and derive conclusions that help improve both the devices and the characterization setup during the next iteration.

Chapter 4 summarizes the main conclusions and describes the future work required for further improvement of the device readout and the characterization setup.

Chapter 2

Resonator Simulation and Parameter Optimization

In this chapter, a theoretical analysis of the angular speed resolution and the robustness of waveguide resonator devices for gyroscopic applications is carried out, taking into account various propagation losses and refractive index values, corresponding to various currently available materials and waveguide fabrication technologies.

Although several theoretical studies regarding the use of micro-ring resonators for gyroscopic applications have been carried out [109, 146], to the best of my knowledge there had not yet been a thorough study of the interdependence of the values of propagation loss, resonator length, coupling coefficients, and off-resonance detuning necessary to achieve a truly optimized angular speed resolution (as mentioned in Chapter 1, resolution is the minimum detectable angular rate). As will be shown in Subsection 2.3.4, the optimal resolution is inversely proportional to the product of the spectral slope and the square of the resonator length. Optimized parameter values for some particular cases have been depicted in references such as [127], but subject to restrictions of a small length-propagation loss product, $L \cdot \alpha$. This precludes a proper analysis for the case of a gyroscope, where long lengths are desirable to enhance the Sagnac effect [101].

In this chapter we propose and analyze optical resonator gyroscopes with millimetre-range optical paths, in either an all-pass (Gires-Tournois, single-bus), or a drop-port (double-bus) configuration, which could be fabricated on a Silicon-on-Insulator (SOI) platform, using currently existing CMOS-compatible techniques, with theoretical resolutions comparable to those of

MEMS-based systems. For computational and modelling simplicity, the resolutions are calculated assuming a circular area for the ring resonators. Since the Sagnac effect is proportional to the area enclosed by the resonator, rather than the resonator length, for a fixed length value, the use of a rectangular shape with a particular aspect ratio will affect the resolution, but does not modify the relationships nor the optimum values for any other parameters. For an easier reading, the most frequent acronyms and variables are summarized in the Glossary and Table 2.1, respectively.

As shown in Fig. 2.1, light from a laser source is injected into, and extracted from, low-loss ring resonators via one or two bus waveguides, which are interrogated with photodetectors, either at the through port in an all-pass configuration, or at the drop port in a double-bus configuration, respectively. A 50%-50% splitter is used to allow for counter-propagating light injection. The output light is directed to two photodetectors.

In the all-pass configuration, there is only one bus waveguide, so $t_b = 1$. Hence, two circulators are required for proper signal detection, which introduces slight insertion losses. Circulators can also be replaced by Y-branch couplers, which also produce insertion losses. In contrast, for the drop port configuration no circulators are required. In both alternatives, the counter-propagating beams undergo different phase shifts whenever the sensor rotates, which allow for differential measurements.

2.1 Waveguide Coupling

For a system formed by two straight parallel waveguides with identical cross-sections, the modal powers in the injection (P_{in}) and the coupled (P_c) waveguides are functions of wavelength, waveguide geometry, core and cladding refractive indices, separation (gap) between the waveguides, and position along the axial coordinate of the waveguides. Power is exchanged between the waveguides obeying a sine-squared law along the propagation direction [141]. Assuming lossless coupling, at a distance $L_{\otimes}$, known as the cross-over length, all the energy is transferred to the coupled waveguide. According to the so-called supermode theory [42, 79], the cross-over length is:

Table 2.1: Most frequent variables

Symbol	**Meaning**
P_{in}	Input power, injection power, [W] or [dBm]
P_{n}	Noise equivalent power, [W] or [dBm]
λ_0	Laser central wavelength, [m]
ν_0	Laser central frequency, [Hz]
$\Delta\nu$	Laser spectral linewidth, [Hz]
$L = \Sigma L_i$	Total resonator length, [m]
T_R	Resonator roundtrip time, [s]
$L_{\otimes}$	Crossover length, [m]
$L_{ca,cb}$	Waveguide coupling length, region a, b, [m]
L_{opt}	Optimum resonator length, [m]
$L_n = \frac{L}{L_{\text{opt}}}$	Normalized resonator length
α	Field propagation loss [m^{-1}]
α_{dB}	Power propagation loss, [dB]
$\tau = e^{-\Sigma L_i \alpha_i}$	Round-trip field amplitude attenuation coefficient
$t_{a,b}$	Transmission amplitude coefficient, region a, b
$\kappa_{a,b}$	Cross-coupling amplitude coefficient,, region a, b
$\Upsilon = t_a t_b \tau$	$\Delta\nu$-independent transmission-attenuation product
$\Psi = \Upsilon e^{-2\pi\Delta\nu}$	$\Delta\nu$-dependent transmission-attenuation product
ϕ	Detuning [rad]
$\lvert\phi_{\text{HM}_\text{T}}\rvert$	Half-Maximum detuning, Through port [rad]
$\lvert\phi_{\text{HM}_\text{D}}\rvert$	Half-Maximum detuning, Drop port [rad]
$\phi_n = \phi/\pi$	Normalized detuning
C_{IL}	Insertion loss coefficient
IL_{dB}	Insertion loss, [dB]
Ω	Angular rate, [rad/s]
Ω_{dps}	Angular rate, [deg/s]
$\lvert\delta\Omega\rvert$	Angular rate resolution, [rad/s]
$\lvert\delta\Omega\rvert_{\text{opt}}$	Optimum angular rate resolution, [rad/s]
$\lvert\delta\Omega\rvert_{\text{norm}} = \frac{\lvert\delta\Omega\rvert}{\lvert\delta\Omega\rvert_{\text{opt}}}$	Normalized angular rate resolution

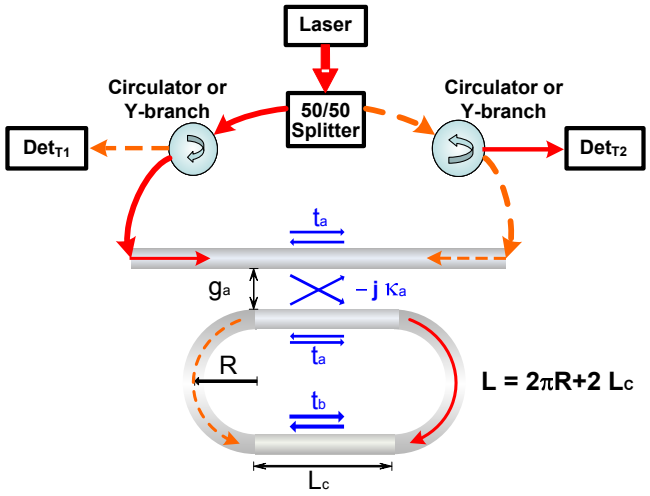

(a) All-pass configuration

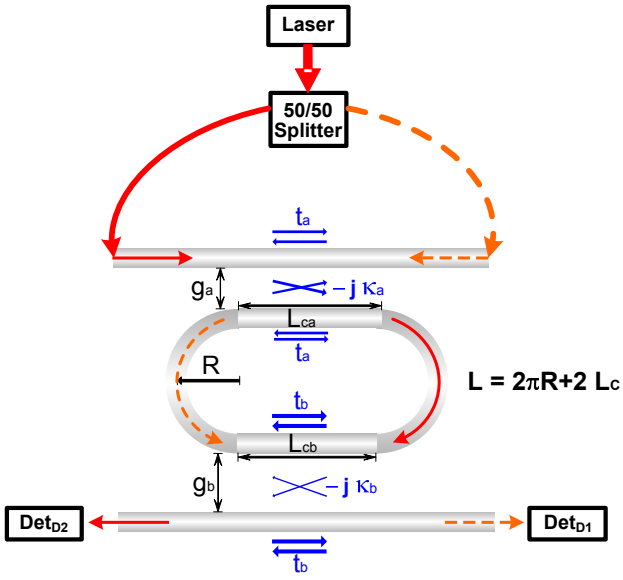

(b) Drop-port configuration

Figure 2.1: Schematic diagram of the All-Pass (top) and Drop-Port (bottom) configurations for a racetrack resonator gyroscope system. Light is split and injected in opposite directions into the racetrack resonators. The output light in each direction is then directed to a photodetector. Circulators are required for proper interrogation in the all-pass configuration, but can be replaced by elements such as Y-branches for easier integration.

$$L_{\otimes} = \frac{\pi}{\beta_{1\text{sym}} - \beta_{1\text{asym}}} = \frac{\lambda_0}{2(n_{\text{eff 1sym}} - n_{\text{eff 1asym}})}, \tag{2.1}$$

where $\beta_{1\text{sym}}$ and $\beta_{1\text{asym}}$ are the propagation constants, and $n_{\text{eff 1sym}}$ and $n_{\text{eff 1asym}}$ are the effective indices of the first (also known as first even) and second (also known as first odd) supermodes of the coupled system, respectively.

For identical coupled waveguides, the modulus of the (dimensionless) field cross-coupling amplitude coefficient, κ, is a function of both $L_{\otimes}$ and the coupling region length, L_c, given by [141]:

$$\kappa = \left| \sqrt{\frac{P_c}{P_{\text{in}}}} \right| = \left| \sin\left(\frac{\pi}{2} \cdot \frac{L_c}{L_{\otimes}} \right) \right|. \tag{2.2}$$

Assuming reciprocity and negligible backscattering in the coupling regions of the rings shown in Fig. 2.1, after obtaining the effective indices of the first two supermodes of the straight couplers a and b, with respective waveguide gaps, g_a and g_b, the cross-over lengths $L_{\otimes\ a,b}$ are obtained for each coupler using Eq. (2.1), and the values of κ_a and κ_b can be determined using Eq. (2.2). Notice that for the all-pass configuration, $g_b \rightarrow\ \infty; \Rightarrow \kappa_b = 0$. Although these moduli are real numbers, a phase shift factor must accompany them to account for the relative phase-shift between the injected and the coupled waves [141], [60]. Assuming $L_c \ll L$, the phase shift between the injected and the coupled waves can be considered constant, and equal to 90 degrees, hence the "$-j$" phase shift factors in Fig. 2.1.

For lossless coupling conditions, the straight-through transmission amplitude coefficient is $t = \sqrt{1-\kappa^2}$. However, if the couplers are lossy, then $t^2 = 1 - \kappa^2 - \gamma^2$, where γ^2 is a coefficient representing the existence of losses in the coupler.

2.2 Sagnac Effect

In any resonator that undergoes a rotation, there is a phase difference proportional to the dot product of the *angular velocity vector* $\vec{\Omega}$ and the *area*

vector $\vec{A}$ of the enclosed optical path [101, 104]. Firstly the equations of the Sagnac effect in vacuum will be derived. Secondly, the case of a resonator made using a waveguide with effective index n_{eff} will be analyzed.

2.2.1 Sagnac Effect in Vacuum

Consider the resonator (assumed circular for simplicity) with radius R, shown in Fig. 2.2, and assume it is built in vacuum, which could be achieved, for instance, by a set of mirrors and a 50/50 beam splitter located at point X. When static, the transit time $t = 2\pi R/c$ for the light to make one round-trip in the ring at a speed $c = 3 \times 10^8$m/s is identical for both beams. However, if the resonator is rotated at an angular speed Ω in a clockwise (CW) direction, the counter-rotating wave, travelling in the counter-clockwise (CCW) direction, represented by the dotted line, will be enhanced in phase when reaching the injection point at position X', as it reaches the displaced beam splitter before geometrically closing the circular path. Conversely, the co-rotating wave, represented by the dashed line, will be retarded in phase when reaching the injection point, as it travels a longer path to reach the coupler, at point X". This can be regarded as an effective travel length change for each beam [8, 44], which will produce a blue- and a red-shift in the resonances of the counter- and co-rotating beams, respectively. To a first order approximation in terms of $\Omega R/c$ the effective travel length changes are:

$$L_{ccw} = 2\pi R - R\Omega t_{ccw} = 2\pi R - \delta L_{ccw} = ct_{ccw} \tag{2.3}$$

$$L_{cw} = 2\pi R + R\Omega t_{cw} = 2\pi R + \delta L_{cw} = ct_{cw}, \tag{2.4}$$

where t_{ccw} and t_{cw} are the travel times of the beams in the CCW and CW direction, respectively.

The travel times for the counter-propagating waves can be expressed as follows:

$$t_{ccw} = \frac{2\pi R}{c + R\Omega} = \frac{\frac{2\pi R}{c}}{1 + \frac{R\Omega}{c}} \approx \frac{2\pi R}{c}\left(1 - \frac{R\Omega}{c}\right) \tag{2.5}$$

$$t_{cw} = \frac{2\pi R}{c - R\Omega} = \frac{\frac{2\pi R}{c}}{1 - \frac{R\Omega}{c}} \approx \frac{2\pi R}{c}\left(1 + \frac{R\Omega}{c}\right), \tag{2.6}$$

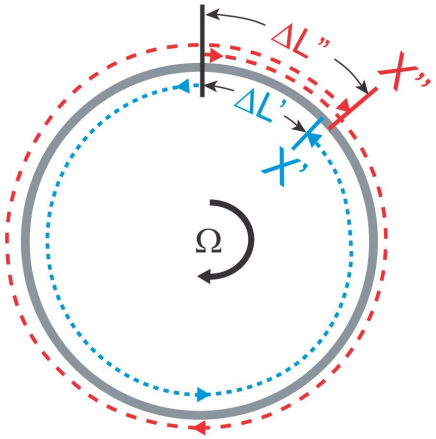

Figure 2.2: Sagnac effect in a clockwise (CW)-rotating resonator.

where first-order Taylor expansions have been used for the last terms of the equalities. The travel time difference is therefore:

$$\Delta t \approx \frac{4\pi R^2 \Omega}{c^2} \tag{2.7}$$

Also to a first order approximation in terms of $\Omega R/c$, valid for $\Omega R \ll c$, both path length differences are equal in magnitude, i.e., points X' and X" are at the same position:

$$\Delta L = L_{cw} - L_{ccw} \approx \frac{4\pi R^2 \Omega}{c}. \tag{2.8}$$

$$\delta L = \delta L_{ccw} = \delta L_{cw} \approx \frac{2\pi R^2 \Omega}{c} = \frac{\Delta L}{2} \tag{2.9}$$

2.2.2 Sagnac Effect in a Dielectric Medium

When the light travels in a waveguide fabricated with a material of refractive index $n = n(\lambda)$, the waveguide will exhibit a wavelength-dependent effective refractive index $n_{\text{eff}} = n_{\text{eff}}(\lambda)$ [39]. In this case, Eqs. (2.3) and (2.4) become:

$$L_{ccw\ n} = 2\pi R n_{\text{eff}} - \delta L_{ccw\ n} \approx (2\pi R - \delta L) n_{\text{eff}} \tag{2.10}$$

$$L_{cw\ n} = 2\pi R n_{\text{eff}} + \delta L_{cw\ n} \approx (2\pi R + \delta L) n_{\text{eff}}. \tag{2.11}$$

Since the medium is not vacuum, and considering the postulates of special relativity, it is no longer possible to consider that the speed of light is the same for both counter-propagating waves as we did before. The speed of light in the medium, $v = c/n_{\text{eff}}$, will be the same for both directions only if the observer is moving along with the rotating medium. Therefore, in order to estimate the speed of light as observed in the laboratory, a relativistic addition of speeds [103, 131] is necessary. The velocities of light u_{cw} and u_{ccw} for the CW and the CCW waves as measured by a stationary observer are given by:

$$u = \frac{c/n_{\text{eff}} \pm \Omega R}{1 \pm \frac{c/n_{\text{eff}} \Omega R}{c^2}} \tag{2.12}$$

To a first order approximation with respect to ΩR:

$$u_{cw} = \frac{c}{n_{\text{eff}}} + \Omega R \zeta \tag{2.13}$$

$$u_{ccw} = \frac{c}{n_{\text{eff}}} - \Omega R \zeta, \tag{2.14}$$

where the term $\zeta = 1 - \frac{1}{n_{\text{eff}}^2}$ is known as the Fresnel-Fizeau Drag coefficient [101, 131]. The travelling times for the CW and CCW waves then are:

$$t_{cw\ n} = \frac{L_{cw\ n}}{u_{cw}} = \frac{n_{\text{eff}}(2\pi R + \delta L)}{\frac{c}{n_{\text{eff}}} + \Omega R \zeta} \tag{2.15}$$

$$t_{ccw\ n} = \frac{L_{ccw\ n}}{u_{ccw}} = \frac{n_{\text{eff}}(2\pi R - \delta L)}{\frac{c}{n_{\text{eff}}} - \Omega R \zeta}. \tag{2.16}$$

Therefore, from Eqs. (2.15) and (2.16), the travel time difference is, to a first order approximation (valid for $\Omega R \ll c$):

$$\Delta t_n \approx \frac{4\pi R^2 \Omega}{c^2} n_{\text{eff}}^2 (1 - \zeta) = \frac{4\pi R^2 \Omega}{c^2} = \Delta t, \tag{2.17}$$

which is the same travel time difference as for vacuum, shown in Eq. (2.7). Thus, to a first order approximation in terms of $\Omega R/c$, the phase shift ex-

perienced by each beam, either in vacuum or in a dielectric medium, is independent of the refractive index. If the medium is a fiber wound in a coil of N turns, then Eq. (2.7 will be multiplied by N [44], but for the case of a resonant optical waveguide gyroscope, $N = 1$, and the resonator length is $L = 2\pi R$. Since $\omega = \Delta\phi/\Delta t$ and $\omega = 2\pi c/\lambda$, where λ is the free-space wavelength of light, the total phase shift between both beams due to the Sagnac effect for a resonant optical waveguide gyroscope is:

$$|\Delta\phi| = \frac{8\pi}{c\lambda_0}\overrightarrow{A}\cdot\overrightarrow{\Omega} = \frac{8\pi^2 R^2\Omega}{c\lambda} = \frac{2L^2\Omega}{c\lambda}. \tag{2.18}$$

In the particular case of a resonant optical waveguide gyroscope, the variable ϕ, known as the *detuning* [60, 127], is different for each propagating beam. The detuning for the co-rotating (counter-rotating) beam, ϕ, is the algebraic sum of the phase undergone by each beam in one roundtrip through the ring, ϕ_{ring}, identical for both beams, plus (minus) the Sagnac phase shift, $\delta\phi = \frac{L^2\Omega}{c\lambda}$, proportional to the path length elongation (reduction) by δL:

$$\phi = \phi_{\text{ring}} \pm \delta\phi = \frac{2\pi n_{\text{eff}}(\lambda)L}{\lambda} \pm \frac{L^2\Omega}{c\lambda}. \tag{2.19}$$

The electric field of the laser light can be described in terms of time and space variables, t and z, respectively, as $E = E_0 e^{j\left(\omega t - \frac{2\pi n_{\text{eff}}}{\lambda} z\right)}$, where ω is the central angular frequency of the laser light. In the case of a resonator (see Fig. 2.2), a roundtrip is completed whenever $z = ML = M2\pi R$. Equivalently, a roundtrip is completed whenever t increases its value by the roundtrip time T_R, i.e., $t = MT_R$, as the total phase of the complex exponential remains the same. Therefore, the electric field in the resonator can be writtten as:

$$E = E_0 e^{j(\omega t - \phi)} \tag{2.20}$$

The first term of Eq. (2.19) can also be written as its time-domain equivalent, i.e., $2\pi L n_{\text{eff}}(\lambda)/\lambda = \omega T_R$, where ω is the central angular frequency of the laser light, and $T_R = Ln_{\text{eff}}(\lambda)/c$ is the time required to complete a roundtrip in the resonator. This substitution will prove useful for the phase noise analysis (Section 2.3.6).

Eqs. 2.19 and 2.20 allow one to see the phase retardation and enhancement caused by the Sagnac effect for each beam. For the co-rotating beam, the effective cavity length increases (positive sign in Eq. 2.19), producing a red shift in the resonance. In order to maintain a constant phase in the argument of Eq. 2.20, more time has to elapse, i.e., the wave is phase retarded. Conversely, for the counter-rotating beam, the effective cavity length decreases (negative sign in Eq. 2.19) producing a blue-shift, and in order to maintain a constant phase in the argument of Eq. 2.20, less time should elapse, i.e., the wave is phase-enhanced. The red- and blue-shifts are illustrated in Fig. 2.3.

2.3 Analytical and Numerical Modelling

By computing an infinite sum of successive round-trip field couplings for the racetrack resonators shown in Figs. 2.1(a) and 2.1(b), in a similar way as done by Vorckel et al. [133], but maintaining the phase sign convention of Eq. 2.20, the S parameters for the through- and drop-port transmission fields, S_{21} and S_{41}, are given by:

$$S_{21} = \frac{t_a - t_b \tau e^{-j\phi}(1-\gamma_a^2)}{\sqrt{C_{\mathrm{IL}}}(1-\Upsilon e^{-j\phi})} \tag{2.21}$$

$$S_{41} = -\frac{\kappa_a \kappa_b \sqrt{\tau} e^{-j\frac{\phi}{2}}}{\sqrt{C_{\mathrm{IL}}}(1-\Upsilon e^{-j\phi})}, \tag{2.22}$$

where $\tau = e^{-\Sigma L_i \alpha_i}$ is the round-trip amplitude (field) propagation attenuation, L_i is the length of the waveguide segment i, $i = 1, 2, ...N$, $L = \sum_{i=1}^{N} L_i$ is the length of the resonator, α_i denotes the field propagation loss of the waveguide segment i, in units of m^{-1}, $\Upsilon = t_a t_b \tau$, t_a and t_b are the (dimensionless) field through-transmission amplitude coefficients of regions a and b, κ_a and κ_b are the field coupling coefficients of regions a and b; γ_a and γ_b are the coefficients representing the existence of coupling losses, such that $t_a^2 = 1 - \kappa_a^2 - \gamma_a^2$ and $t_b^2 = 1 - \kappa_b^2 - \gamma_b^2$; $C_{\mathrm{IL}} = 10^{\frac{IL_{\mathrm{dB}}}{10}} e^{\alpha L_{\mathrm{bus}}}$ is a coefficient representing the amplitude decrease due to insertion loss, IL_{dB}, (in dB),

as well as the propagation losses in the bus waveguide(s). Assuming that the waveguide directional coupler (WDC) is small in comparison to the total resonator length, its phase shift contribution has been neglected. In all cases, $\alpha \geq 0$ m^{-1}; $0 \leq t_{a,b} \leq 1$; $0 \leq \kappa_{a,b} \leq 1$; $0 \leq \gamma_{a,b} \leq 1$; $IL_{\mathrm{dB}} \geq 0$ dB; and $C_{\mathrm{IL}} \geq 1$, are real numbers. In the case of lossless coupling, $\gamma_{a,b} = 0$ and $t_{a,b}^2 = 1 - \kappa_{a,b}^2$.

Fig. 2.3 illustrates the resonant Sagnac gyroscope concept. At rest, the spectra for light beams propagating in the resonator in opposite directions are identical, and depicted by the solid line. As per Fig. 2.2, and Eqs. (2.3), (2.4), (2.9), (2.19), and (2.20), for a CW-rotating resonator, the co-rotating (i.e., CW) beam will be red-shifted due to its longer equivalent resonator length, $L_{\mathrm{CW}} = L_{\mathrm{ring}} + \delta L$. Conversely, the counter-rotating (i.e., CCW) beam will be blue-shifted due to its shorter equivalent resonator length, $L_{\mathrm{CW}} = L_{\mathrm{ring}} - \delta L$. The co-rotating beam is considered to be retarded in phase, and its resonance shifts towards more negative values of ϕ_{ring} (red dashed curve). The counter-rotating beam is considered to be enhanced in phase, and its resonance shifts towards more positive values of ϕ_{ring} (blue dashed curve). This produces a difference between the light intensities of both counter-propagating beams, which can be used for a differential measurement of the angular velocity.

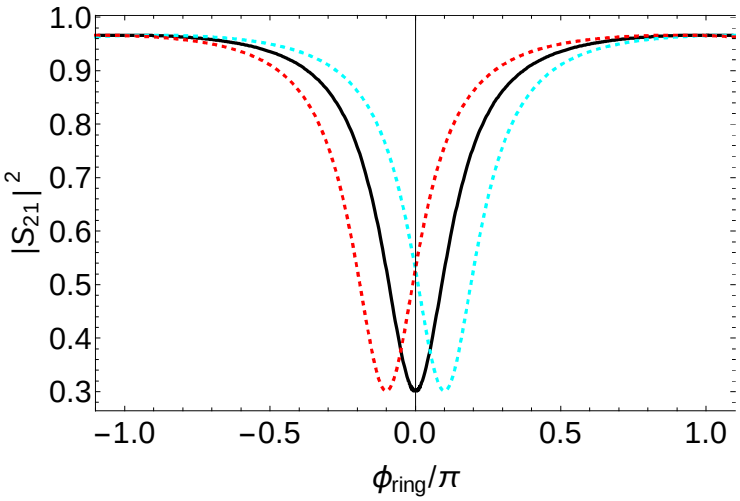

(a) Amplitude response

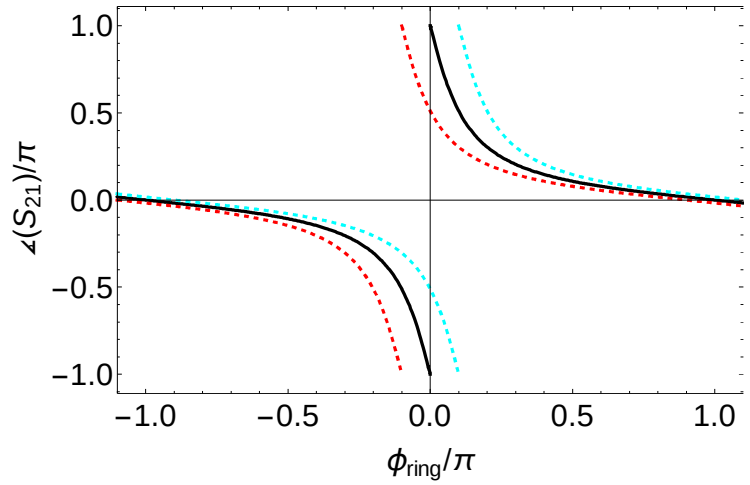

(b) Phase response

Figure 2.3: Normalized spectra of the counter-propagating light beams in an all-pass (single-bus) racetrack resonator. Solid curve: resonator at rest. Dashed curves: spectra for the co-rotating (red curve, red-shifted) and the counter-rotating (cyan curve, blue-shifted) beams. For this example, $\alpha_{\text{dB}} = 0.01$ dB/cm, $L = 1$ m, $\kappa = 1/\sqrt{2}$. A Sagnac phase shift $\delta\phi = 0.1\pi$ rad has been used to produce a noticeable phase shift.

Although the proper units of α are m^{-1}, in the literature propagation losses are usually reported in units of dB/cm. In the present work, α represents field attenuation, not power attenuation. In order to avoid confusions, a "dB" subscript will be added in the case of power attenuations, reported in dB/cm, and the equation below will be used to transform one to the other:

$$\alpha[\mathrm{m}^{-1}] = 5 \cdot \ln(10) \cdot (\alpha_{\mathrm{dB}}[\mathrm{dB/cm}]) \tag{2.23}$$

2.3.1 Through- and Drop-Port Power Transmission

The expressions for the through- and drop-port power transmission amplitudes are, based on Eqs. (2.21) and (2.22):

$$|S_{21}|^2 = \frac{t_a^2 - 2\Upsilon\Gamma_a \cos(\phi) + t_b^2\Gamma_a^2\tau^2}{C_{\mathrm{IL}}\left[1 - 2\Upsilon\cos(\phi) + \Upsilon^2\right]} \tag{2.24}$$

$$|S_{41}|^2 = \frac{\kappa_a^2\kappa_b^2\tau}{C_{\mathrm{IL}}\left[1 - 2\Upsilon\cos(\phi) + \Upsilon^2\right]}, \tag{2.25}$$

where $\Gamma_a = 1 - \gamma_a^2$. Since the amplitude responses $|S_{21}|^2$ and $|S_{41}|^2$ represent normalized power transmissions, they can also represent the normalized current in a photodetector. From the numerator of Eq. (2.21), at resonant steady state (i.e., $\phi = 2m\pi$, m is an integer), and assuming lossless coupling (i.e., $\gamma_{a,b} = 0$), it is possible to see that whenever:

$$t_a = t_b\tau, \tag{2.26}$$

the through-port signal is cancelled, i.e., $S_{21} = 0$, and for an add-drop ring, the output at the drop port is maximal. This particular case, known as critical coupling (CC), reduces to $t_a = \tau$ for the single-bus waveguide case ($t_b = 1$), a particular case depicted in [141]. For a symmetrically-coupled ring (i.e., $t_a = t_b$), critical coupling is strictly possible only if the waveguides are lossless ($\alpha = 0\ \mathrm{m}^{-1}$).

In contrast to the single-bus waveguide case, where the critical coupling condition requires a unique value of t_a (and hence a unique value of κ_a), for

the double-bus resonator case, Eq. (2.26) is satisfied for an infinite number of values of κ_b. In fact, for any given α, the slope of the spectral notch (through port) or the spectral spike (drop port) of any double-bus resonator depends on L, κ_a, κ_b and ϕ. Our initial, intuitive assumption was that the CC condition would show the largest extinction ratio due to its null through-port output at resonance. However, as shown in the modelling of Sections 2.3.4 and 2.3.5, this is not the case.

2.3.2 Figures of Merit of the Spectral Response

Extinction Ratio

From Eqs. (2.24) and (2.25), the extinction ratios $ER_{dB_{21}}$ and $ER_{dB_{41}}$, in dB, for the through and the drop ports are, respectively:

$$ER_{dB_{21}} = 10\ \log_{10}\left[\frac{(t_a + t_b\tau)^2(1-\Upsilon)^2}{(t_a - t_b\tau)^2(1+\Upsilon)^2}\right] \tag{2.27}$$

$$ER_{dB_{41}} = 10\ \log_{10}\left[\frac{(1+\Upsilon)^2}{(1-\Upsilon)^2}\right], \tag{2.28}$$

Full Width at Half Maximum

The full width at half-maximum (FWHM) is defined as the difference of the values of the independent variable (either frequency, wavelength, or phase), for which the spectral response is at the midpoint between the normalized baseline and the resonance trough or dip, for the through and the drop port, respectively.

Quality Factor

In this work, we followed the definition of quality factor as the resonance wavelength divided by the (wavelength) FWHM: $Q = \frac{\lambda_0}{\Delta\lambda}$. In order to derive it, we firstly obtained the values of ϕ that yield, for each port, half of the maximum normalized amplitude, $|\phi_{\mathrm{HM}}|$. After algebraic manipulation of Eq. (2.25), based on the definition of FWHM described above, we have

the same result for both ports:

$$|\phi_{\mathrm{HM_T}}| = |\phi_{\mathrm{HM_D}}| = |\phi_{\mathrm{HM}}| = \cos^{-1}\left[\frac{1-2(1-\Upsilon)^2+\Upsilon^2}{2\Upsilon}\right]. \tag{2.29}$$

Thus, the bandwidth in terms of wavelength is:

$$\Delta\lambda = \frac{\lambda^2\phi_{\mathrm{HM}}}{\pi\Sigma\left(n_{g_i}L_i\right)} \tag{2.30}$$

where n_{g_i} and L_i are the group index and length of the i^{th} waveguide segment of the racetrack resonator. Finally, the quality factor is:

$$Q_{=}\frac{\pi\Sigma\left(n_{g_i}L_i\right)}{\lambda_0\,\cos^{-1}\left[\frac{1-2(1-\Upsilon)^2+\Upsilon^2}{2\Upsilon}\right]} \tag{2.31}$$

Free Spectral Range

The free spectral range (FSR) [60] of the resonator can be defined in terms of the (group) optical path and the resonant wavelength for a resonator with N segments of different lengths L_i and group indices n_{g_i}, $i = 1, 2, ..., N$, as:

$$\mathrm{FSR} = \frac{\lambda_0^2}{\sum_{i=1}^{N} n_{g_i}L_i} \tag{2.32}$$

Finesse

The finesse of the ring resonators is the ratio of the FSR and the FWHM, which can be expressed as:

$$F = \frac{\mathrm{FSR}}{\mathrm{FWHM}} = \frac{Q\lambda_0}{n_g L} = \frac{\pi}{\cos^{-1}\left[\frac{1-2(1-\Upsilon)^2+\Upsilon^2}{2\Upsilon}\right]} \tag{2.33}$$

2.3.3 Loss Impact on Performance

For the CC double-bus case, κ_b was chosen as our independent coupling variable. Fig. 2.4 shows κ_a as a function of κ_b at CC, assuming lossless coupling (i.e., $\gamma_a^2 = \gamma_b^2 = 0$), for a resonator with a length $L = 50$ mm.

Four different propagation loss values are used in this figure. The first three, $\alpha_{\mathrm{dB}} = 0.06$ dB/cm, $\alpha_{\mathrm{dB}} = 0.12$ dB/cm, and $\alpha_{\mathrm{dB}} = 3.0$ dB/cm, correspond respectively to propagation loss levels reported for waveguides fabricated in SiN [53, 91] and SOI [13] technologies. The fourth value is a theoretical average propagation loss value of $\alpha_{\mathrm{dB}} = 1.17$ dB/cm, achievable by using SOI waveguide segments of different widths (and thus, propagation losses) to create the resonator. For small propagation losses, κ_a tends to a non-zero value for low values of κ_b, and behaves almost as an identity function (i.e., $\kappa_a \approx \kappa_b$) for medium to large values of κ_b. In the limit when $\alpha \to 0 \Rightarrow \ \kappa_a \to \kappa_b$.

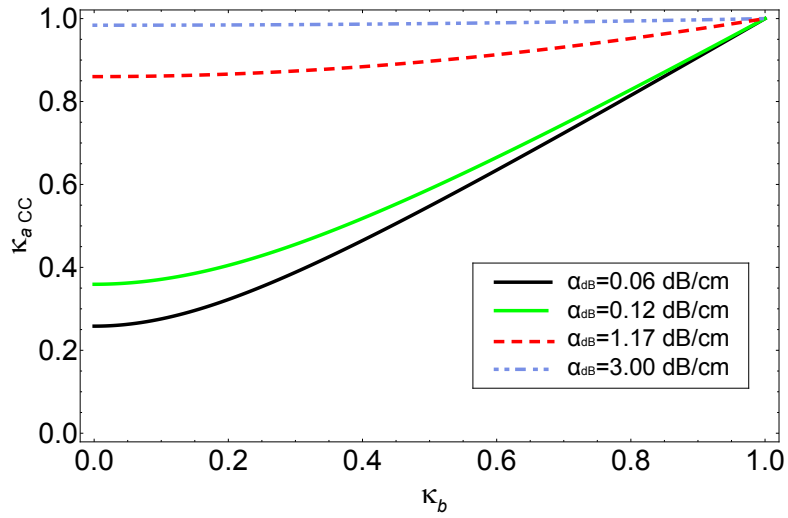

Figure 2.4: Magnitude of field coupling coefficient of waveguide a, (κ_a), as a function of coupling coefficient κ_b, for critically coupled, 50-mm long ring resonators, for propagation loss levels of different technologies: $\alpha_{\mathrm{dB}} = 0.06$ dB/cm (SiN, [91]), $\alpha_{\mathrm{dB}} = 0.12$ dB/cm(SiN, [53]), $\alpha_{\mathrm{dB}} = 3.0$ dB/cm(SOI, [13]), and $\alpha_{\mathrm{dB}} = 1.17$ dB/cm (estimate for SOI material with waveguide width variation, proposed in the present work as a low-loss alternative for SOI technology).

If the product αL is too large, most of the energy will be lost after a few roundtrips in the resonator, as can be concluded based on the finesse values of Fig. 2.5, which hinders the resolution. In particular for the CC

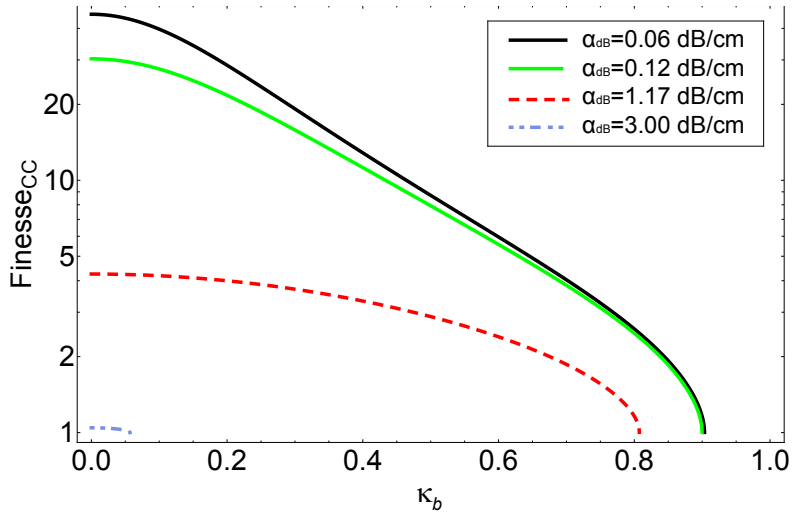

Figure 2.5: Finesse as a function of coupling coefficient κ_b, for critically coupled, 50-mm long ring resonators, for propagation loss levels of different technologies: $\alpha_{\mathrm{dB}} = 0.06$ dB/cm (Si_3N_4, [91]), $\alpha_{\mathrm{dB}} = 0.12$ dB/cm(Si_3N_4, [53]), $\alpha_{\mathrm{dB}} = 3.0$ dB/cm(SOI, [13]), and $\alpha_{\mathrm{dB}} = 1.17$ dB/cm (proposed SOI design with waveguide width variation).

case, as the product αL increases, the value of κ_a becomes larger and less dependent on κ_b in order to fulfill Eq. (2.26), describing an almost-flat line that quickly tends to unity (see Fig. 2.4). For $\alpha L \approx$ 2.5, we can consider that the value of κ_a is already unity regardless of the value of κ_b. As will be shown in the following section, large coupling values imposed by the CC condition imply that energy is drained out of the resonator faster than if the ring is optimally coupled (OC) below the CC value.

For both the CC and the OC case, ever decreasing losses are required so that the resonator length and enclosed area can be increased, and the coupling values can be decreased, thus enhancing the Sagnac effect and achieving better resolution values. For any given propagation loss α, (dictated by the material and fabrication technology), there is an optimal set of values for L, κ_a, κ_b and ϕ that globally optimize the resolution, even though they do not yield the absolute maximum in the spectral response slope. Such parameters are different for the through and the drop configurations

because the optimal configuration for the through-port cases is always a Gires-Tournois (all-pass) [60] configuration, which implies that the resonant cavity is less loaded due to the absence of a drop port.

2.3.4 Spectral Response for the Through Port

In this section, the spectral characteristics of the through port will be described, and expressions for finding the value of ϕ that maximizes the slope of the spectral response as a function of the resonator length and couplings will be derived. For simplicity, lossless coupling and negligible ILs are assumed from now on, unless otherwise stated, i.e., $\gamma_a = \gamma_b = 0$; $C_{\mathrm{IL}} = 1$. The ILs can be incorporated later on without loss of generality. The first and second derivatives of the through-port spectral response are:

$$\frac{\partial |S_{21}|^2}{\partial \phi} = \frac{2\kappa_a^2 \Upsilon \left(1 - t_b^2 \tau^2\right) \sin(\phi)}{\left[1 - 2\Upsilon \cos(\phi) + \Upsilon^2\right]^2} \tag{2.34}$$

$$\frac{\partial^2 |S_{21}|^2}{\partial \phi^2} = \frac{2A\kappa_a^2 \Upsilon \left[B\cos(\phi) + \Upsilon[\cos(2\phi) - 3]\right]}{\left[1 - 2\Upsilon \cos(\phi) + \Upsilon^2\right]^3}, \tag{2.35}$$

where $A = 1 - \tau^2 t_b^2$ and $B = 1 + \Upsilon^2$. For a given length L and propagation loss α, there is a certain combination of couplings κ_a, κ_b and detuning ϕ that produces a maximum slope in the spectral response. At such a point the numerator of Eq. (2.35) is zero. By solving for ϕ (modulo 2π), and discarding any complex roots:

$$\phi_{\mathrm{MS}_T} = \pm \cos^{-1}\left[\frac{-1 - \Upsilon^2 + \sqrt{1 + 34\Upsilon^2 + \Upsilon^4}}{4\Upsilon}\right]. \tag{2.36}$$

Eq. (2.36) yields the same results as Eq. (6) in [127], but it is a more general expression, due to the inclusion of the drop port (κ_b) in the model.

Fig. 2.6 shows the through-port spectral response and its first derivative as a function of the normalized detuning, ϕ/π, for two all-pass resonators[1] with identical propagation loss $\alpha_{\mathrm{dB}} = 0.06$ dB/cm and identical length, in

[1] As will be shown in Subsection 2.3.7, all optimized through-port resonators are all-pass resonators, i.e., $\kappa_b = 0$.

CC and OC conditions, respectively. The length $L = 1.63$ m $= L_{\text{opt21CC}}$ corresponds to the optimum length for the CC resonator. It is noticeable that, as long as the length is the same, the maximum OC slope is almost twice as large as the maximum CC slope, even though the OC resonator lacks zero response at resonance. This trend is the same for all values of propagation loss, demonstrating that OC resonators perform better than their CC counterparts.

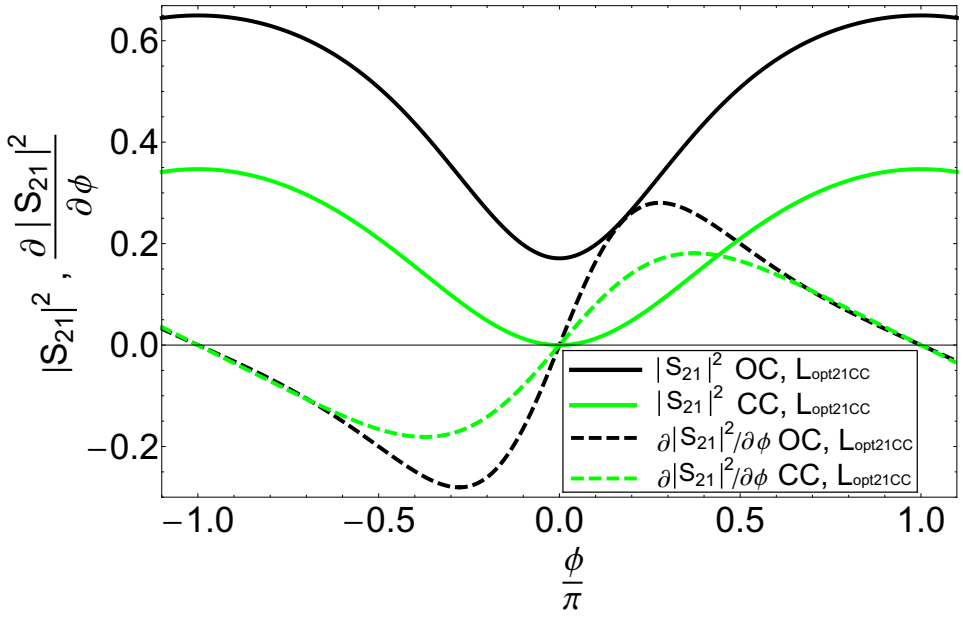

Figure 2.6: Through port response, $|S_{21}|^2$ (solid), and first derivative, $\frac{\partial |S_{21}|^2}{\partial \phi}$ (dashed), as a function of ϕ/π, for $\alpha_{\text{dB}} = 0.06$ dB/cm and $L = L_{\text{opt21CC}} = 1.63$ m. In all cases, $\kappa_b \to 0$ (all-pass resonators). In spite of lacking a zero output at resonance, the OC case shows a larger maximum slope, at a smaller detuning in comparison to the CC case (see Table 2.2).

A resonator with a steeper slope *for a fixed resonator length value* will indeed yield a better resolution. This fact initially led us to the intuitive misconception that ever growing slopes would always yield better performance. In fact, as shown in Fig. 2.7 and in Table 2.2, for low-loss waveguides ($\alpha_{\text{dB}} = 0.06$ dB/cm), the largest slopes occur at very small resonator lengths, but from a gyroscopic viewpoint, the optimum length is larger. Even

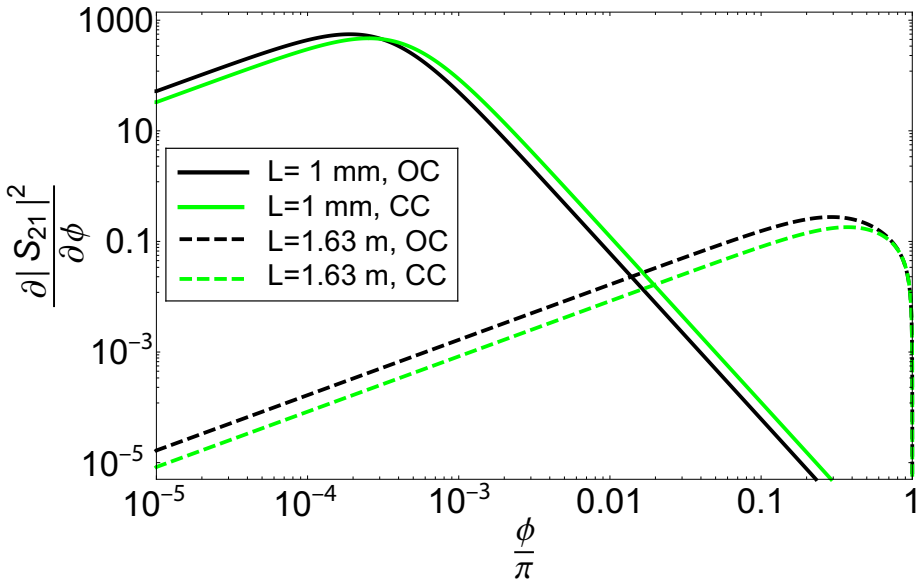

Figure 2.7: Slope of the optimized all-pass frequency response, $\frac{\partial|S_{21}|^2}{\partial\phi}$, as a function of ϕ/π, for $\alpha_{\mathrm{dB}} = 0.06$ dB/cm (i.e., $\alpha = 0.69$ m^{-1}), $L =$ 1 mm (solid) and $L = L_{\mathrm{opt21}} = 1.63$ m (dashed). Black curves: OC; Light curves: CC. The small resonators yield larger slopes at smaller detunings. However, as shown in Table 2.2, they do not yield the best resolutions.

if the spectral slope (and thus the extinction ratio) is considerably larger for lengths $L < L_{\mathrm{opt}}$, the resolution at L_{opt} will always be the best, since the resolution is inversely proportional not only to the spectral slope, but also to L^2 (see subsection 2.3.7). Therefore, maximizing the product $L^2\frac{\partial|S_{21}|^2}{\partial\phi}$, rather than just the slope, is necessary to ensure the best resolution.

In order to compare the slopes of the four resonators considered in Fig. 2.7, logarithmic scales are needed, hence, only positive detuning values were plotted. However, the ordinate-axis-symmetry of the spectrum and the origin-symmetry of its derivative, are conserved in a linear scale. The slopes of the small resonators are almost four orders of magnitude larger than those of the large resonators. However, as shown in Table 2.2, the resolutions of the small resonators are ~ 3 orders of magnitude worse than

Table 2.2: Parameters for different lengths and coupling conditions, through port, all-pass configuration, for $\alpha_{\mathrm{dB}} = 0.06$ dB/cm

Param. \ L	1 mm (CC)	1 mm (OC)	1.63 m (CC)	1.63 m (OC)
$\kappa_{\mathrm{a\ opt}}$	0.037	0.0263	0.945	0.759
$\frac{\phi_{\mathrm{MT}}}{\pi}$	250×10^{-6}	190×10^{-6}	0.373	0.277
Max. slope [rad^{-1}]	470.7	558	0.181	0.276
$\lvert\delta\Omega\rvert$ [deg/s]	3.98	3.37	0.00392	0.00253

those of the large resonators. Once again it is possible to observe that for identical values of α and L, the maximum spectral slope for the OC case (solid) is always larger than that of the CC case (dashed), and it occurs for smaller values of ϕ, despite not having a zero output at resonance, due to the under-coupling of any OC case.

2.3.5 Spectral Response for the Drop Port

For the drop port case, the OC condition also shows larger slopes than the CC condition for resonators with identical lengths and propagation losses. The first and second derivatives of the drop-port response are:

$$\frac{\partial |S_{41}|^2}{\partial \phi} = \frac{-2\kappa_a^2 \kappa_b^2 \tau \Upsilon \sin(\phi)}{\left[1 - 2\Upsilon \cos(\phi) + \Upsilon^2\right]^2} \tag{2.37}$$

$$\frac{\partial^2 |S_{41}|^2}{\partial \phi^2} = \frac{2\kappa_a^2 \kappa_b^2 \tau \Upsilon \left[B \cos(\phi) + \Upsilon[\cos(2\phi) - 3]\right]}{\left[1 - 2\Upsilon \cos(\phi) + \Upsilon^2\right]^3} \tag{2.38}$$

Due to its numerator structure, the roots (real, modulo 2π) of Eq. (2.38) are the same as those for Eq. (2.36):

$$\phi_{\mathrm{MS}_D} = \pm \cos^{-1}\left[\frac{-1 - \Upsilon^2 + \sqrt{1 + 34\Upsilon^2 + \Upsilon^4}}{4\Upsilon}\right]. \tag{2.39}$$

However, the spectral response values (Eqs. (2.24) and (2.25)) and their

first derivatives (Eqs. (2.34) and (2.37)) are quite different for the through and drop ports, and thus a new optimization is necessary to find the combination of L, $\kappa_{a,b}$ and ϕ_{MD} that yields the best resolution.

Fig. 2.8 shows the drop-port normalized spectral response ($|S_{41}|^2$, solid), and its first derivative with respect to ϕ (dashed) as a function of the normalized detuning, $\phi_n = \phi/\pi$, for an OC (black) and a CC (light) resonator, both with identical lengths and propagation losses.

From Figs. 2.6 and 2.8, and as will be shown in detail in Section 2.4, it is possible to conclude that *the all-pass configuration offers a higher performance thanks to its longer optimum length, larger maximum slope and thus better resolution.* Its lower cavity loading contributes to smaller round trip losses, which in turn allow for larger slopes and larger optimum lengths. In both the all-pass and the drop cases, OC resonators perform better than CC resonators, even at the optimum CC lengths, $L_{\mathrm{opt}_{21\mathrm{CC}}}$ and $L_{\mathrm{opt}_{41\mathrm{CC}}}$, respectively. For the sake of clarity and briefness, only OC cases will be plotted and discussed from now on, unless stated otherwise.

We will see in the next subsection that the best resolution, $|\delta\Omega|_{\mathrm{opt}}$ for a particular α, will depend upon the optimization of L, ϕ, κ_b and κ_a for the particular port under study. The examples depicted in Figs. 2.6 and 2.8 were obtained with globally optimized all-pass- and drop-port parameters, respectively; i.e., the only restrictions for the values of the parameters were those imposed by the propagation losses and the physical model of the system. This is useful for illustration purposes, but rather impractical for fabrication, as the lengths are not feasible in a standard 200-mm SOI wafer.

In case of lengths smaller than the optimum length L_{opt}, the parameters ϕ, κ_b and κ_a can, and should still be, tuned for achieving the best possible resolution. The best achievable resolution in such a case will obviously be worse than the global, unconstrained optimum, due to the decrease of length and thus smaller Sagnac phase shift. The parameters ϕ, κ_b and κ_a are identical for different values of α if expressed in terms of a normalized length $L_{\mathrm{n}} = L/L_{\mathrm{opt}}$.

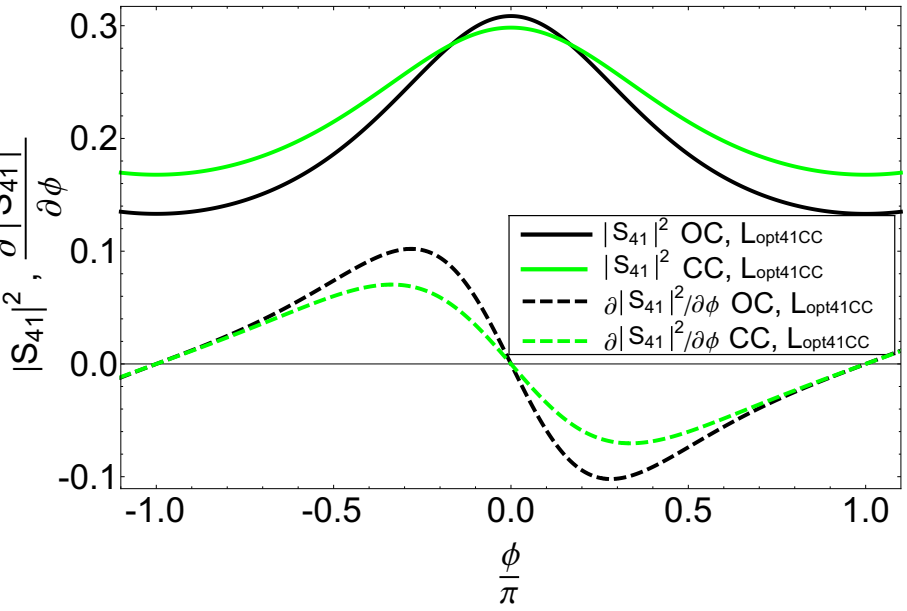

Figure 2.8: Drop-port frequency response, $|S_{41}|^2$ (solid), and first derivative, $\frac{\partial|S_{41}|^2}{\partial\phi}$, (dashed), as a function of ϕ/π, for $\alpha_{\mathrm{dB}} = 0.06$ dB/cm and $L = L_{\mathrm{opt}_{41\mathrm{CC}}} = 0.93$ m, for OC and CC cases. The parameters are: $\kappa_{b_{CC}} = 0.697 \Rightarrow \kappa_{a_{CC}} = 0.926$, $\kappa_{a_{OC}} = \kappa_{b_{OC}} = 0.779$. From the dotted curves, it is evident that the OC case has a larger maximum spectral slope, which occurs at a smaller normalized detuning.

2.3.6 Noise Analysis

In order to compute the minimum resolvable angular rate $\delta\Omega_n$, it is necessary to first determine the amplitude noise level of the system, as well as the effect of the laser linewidth (phase noise) on the resonator spectral response.

Amplitude Noise

The amplitude noises that were taken into account in the present section are the shot noise, thermal noise and laser noise [141]. Amplitude noise effects related to Rayleigh backscattering [27, 67, 90, 92, 124] were neglected in this section, as spectral modulation techniques [30, 62, 63, 82] allow for reducing backscattering noise and achieve shot-noise limited resolution. Based on

the formulae for the aforementioned noise components (e.g., see [141]) and considering them statistically independent, the standard deviation of the photocurrent (i.e., the noise rms current) is:

$$\delta i = \sqrt{\left(2qi_D + \frac{4k_BT}{R_L} + i_D^2 RIN\right) B}, \tag{2.40}$$

where $q = 1.6 \times 10^{-19}$ C is the fundamental electric charge, $i_D = RP_{in}$ is the maximum photodiode current, P_{in} is the maximum power incident onto the photodetector, $R = \frac{q\eta}{h\nu}$, in units of A/W, is the responsivity of the photodiode, $h = 6.626 \times 10^{-34}$ J $\cdot$ s is Planck's constant, ν is the optical wave frequency in Hz, η is the quantum efficiency, B is its bandwidth in Hz, $k_B = 1.38 \times 10^{-23}$ J/K is Boltzman's constant, R_L denotes the photodetector load resistance, and RIN is the relative intensity noise of the laser, usually expressed in dB/Hz [141].

Fig. 2.9 shows the different noise components, the total noise and the SNR as a function of the power incident upon the photodetector, for the case depicted in Table 2.3. For $P_{in} = 0$ dBm and RIN$=-145$ dB/Hz (consistent with our Agilent 81682A tuneable laser), the system is theoretically laser-noise limited, with SNR$\approx$ 67 dB for a 10-Hz bandwidth. According to our simulations, a RIN≈ -160 dB/Hz is required to achieve shot-noise limit. This can be achieved using low-RIN laser sources [16, 47]. The remainder of this Section and Section 2.4 show resolution estimations for a shot-noise limited case, as originally published in [54]. Subsection 2.4.5 shows the impact of SNR degradation on the achievable resolution.

Phase Noise

Due to phase fluctuations associated with spontaneous emission and carrier density fluctuations [24], laser sources exhibit a (normalized) Lorentzian optical power spectral density of the form:

$$\mathcal{P}(\nu) = \frac{2\Delta\omega}{(\Delta\omega)^2 + (\omega - \omega_0)^2}, \tag{2.41}$$

where $\omega = 2\pi\nu$ is the instantaneous angular frequency, $\omega_0 = 2\pi\nu_0$ is the central angular frequency, $\Delta\omega = 2\pi\Delta\nu$, and $\Delta\nu$ is the full linewidth at half maximum [24, 97], expressed in Hz. The electric field in the time domain is:

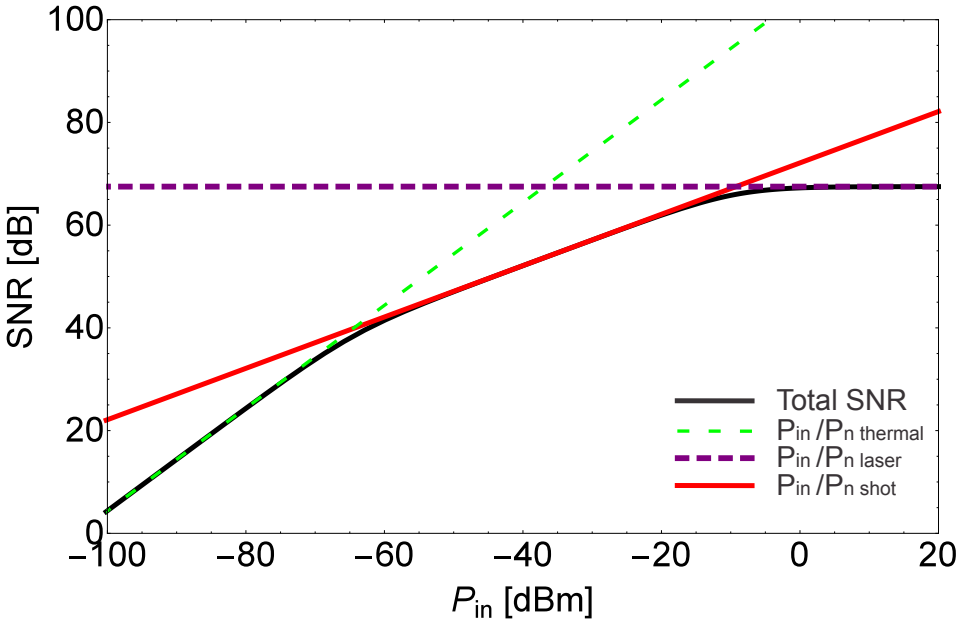

Figure 2.9: Signal-to-noise ratio (SNR) of various noise components (thermal noise, laser noise, and shot noise) and total SNR as functions of input power, for a photodetector with the parameters shown in Table 2.3 (see legend for proper identification).

$$E_{in}(t) = E_0 e^{j\omega_0 t + \vartheta(t)}, \tag{2.42}$$

where $\vartheta(t)$ is the stochastic phase variation, and E_0 is the electric field modulus. It is possible to characterize the behaviour of this field using its normalized autocorrelation function [99]:

$$C_{EE}(T_R) = \overline{E(t)E\,(t+T_R)^*}/\overline{|E(t)|^2}, \tag{2.43}$$

where the upper bar denotes time averaging, the asterisk (*) represents the complex conjugate, and T_R is the correlation time shift. As thoroughly

Table 2.3: List of Simulation Parameters

Parameter	**Symbol**	**Value**	**Units**
General parameters			
Light speed in vacuum	c	3×10^8	m/s
Temperature	T	298.15	K
Photodetector			
Input power	P_{in}	-100 to 20	dBm
Responsivity	R	0.85	A/W
Quantum efficiency	$\eta = \frac{Rhc}{q\lambda_0}$	0.6813	
Integration time	τ_{PD}	50	ms
Bandwidth	$B_{\text{Hz}} = \frac{1}{2\tau_{PD}}$	10	Hz
Thermal noise power	$P_{n_{Th}}$	2.182	fW
Noise Figure	F	1 (ideal)	
Dark current	I_{dark}	0 (ideal)	mA
Laser			
Free space wavelength	λ_0	1.55	µm
Relative Intensity Noise	RIN	-145	dB
Output power	P_{in}	-100 to 20	dBm

described in [96, 97], taking into account that the time average of the autocorrelation function and the normalized power density spectrum form a Fourier transform pair, and considering the phase noise $\vartheta(t)$ to be an ergodic random process, it is proven that the variance of the phase fluctuation is proportional to the spectral width, and it is possible to obtain the two following equations:

$$C_{EE}(T_R) = e^{j\omega_0 T_R} e^{-2\pi\Delta\nu|T_R|}, \tag{2.44}$$

$$\overline{e^{j\vartheta(t-T_R)} e^{-j\vartheta(t)}} = e^{-2\pi\Delta\nu T_R}. \tag{2.45}$$

Recomputing the fields at the through- and drop-port of the resonators shown in Fig. 2.1, now in the form of the time average of infinite summations of time-dependent round-trip field components, after proper algebraic manipulation and using Eq. (2.45) under the assumption of phase noise

ergodicity [96, 97, 99], we have, neglecting ILs:

$$|S_{21}|^2 = \frac{t_a^2 - 2\Psi cos(\phi) + \Psi^2(k_a^2+1) + \frac{(\kappa_a^2 t_b \tau)^2 G}{D}}{[1 - 2\Psi cos(\phi) + \Psi^2]}, \tag{2.46}$$

$$|S_{41}|^2 = \frac{\kappa_a^2 \kappa_b^2 \tau}{D}\left[\frac{G}{1 - 2\Psi cos(\phi) + \Psi^2}\right] \tag{2.47}$$

where the detuning ϕ is now expressed in the time domain, as $\phi = \omega_0 T_R \pm \frac{L^2\Omega}{c\lambda_0}$, T_R is the resonator roundtrip time, $\Psi = \Upsilon e^{-2\pi\Delta\nu T_R}$, $D = 1 - \Upsilon^2$ and $G = 1 - \Psi^2$. Notice the intentional use of T_R for both the roundtrip time and the phase noise autocorrelation timeshift in Eqs. (2.43) through (2.45). The spectral slopes are then:

$$\frac{\partial|S_{21}|^2}{\partial\phi} = \frac{-2\Psi\left[(t_b\tau)^2\kappa_a^4 G + D\left(\kappa_a^2\Psi^2 + t_a^2 - 1\right)\right]\sin(\phi)}{D\left[1 + \Psi^2 - 2\Psi\cos(\phi)\right]^2} \tag{2.48}$$

$$\frac{\partial|S_{41}|^2}{\partial\phi} = \frac{-2\kappa_a^2\kappa_b^2\tau\Psi G\sin(\phi)}{D\left[1 + \Psi^2 - 2\Psi\cos(\phi)\right]^2}. \tag{2.49}$$

In the ideal case ($\Delta\nu \to 0$ Hz), $\Psi \to \Upsilon$, $G \to D$, and Eqs. (2.46) through (2.49) become their phase-noiseless counterparts, obtained in Sections 2.3.4 and 2.3.5. Ψ decays exponentially as the product $\Delta\nu \cdot T_R$ grows, and thus the effect of the linewidth can be regarded as a flattening of the spectrum, as exemplified in Fig. 2.10. Notice that the difference between the spectra and slopes for $\Delta\nu = 0$ Hz (ideal) and $\Delta\nu = 100$ kHz (nominal linewidth for an Agilent 81682A tuneable laser) is negligible for the selected length of ~ 2.8 m, while the maximum slope for $\Delta\nu = 2.5$ MHz is only $\sim 50\%$ of the ideal value. Since the argument of the exponential includes both $\Delta\nu$ and T_R, the longer the resonator, the smaller the linewidth must be. This is why interferometric fiber gyroscopes with several meters in length require lasers with sharp linewidths. The narrow linewidth requirement is less stringent as the resonator length decreases, but so does the Sagnac effect in a quadratic law with length, and thus the resolution can be severely hindered for too

small a length.

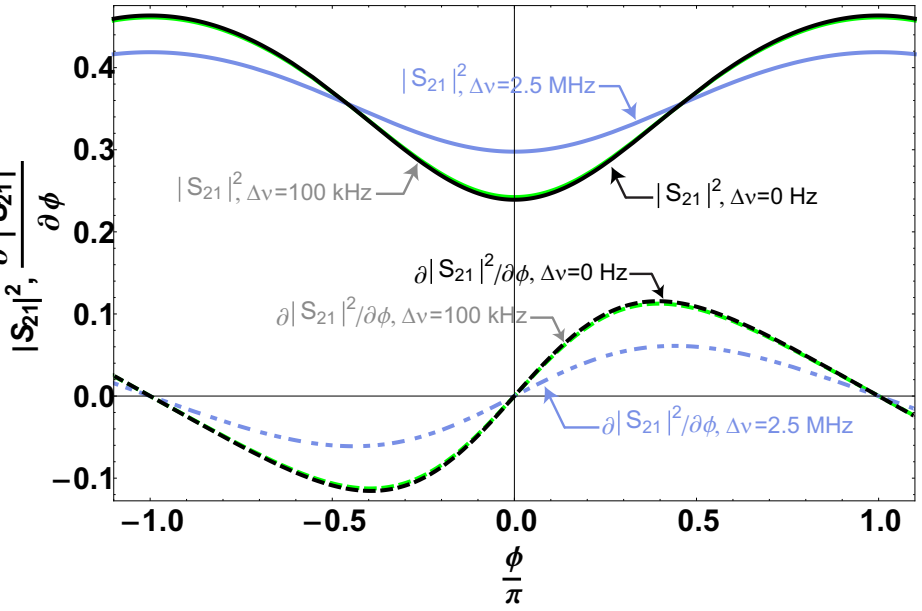

Figure 2.10: Normalized spectrum and its first derivative as a function of normalized detuning, all-pass configuration, for $\alpha_{\mathrm{dB}} = 0.06$ dB/cm, $L_{\mathrm{opt}_{21\mathrm{OC}}} = 2.78$ m, and $\kappa_a = 0.805$, for three different linewidth values. Notice how the curves for $\Delta\nu = 0$ Hz and 100 kHz are practically identical.

Fig. 2.11 shows the normalized resolution (considering also amplitude noise, section 2.3.6) as a function of normalized length for the aforementioned linewidth examples, for Locally-Optimized, under-Coupled rings (LOC, see Section 2.4.1). As predicted by the spectra, the resolutions for $\Delta\nu = 0$ Hz (ideal) and $\Delta\nu = 100$ kHz are practically the same. Only for $L_{\mathrm{n}} > 2.5$ the difference starts to be noticeable. In contrast, for $\Delta\nu = 2.5$ MHz the deterioration is evident at all lengths, and worsens remarkably for $L_{\mathrm{n}} > 1$. The dependence of the phase noise on the round-trip time makes the phase noise more deleterious for smaller propagation losses, which, as will be explained in Section 2.4, allow for larger values of L_{opt}.

The present work focuses on chips with $L_{\mathrm{max\ chip}} \approx 114$ mm, twenty times smaller than the length considered for Figs. 2.10 and 2.11. This

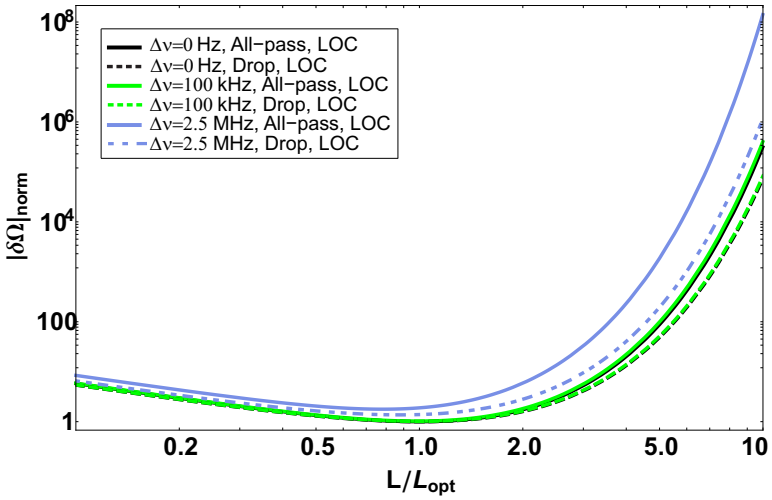

Figure 2.11: Normalized resolution as a function of normalized length for all-pass (solid) and drop (dashed) configurations, using the parameters shown in Table 2.3, with the laser linewidth, $\Delta\nu$, as a parameter.

means that the linewidth $\Delta\nu = 100$ kHz of our chosen tuneable laser source (Agilent 81682A) will produce negligible deterioration. Hence, from now on phase noise is neglected unless stated otherwise.

2.3.7 Resonator Gyroscope Resolution Estimations

From Eqs. (2.24) and (2.25), assuming lossless coupling, the photocurrents for the through- and the drop-port are, respectively:

$$i_{21} = i_D|S_{21}|^2 = i_D \frac{t_a^2 - 2\Upsilon\cos(\phi) + t_b^2\tau^2}{C_{\mathrm{IL21}}\left[1 - 2\Upsilon\cos(\phi) + \Upsilon^2\right]} \tag{2.50}$$

$$i_{41} = i_D|S_{41}|^2 = i_D \frac{\kappa_a^2\kappa_b^2\tau}{C_{\mathrm{IL41}}\left[1 - 2\Upsilon\cos(\phi) + \Upsilon^2\right]}, \tag{2.51}$$

where C_{IL21} and C_{IL41} represent the ILs of the through and drop port configurations, which are considered different due to the use of circulators or Y-branches for the former. When the intensity of the light source fluctuates due to noise, this cannot be distinguished from a variation in intensity due

to rotation. In order to estimate the minimum detectable angular rate, the uncertainty in light intensity (or in photocurrent) has to be translated to an uncertainty in the phase shift $\delta\phi = \frac{\delta i}{m}$ where δi is the noise rms current and m is the slope of the current-phase curves, given by $m = \frac{i_D}{C_{\mathrm{IL}21}} \frac{\partial |S_{21}|^2}{\partial \phi}$ and $m = \frac{i_D}{C_{\mathrm{IL}41}} \frac{\partial |S_{41}|^2}{\partial \phi}$ for the through and the drop ports, respectively.

Assuming a constant resonator length and for simplicity, an invariant wavelength, for each of the counter-propagating beams we have:

$$\delta\phi = \frac{L^2}{c\lambda}\Delta\Omega \Rightarrow \delta\Omega = \frac{c\lambda}{L^2}\delta\phi = \frac{c\lambda}{L^2}\frac{\delta i}{m} \tag{2.52}$$

Using both counter-propagating beams, the resolution for the through port is:

$$|\delta\Omega_{21}| = \frac{c\lambda}{2L^2}\frac{C_{\mathrm{IL}21}\delta i}{i_D \frac{\partial |S_{21}|^2}{\partial \phi}}, \tag{2.53}$$

and for the drop port is:

$$|\delta\Omega_{41}| = \frac{c\lambda}{2L^2}\frac{C_{\mathrm{IL}41}\delta i}{i_D \frac{\partial |S_{41}|^2}{\partial \phi}}. \tag{2.54}$$

2.4 Resonator Parameter Optimization

2.4.1 Local and Global Optimization

For any given propagation loss value α, the values of L, ϕ, κ_b and κ_a can be optimized for maximizing the products $\frac{\partial |S_{21}|^2}{\partial \phi} L^2$ and $\frac{\partial |S_{41}|^2}{\partial \phi} L^2$, thus obtaining the global minima of Eqs. (2.53) and (2.54), respectively. On the other hand, $\frac{C_{\mathrm{IL}}\delta i}{i_D}$ depends on the input power and the ILs. Fig. 2.12 shows the effect of ILs on the resolution. The optimum parameters remain the same, but the increase of C_{IL} produces an exponential deterioration of the resolution.

The ILs depend on the light injection/probing methods. In the present work, an intrinsic IL of 3 dB will be considered, consistent with low-IL grating couplers. This is a relatively low, and yet conservative theoretical

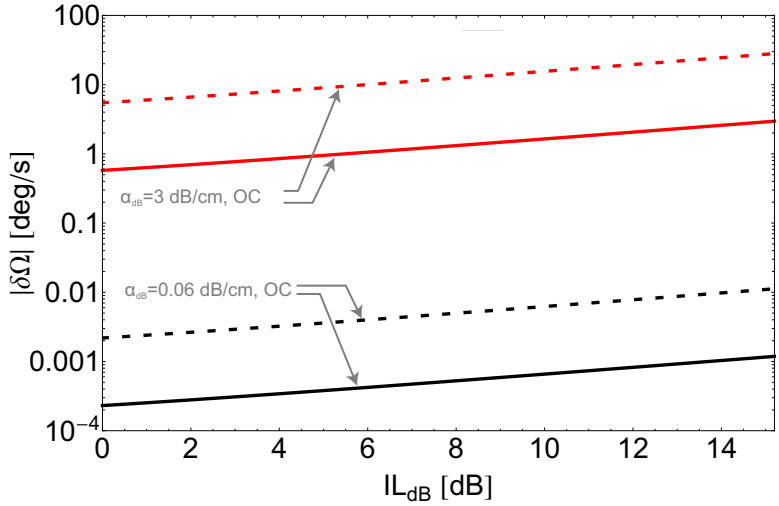

Figure 2.12: Optimum angular rate resolution as a function of the insertion loss, IL_{dB}, for optimized all-pass (solid) and drop (dashed) configurations, for two different values of propagation losses.

level, considering that the lowest IL reported are in the order of 1 dB, for apodized grating couplers [87]. The use of Y-branches as an in-chip alternative to circulators increases the insertion loss by $IL_Y \approx 4$ dB [105]. Optical PM fibre 1550-nm circulators offer smaller ILs than Y-branches, (e.g., $IL_{circ} = 1.5$ dB, AC Photonics PMOC315P), but have the disadvantage of not being integrated on the chip. Therefore, the total ILs for the all-pass and the drop-port cases will be considered to be $IL_T = 7$ dB and $IL_T = 3$ dB, respectively, unless explicitly stated otherwise.

Fig. 2.13 shows the resolution $|\delta\Omega|$, in deg/s, as a function of L for three propagation loss values, assuming the noise parameters of Table 2.3 and $P_{in} = 0$ dBm, for all-pass and drop-port configurations. For each α_{dB} and each port configuration, the optimum values L_{opt}, ϕ_{opt}, $\kappa_{a_{opt}}$ and $\kappa_{b_{opt}}$ were numerically found to obtain the global minimum of $|\delta\Omega|$, and then L was varied, while the other parameters remained constant. Despite their greater IL levels, all-pass resonators perform better than drop-port resonators.

It is possible to observe that L_{opt} is larger for smaller propagation losses. For every value of α, $|\delta\Omega_{21}|_{\min} < |\delta\Omega_{41}|_{\min}$, by approximately one order of

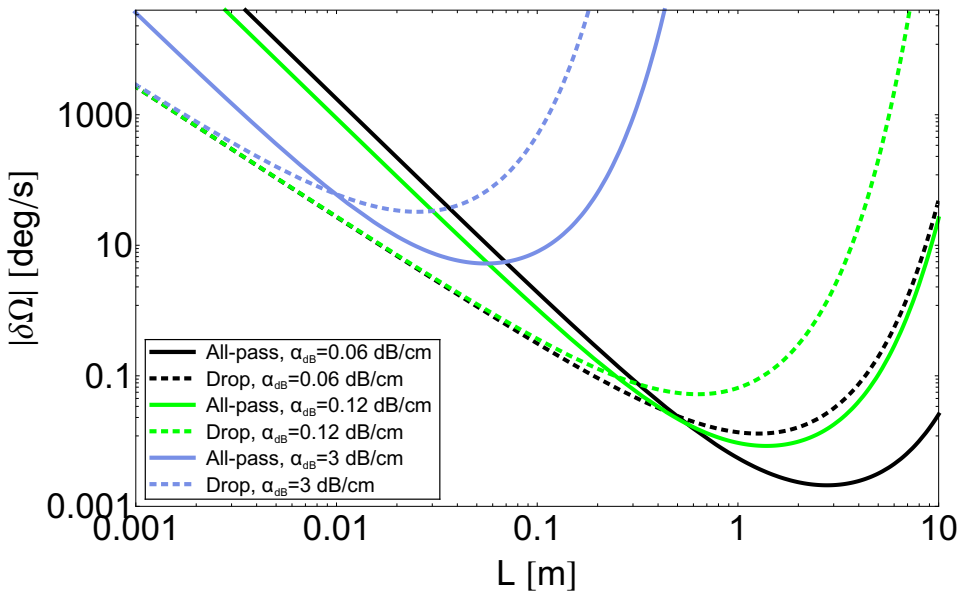

Figure 2.13: Angular rate resolution as a function of resonator length for the all-pass (solid) and drop port (dashed) configurations of racetrack resonator gyroscopes, for three different values of propagation losses. In all cases, the parameters ϕ and κ are fixed at their global optimum values.

magnitude. In all cases, for $L > L_{\text{opt}}$ the resolution deteriorates very rapidly as L increases (notice the graphic has a logarithmic scale and yet the plot describes an exponential curve). This is explained by the fact that the Sagnac effect is proportional to the area of the resonator, (i. e. $\propto L^2$), whereas the propagation losses increase exponentially with the length, (i.e., $\propto e^{2\,\Sigma\alpha_i L_i}$). As previously mentioned, the deterioration of the resolution for $L < L_{optCC}$ is due to the decrease of the Sagnac effect phase shift for smaller resonator lengths.

Fig. 2.13 properly depicts the abrupt deterioration of the resolution for lengths beyond each optimum length L_{opt}. However, the Figure can be misleading if one observes the sensitivities for small lengths: For each propagation loss value, the global optimum values of ϕ, κ_a, and κ_b are found and remain constant as L is varied. Therefore, at short enough lengths for

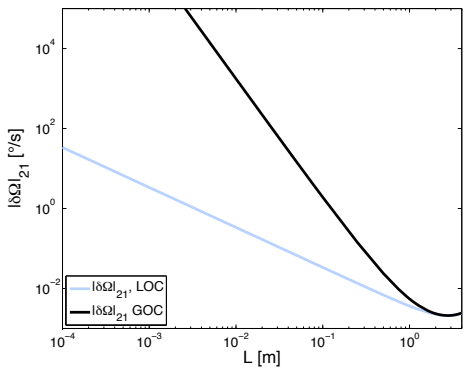

(a) All-pass resolution

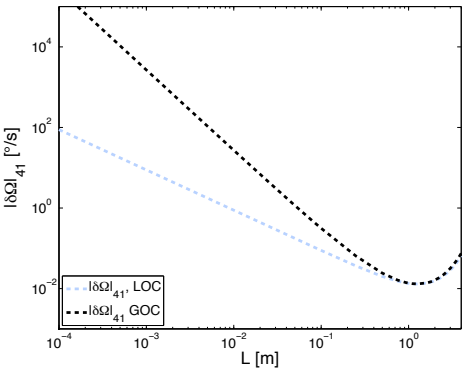

(b) Drop-port resolution

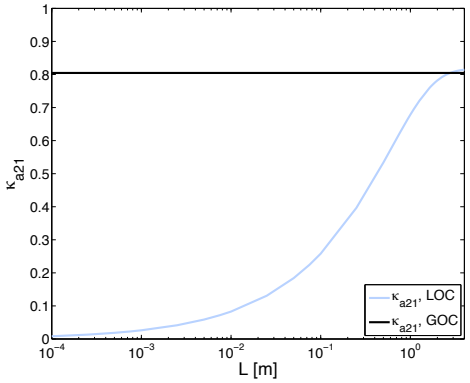

(c) All-pass couplings

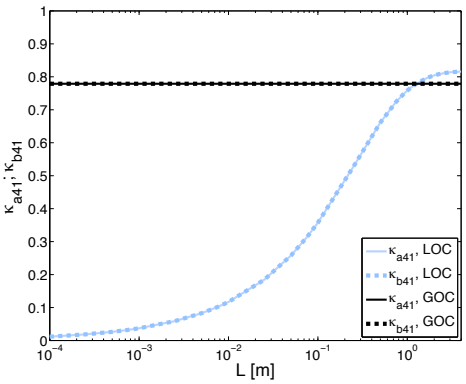

(d) Drop-port couplings

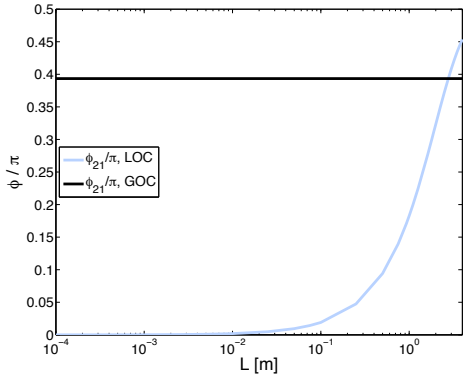

(e) All-pass normalized detuning

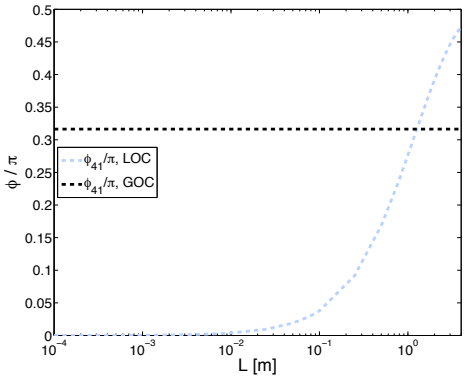

(f) Drop-port normalized detuning

Figure 2.14: **(a, b)** Resolution $|\delta\Omega|$, **(c, d)** optimized couplings κ_a and κ_b, and **(e, f)** optimized normalized detuning $\phi_n = \phi/\pi$ as functions of resonator length L, for various port and optimization conditions. LOC: Locally-optimized coupling (computed at each value of L). GOC: Globally-optimized coupling. In all cases, $\alpha_{\mathrm{dB}} = 0.06$ dB/cm.

each value of α, the unvaried values of coupling and detuning (not optimal at such a length) allow for better sensitivities in the drop-port configuration instead of the all-pass configuration, incorrectly suggesting that higher values of α allow for better resolutions at short lengths. This is due to the fact that for each propagation loss value, the globally optimum values of ϕ, κ_b, and κ_a were kept constant, and thus they yield resolution minima only at each L_{opt}. In order to achieve the best possible resolution for particular values of propagation loss α and arbitrary length L, it is necessary to maximize the products $L^2 \frac{\partial |S_{21}|^2}{\partial \phi}$ and $L^2 \frac{\partial |S_{41}|^2}{\partial \phi}$, for the all-pass and the drop configurations, respectively, in terms of the variables ϕ, κ_a, and κ_b.

Figs. 2.14(a) and 2.14(b) show the resolution for the all-pass (solid) and the drop-port (dashed) configurations, with $\alpha_{\text{dB}} = 0.06$ dB/cm, for two different cases: 1) OC, local optimization (LOC) of ϕ, κ_a and κ_b at each value of L (bottom line); and 2) OC, with ϕ, κ_b and thus κ_a fixed at their global optimum values (GOC, top, black line). The latter are the same black curves shown in Fig. 2.13. For the sake of image clarity, only the plots for $\alpha_{\text{dB}} =$ 0.06 dB/cm are shown, but the trend is similar for different propagation loss values. For either configuration, LOC rings offer considerably better resolutions than their globally optimized counterparts.

Figs. 2.14(c) and 2.14(d) show respectively the all-pass and the drop-port coupling coefficients κ_a and κ_b for each ring configuration. For the all-pass cases, (Fig. 2.14(c)), $\kappa_b = 0$ so it has been omitted in the plots. From Fig. 2.14(d) it is possible to conclude that the LOC for the drop port configuration is symmetric. Figs. 2.14(e) and 2.14(f) show the normalized detuning for each case, for the all-pass and the drop-port configurations, respectively. The optimum values of ϕ for the drop port are always larger than their through-port counterparts for a given length, and in all cases, $\phi \to \frac{\pi}{2}$ as $L \to \infty$.

Table 2.4 summarizes the global optimum (GOC) values of resolution, resonator length, coupling coefficients and normalized detuning for propagation loss values of $\alpha_{\text{dB}} =$ 0.06 dB/cm, 0.12 dB/cm, and 3 dB/cm, for all-pass and drop-port configurations. The GOC values of $\kappa_{a,b}$ and ϕ are the same for all values of α, and the product αL_{opt} is a constant for the

same port and coupling conditions. As can be observed in such a table, the all-pass configuration always offers the best resolution.

Table 2.4: Global optimum parameters and resolutions for different port configurations and losses

Parameter \ α_{dB}	0.06 dB/cm	0.12 dB/cm	3.0 dB/cm
$\alpha[\mathrm{m}^{-1}]$	0.69	1.382	34.5
All-pass, GOC, $IL_T = 7$ *dB*			
$\lvert\delta\Omega\rvert$ [deg/s]	2.1×10^{-3}	8.42×10^{-3}	5.26
L_{opt} [m]	2.77	1.386	55.5×10^{-3}
$\kappa_{a\ opt}$	0.805	0.805	0.805
ϕ_{opt}/π	0.393	0.393	0.393
αL_{opt}	1.915	1.915	1.915
Drop port, GOC, $IL_D = 3$ *dB*			
$\lvert\delta\Omega\rvert$ [deg/s]	13×10^{-3}	52.3×10^{-3}	32.6
L_{opt} [m]	1.263	0.63	25.3×10^{-3}
$\kappa_{a\ opt}$	0.779	0.779	0.779
$\kappa_{b\ opt}$	0.779	0.779	0.779
ϕ_{opt}/π	0.336	0.336	0.336
αL_{opt}	0.871	0.871	0.871

Fig. 2.15 compares the resolutions for LOC all-pass and drop-port resonators as a function of the normalized length $L_n = L/L_{\mathrm{opt}}$, for the three values of α in Table 2.4. LOC all-pass rings offer the best resolution for any particular propagation loss value, by approximately one order of magnitude at all lengths, in comparison to the drop-port LOC configuration.

The deterioration of the resolution due to length variations is less tolerant for larger propagation losses, as the values of L_{opt}, shown in Fig. 2.16, and the values of $|\delta\Omega|_{opt}$, shown in Fig. 2.17, are considerably smaller and larger, respectively.

Materials with smaller propagation losses can achieve considerably better sensitivities: as shown in Fig. 2.16, if the average propagation loss decreases below 1 dB/cm, there is an abrupt enhancement of both the resolution and

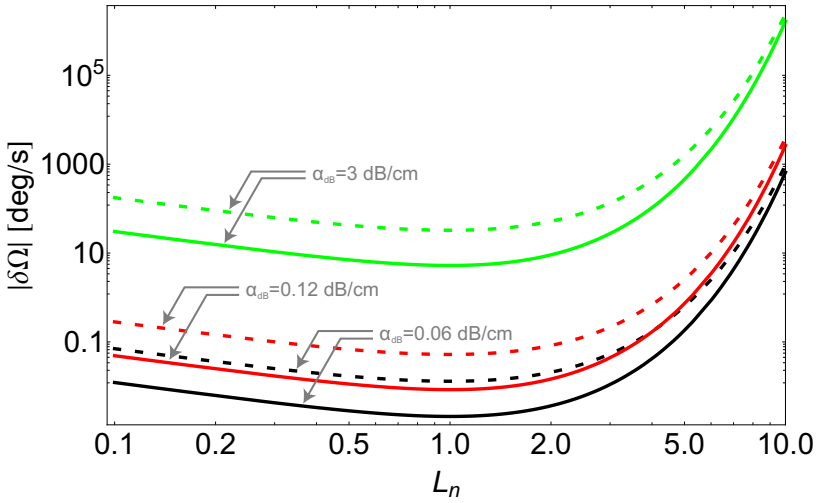

Figure 2.15: Resolution for LOC resonators as a function of normalized length, L_{n}, for all-pass (solid) and drop port (dashed) rings, for $\alpha_{\mathrm{dB1}} = 0.06$ dB/cm, $\alpha_{\mathrm{dB2}} = 0.12$ dB/cm and $\alpha_{\mathrm{dB3}} = 3$ dB/cm. L_{opt} is different for each value of α and port configuration, as shown in Fig. 2.16.

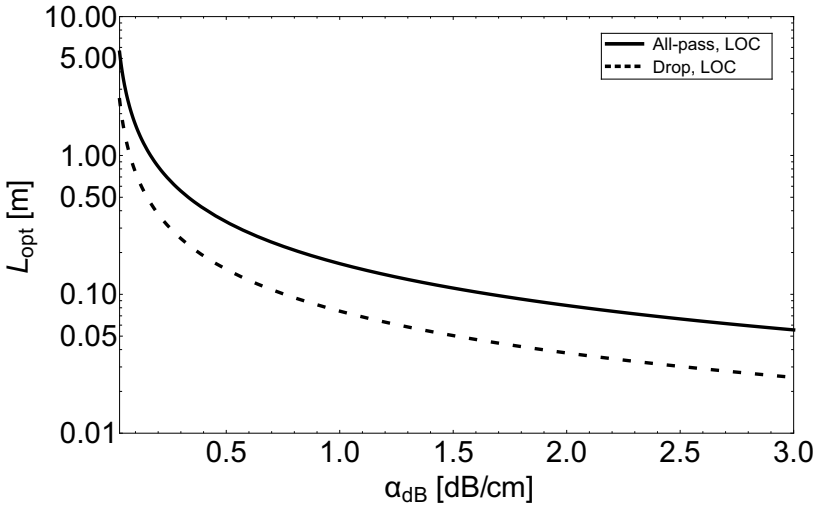

Figure 2.16: Optimum resonator length L_{opt} as a function of average waveguide propagation loss α_{dB} for the through (solid) and the drop (dashed) ports of LOC ring resonators. The value of L_{opt} is IL-independent.

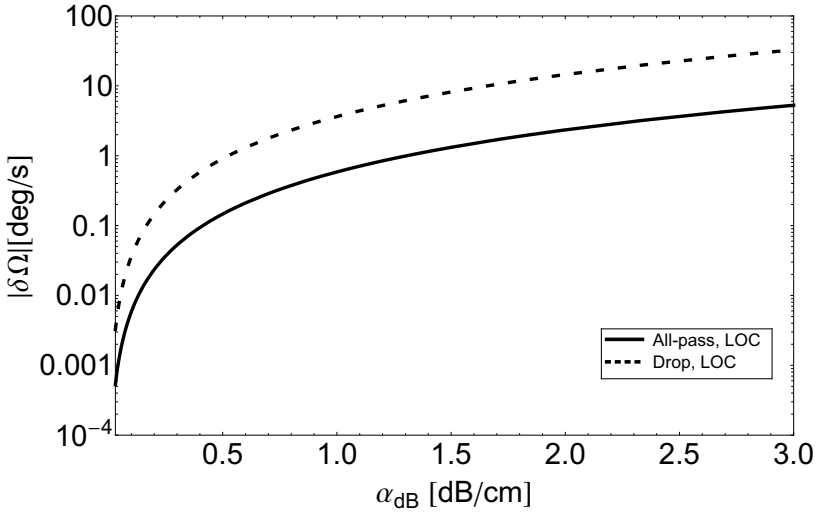

Figure 2.17: Optimum resolution as a function of average waveguide propagation loss α_{dB} [dB/cm] for all-pass (solid) and drop (dashed) LOC ring resonators.

the optimum length value, as can be concluded from the exponential shape of the plots in both figures for $\alpha_{\mathrm{dB}} < 1$ dB/cm, in spite of the fact that both plots are already in a log-log scale.

2.4.2 Chip-Sized vs. Globally-Optimized Gyroscopes

Based on the constant $\alpha \cdot L$ products for GOC (see Table 2.4) and the maximum on-chip resonator length, $L_{\mathrm{max\ chip}} = 114$ mm, the largest permissible average propagation losses for the all-pass and drop-port configurations are $\alpha_{\mathrm{dB\ maxAP}} = 1.46$ dB/cm and $\alpha_{\mathrm{dB\ max41}} = 0.66$ dB/cm, respectively. Table 2.5 compares the resolutions of chip-sized ring gyroscopes for different values of α_{dB}, and Table 2.6 shows the optimum resolutions and lengths for the same values of α_{dB}.

2.4.3 Target Applications

Table 2.7, adapted from [143] following the formulae derived in [139], summarizes the resolution requirements for three existing standard gyroscope

Table 2.5: Resolutions for LOC resonator gyroscopes with $L = L_{\text{max chip}}$

α_{dB} [dB/cm] \ $\lvert\delta\Omega\rvert$ [deg/s]	All-pass	Drop
0.06	0.0234	0.0619
0.12	0.047	0.128
0.66 ($\alpha_{\text{dB max41}}$)	0.314	1.60
1	0.595	5.37
1.2	0.844	10.56
1.46 ($\alpha_{\text{dB maxAP}}$)	1.25	25.1
3	16.91	4133

Table 2.6: Optimum resolutions and lengths for GOC resonator gyroscopes

Param. / α_{dB}	All-pass		Drop	
	$\lvert\delta\Omega\rvert$ [°/s]	L_{opt} [m]	$\lvert\delta\Omega\rvert$ [°/s]	L_{opt} [m]
0.06 dB/cm	0.0021	2.78	0.013	1.262
0.12 dB/cm	0.0084	1.386	0.052	0.63
0.66 dB/cm	0.258	0.251	1.60	0.114
1 dB/cm	0.585	0.166	3.63	0.075
1.2 dB/cm	0.843	0.139	5.22	0.063
1.46 dB/cm	1.25	0.114	7.72	0.0518
3 dB/cm	5.26	0.0555	32.6	0.025

grades. It is possible to conclude that if α_{dB} is in the range of ~ 0.7 to 2 dB/cm, resonators with lengths in the range of $L_{\text{max chip}}$ would achieve resolutions appropriate for tactical- and rate-grade applications.

Table 2.8 compares the performance of commercially available MEMS gyroscopes from Analog Devices (A.D., [37]), Melexis [2], and ST Microelectronics (STM, [117]) against the theoretical performance of LOC optical resonator gyroscopes.

One can see that the propagation losses are the critical parameter that, if properly dealt with, allow optical gyroscopes to offer similar resolutions to those of commercially available devices for rate- and tactical-grade appli-

Table 2.7: Resolution requirements for different classes of gyroscopes

	Rate grade	Tactical grade	Inertial grade
$\|\delta\Omega\|$ [°/h]	> 300	30 to 300	< 1

Table 2.8: Comparison with commercially available gyroscopes

Device	$\|\delta\Omega\|$ [deg/s]	Grade
A.D. ADXRS450	0.14	Rate
STM L3G3250A	0.18	Rate
Melexis MLX90609	0.30	Rate
AP ring, 1 dB/cm, $L_{\text{max chip}}$	0.595	Rate
AP ring, 0.06 dB/cm, $L_{\text{max chip}}$	0.0234	Tactical

cations. If properly integrated with the light source and readout circuitry, these optical gyroscopes would then have the advantage of a longer lifetime thanks to the lack of moving parts. As previously stated, the use of a rectangular reticle will worsen by $\sim 22\%$ the value of the resolution, but this does not affect the target application grades for these devices.

2.4.4 Design Robustness

Based on the model developed so far, it is possible to vary some of the parameters and observe their impact on the resolution. In this way, parameter spread ranges can be defined, to assess the effect of possible variations in tuning and fabrication conditions. Thus, the 3-dB bandwidths ΔL, $\Delta\phi$ and $\Delta\kappa$ will define ranges for such parameters around their optimum values, within which the resolution deteriorates by a factor of two.

Fig. 2.18 shows a plot of the normalized resolution, $|\delta\Omega_{\text{norm}}| = |\delta\Omega/\delta\Omega_{\text{opt}}|$, as a function of the normalized length $L_n = L/L_{\text{opt}}$ for the all-pass (solid) and drop-port (dashed) configurations of LOC resonators. Due to normal-

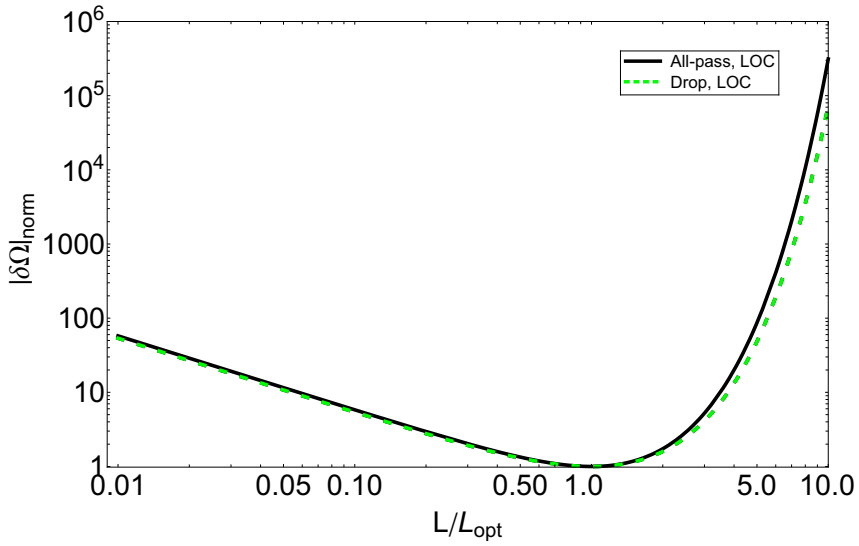

Figure 2.18: Normalized resolution $|\delta\Omega|_{\text{norm}}$ versus normalized length $L_n = L/L_{\text{opt}}$ for all-pass (solid) and drop-port (dashed) LOC resonators. Due to normalization, all plots coincide for all values of α and are IL-independent.

ization, these plots are valid for all values of α, and they are independent of the value of IL. The 3-dB-cutoff normalized lengths for through- and drop-port LOC resonators are shown in Table 2.9. These normalized cutoff values are all the same for all values of α. However, smaller propagation losses will allow for more flexible design constraints, as L_{opt} increases considerably for decreasing values of α, as shown in Fig. 2.16.

Fig. 2.19 shows the optimum values of the coupling coefficient, κ, as a function of the normalized length L_n for all-pass (solid) and drop (dashed) LOC resonators. It also shows contour plots of the values of κ at which the resolution is two times (3-dB) and four times (6-dB) worse than the optimum resolution for each port.

Table 2.9: 3-deciBel cut-off normalized lengths and length bandwidth for LOC resonators

Parameter \ Port	All-pass	Drop
$L_{\text{n low}}$	0.30505	0.2869
$L_{\text{n high}}$	2.1502	2.2719
ΔL_{n}	1.84515	1.985

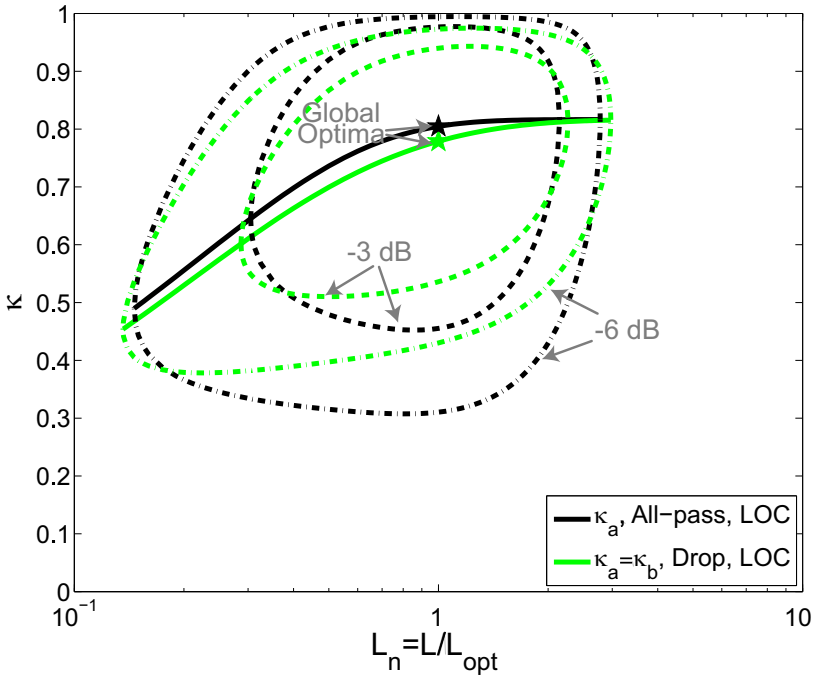

Figure 2.19: Global optimum values (stars), locally-optimized (LOC, solid), 3-dB (dashed), and 6-dB (dash-dotted) contour plots for the coupling coefficients of all-pass (κ_a) and drop-port ($\kappa_a = \kappa_b$) resonators, as a function of the normalized length $L_n = L/L_{\text{opt}}$. Due to normalization, all plots coincide for all values of α and are IL-independent.

In all cases, ϕ is locally optimized, to emulate the the fact that in any experiment, the user would still tune the wavelength of the light source in the best possible way, despite the imperfections of the fabricated device.

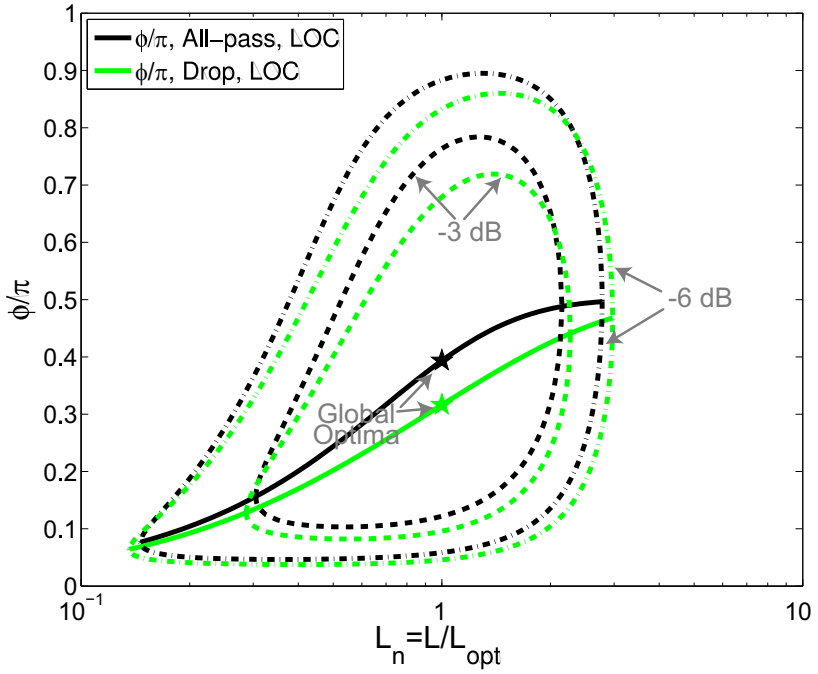

Figure 2.20: Global optimum values (stars), locally-optimized (LOC, solid), 3-dB (dashed), and 6-dB (dash-dotted) contour plots for ϕ/π, as a function of the normalized length $L_n = L/L_{\text{opt}}$, for all-pass and drop-port resonators. Due to normalization, all plots coincide for all α values, and are IL-independent.

Both $\kappa_a = \kappa_b$ are detuned simultaneously for the drop port, as in reality, fabrication errors and tolerances affect both coupling regions.

Fig. 2.20 shows the optimum values of the normalized detuning, $\phi_n = \phi/\pi$, as well as 3- and 6-dB contour plots for ϕ_n versus the normalized length L_n. Once again, the largest tolerance occurs for values in the vicinity of $L_n = 1$. As expected, these contour plots are independent of α and IL. It is possible to notice that in all cases, the *detuning bandwidth* favours the region towards smaller lengths, consistent with the smaller deterioration rate for $L_n < 1$ shown in Fig. 2.18. The farther from the optimum point, the smaller the range within which the coupling coefficient and detuning can vary.

Fig. 2.21 shows the resolution as a function of propagation loss for an all-pass (solid) and a drop-port (dashed) ring gyroscope, each optimized for

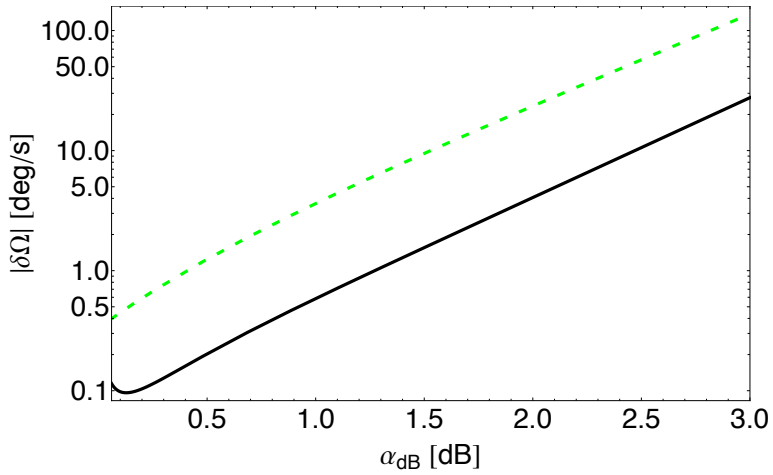

Figure 2.21: Resolution vs. α_{dB} for an all-pass (solid) and a drop-port (dashed) resonator gyroscope optimally designed for $\alpha_{\mathrm{dB}} = 1$ dB/cm.

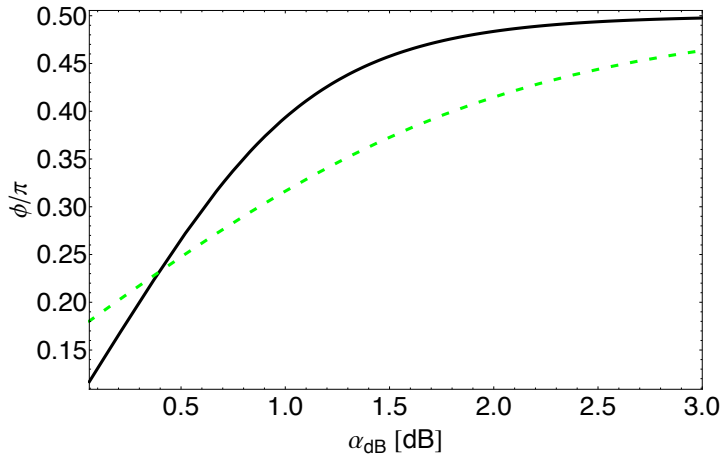

Figure 2.22: Optimized detuning as a function of α_{dB} for an all-pass (solid) and a drop (dashed) resonator gyroscope optimally designed for $\alpha_{\mathrm{dB}} = 1$ dB/cm.

a propagation loss $\alpha_{\mathrm{dB}} = 1$ dB/cm. In each case, $L = L_{\mathrm{opt}}$ and $\kappa_{a,b} = \kappa_{a,b_{\mathrm{opt}}}$, since after fabrication, only the detuning can be optimized, as shown in Fig. 2.22. As a result, it is noticeable the greater deterioration for increasing propagation losses in comparison to the trends shown in Fig. 2.17, and even though the resolution is better for decreasing propagation losses, there is a value ($\alpha_{\mathrm{dB}} \approx 0.1$) below which the sensitivity actually starts to deteriorate for the all-pass configuration, due to the fixed length and couplings.

2.4.5 Predictions with Experimental SNRs

In the previous sections we have assumed a close-to-ideal SNR. Here, we look at the impact of lower SNR values on the gyro resolution. For the all-pass resonator case, by substituting the expression $C_{IL21} i_D / \delta i$ in equation (2.53) with the signal to noise ratio, $\mathrm{SNR} = 10^{\mathrm{SNR_{dB}}/10}$, we have:

$$|\delta\Omega_{21}| = \frac{c\lambda}{2L^2 \frac{\partial |S_{21}|^2}{\partial \phi}} \frac{1}{\mathrm{SNR}}, \tag{2.55}$$

Figure 2.23 shows the best theoretically achievable resolution as a function of SNR, for two resonators of identical length, $L = 114$ mm, but different propagation losses. The resonator geometry used for this modelling is consistent with the design described in Section 3.4, with 200 µm-long linear tapers for SMWG to MMWG conversion. For both resonators, the length is $L_{\mathrm{max\ chip}} = 114$ mm, with an SMWG length fraction of 0.1%. The propagation losses for rib and strip SMWG are considered to be 1.4 dB/cm [15] and 2 dB/cm [78], respectively. The rib MMWG propagation losses used for the first resonator (dashed curve) are 0.026 dB/cm [78], whereas, for the second resonator (solid curve), a value of 0.085 dB/cm is used, based on our experimental results [56]. In practice, the SNR can be estimated based on time-domain experimental data, by calculating the ratio of the mean photodetector power divided by its standard deviation, as shown in Section 3.4.3.

Phase modulation techniques, primarily intended for frequency tracking, should be used in order to reduce undesirable effects produced by backscat-

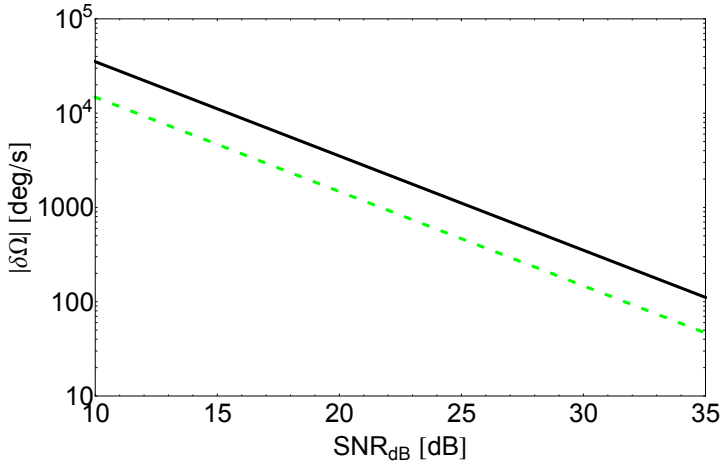

Figure 2.23: Angular speed resolution as a function of SNR for two all-pass, large-area resonators, both with 114 mm in length, and MMWG propagation losses of 0.085 dB/cm (solid curve) and 0.026 dB/cm (dashed curve).

tering. Otherwise, the contribution of backscattering to the overall resolution error can be significant, if not dominant [27]. Frequency tracking can be achieved by acusto-optic modulation [30, 45, 46] or phase modulation [62, 118]. Since silicon photonic waveguides have a smaller cross-section than low-contrast waveguides and optical fibres, their backscattering level is considerably greater. This is exacerbated for small cross-section SMWG wires, as surface imperfections are the source of propagation loss and backscattering, contributing to backscattering levels in the order of -30 dB, according to the literature [92].

In the specific case of SOI devices interrogated via grating couplers, depending on the grating coupler designs one can expect backreflections at the fibre-coupler interface ranging from -30 dB to -16 dB [136, 138]. These backreflections, if not phase-modulated, will produce undesirable interference with the light propagating in the same direction. Also, due to the smaller size of the SOI chips, the roundtrip time is much shorter than that of optical fibre gyros, and despite their high Q factors, the frequency shifts required for appropriate frequency tracking (in the order of hundreds of MHz) pose challenges for large ramp signal generation.

2.5 Phase Modulation Requirements

The reason for requiring frequency tracking techniques for enhancing sensitivity is the minute order of magnitude of the wavelength shift due to the Sagnac effect, which is, in general, too small a change to track based solely on amplitude measurements. From equation (2.19), at resonance we have:

$$\phi_{\text{res}} = 2M\pi = \frac{2\pi n_{\text{eff}}(\lambda_0)L}{\lambda_0} \pm \frac{L^2\Omega}{c\lambda_0}, \tag{2.56}$$

where the integer M denotes the optical resonator mode. At rest, this number can be obtained as:

$$M = \frac{n_{\text{eff}}(\lambda_0)L}{\lambda_0}. \tag{2.57}$$

For an arbitrary angular speed, the resonance wavelength for mode number M will undergo a shift, depending on the propagation direction of the light, given by:

$$\lambda_{0\text{ new}} = \lambda_0 \pm \frac{L^2\Omega n_{\text{eff}}}{2\pi cMn_{\text{g}}}. \tag{2.58}$$

The second term in equation (2.58) is a very small quantity, especially for small footprint resonators. As an example, let us consider a resonator with a length $L = 37.7$ mm, $\lambda_0 = 1550.2$ nm, $n_{\text{eff}}(\lambda_0) \approx 2.83$, and $n_{\text{g}}(\lambda_0) \approx 4$, consistent with a 12-mm diameter resonator design in an SOI chip. Then, M=68833 (rounded to the nearest integer). For an angular speed of 1 dps, the resonance wavelength shift for each beam is $\delta\lambda_0 \approx 1.353 \times 10^{-19}$ m. The total resonance wavelength difference is thus $\Delta\lambda_0 \approx 2.7 \times 10^{-7}$ pm, equivalent to a frequency difference $\Delta f = |-\frac{c\Delta\lambda}{\lambda_0^2}| \approx 34$ Hz. This result is consistent with the expression in the literature for the total frequency difference due to the Sagnac effect [46]:

$$\Delta f = \frac{4A\Omega}{\lambda P}, \tag{2.59}$$

where A denotes the area within the resonator, and P its perimeter. The frequency shift can be considered to vary linearly with angular speed. For a shot-noise limited system, the resolution for an optical gyroscope is given

by [22, 45, 107]:

$$\delta\Omega = \frac{\pi c}{QL}\sqrt{\frac{2cBhC_{\mathrm{IL}}}{\lambda\eta P_{\mathrm{in}}}} \tag{2.60}$$

where P_{in} is the optical input power and C_{IL} represents the insertion losses.

As previously mentioned, if shaped as a rectangle rather than a circle, the resonator aspect ratio will reduce the enclosed area, thus affecting the gyroscope resolution. Considering these small frequency shifts, relying exclusively on amplitude techniques can render the device insensitive to small angular speeds, especially considering waveguides with high backscattering levels. Backscattering in optical fibres and waveguides has been studied for several years [10, 76, 89, 90, 92, 98], and is an important if not dominant error source in passive resonator-based optical gyroscopes [67, 71, 82, 124]. In order to reduce its effects and achieve shot-noise limited performance, fibre optic gyroscopes typically use frequency-domain techniques for tracking the resonance of each counterpropagating light beam [63, 82, 120, 121], and read out the angular speed of the device based on the frequency difference between these two signals. The first techniques used for this purpose, based on frequency shifting using acusto-optic modulators (AOMs), were implemented in optical fiber gyroscopes with spool lengths of the order of hundreds of meters [31], and in fibre resonators with lengths of the order of 1 meter [46]. However, due to inherent AOMs disadvantages such as bulkiness and unintended intensity modulation, integrated-optics phase modulators have been preferred for frequency tracking and feedback techniques [62, 118]. The phase modulation implementation known as the serrodyne modulation technique [62] consists of creating an alternating frequency shift in the optical signal by driving the phase modulators with ramp functions of constant amplitude and two alternating frequencies.

Figures 2.24 and 2.25 illustrate the principle of operation of serrodyne phase modulation for a passive resonator optical gyroscope, described as well in [62, 118]. As shown, we assume that the optical gyroscope shown in Figure 2.24 rotates in CCW direction. The optical signal of a tuneable laser source is equally split at the 50/50 polarization maintaining beam splitter. Each

beam is then phase modulated by separate phase modulators, each fed with frequency-modulated ramp signals of constant amplitude $V_p = 2V_\pi$, where V_π is the half-wave voltage of the phase modulators. As previously explained, the corrotating (CCW) light, detected in Photodetector 2, experiences an effective elongation of the resonator due to the Sagnac effect, so it is retarded in phase. Its resonance wavelength is increased, or equivalently, its resonance frequency is decreased by an amount given by Eq. (2.59).

The laser wavelength, λ_{laser} should be initially tuned at a value slightly greater than the resonance at rest, so that its frequency, f_{laser}, is tuned below resonance. The lock-in amplifier LIA 1b is used to tune the laser frequency to track the CCW resonance. Phase modulator 1 is driven by serrodyne ramps with alternating frequencies f_1 and $2f_1$ for equal periods. The value of f_1 depends on the finesse of the resonator, and is usually on the order of hundreds of MHz. The driving signal is switched between frequencies f_1 and $2f_1$ at the lower frequency f_{s1}, which is on the order of kHz. Therefore, the optical frequency switches symmetrically at a (slow) frequency f_{s1} around the optical frequency $f_{laser} + \frac{3}{2}f_1$. If such a frequency does not exactly coincide with the CCW resonance, the photodetector PD2 creates rectangular pulses of frequency f_{s1}. This frequency is used as the reference frequency in the lock-in amplifier LIA 1b, which creates a feedback signal V_{fb1} whenever the amplitudes at points B and C in Fig. 2.25 are different. This feedback signal is used to adjust the laser frequency. When the laser is perfectly tuned, the amplitude at both points B and C in figure 2.25 is exactly the same, which implies that the photodetector PD2 produces a pure DC output, and thus V_{1b} is zero. The lock-in amplifier LIA 1a corrects for imperfections in the serrodyne amplitude (i.e., deviations from $2V_\pi$), which generate exponentially decaying pulses at the frequency of the serrodyne signal being generated [118], in this case, either f_1 or $2f_1$.

On the other branch, the counter-rotating (CW) beam, detected in photodetector PD1, experiences an effective shrinkage of the resonator length due to the Sagnac effect, so it is enhanced in phase. As its resonance wavelength is shortened, its resonance frequency is increased. Thus, the phase modulator PM2 must apply a frequency f_2, slightly greater than f_1, in order

to track the CW resonances rising edge, depicted by point D in Fig. 2.25. The ramp frequency is switched between f_2 and $f_2 + f_1$ at a slow frequency f_{s2}, for tracking the resonance in a similar way to the CCW case. If f_2 is improperly tuned, PD1 produces a rectangular wave output of frequency f_{s2}, which is also the reference frequency of the lock-in amplifier LIA 2b, thus producing a strong error signal V_{2b}, used to adjust the value of f_2 until the amplitudes of points D and E are the same. The lock-in amplifier LIA 2a corrects for amplitude imperfections to achieve a voltage excursion of exactly $2V_\pi$.

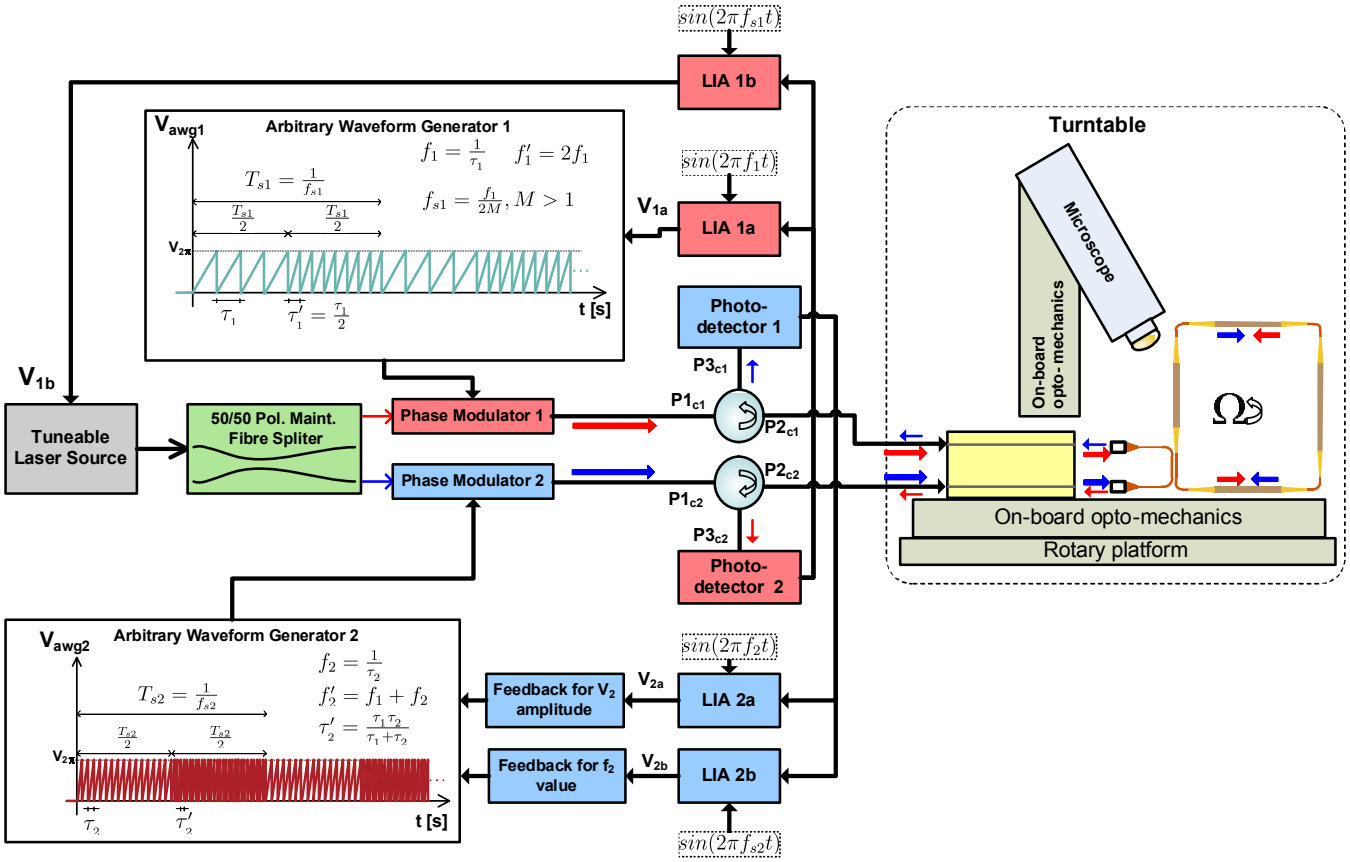

Figure 2.24: Frequency tracking using serrodyne phase modulation.

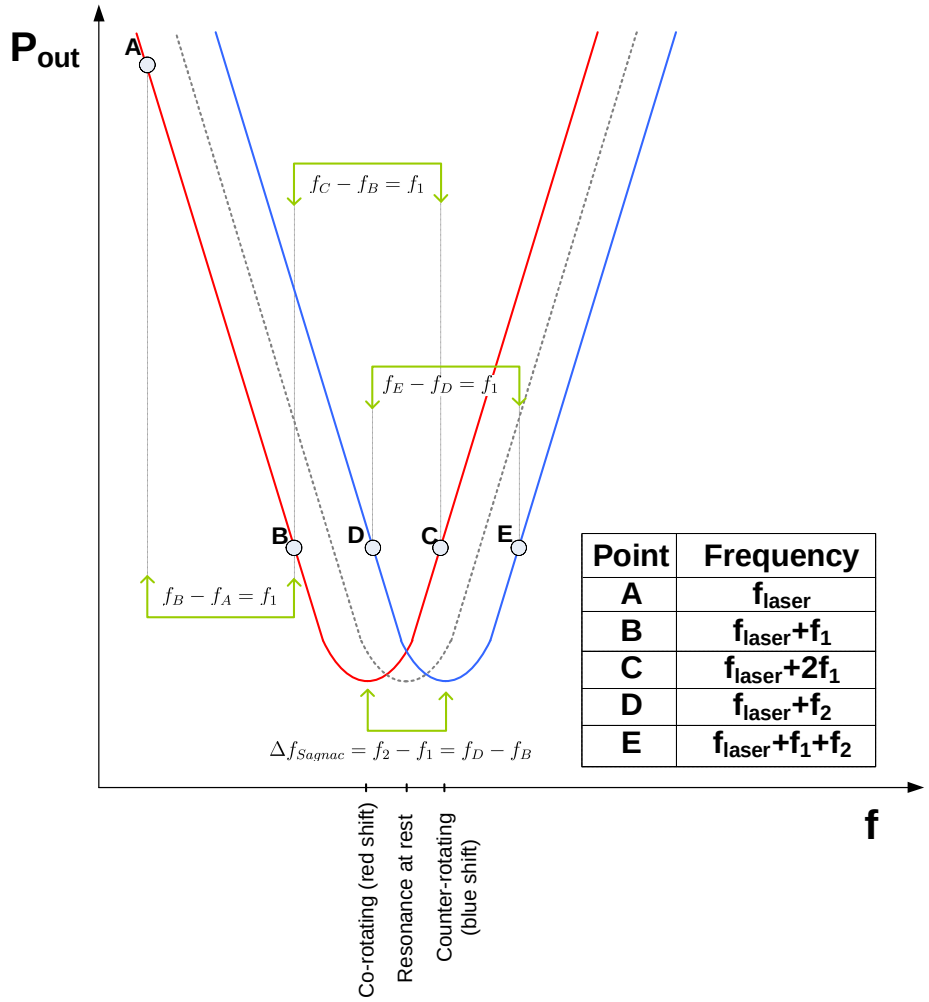

Figure 2.25: Resonance frequency tracking using modulation techniques.

Chapter 3

Design Process

During this work, cycles of device design, fabrication, characterization, and critical evaluation were conducted iteratively, in order to identify problems, envision approaches to solve them, and derive conclusions that lead to improvements for the next device generation. This iterative process also involved the creation and evolution of the experimental setups used to characterize the devices.

Taking into consideration that UBC does not currently have a CMOS-compatible nanofabrication facility capable of creating SOI devices, all our designs were submitted for fabrication as part of multi-project wafer (MPW) shuttles to various foundries around the world, such as the Interuniversity Microelectronics Centre (IMEC), in Belgium, the Institute of Micro Electronics (IME), in Singapore, and the Micro and Nanofabrication Facility at the University of Washington (UW), in the USA. Each of these foundries has its own design specifications, rules, and fabrication technologies. Thus, the time from design to measurement and evaluation could range from a few months to a year.

This chapter will guide the reader through the iterative process, stating for each cycle the initial objectives, the device designs, the device characterization, the evaluation of the results, the difficulties encountered along the way, and the improvements planned for the next cycle.

3.1 First Design Cycle

The main objectives during this cycle were the creation of large resonators and test structures for determining insertion and propagation losses, as well as the design and assembly of a characterization setup. The first devices

were fabricated using an IMEC epixFab process, based on 193-nm deep ultraviolet (DUV) lithography, to fabricate air-clad strip waveguides with heights of 220 nm, on SOI wafers with a 2 µm-thick buried oxide layer (BOX). The SOI wafers were diced into chips arranged in a number of columns and rows, as depicted in Fig. 3.1.

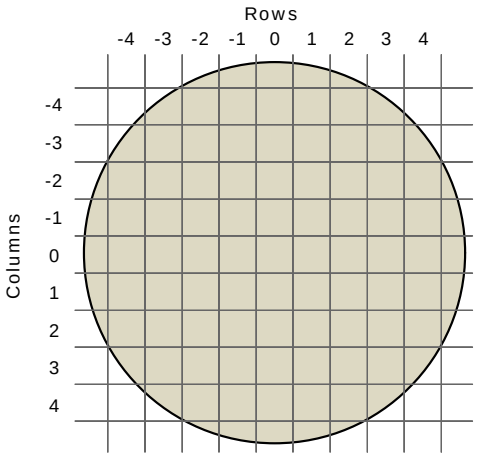

Figure 3.1: Wafer dicing schematic. Chips are identified according to their position in the row and column pattern.

The UV illumination dose for each column was intentionally varied, to produce waveguide width and gap variations for devices located in different columns across the wafer. Chips from various columns were then shipped to each participant in the MPW shuttle.

3.1.1 Layout Design

IMEC provided the grating coupler (GC) design to interrogate the devices. Each GC required a 1 mm-long linear waveguide taper. Since in practice optimal coupling conditions would be difficult to achieve due to fabrication imperfections, a methodology of parameter variation was adopted for our mask design. In order to vary the coupling to the various resonators studied, the gaps in the WDCs were varied between 150 nm and 450 nm, while the WDC lengths were fixed at $L_c = 10$ µm.

The multi-user nature of the MPW required the designs to be space-efficient and rectangular, rather than circular, in order to efficiently frame devices designed by other users. Figure 3.2 shows a panoramic view of the large resonator designs, and a zoom-in to a subset of them. Nested sets of rings were created using single-mode (SM) strip waveguides. Their lengths ranged from 3 to 33 mm, with their aspect ratios dictated by the available layout space. To vary the amount of coupling to the resonators, the WDC gaps were varied as described above.

For the sake of space efficiency, and due to the considerable length of the GC tapers, both the input and the output GC for each resonator were oriented in the same direction, as shown in Fig. 3.2(b). However, this proved to be a difficulty with regard to interrogation, as the dimensions of the fibre holders and positioning opto-mechanics prevented the fibres from being located on the same side of the chip in close proximity (see Fig. 3.5).

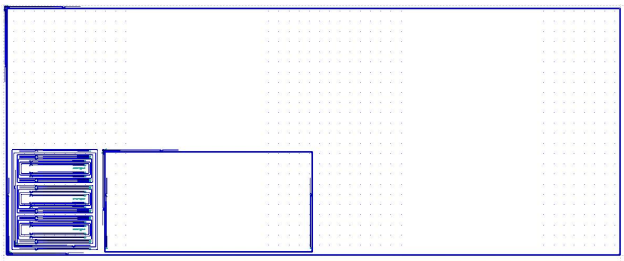

(a)

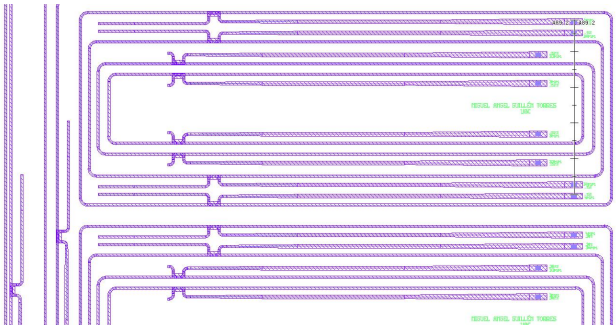

(b)

Figure 3.2: **(a)** First device layout panoramic schematic and **(b)** Zoom-in to top left nested rings. Text tags are only shown for illustration purposes.

Waveguide Parameters

Theoretical estimations of the effective and group indices for these waveguides were also necessary in order to estimate resonator parameters such as Q and FSR, as well as cross-over length values for the WDCs. The effective and group indices for different air-clad waveguide geometries were obtained using MODE Solutions^{TM} eigenmode solver. Figure 3.3(a) shows the TE mode profile for a 500-nm wide, 220-nm tall strip SMWG. The effective and group indices for this waveguide were obtained using five equally spaced wavelength values, and curve-fitted using a third-order polynomial model. Fig. 3.3(b) shows the resulting polynomial curve-fits for the effective and group indices. The values of the effective and group indices at $\lambda_0 = 1550\ nm$ are $n_{\text{eff}} = 2.3826$ and $n_{\text{g}} = 4.3547$, respectively.

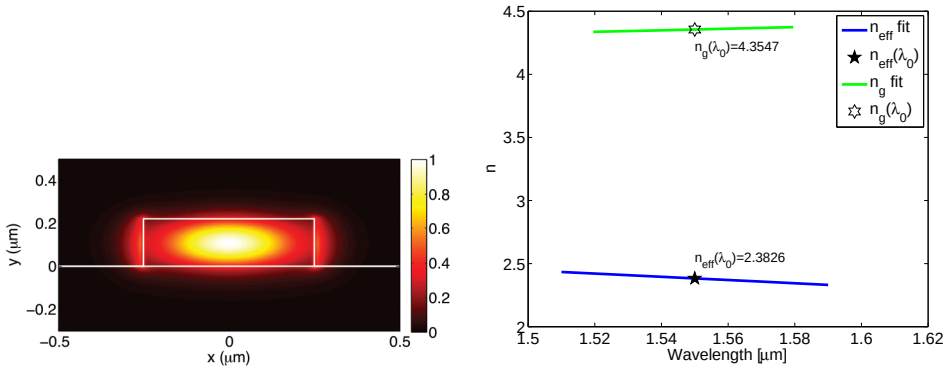

(a) (b)

Figure 3.3: **(a)** TE mode profile for a 220-nm high, 500-nm wide, air-clad strip SMWG. **(b)** Effective index (green) and group index (blue) curve-fits.

The effective indices for two-waveguide systems with varying gaps were obtained for discrete wavelength values and curve-fitted, as shown in 3.4(a) for 500 nm-wide strip WDC. Using these curve fits and equation (2.1, the cross-over lengths, $L_{\otimes}$, for WDCs with various gap values were obtained as a function of wavelength, as shown in Fig. 3.4(b). Table 3.1 shows theoretical values of $L_{\otimes}$ and κ for WDCs with constant length $L_c = 10$ µm and various gap values, used in various resonator designs.

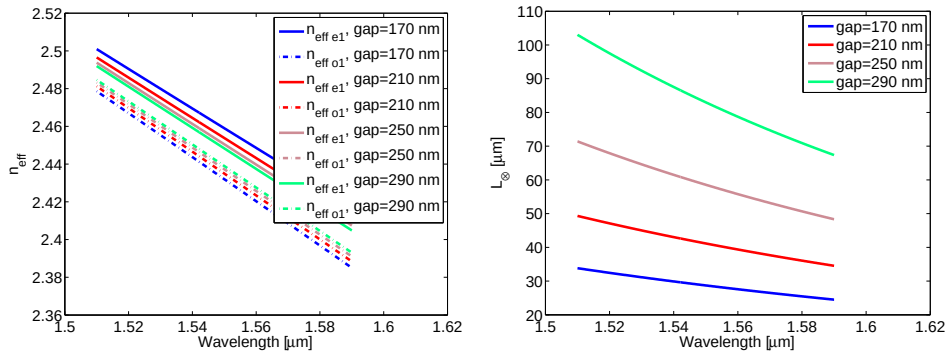

(a) (b)

Figure 3.4: **(a)** Effective indices for the even (solid) and odd (dashed) modes for WDCs made with 500-nm wide, strip SMWGs. (b) Corresponding WDC cross-over lengths as a function of wavelength.

Table 3.1: Parameters for WDCs made with 500-nm wide strip SMWGs, with $L_c = 10$ µm, at $\lambda_0 = 1550$ nm.

Gap [nm]	$L_\otimes$	$\kappa(L_c,\ \lambda_0)$
150	32.5	0.465
200	51.52	0.3
250	81.4	0.192
300	128.52	0.122
350	202.88	0.077

In order to create the resonator corners, 90° waveguide bends with constant radii were used. Since bend losses are greater for smaller radii, all 90° bends were designed with a constant radius of 20 µm, in order to ensure negligible bending losses (expected to be below 0.01 dB [13]). Table 3.2 summarizes the results of eigenmode solver simulations to assess the theoretical coupling between the modes of straight and bent strip waveguides, with horizontal and vertical meshing steps dx=15 nm and dy=20 nm, respectively. Other structures, such as long waveguide serpentines and small, circular ring resonators were also created in the mask layout in collaboration

with other group members, in order to assess SMWG propagation losses.

Table 3.2: Numerical results for mode power coupling between 500 nm-wide straight and bent strip waveguides (R=20 µm), at $\lambda_0 = 1550$ nm

Straight waveguide mode	Bent waveguide mode	Coupling [dB]
Fundamental (TE-like)	Fundamental (TE-like)	−0.0002
Fundamental (TE-like)	Mode 2 (TM-like)	−56.9
Mode 2 (TM-like)	Fundamental (TE-like)	−53.5
Mode 2 (TM-like)	Mode 2 (TE-like)	−0.005

3.1.2 Setup Design

Figure 3.5(a) shows a block diagram of the first measurement setup, which consisted of a sweep-tuneable laser source (TLS), optical power sensors, bare optical fibers, and manual XYZ stages for sample and fibre positioning. In this figure, the fibres are mounted on brass fibre chucks, and these are attached to XYZ stages. A sample pedestal is placed on a shorter XYZ stage, on top of a thermo-electric Peltier cooler (TEC) set to a constant temperature (usually 25 °C) using a Stanford Research Systems SRS LDC500$^{\text{TM}}$ 36-W TEC controller [122].

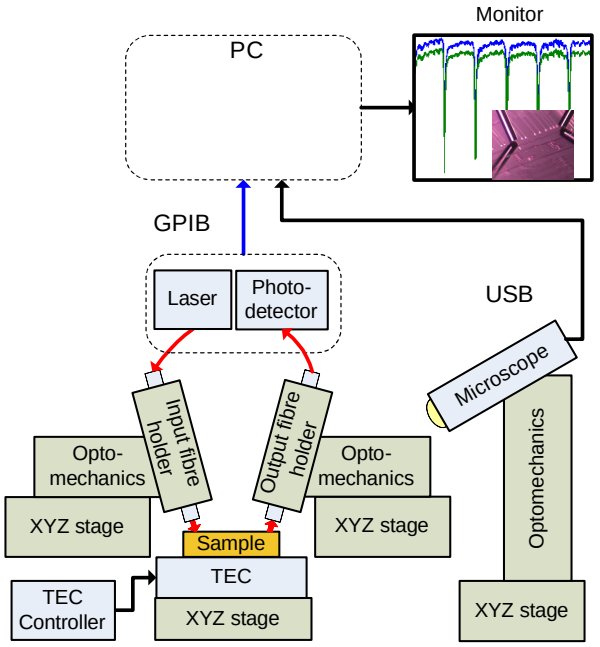

(a)

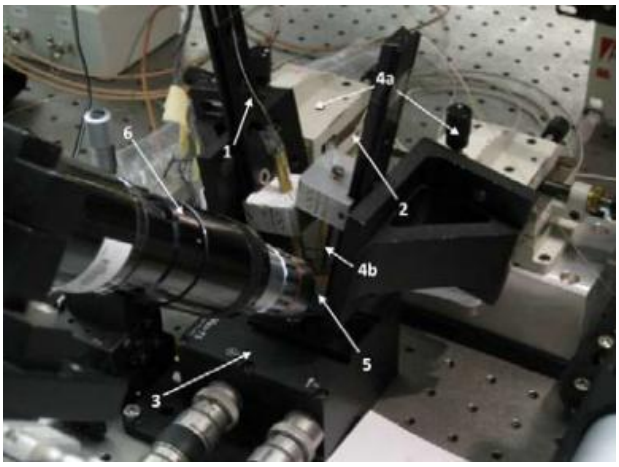

(b)

Figure 3.5: First characterization setup. **(a)** Block diagram. **(b)** Optomechanics assembly. (1) PM input fibre. (2) MM output fibre. **(3)** Pedestal on XYZ stage. **(4a)** Fiber XYZ Stages. **(4b)** Fiber chuck. **(5)** TEC. **(6)** Microscope. Image: G. Sterling.

In the actual setup, shown in Fig. 3.5(b), the optical signal from the TLS was injected into the chip using a polarization maintaining (PM) fibre. The output optical signal was collected by a multimode (MM) output fibre and directed to a photodetector. The reason for using a MM output fibre was to maximize the collected power. Both fibres were mounted at a 10°-angle with respect to the vertical, in agreement with the specifications of IMEC's 1D grating coupler design [13]. The TLS and the photodetectors were controlled using MATLAB^{TM} via General Purpose Interface Bus (GPIB), to sweep the wavelength and to record the received power. The microscope camera images were sent to the system computer via Universal Serial Bus (USB). All alignments were performed manually, using the microscope images as a visual aid. The alignments were considered optimal when the power reading at the photodetector mainframe was maximized, within a 0.1-dB accuracy.

3.1.3 Measurements

For this run, typical IL values ranged from -25 to -35 dB, with an average $IL_{avg} \approx -30$ dB). The fibre positions drifted over a period of several minutes. After realignment, the IL could vary significantly. This was attributed to the fact that the alignment was performed manually.

Ring Resonators

After several modifications to the opto-mechanical setup, it was possible to access the GCs of only some resonators on these chips. Figure 3.6(a) shows the spectrum for a 3.3-mm long resonator (see layout in Fig. 3.2(b)). The quality factor, Q, was calculated by dividing the resonance wavelength and the FWHM at each resonance. Fig 3.6(b) shows Q as a function of wavelength, and its average value, $Q_{avg} \approx 28000$. Based on the resonator length and the FSR value, the group index for this particular device was $n_g \approx 4.086$.

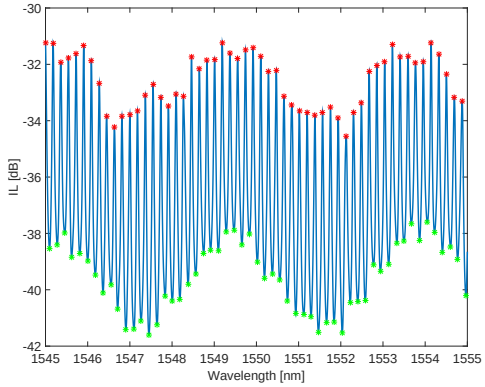

(a)

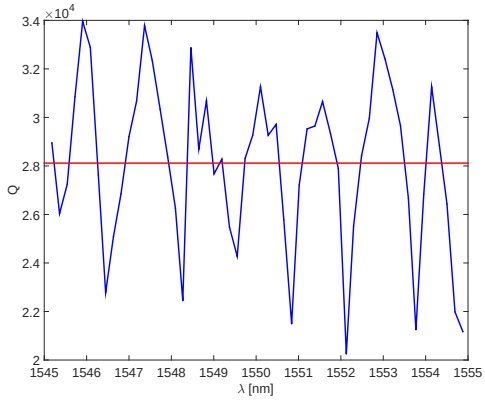

(b)

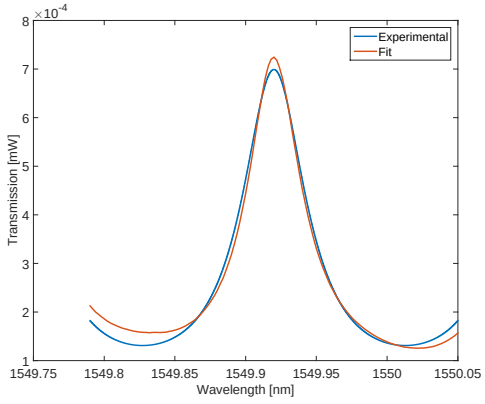

(c)

Figure 3.6: **(a)** Drop-port spectrum for a 3.3 mm-long resonator, showing maxima (red stars) and minima (green stars). **(b)** Q factor for each resonance (blue) and average Q (red). **(c)** Resonance curve-fit.

The spectrum was curve-fitted using equation (2.25), considering a symmetrical coupled case ($\kappa_a = \kappa_b = \kappa$), neglecting coupler losses ($\gamma = 0$), and using the nominal coupling as the initial guess ($\kappa_{\text{design}} = 0.465$ for this particular device). The curve fit shown in Figure 3.6(c) suggests a coupling $\kappa \approx 0.38$, and a propagation loss α_{dB} =20.2 dB/cm. However, different initial guess values yielded significantly different values for coupling, propagation loss, and IL. Further tests to verify these parameters were not possible, due to the lack of a through-port GC in these particular devices.

3.1.4 Fibre Attachment

In order to reduce the alignment variations over time, and foreseeing eventual rotary tests, I decided to perform fibre attachment tests with some of the chips, using optically-transparent, ultra-violet-curable adhesives. The DUTs for these experiments were 16-mm-long SMWG serpentines.

Firstly, in dry conditions, the input and output fibres were adjusted to a pitch angle $\theta_{\text{p air}} = 10^\circ$ with respect to the vertical. The fibres were aligned to the GCs of the device under test (DUT), and the spectrum was recorded.

Secondly, the fibres were raised to allow for the deposition of droplets of Norland^{TM} NOA 61 UV-curable adhesive on top of the input and output GCs of the DUT. The nominal refractive index of the adhesive was calculated based on the data provided by the manufacturer, as per the equation $n_{\text{glue}} = A + B/\lambda_{nm}^2 - C/\lambda_{nm}^4$, where $A = 1.5375$, $B = 8290.45$, $C = 2.11046 \times 10^8$, and λ_{nm} is the wavelength expressed in nm. In order to compensate for the transmission peak shift produced by the adhesive, the pitch angle was adjusted as follows, based on Snell's law:

$$\theta_{\text{p glue}} = \arcsin\left(\frac{\sin(\theta_{\text{p air}})}{n_{\text{glue}}}\right) = \arcsin\left(\frac{\sin 10^\circ}{1.5409}\right) \approx 6.5^\circ \qquad (3.1)$$

The fibres were submerged in the glue droplets, and realigned. The insertion losses in wet (uncured) adhesive showed an improvement between 5 and 6 dB. However, the simultaneous 1-minute-long curing of both adhesive droplets produced misalignment, increasing the IL. Figure 3.7 shows a com-

parison of the spectra for a particular DUT prior to applying any adhesive (blue), after applying the adhesive but prior to curing it (green), and after curing the adhesive (red).

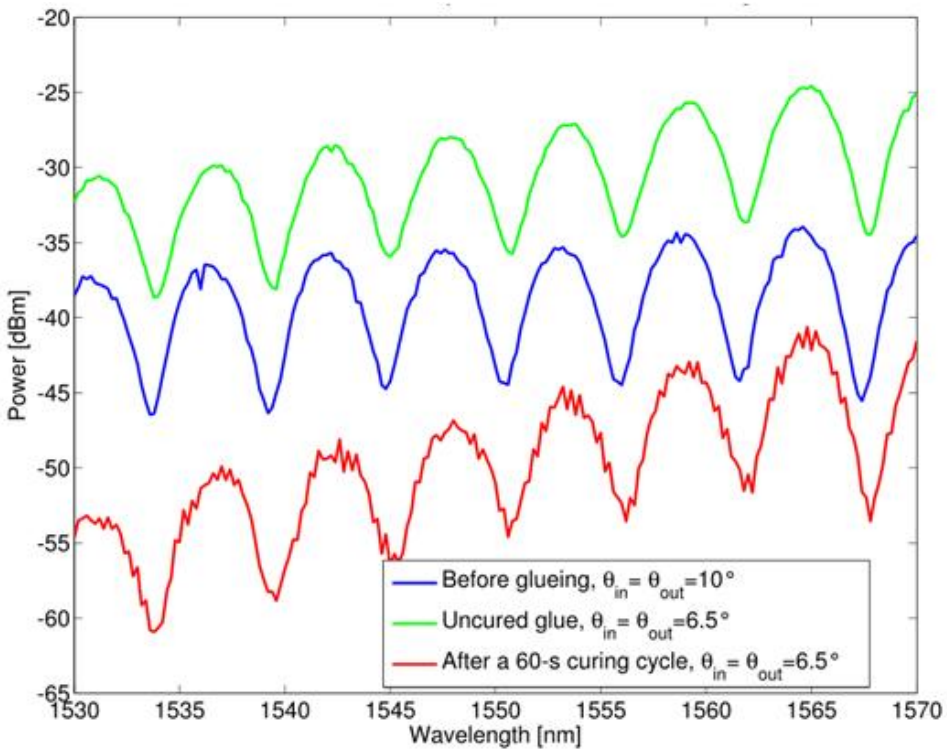

Figure 3.7: Comparison of spectra for a $16-$ mm long SMWG serpentine during a fibre attachment experiment.

In order to detach the fibres, it was necessary to cut the fibre tips, dismount the fibres from the chucks, strip them, cleave them, mount them in the chucks, and in the case of PM fibres, perform axial alignment to ensure proper mode injection into the GCs.

3.1.5 Iteration Challenges and Conclusions

The main difficulty faced during this design iteration was the lack of through-port output GCs for the large resonator designs. This prevented the disam-

biguation of experimental values of IL and coupling. No extracted parameter values other than the FSR, n_g, and Q factor could be trusted based solely on drop-port spectra. The GC orientation in the mask layout (Fig. 3.2(b), and the geometrical constraints imposed by the opto-mechanics (Fig. 3.5(b)) required modifications to reduce the distance between fibres. Therefore, the designs for the next iteration would have the GCs facing in opposite directions.

Due to adhesive viscosity and fibre flexibility, proper alignment of bare fibres was considerably more difficult in the uncured adhesive than without it. In a wet (uncured) adhesive, the fibres would not return to the same position after equal translations in opposite directions, i.e., they showed positional hysteresis. I also realized that samples with uncured adhesive had to be protected from light sources other than the UV curing gun light, as these light sources could initiate curing of the adhesive. Long curing cycles should be avoided early in the procedure, to allow for necessary positional adjustments. The minimum tip separation of fibres pointing in opposite directions was affected when performing wet alignments, as the pitch angles were closer to the vertical in that case. Finally, the fibre detachment was a destructive procedure, and preparing the fibres for the next alignment involved several delicate, time-consuming tasks.

3.2 Second Design Cycle

In the second iteration, one year later, IMEC offered two different fabrication batches, one known as the *standard* batch, with air cladding, and another one called the *custom* batch, which had a glass cladding and allowed for greater design parameter flexibility. The glass cladding offered the advantage of protecting the waveguides from scratches and contaminants such as dust. Once again, the UV illumination dose was intentionally varied during the lithography process.

3.2.1 Layout Design

Figures 3.8(a) and 3.8(b) show panoramic views of the designs included on chips with air and glass cladding, respectively. Table 3.3 summarizes the ranges of length, theoretical τ (assuming propagation losses of 3 dB/cm), and gap values for each resonator group. With a few exceptions, all gaps were multiples of 100 nm, and all coupler lengths were $L_c = 200$ µm.

Table 3.3: Length and gap ranges for various resonator groups shown in Figure 3.8

Resonator group	L range [mm]	τ range	g range [nm]
1 (custom)	14.27 to 16.37	0.607 to 0.564	200 to 700
2 (custom)	14.15 to 14.96	0.609 to 0.592	400 to 600
3 (custom)	16.49 to 17.02	0.561 to 0.551	150 to 700
4 (custom)	15.88 to 16.50	0.574 to 0.561	500 to 700
5 (custom)	6.47 to 7.90	0.797 to 0.758	200 to 500
A (std)	5.91 (all)	0.813	200 to 600

Waveguide Parameters

In addition to air-clad SMWG parameters, glass-clad SMWG parameters were required. These were obtained in a similar fashion as was done for the air-clad waveguides during the first iteration. Curve fits for the effective and group indices for glass-clad strip SMWGs are shown in 3.9(a), and cross-over length values for glass-clad strip SMWG directional couplers with various gap values are shown in Fig. 3.9(b). Tables 3.4 and 3.5 show theoretical values of $L_\otimes$ for various gap values, for air- and glass-clad directional couplers, respectively. These tables also show the L_c value required to achieve a 50% power coupling at $\lambda_0 = 1550$ nm, as well as the theoretical coupling for a fixed coupler length $L_c = 200$ µm. By comparing these two tables, as well as Fig. 3.9 to its first iteration counterpart (Section 3.1), one can see that the glass cladding produces an increase in n_{eff}, a slight decrease in n_g, and a decrease in the cross-over length values for the same gap.

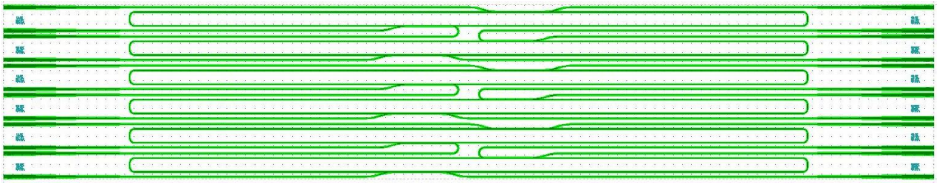

(a) Standard (air-clad) chip designs

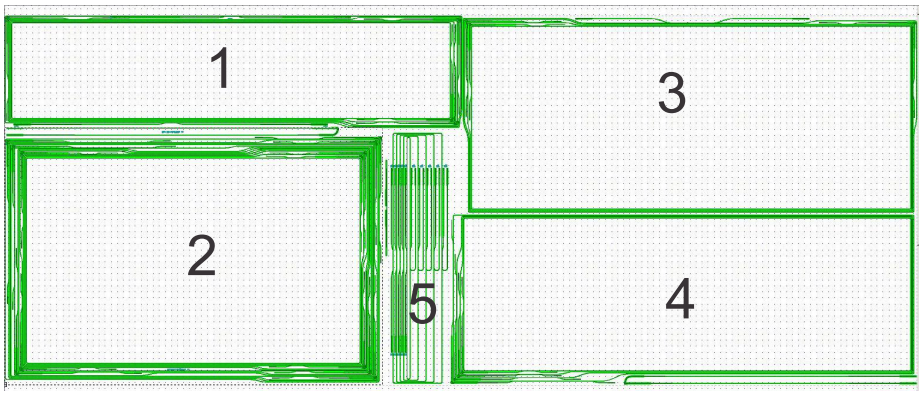

(b) Custom (glass-clad) chip designs

Figure 3.8: Second iteration mask designs (not to scale). **a** Standard process (air-clad) designs. **b** Custom process (glass-clad) designs.

Table 3.4: Cross-over length and selected parameters at $\lambda_0 = 1550$ nm, for air-clad strip WDCs with various gaps.

Gap [nm]	$L_{\otimes}$ [µm]	$L_c(\kappa = \frac{1}{\sqrt{2}})$ [µm]	$\kappa(L_c = 200$ µm)
150	46.2	23.1	0.492
200	73.6	36.8	0.902
300	180.7	90.4	0.986
400	438.7	219.3	0.656
500	1058.7	529.4	0.292
600	2543.1	1271.5	0.1232

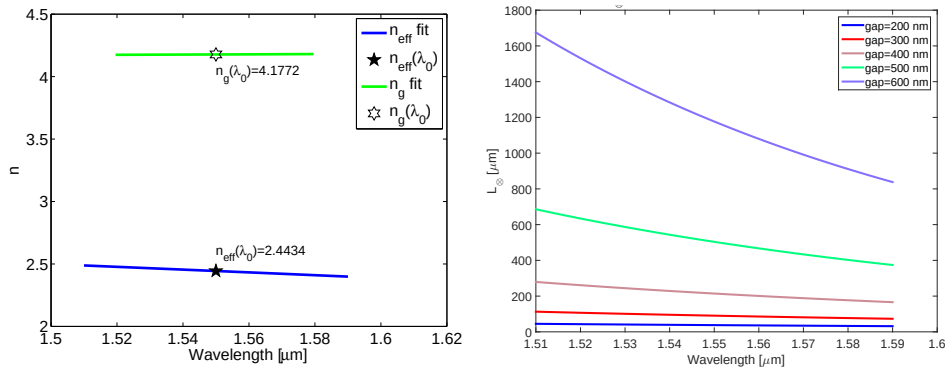

(a) (b)

Figure 3.9: **(a)** Effective index (green) and group index (blue) curve-fits, and **(b)** Cross-over length as a function of wavelength, for glass-clad strip WDCs with various gaps.

Table 3.5: Cross-over length and selected parameters at $\lambda_0 = 1550$ nm, for glass-clad strip WDCs with various gaps.

Gap [nm]	$L_\otimes$ [µm]	$L_c(\kappa = \frac{1}{\sqrt{2}})$ [µm]	$\kappa(L_c = 200$ µm)
170	28.7	14.4	0.998
200	37.6	18.8	0.877
210	41.2	20.6	0.974
250	58.6	29.3	0.797
290	83.0	41.5	0.60
300	90.5	45.3	0.324
400	214.3	107.2	0.995
500	503.7	251.8	0.584
600	1177.0	588.5	0.264

3.2.2 Setup Improvements

In an effort to decrease the ILs, lensed fibres were used as the input fibres for measurements being made by several group members. Initially, I used them as well for dry alignments (i.e., with no adhesive), however, due to the special geometry, fragility, and high cost of lensed fibres, attaching them

with adhesive would not have been viable, as this would have unavoidably affected their lensing properties. Also, as the realignment and detachment procedures required me to cut the fibre tips, one would not be able to recover from a misalignment at a reasonable cost. Therefore, in parallel to standard alignment and measurements (Subsection 3.2.3), I developed a set of 3D printed supports to glue my fibres prior to alignment (Subsection 3.2.4), as an alternative to the destruction and excessive cutting of fibres, with the idea that the supports would reduce position hysteresis during alignment, and would facilitate attachment, detachment, and fibre tip polishing.

3.2.3 Measurements

Table 3.6 shows the as-fabricated widths of waveguides designed to be 500 nm wide, based on IMEC metrology information relayed by Dr. D. Deptuck, from CMC Microsystems. The on-target doses were in column -2 for the standard (air-clad) wafer, and in column -1 for the custom (glass-clad) wafer.

Table 3.6: As-fabricated widths for 500 nm WGs, standard (air-clad) and custom (glass-clad) wafers.

Air-clad		Glass-clad	
Column	Width [nm]	Column	Width [nm]
-6	554.69	-6	532.37
-5	542.81	-5	526.97
-4	525.08	-4	520.04
-3	515.47	-3	514.95
-2	**502.49**	-2	504.31
-1	496.04	-1	**503.24**
0	486.63	0	494.54
1	479.62	1	489.96
2	465.11	2	482.84
3	463.28	3	477.33
4	441.49	4	467.33
5	452.69	5	465.84
6	433.07	6	458.63

Figure 3.10 shows the measured spectrum (dotted curve) for the through-port of an asymmetrically-coupled 5.91 mm-long resonator (Fig. 3.8(a)), from the air-clad chip at row "0", column "−3" (R0C−3). Both couplers had identical lengths $L_c = 200$ µm, and their gaps were $g_a = 400$ nm and $g_b = 500$ nm. As shown in Table 3.4, the as-fabricated width for 500 nm-wide waveguides for that particular column was 502.49 nm. Hence, the nominal field cross-coupling values were $\kappa_a = 0.656$, $\kappa_b = 0.292$. The respective through-coupling values, $t_a = 0.754$ and $t_b = 0.956$, were used as initial curve-fit guesses. Based on Eq. (2.24), assuming lossless directional coupling, the following equation was used for curve-fitting purposes:

$$|S_{21}|^2 = \frac{t_a^2 - 2t_a t_b \tau \cos(\phi) + t_b^2 \tau^2}{C_{\mathrm{IL}} \left[1 - 2t_a t_b \tau \cos(\phi) + t_a^2 t_b^2 \tau^2\right]} \tag{3.2}$$

The curve-fit algorithms are based on non-linear least-square-fits, computed using MATLAB$^{\mathrm{TM}}$. The initial algorithms proved very sensitive to the initial guess values. Considerable refinement efforts of the curve-fit algorithms were conducted by myself and various members of the research group. The red curve in Fig. 3.10 shows the curve-fit obtained with an algorithm developed by Dr. L. Chrostowski that estimates the refractive index and its dispersion based on the FSR of the DUT prior to performing the curve-fit based on Eq. (3.2). These refractive index parameters are used to create wavelength-dependent guess values of ϕ that allow for repeatable curve-fits encompassing several resonances. Although the ER is not perfectly matched, there is a high correlation between the measured and the fit data, regardless of the initial guess values. Table 3.7 shows the extracted parameter values and compares it to the nominal expected values. Figure 3.11 shows the measurement results for the through- and the drop-ports of the aforementioned ring.

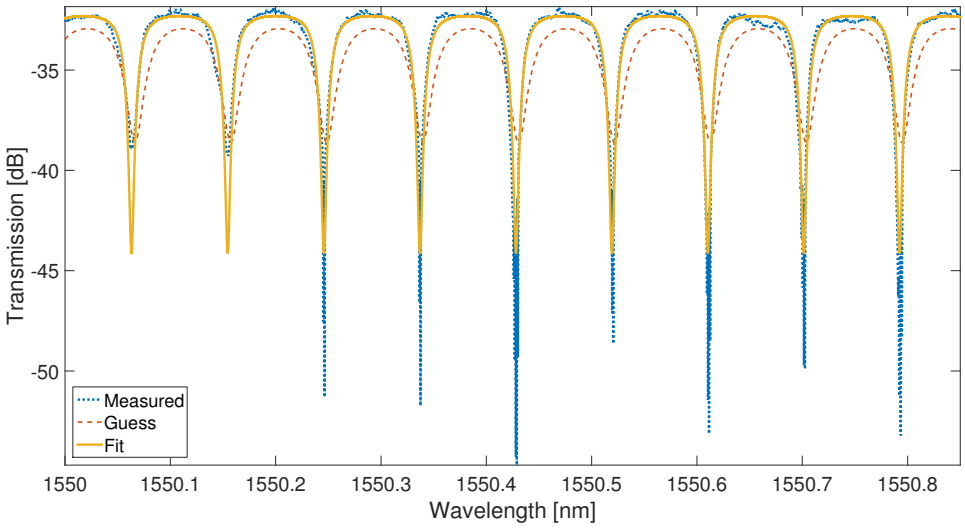

Figure 3.10: Through-port spectrum and curve-fits for a symmetrically-coupled, air-clad, 5.91 mm-long resonator (Ring 2, Std. Chip R0C−3).

Table 3.7: Through-port spectral curve-fit parameters for a 5.91 mm-long resonator (Ring 2, Std. Chip R0C−3), with a correlation value between measured and fit data $r^2 = 0.856$

.

Parameter	Nominal	Fit
IL_{dB}	~ 10	32
α_{dB}	3	4.65
n_g	4.3547	~ 4.46
κ_a	0.656	0.57
κ_b	0.292	0.07
t_a	0.754	0.821
t_b	0.956	0.997

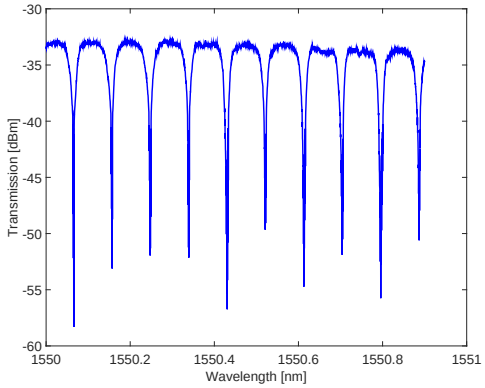

(a)

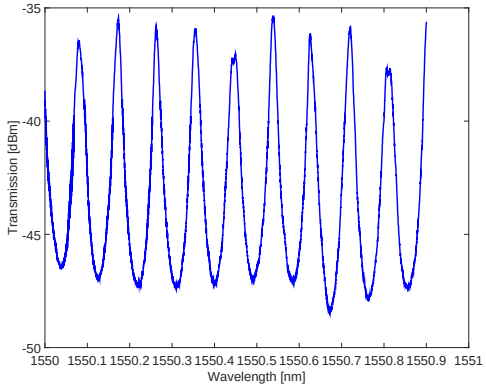

(b)

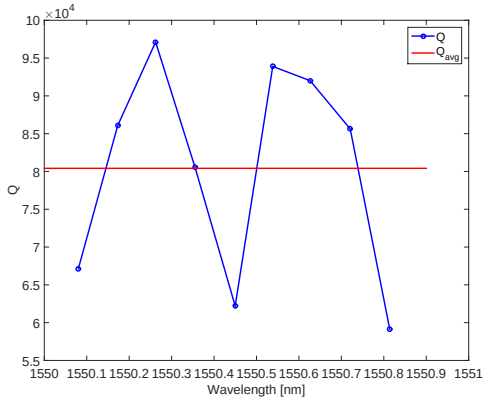

(c)

Figure 3.11: Spectra and Q for an air-clad, 5.91 mm-long resonator (Chip R0C−3, Dev. 2) with nominal field coupling values $\kappa_a = 0.656$ (through port), and $\kappa_b = 0.292$ (drop port). **(a)** Through-port transmission. **(b)** Drop-port transmission. **(c)** Q vs. wavelength, and average.

3.2.4 Fibre Attachment

In order to minimize breakage and shortening of fibres during detachment, Dr. H. Kato (CEO of Versawave Inc., and a collaborator with our research group) suggested using optical adhesives with relatively low glass transition temperatures, $T_g \leq 100\ ^{\circ}C$, and heating the chips to a temperature above T_g to detach the fibres. The value of T_g depends on the specific adhesive, being usually in the range between 80 °C and 100 °C [40, 61]. I designed fibre holders with various end-face angles in an effort to reduce insertion losses and to provide support for the fibre tips, thus decreasing the tip bending during alignment and attachment. Mr. A. Sharkia and I laid out and 3D-printed the fibre holder designs shown in Fig. 3.12. We also printed supports for mounting these holders to more compact opto-mechanics, e.g., mini-goniometres, that allowed for more precise angular adjustments. Metallic and plastic polishing jigs, with suitable angles, were also machined and 3D-printed. Each fibre holder had 3 trenches to allow multiple fibres to be attached. After fabrication of the initial holders, I noticed only 2 trenches, instead of 3, were printed on each holder. These trenches were shallower than expected, and their separation was not very repeatable. It was still possible to align and attach single fibres. Nevertheless, we considered that this approach should work for precision-machined holders, which we eventually acquired in the form of fibre arrays, as described in Section 3.4. Figure 3.13(a) shows the

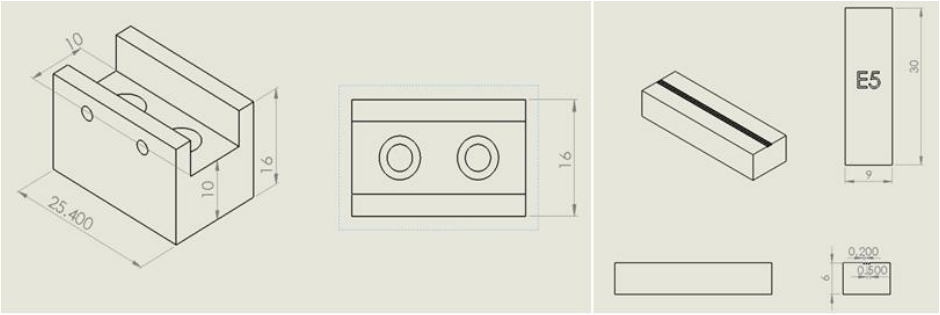

Figure 3.12: Fibre holders and support designs for 3D printing. Dimensions in mm.

station I created to align and attach the fibres to the holders. UV curable adhesive was deposited along the holder trench. A long-working-distance microscope, a fibre rotator, and two XYZ stages were used to align stripped fibres along the holders. This was followed by UV curing, as shown in Fig. 3.13(b). Initially I envisioned attaching PM fibres to these holders as well, however, aligning the polarization axes with those of the holders proved difficult. Thus, these holders were used exclusively with SM fibres. After fibre attachment, the end faces of the holders were polished in a portable fibre polishing station, shown in Fig. 3.13(c) in 30-minute coarse- and fine-grit cycles, with intermediate iso-propyl alcohol (IPA) and de-ionized water (DIW) washing cycles, to avoid grit cross-contamination. They were then viewed under a stereoscopic microscope, to inspect the polishing quality. Figure 3.13(d) shows fibre holders mounted on mini-goniometres, which are, in turn, mounted on manual linear stages using aluminium spacers.

3.2.5 Iteration Challenges and Conclusions

The experimental quality factors of devices fabricated in this iteration were more than double than those from the previous iteration (cf. $Q_{\text{avg }1} \approx 2.8 \times 10^4$ to $Q_{\text{avg }2} \approx 8 \times 10^4$). The finesse of these resonators is $F = \frac{Q\lambda_0}{n_g L} \approx 5$.

A 2D GC design provided by IMEC, and intended for on-chip optical power splitting, was used in most of my glass-clad resonator designs. However, the as-fabricated GCs showed uneven power splitting ratios and considerable IL, which rendered these devices inoperable.

Until that point in time, the spectral measurements in the characterization setup were slow, as the TLS wavelength tuning and the detector power acquisition was made through MATLAB$^{\text{TM}}$ by sending GPIB commands for point-by-point tuning and recording. This caused, for instance, single spectral sweeps with over 1000 data points to take longer than 15 minutes to be acquired. Based on written and oral communications with applications engineers from Agilent Technologies Inc. (now Keysight Technologies Inc.), I learned of alternative, faster spectral sweeps, based on a proprietary Plug and Play driver known as *"hp816x PnP"*, that could be used on various

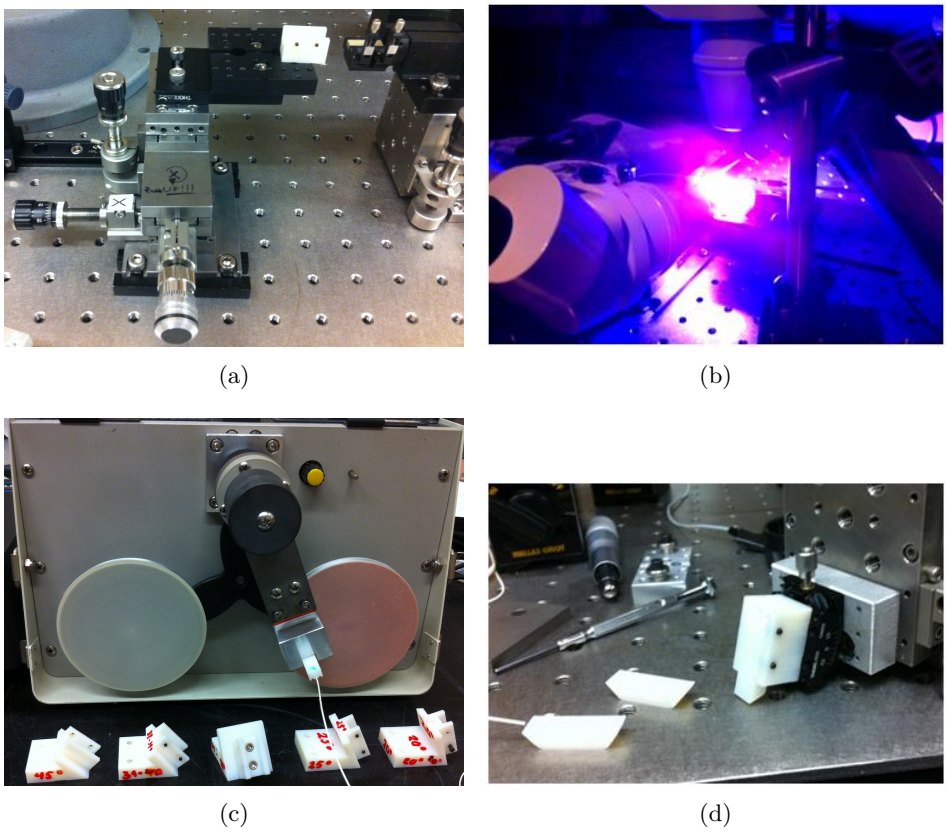

(a) (b)

(c) (d)

Figure 3.13: **(a)** Fibre holder glueing platform. **(b)** Fibre attachment to holder. **(c)** Polishing station and jigs. **(d)** Finished holders.

platforms, such as MATLAB™, LabVIEW™, and Python. Thus, during the next iteration, I implemented faster measurements using these drivers.

The 3D printed holders helped prevent the fibre tips from vibrating or bending during alignment. However, the far end of the holders, near the fibre jacket, had a brittle zone where bare fibre was exposed, which easily broke during either polishing, mounting, or alignment. Adjustments to the trench dimensions were also required, since the as-printed parts had shallower trench depths than the designs. Therefore, I improved the designs by adding 20-mm long, 1.2-mm wide channels at the far end of the holders, for robust fibre jacket attachment, as shown in Subsection 3.3.4.

3.3 Third Design Cycle

In our previous devices, we had resonators with Q factors in the range of 6×10^4 to 1×10^5, with an average value $Q_{avg} = 8\times10^4$. Assuming the ring is near critical coupling condition (based on the large ER values) the Q factor and the average field attenuation, α_{avg}, are related as follows [68, 141]:

$$Q = \frac{\pi n_g}{2\alpha_{avg}\lambda_0} \Rightarrow \alpha_{avg} = \frac{\pi n_g}{2\lambda_0 Q} \tag{3.3}$$

For $Q_{avg} = 8\times10^4$, $\lambda_0 = 1.55$ µm, and $n_g \approx 4$, the average field attenuation value is $\alpha_{avg} \approx 50$ m^{-1} $= 0.05$ mm^{-1}. This translates to a power attenuation $\alpha_p \approx 0.1$ mm^{-1}, which means that for a 6 mm-long resonator, the optical signal makes less than two roundtrips (1.67 roundtrips) before its original intensity decreases by a factor of e. Thus, in order to enhance the sensitivity of the devices, it was imperative to increase the Q factor of our resonators.

Since absorption in silicon is negligible for infrared wavelengths in the range from ~ 1 µm to ~ 4 µm [43], the main source of losses in the SMWGs is sidewall scattering [17, 78, 114]. As discussed by Payne and Lacey [98], Yap et al. [140], and Li et al. [78], for a fixed sidewall roughness value (determined by the fabrication process), the scattering losses decrease exponentially for increasing waveguide widths, as the field intensity of the fundamental mode at the sidewall edges is considerably smaller for wide multimode waveguides (MMWGs) as compared to SMWGs.

Therefore, we decided to use MMWGs as the straight segments of our resonators, which account for most of their length. SMWGs were still used for the directional couplers and corner bends, and were connected to the MMWG segments using linear tapers, as to avoid excitation of higher order modes [115]. This contributed to a significant reduction of the roundtrip loss and the achievement of greater Q values. Specifically, as shown in Section 3.3.3, the Q values for our strip waveguide resonators in this iteration ranged from 2×10^5 to 6×10^5, with an average $Q_{avg} \approx 3.4\times10^5$. As shown in Section 3.4.3, the eventual use of rib waveguides led to even lower roundtrip losses.

In this way, we achieved Q values as high as $\sim 4.5 \times 10^6$, with an average $Q_{avg} \approx 1.7 \times 10^6$, the largest Q values obtained to date using standard SOI techniques. Our results were published in [56].

Foreseeing eventual rotary tests, considerable improvements were made to the setup hardware and software. Specifically, I assembled a new optical characterization setup on a portable optical breadboard, and eventually placed it on top of a turntable, for which I designed the rotary control and signal acquisition system, in collaboration with other colleagues, as described in Subsection 3.3.2 and published in [55].

3.3.1 Layout Design

During this iteration, we submitted designs to the Nanofabrication Facility at the University of Washington, which had a single-etch process and used a 100 keV electron beam (e-beam) lithography system. Although still in development at the time, this particular process had turnaround times of a few weeks, rather than a year or longer. The GC designs for this fabrication run were provided by Dr. M. Hochberg's group, at the University of Washington. These were air-clad focusing GCs with a nominal incidence angle of 40°, and did not require long waveguide tapers. Depending on the refractive index of the adhesives used, an incidence angle between 23° and 25° would be required to shift the transmission peak back to a wavelength near 1550 nm, according to Eq. (3.1). The e-beam runs offered more layout area, thus allowing me to create larger resonators, with lengths ranging from 7 to 70 mm, and aspect ratios (ARs) closer to 1 as compared to resonators from previous runs, i.e., with shapes closer to a square, to maximize the area for a given length.

The idea behind the splitting/merging coupler design for these resonators, shown in Figure 3.14, is to split on chip the optical input signal, to inject two counter-propagating signals into the resonator, and to merge the two corresponding output signals upon exit. We expect intensity variation of the optical signals during rotation, as described below.

The optical input signal is coupled into the device using the main in-

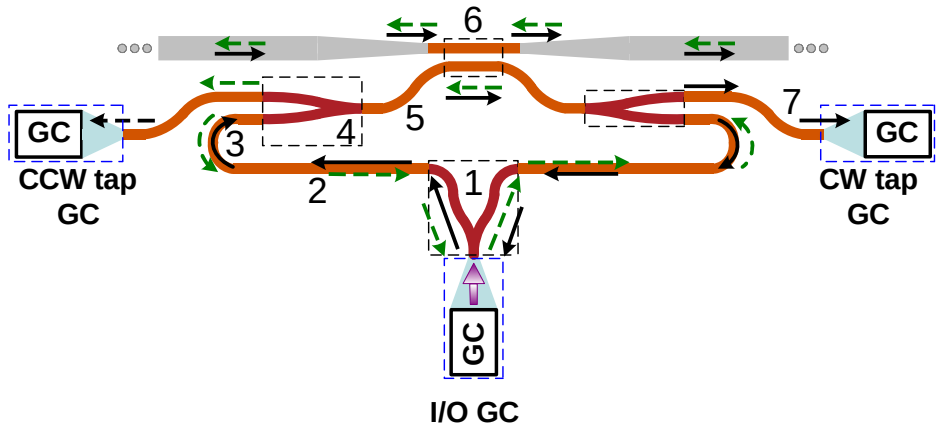

(a) Schematic

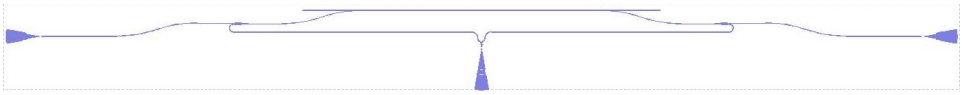

(b) Mask layout

Figure 3.14: **(a)** Splitting coupler schematic. **I/O GC**- Main Input/Output Grating Coupler. **1**- Central Y-branch. **2**- Straight SMWGs. **3**- SMWG 180° bends ($R_3 = 6$ µm). **4**- Tap Y-branches. **5** and **7**- SMWG S-bends ($R_5 = R_7 = 200$ µm). 6- SMWG directional coupler. **Tap GCs**- GCs for CW- and CCW-resonance monitoring. **(b)** Mask layout. Span: $\sim 1.5 \times 0.12$ mm.

put/output grating coupler (I/O GC). The central Y-branch (1) splits the input signal upon entrance, and merges the output signals upon exit. On each branch, the split signals travel through straight SMWGs (2) and 6-µm radius, 180° SMGW bends (3) towards 6°-angle Y-branches (4) that serve as output signal "taps", to independently monitor the spectra of the two optical signals travelling in opposite directions. SMWG S-bends with 200 µm radii and 20 µm vertical offsets (5) connect the stems of these tap Y-branches to the SMWG directional coupler (6), which injects light into, and collects light from, the large area resonator (grayed out) in opposite directions. The directional coupler lengths are designed to achieve optimal coupling depending on the resonator length, SMWG-to-MMWG length ratio, and a-priori propagation loss estimations, as per the optimization study

developed in Section 2.4 and published in [54].

Each counter-propagating output signal exiting the directional coupler is split by its corresponding tap Y-branch. Each top branch is connected via an S-bend (7) to a tap GC. This allows for monitoring the CCW and CW ring resonances using the left and right GC, respectively. The rationale behind the output S-bends (7) is to create sufficient separation between the tap GCs and the large resonator waveguides, thus avoiding damage to the resonator during fibre alignments. The bottom branch of each tap Y directs a fraction of each counter-propagating output signal towards the central Y-branch (1), where both are interfered.

Figure 3.15 shows the schematic of a resonator with its splitting/merging coupler and its interrogation block diagram. The I/O GC is interrogated using a polarization maintaining optical circulator. The tap GCs are interrogated using single mode fibres. Each signal is injected in a photodetector for intensity readout.

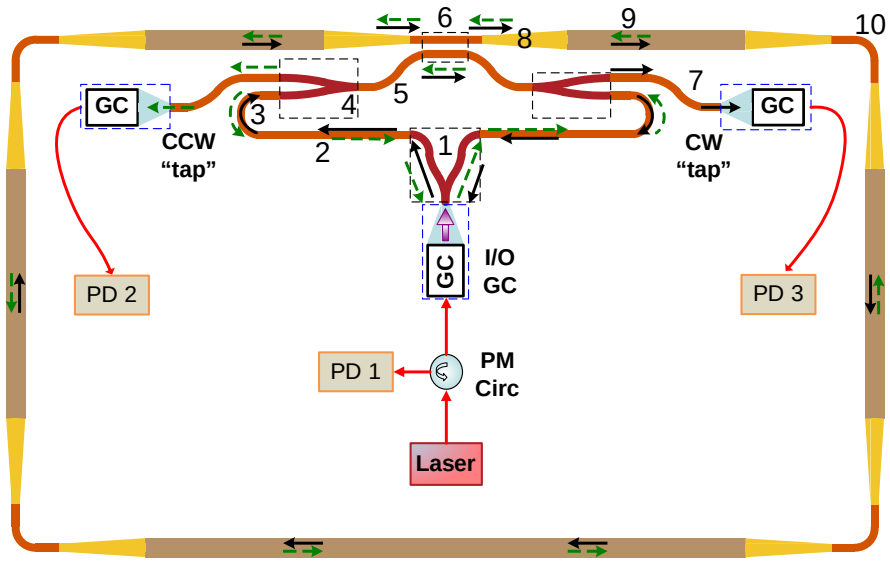

Figure 3.15: Gyro resonator schematic and interrogation block diagram. **1** through **7**- See nomenclature in Fig. 3.14. **8**- Linear waveguide tapers. **9**-Straight MMWGs. **10**-SMWG 90° bends (R_{10} = 20 µm), with 15 µm-long straight stubs on both ends.

Assuming a CW rotation, based on Eqs. (2.21) and (2.22), the electric fields at the CW and CCW taps are described by the following equations:

$$E_{\mathrm{CCW}} = \frac{e^{-j\Phi_{\mathrm{sct}}}}{2\sqrt{2}\sqrt{C_{\mathrm{IL}}}} \cdot T\left(-\Phi_S\right), \tag{3.4}$$

$$E_{\mathrm{CW}} = \frac{e^{-j\Phi_{\mathrm{sct}}}}{2\sqrt{2}\sqrt{C_{\mathrm{IL}}}} \cdot T\left(\Phi_S\right), \tag{3.5}$$

where $\Phi_{\mathrm{sct}} = -j\alpha_{\mathrm{sc}}L_{\mathrm{sct}} + \phi_{\mathrm{sct}}$, α_{sc} is the average propagation loss of the splitting coupler waveguides, L_{sct} and ϕ_{sct} are, respectively, the waveguide path length and the phase shift undergone from the central Y-branch to each tap GC, $C_{\mathrm{IL}} = 10^{\frac{IL_{\mathrm{dB}}}{10}}$ is a coefficient corresponding to an insertion loss IL_{dB} in dB, and the function $T(\Phi_S)$ represents the Sagnac-phase-shifted transfer function of the resonator, given by:

$$T\left(\Phi_S\right) = \frac{t - e^{-j(\Phi_{\mathrm{ring}}+\Phi_{\mathrm{S}})}}{1 - te^{-j(\Phi_{\mathrm{ring}}+\Phi_{\mathrm{S}})}}, \tag{3.6}$$

where $t = \sqrt{1-\kappa^2}$, κ is the field cross-coupling of the WDC depicted by (6) in Fig. 3.15, $\Phi_{\mathrm{ring}} = -j\alpha_{\mathrm{ring}}L + \phi_{\mathrm{ring}}$, α_{ring} is the average propagation loss of the ring resonator, L is the resonator length, $\phi_{\mathrm{ring}} = 2\pi n_{\mathrm{eff}}L/\lambda$ is the phase undergone by the beams due to the resonator optical path, Φ_{S} is the Sagnac phase shift.

The merged output signal exits the device via the I/O GC, and shows an amplitude modulation that depends on the phase difference between the CW and CCW resonances due to $\delta\phi$. Based on Eqs. (3.4) and (3.5), the electric field of the merged output signal is:

$$\begin{aligned} E_{\mathrm{merged}} &= \frac{e^{-j\Phi_{\mathrm{scl}}}}{4\sqrt{C_{\mathrm{IL}}}} \cdot \left(T\left(\Phi_S\right) + T\left(-\Phi_{\mathrm{S}}\right)\right) \\ &= \frac{e^{-j\Phi_{\mathrm{scl}}}}{2\sqrt{C_{\mathrm{IL}}}} \cdot \frac{t\left(e^{j\Phi_{\mathrm{ring}}} + e^{-j\Phi_{\mathrm{ring}}}\right) - \left(t^2+1\right)\cos(\Phi_{\mathrm{S}})}{e^{j\Phi_{\mathrm{ring}}} - 2t\cos(\Phi_{\mathrm{S}}) + t^2e^{-j\Phi_{\mathrm{ring}}}} \end{aligned} \tag{3.7}$$

where $\Phi_{\mathrm{scl}} = -j\alpha_{\mathrm{sc}}L_{\mathrm{scl}} + \phi_{\mathrm{scl}}$, L_{scl} is the length of the waveguide loop be-

tween the arms of the central Y-branch, and ϕ_{scl} is the phase shift undergone by traversing this loop. The power for each port, P_{CCW}, P_{CW}, and P_{merged}, can be obtained as the modulus squared of the expressions given by Eqs. (3.4) through (3.7).

Figure 3.16 compares the theoretical output power levels at rest and under rotation with a Sagnac phase shift $\Phi_{\mathrm{S}} = 0.02\pi$ rad, as functions of the ring normalized detuning, ϕ_{ring}/π, for a resonator with length $L = 7.5$ mm, coupling $\kappa_a = 0.255$, average propagation loss $\alpha_{\mathrm{dB}} = 1$ dB/cm, and negligible attenuation and IL at the splitting coupler ($\alpha_{\mathrm{sc}} = 0$ m^{-1}, $IL_{\mathrm{dB}} = 0$ dB).

The brown dotted curve shows the power at the merged output at rest, $P_{\mathrm{merged}}(\Phi_{\mathrm{S}} = 0)$. The orange dotted curve shows power of both tap outputs at rest, $P_{\mathrm{CCW}}(\Phi_{\mathrm{S}} = 0) = P_{\mathrm{CW}}(\Phi_{\mathrm{S}} = 0)$. The green solid curve shows the power of the merged output under rotation $P_{\mathrm{merged}}(\Phi_{\mathrm{S}} = 0.02\pi)$, and the red and blue solid curves show the phase-shifted power spectra for the CW tap, $P_{\mathrm{CW}}(\Phi_{\mathrm{S}} = 0.02\pi)$, and the CCW tap, $P_{\mathrm{CCW}}(\Phi_{\mathrm{S}} = 0.02\pi)$, respectively. The magenta dash-dotted curve shows the ratio between the merged output power at rest and under rotation, $P_{\mathrm{merged}}(\Phi_{\mathrm{S}} = 0.02\pi)/P_{\mathrm{merged}}(\Phi_{\mathrm{S}} = 0)$. The cyan dash-dotted curve shows the ratio between the CW and the CCW tap under rotation, $P_{\mathrm{CW}}(\Phi_{\mathrm{S}} = 0.02\pi)/P_{\mathrm{CCW}}(\Phi_{\mathrm{S}} = 0.02\pi)$. The CW and CCW spectra shift under rotation, and this produces a power variation between them at each ϕ_{ring}. The maximum and minimum ratio occur at a value of ϕ_{ring} that is phase-shift dependent, as shown by the cyan dash-dotted curve, and shift further away from the static resonance null for greater $\delta\phi$. Frequency tracking is required in order to follow the resonance shifts. However, the resonant frequency difference created by the Sagnac effect is much smaller than the temperature-induced drifts [102], which require frequency and phase spectroscopy techniques [82, 118, 121, 144]. As shown by the magenta dash-dotted curve, the phase-shift-dependent power variation of the merged output has its greatest variation at the original resonance null, and as it does not require frequency tracking techniques, we decided to use it as our sensing signal at this stage.

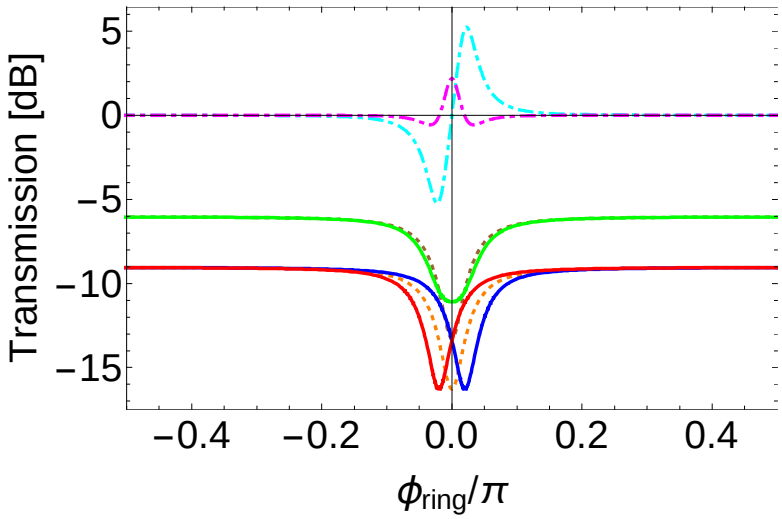

Figure 3.16: Theoretical power levels for the tap and merged outputs versus ring normalized detuning, ϕ_{ring}/π, at rest (dashed curves) and under CW rotation (solid curves) with a Sagnac phase shift $\Phi_{\text{S}} = 0.1\pi$ rad, and $IL_{\text{dB}} = 0$ dB. Resonator parameters: $L = 7.5$ mm, $\kappa_a = 0.255$, and average propagation loss $\alpha_{\text{avg dB}} = 1$ dB/cm. Dotted orange curve: CW and CCW taps at rest. Solid red and blue curves: CW and CCW taps, under rotation. Dotted brown curve: Merged output at rest. Solid green curve: merged output, under rotation. Cyan dot-dashed curve: Tap power ratio under rotation, $P_{\text{CW}}(\Phi_{\text{S}} = 0.02\pi)/P_{\text{CCW}}(\Phi_{\text{S}} = 0.02\pi)$. Magenta dot-dashed curve: merged output power ratio, $P_{\text{merged}}(\Phi_{\text{S}} = 0.02\pi)/P_{\text{merged}}(\Phi_{\text{S}} = 0)$.

Waveguide Parameters

We chose a MMWG width of 3 μm, i.e., one micrometre wider than the waveguides studied by Yap et al [140]. The widths of the SMWGs remained 500 nm. All waveguides had heights of 220 nm, and all were air-clad strip waveguides, due to the single-etch option. 200 µm-long linear tapers were used for conversion between SMWGs and MMWGs. Figure 3.17 shows the polynomial curve-fits for the effective and group indices as functions of wavelength for straight strip SM and MMWGs. Table 3.8 summarizes the effective and group index values at $\lambda = 1550$ nm, for the fundamental modes of strip waveguides with various widths and radii, obtained using MODE

Solutions^{TM} eigenmode solver with a 15-nm mesh.

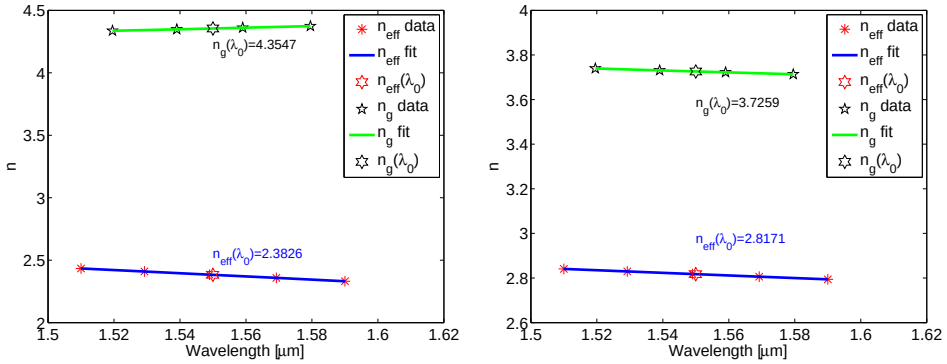

(a) W=500 nm (b) W=3 µm

Figure 3.17: Effective and group index curve fits for air-clad strip waveguides of different strip widths. Also shown, original data points and fitted values for $\lambda_0 = 1550$ nm.

Table 3.9 shows the results of numerical simulations carried out to assess the cross-talk between the various modes of straight SMWGs and those of bent waveguides with radii $R_3 = 6$ µm and $R_5 = 200$ µm. Each waveguide supports two guided modes with different polarizations, a TE-like mode and a TM-like mode. The cross-talk between straight SMWGs and bent SMWGs with 20 µm radius are shown in Table 3.2. An initial estimate for the propagation loss values of the SMWGs and MMWGs, shown in Table 3.10, was required to determine the coupling for each resonator, as the optimum coupling depends mainly on the resonator length and roundtrip loss, as per our optimization study in [54]. I created algorithms to determine the optimum coupling values based on resonator port configuration, loss parameters, AR, total length, and SM-to-MM length ratio. For simplicity, and considering their short lengths in comparison to the resonator dimensions, the indices and propagation loss of linear tapers were approximated to be the averages of the respective SM and MM values.

Table 3.8: Effective and group indices at $\lambda_0 = 1550$ nm for strip waveguides of various geometries. In all cases the height is $H = 220$ nm

Width [nm]	Radius [µm]	Mode	n_{eff}	n_{g}
500	∞	TE-like	2.3826	4.3547
500	∞	TM-like	1.5821	3.3895
500	200	TE-like	2.3823	4.3546
500	200	TM-like	1.5821	3.4395
500	20	TE-like	2.3824	4.1977
500	20	TM-like	1.5827	3.4276
500	6	TE-like	2.3976	4.1967
500	6	TM-like	1.728	2.119
1750	∞	TE-like	2.7942	3.7543
1750	∞	TM-like	2.6876	3.9029
3000	∞	TE-like	2.8171	3.7251
3000	∞	TM-like	2.7813	3.7726

Table 3.9: Coupling between straight and bent strip SMWG modes at $\lambda_0 = 1550$ nm. W=500 nm, $R_3 = 6$ µm, and $R_5 = 200$µm.

Straight WG mode	Bend radius, mode	Coupling [dB]
TE-like	R_3, TE-like	-0.0027
TE-like	R_3, TM-like	-56.9
TM-like	R_3, TE-like	-42.7
TM-like	R_3, TM-like	-0.012
TE-like	R_5, TE-like	-4.34×10^{-6}
TE-like	R_5, TM-like	-75.0
TM-like	R_5, TE-like	-71.3
TM-like	R_5, TM-like	-9.9×10^{-5}

The WDCs in this run had 500 nm gaps, with a theoretical $L_{\otimes} = 1058.7\ \mu$m (see Table 3.4). Table 3.11 shows the theoretical field coupling for various coupler lengths used in the devices.

Table 3.10: A-priori propagation loss estimates for air-clad strip waveguides

Parameter \ Kind	SM strip	MM strip
α_{dB} [dB/cm]	4	1
α [1/m]	46.05	11.513

Table 3.11: Theoretical field coupling for air-clad strip SMWG directional couplers, $g = 500$ nm ($L_{\otimes} = 1058.7$ μm)

L_c [μm]	κ
90	0.1331
174	0.255
315	0.451
400	0.0.559
435	0.602
527	0.705

Layout Scripting

Considering the significant amount of time invested on manually drawing the layouts in the first two iterations, we considered more efficient to create codes for semi-automatic layout generation. During this design iteration, I used MATLAB$^{\mathrm{TM}}$ codes to generate and place basic waveguide shapes in WieWeb CleWin$^{\mathrm{TM}}$, to create resonator shapes. Various elaborate structures such as Y branches, S bends, and GCs were created separately (either manually or by script), saved as layout cells, and instanced in the main layout code.

Figure 3.18(a) shows a panoramic view of an e-beam layout design, and Fig. 3.18(b) shows a zoomed-in view of the area enclosed by the blue rectangle. The resonator lengths in this design range from 7 mm to 70 mm. Several straight SM and MM waveguides with various lenghts were included across the layout, in an effort to experimentally estimate the propagation losses in both SMWGs and MMWGs.

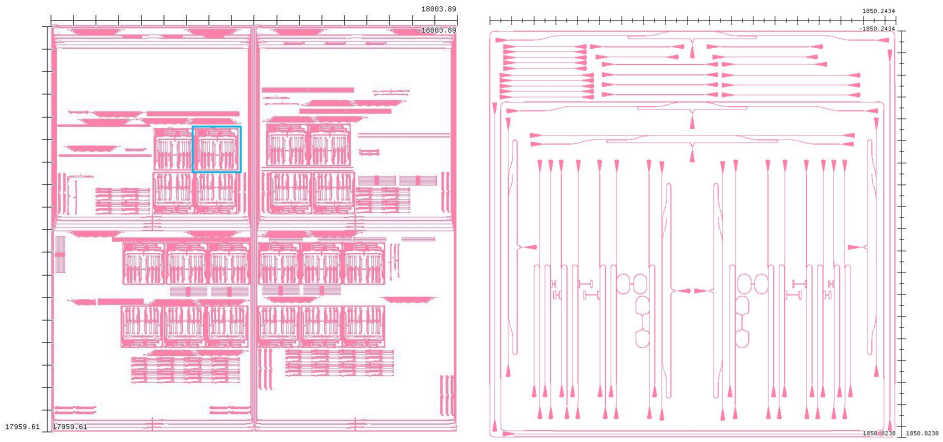

(a) Panoramic view (b) Zoom in

Figure 3.18: First E-beam layout design.

3.3.2 Setup Design

During my literature review, I noticed that many research groups working on this subject inject artificial rotation signals into their devices, rather than facing the challenges posed by mechanical rotation, vibration, and packaging, see for example [34, 36, 83, 121]. In contrast, I decided to create a mechano-opto-electrical setup for characterizing SOI gyroscopes under actual rotation conditions. The first priority was, thus, to create a new optical characterization setup assembled on an optical breadboard. The optical breadboard was portable so that it could, eventually, be placed on top of a turntable. The second priority was to improve the fibre attachment supports.

First Rotary Setup

I built the opto-mechanical setup shown in Fig. 3.19(a) on a portable mini-breadboard, using several mounting posts and five manual-adjustment translation stages. Three linear stages are used for positioning optical fibre holders and rotators. Another stage is used for mounting a heatsink and a TEC for temperature control of the sample pedestal. A fifth translation stage is

used as a detachable jig for adhesive dispensing and curing. As a result, the opto-mechanical setup weighs over 20 kg and spans $46 \times 30 \times 60$ cm in length, width and height, respectively. This setup was eventually transferred on top of a rotary platform, shown in Fig. 3.19(b). Additional payload capability and off-breadboard area were required for mounting a long-working-distance microscope, used during fibre alignment and attachment (Fig. 3.24(b)). The fibre attachment in this setup was carried out with bare fibres, as the second fibre holder generation was being developed in parallel.

In order to support the optical breadboard, a 52-cm diameter acrylic platform was mounted on a 38-cm diameter ball bearing ring, which in turn was attached to a wooden frame. A timing belt was glued to the outer edge of the ball bearing ring and was actuated by a pulley, mounted on a DC motor with a nominal working voltage of 12 V, and a torque of 16.7 kg-cm. Motor drivers and a microcontroller were also attached to the wooden frame for angular speed and direction control. A MEMS gyroscope with a sensing range of ± 400 dps, a sensitivity of 0.02 dps $\cdot$ Hz$^{-\frac{1}{2}}$, a bandwidth of 140 Hz, and a nominal noise level of 0.236 dps [117], was mounted on the rotary platform as a calibration reference. The turntable was modelled as a first-order system with a transfer function of the form:

$$H(\omega) = \frac{A \cdot e^{j\phi_0}}{j\omega/\omega_0 + 1}, \tag{3.8}$$

where $\omega = 2\pi f$ is the angular frequency in rad/s, f is the frequency in Hz, $\omega_0 = 2\pi f_0$ is the cut-off angular frequency, f_0 is the system bandwidth, in Hz, A is the DC gain, and ϕ_0 is a phase offset to represent a constant delay between the input and output signals. This transfer function has a magnitude and a phase response given respectively by:

$$|H(\omega)|^2 = \frac{A^2}{(\omega/\omega_0)^2 + 1}, \tag{3.9}$$

$$\measuredangle H(\omega) = \phi_0 - \arctan(\omega/\omega_0). \tag{3.10}$$

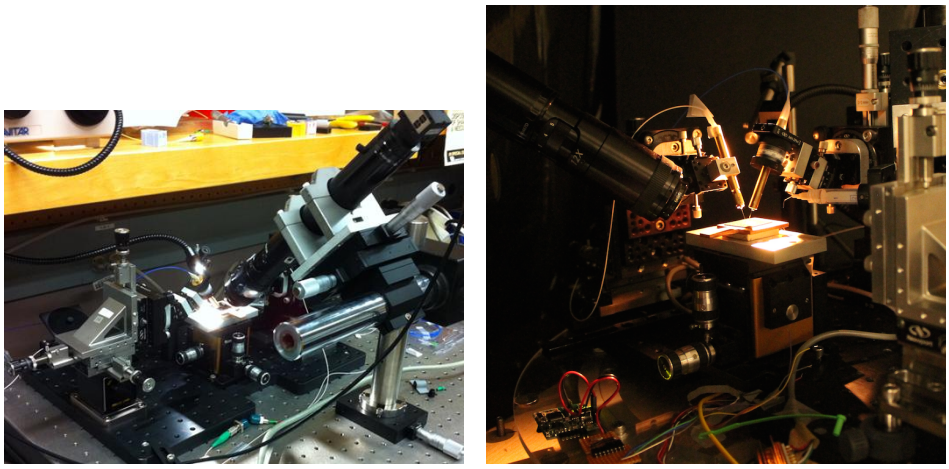

(a) (b)

Figure 3.19: Mini-breadboard characterization setup. **(a)** Initial benchtop configuration. **(b)** On rotary platform, showing on-board reference gyroscope (bottom left), and off-platform microscope (top left).

System Control

The control system uses an NI^{TM} PXIe 1062Q mainframe with a PXIe 8133 central processing unit (CPU), a DC power supply, and an PXI 7852R Field-Programmable Gate Array (FPGA) module with multiple digital and analogue I/O channels [65, 66]. As depicted in Fig. 3.20, the PXIe 1062Q controls an optical mainframe (laser source and photodetectors) as well as the TEC driver using a General-Purpose Interface Bus (GPIB) interface, and communicates with the microcontroller via RS-232.

In order to simultaneously monitor signals and send commands to the rotation microcontroller, a Graphical User Interface (GUI) was implemented using LabVIEW^{TM}-FPGA. The FPGA target-host communication is made through a 128-bit Direct Memory Access First Input/First Output block (DMA FIFO) for recording the motor control digital signals, as well as the analogue signals from the DUT and reference gyroscope.

The optical input signal is generated by a C-band Tuneable Laser Source (TLS). The light is coupled to the input GC using polarization-maintaining

(PM) patch cords. Depending on the specific interrogation configuration, the optical output signal(s) are collected using either a PM optical circulator, or independently-positioned multi-mode output fibre patch cords. Up to three photodetectors are used simultaneously. To avoid fibre entanglement, the turntable was operated using *bow-tie* rotation patterns, consisting of periodic, angle-limited movements.

The micro-controller generates two digital signals: a slowly varying signal which defines the motor rotation direction, and a 500-Hz Pulse-Width-Modulated (PWM) signal, whose duty cycle is directly proportional to the normalized angular speed, S_n. During rotation electrical signals were sent to, and collected from, the reference gyroscope and the TEC, via a slip ring.

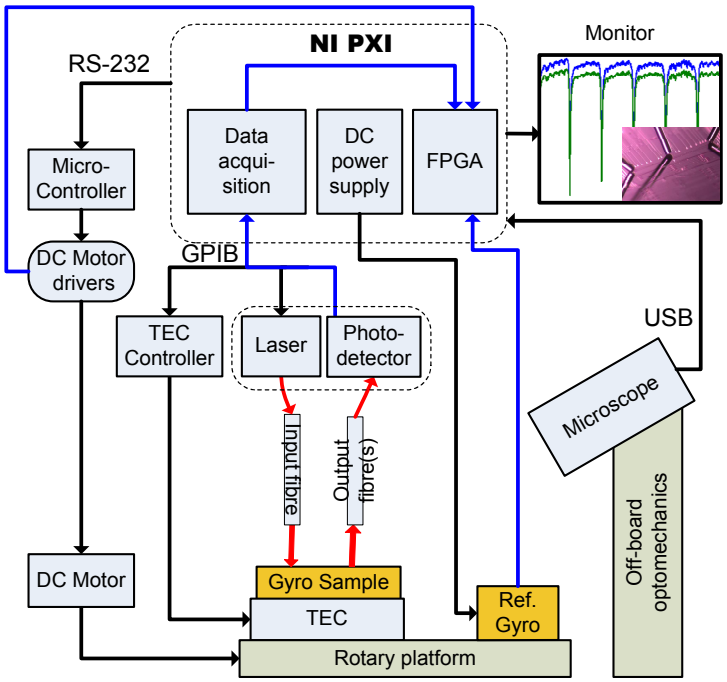

Figure 3.20: SOI gyroscope characterization platform block diagram.

Rotation Patterns

Four different rotation patterns, which are described below, were programmed into the micro-controller.

1. Continuous rotation: The rotation direction and the value of S_n are defined in the GUI, in order to rotate the platform at the specified speed and direction. This pattern was mainly used to characterize the turntable speed response.

2. Rectangular *bow-tie* rotation: The user defines values of S_n and travel angle, θ. The turntable will rotate in the clock-wise (CW) direction at the given speed until the travel angle is reached, then stop and rotate the same amount in the counter-clock-wise (CCW) direction. This motion creates a rectangular *bow-tie* angular speed pattern, which is repeated until stopped by the user via the GUI.

3. Sinusoidal *bow-tie* rotation: A sinusoidal *bow-tie* speed pattern, rather than a rectangular one, was necessary for obtaining the frequency response of the turntable, and characterizing the DUT. Appendix B shows a detailed explanation of the generation of these patterns.

4. User-defined rotation: created using an array of angular speed and angular travel values. In this case, a sign is added to the normalized speed for defining the rotation direction. The angular travel is always a positive number, in degrees. The motion stops after executing as many steps as entered in the array.

3.3.3 Measurements

As the rotational pattern would be sinusoidal, we wished to have a quantitative idea of the frequency and speed ranges at which our turntable setup would be able to work. We carried out tests to determine these parameters, followed by static and rotational tests on our photonic devices.

Speed Range and Noise Level

We measured the turntable step-response, i.e., going from rest to continuous rotation, at different speeds. As shown in Fig. 3.21, the relationship between the turntable angular speed and the value of S_n was non-linear. Even though angular speed values below 20 dps could be achieved, these could not be sustained, because vibrations and the payload occasionally hindered or stopped the movement. These problems did not arise at high angular speeds nor during unloaded motor tests, suggesting that this may be caused by a combination of insufficient motor torque, unbalanced payload coupling, and a weak motor base condition [49]. The minimum repeatable angular speed was $\Omega_{min} \approx 27$ dps (for $S_n = 0.175$), whereas the maximum angular speed was $\Omega_{max} \approx 74.3$ dps (for $S_n = 1$). The angular acceleration values range from 9.4 to 171.2 dps^2. As shown by the error bars in Fig. 3.21, the noise level decreased as the normalized angular speed increased. For example, the noise level was $\delta\Omega = 2$ dps for $S_n = 0.175$, and $\delta\Omega = 0.73$ dps for $S_n = 1$.

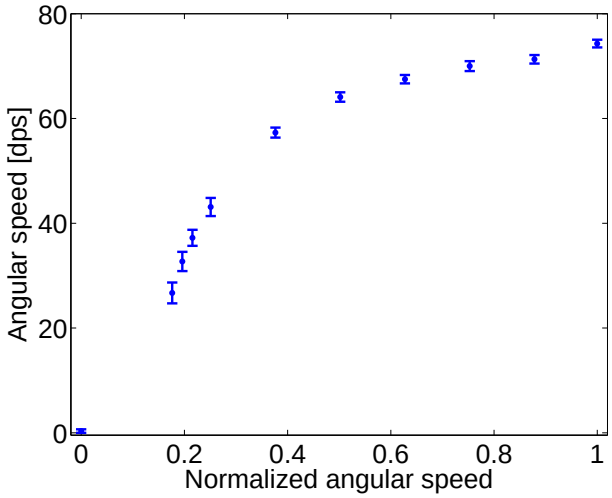

Figure 3.21: Average angular speed (dots) and noise level (error bars), as a function of normalized speed, S_n.

Frequency Response

We operated the turntable in a sinusoidal bow-tie fashion, and used the reference gyroscope output signal to characterize the frequency response of the turntable. The input consisted of over forty sinusoidal pulses, stepped in frequency between 0.05 and 5 Hz. To avoid damaging the optical setup, a maximum normalized angular speed value $S_{n_{max}} = 0.4$ was used for all frequencies. Figure 3.22 shows the input and output signals for a frequency $f_{in} = 0.89$ Hz. The PWM duty cycle (red curve), is signed according to the rotation direction (black curve) for fitting purposes and easier visualization.

For each sinusoid frequency, we curve-fitted both the normalized angular speed of the motor (red curve), and the reference gyroscope output signal (orange curve), in order to obtain the phase shift between both signals. We also extracted the magnitude of the reference gyroscope signal, as explained in Appendix B. The magnitude and phase responses of the turntable are shown in Fig. 3.23. We curve-fitted both the magnitude and the phase responses using Eqs. (3.9) and (3.10). According to the fit parameters, $f_0 = 0.54$ Hz, $A = 0.383$ ($A_{\text{dB}} = -8.33$ dB), and $\phi_0 = -11.9$ degrees.

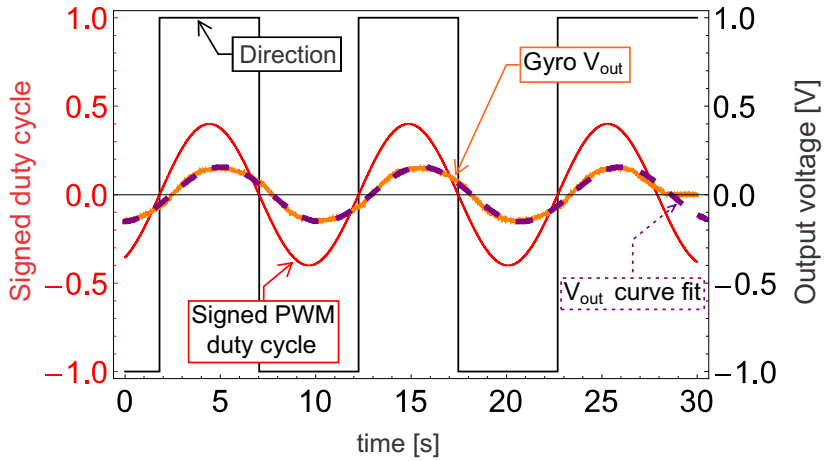

Figure 3.22: Input and output signals for a sinusoid of frequency $f_{in} = 0.885$ Hz.

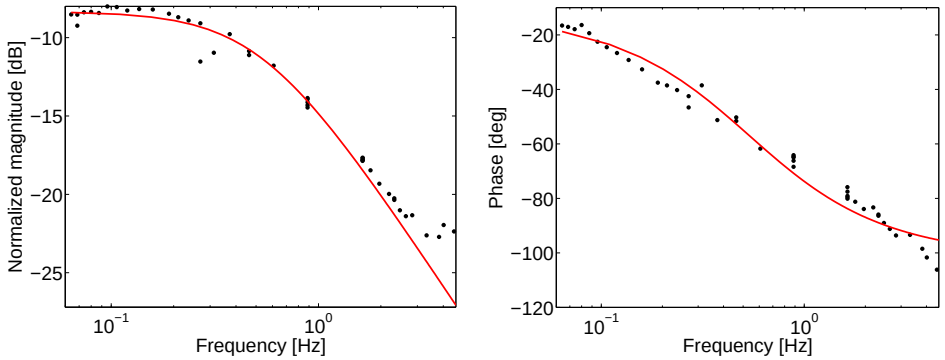

(a) (b)

Figure 3.23: Turntable frequency response and first-order model fitting. **(a)**: Magnitude response. **(b)** Phase response.

Static Optical Tests

Due to space constraints, stripped fibres were used to interrogate these samples. Figures 3.24(a) and 3.24(b) show microscope images of optical fibres aligned to the GCs of the splitting coupler of a gyro resonator before and after permanent attachment. The central fibre, aligned upon the main I/O GC, is PM, whereas the two lateral fibres, aligned upon the tap GCs, are SM. For initial dry alignments, a pitch angle $\theta_p = 40°$ was used for all fibres. Norland NOA 61 adhesive was deposited afterwards, and the angle was set to $\theta_p = 25°$. Fine angle and position adjustments were made to minimize the IL.

After fibre attachment, spectra were obtained with the turntable at rest. Figure 3.24(c) shows the spectra for the CW and CCW resonances of an all-pass, 7.4-mm-long resonator, which exhibits an insertion loss (IL) of approximately 25 dB, a free spectral range (FSR) of 81-pm, extinction ratio values ranging from 8 to 15 dB. The FSR value suggests an average group index of $n_{g_{avg}} \approx 4$, consistent with our theoretical group indices of $n_{g_{SM}} = 4.177$ for SMWGs, and $n_{g_{MM}} = 3.706$ for MMWGs, shown in Table 3.8. Figure 3.24(d) shows the Q as a function of wavelength for the CW and CCW resonances, as well as their respective averages. The average quality factor is

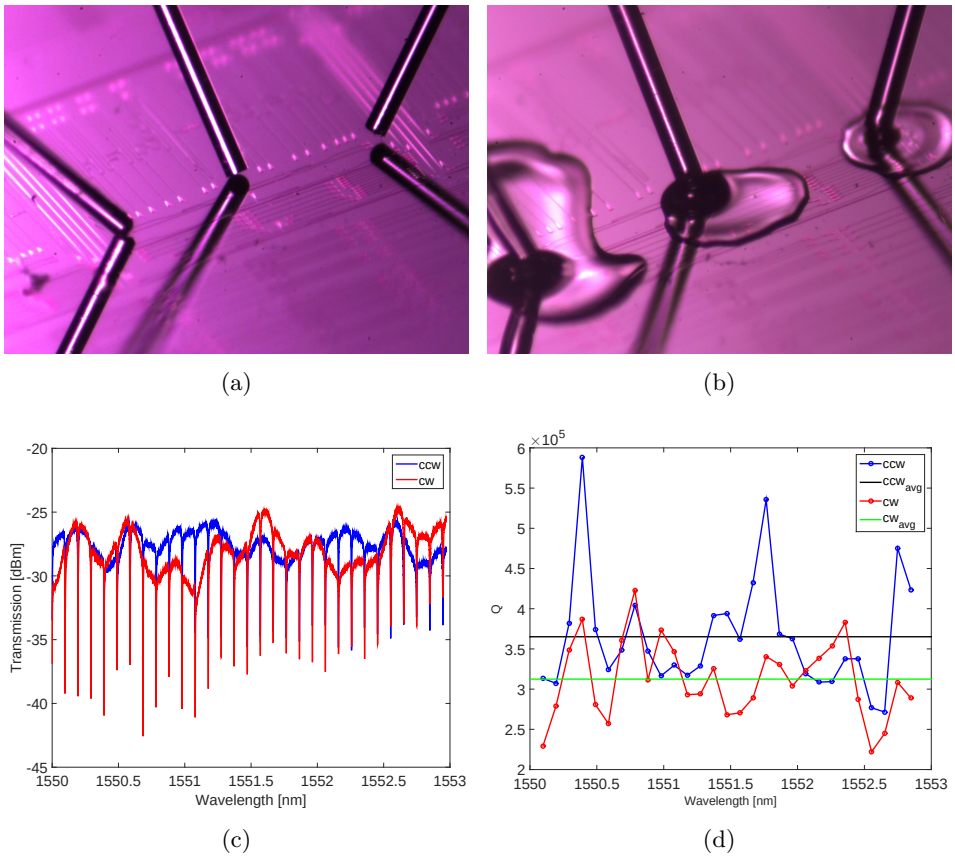

Figure 3.24: Fibre alignments upon splitting coupler in **(a)** dry conditions, and **(b)** UV curable adhesive. **(c)** Spectra and **(d)** Q factor for the CW and CCW resonances of a 7.4-mm-long resonator.

$Q_{avg} \approx 3.4 \times 10^5$, more than 4 times greater than the Q of resonators from previous iterations.

Dynamic Tests

Based on spectra such as that shown in Fig. 3.24(c), the TLS wavelength was tuned to single wavelength values, to perform time-domain measurements. Wavelength values with large spectral slope near resonances were tested in search for greater sensitivity to manual turntable rotations. The turntable

was then rotated using sinusoidal bow-tie patterns. Figure 3.25(b) shows the signed PWM duty cycle, as well as the corresponding output voltages of the reference gyroscope and the photodetector connected to the PM circulator. The experimental optical gyroscope resolution, limited by the setup performance, was $\delta\Omega_{opt} \approx 27$ dps. However, the amplitude variations showed by the optical output signal were considerably larger than those expected solely to the Sagnac effect. We associated this variations with the vibrations of the characterization setup. The optical output signal also showed drift, likely due to thermal variations across the chip, despite having temperature control in the sample pedestal.

3.3.4 Fibre Attachment

In order to improve the robustness of the 3D-printed fibre holders to be used with future samples, I designed a second holder generation with 20-mm long, 1.2-mm wide channels on their back end, for a firm and safe grasp of the fibre jacket, as shown in Fig. 3.26. The fibre trenches were deeper (0.3 mm radius) and more widely spaced (2.5 mm separation) in comparison to the first designs. Foreseeing the need for various incidence angles, I created holders and polishing jigs with various front end angles, namely, 6, 10, 23, 25, and 39 degrees. The fibres were attached to the holders and polished using the same setup and procedure as was described in Subsection 3.2.4.

As the detachment would be heat assisted from now on, two adhesives with different glass transition temperatures (T_g) were used. An adhesive with a relatively high T_g (Loctite 3492$^{\text{TM}}$, $T_g = 64°\text{C}$ [61]) was dispensed over the trenches to attach the fibres to the holders, whereas an adhesive with a lower T_g (Dymax 429$^{\text{TM}}$, $T_g = 59°\text{C}$ [40]), was used for attachment between fibres and samples.

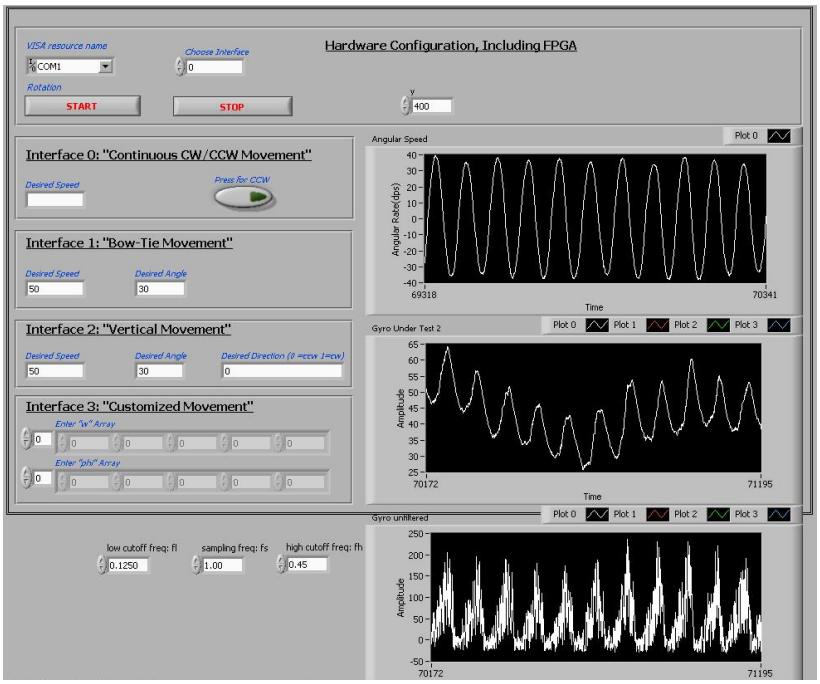

(a)

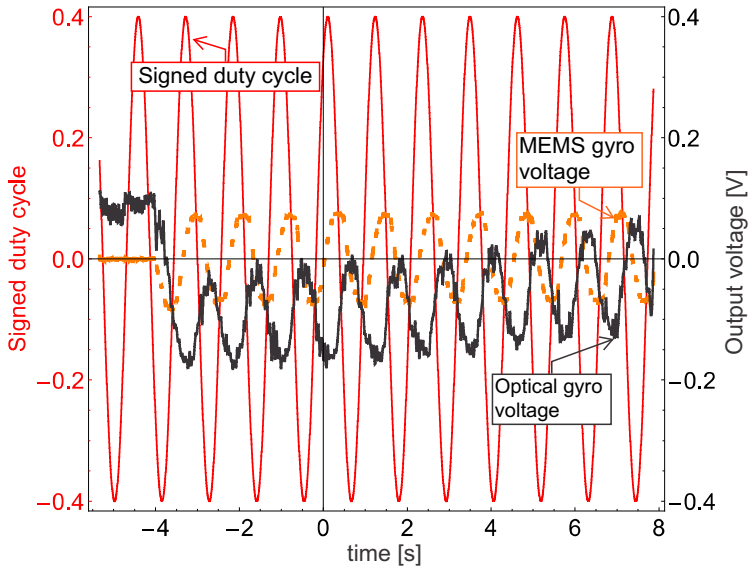

(b)

Figure 3.25: **(a)** Reading on VI front panel, and **(b)** input and output signals during a sinusoidal rotation test with frequency $f_{in} = 0.885$ Hz.

SMWG test structures from previous fabrication runs were chosen to perform the attachment tests. Samples were mounted on top of the temperature controlled sample pedestal shown in Fig. 3.27(a) using double-sided adhesive tape. This was eventually replaced by a metallic vacuum chuck, as shown in Fig. 3.27(b), since the tape elasticity allowed for undesirable displacements during fibre positioning and adhesive curing.

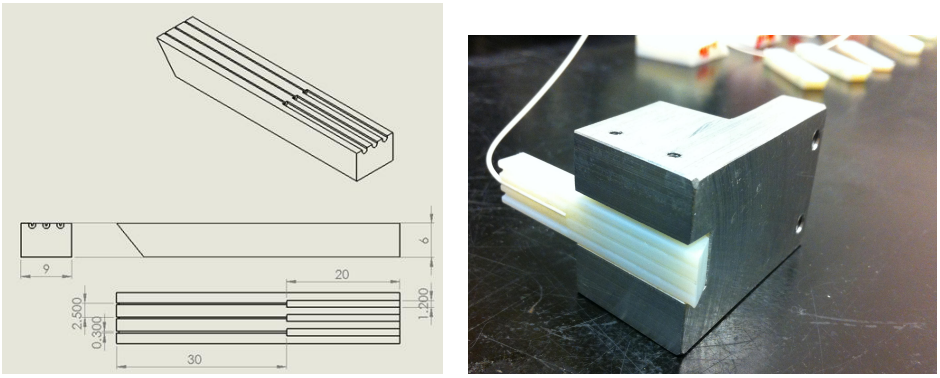

(a) (b)

Figure 3.26: **(a)** Second fibre holder design schematic. **(b)** Holder with attached fibre on polishing jig.

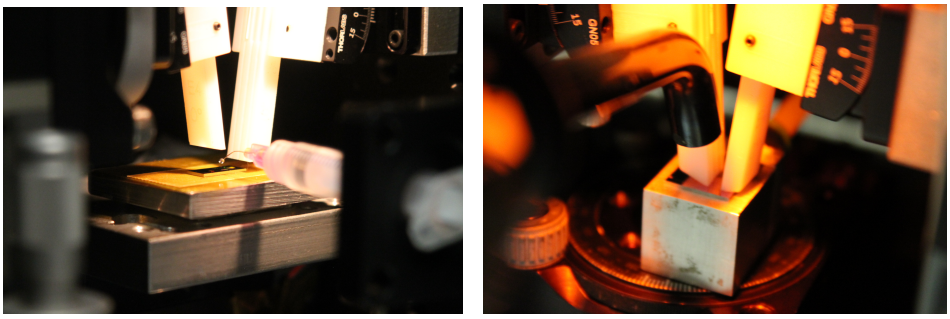

(a) Adhesive tape chuck (b) Vacuum chuck

Figure 3.27: Sample pedestal versions.

Figure 3.28 illustrates the evolution of the fibre attachment process for an air-clad device with a 10° incidence angle in air. SM fibres were attached to both the input and the output fibre holders, and these were polished at

6.5° angles. The pitch angles and positions were adjusted as to maximize the transmitted power without adhesive, with uncured adhesive, and during the curing cycles. The optimum pitch angle for each case is depicted in the figure legends. As shown in Fig. 3.28(a), the IL improved approximately 12 dB after depositing adhesive on top of the input GC, thanks to a smaller index mismatch with the fibre. The spectral peak shifted due to the angle and position adjustments.

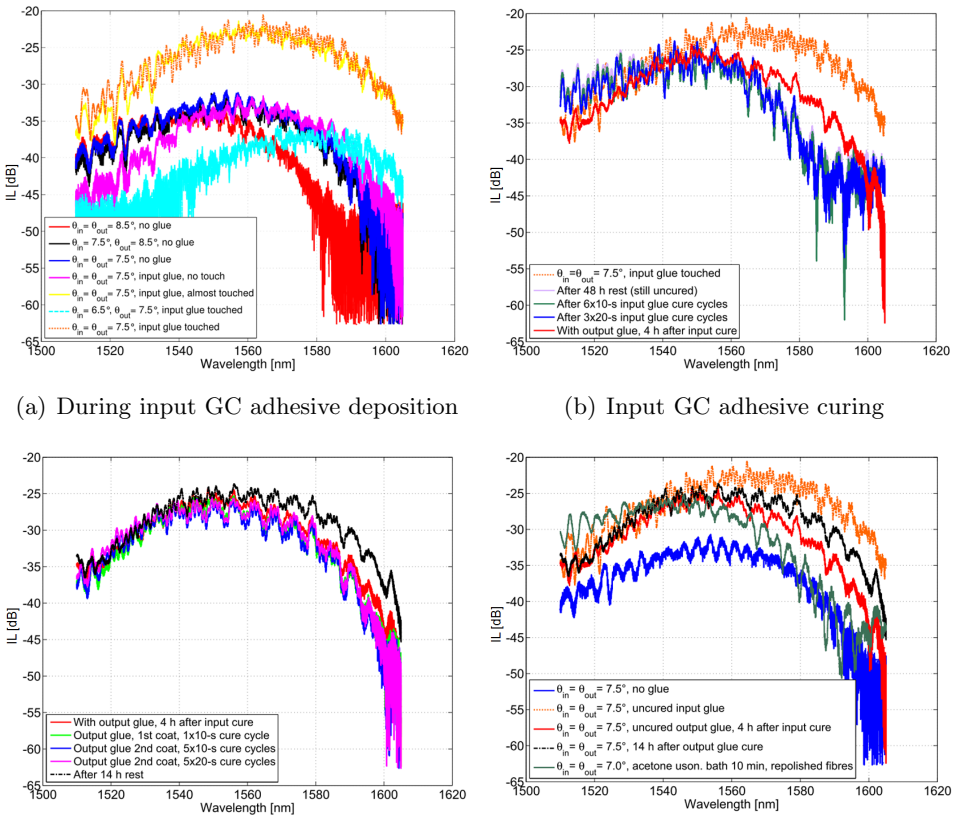

(a) During input GC adhesive deposition

(b) Input GC adhesive curing

(c) Output GC adhesive curing

(d) Spectrum after each subcycle

Figure 3.28: Selected spectra during adhesive deposition and curing on an air-clad SMWG structure. Chip IMEC2009-R6C5.

The IL increased during the curing cycles due to adhesive shrinkage. Depending on the curing time, the position of the fibres could shift and

show hysteresis, requiring position adjustments to minimize the IL. After a rest period of 5 minutes, the power increased between 1 and 3 dB for short- (10 s) and medium- (20 s) curing cycles without requiring re-positioning. Therefore, the attachment procedure was divided into several short- and medium-length-curing cycles (10 s and 20 s, respectively), followed by long-curing cycles (60 s), carried out sequentially for the input and output fibres. Spectra obtained before, during, and after the adhesive curing cycles are shown in Figures 3.28(a), 3.28(b), and 3.28(c). Figure 3.28(d) shows spectra at the end of each cycle, as well as the spectrum after fibre detachment and a 15-minute ultrasonic bath in warm acetone.

The greater IL increase and misalignment observed for longer curing cycles motivated a study of the insertion loss and peak wavelength values over time, for which glass-clad SMWG test structures were used. Additional spectra were recorded during the sequential curing cycles. Figure 3.29(a) compares the spectra of alignments performed without adhesive to those having uncured adhesive at the input GC. An improvement of ~ 2 dB was observed after angular and positional adjustments. As expected due to the relatively small index contrast between the adhesive and the cladding, the optimal incidence angle was only slightly changed. Figure 3.29(b) compares spectra before and after curing the adhesive at the input GC. Five 20-s curing cycles were performed, each with a 5-minute rest. One 60-s curing cycle followed, and after several hours of rest, a small realignment was required. A final 60-s curing cycle followed, requiring no further realignment.

Figures 3.29(c) and 3.29(d) show, respectively, the evolution over time of spectral peak power and wavelength during the first 20-s curing cycle. Immediately after this curing cycle there was an excess loss of ~ 1 dB. After a 5 minute rest period, the excess loss decreased to ~ 0.5 dB with no alignment required. As per the procedure described earlier, four 20-s and two 60-s curing cycles followed. Figures 3.29(e) and 3.29(f) show the spectral peak power and wavelength evolution over time for the last 60-s curing cycle. One can see that by this last cycle, the peak power and wavelength value excursions are smaller, and follow smoother trends.

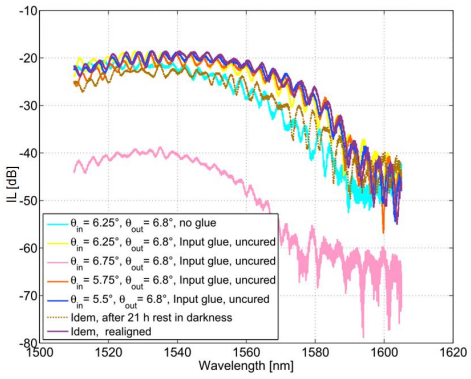

(a) Spectra before input GC curing

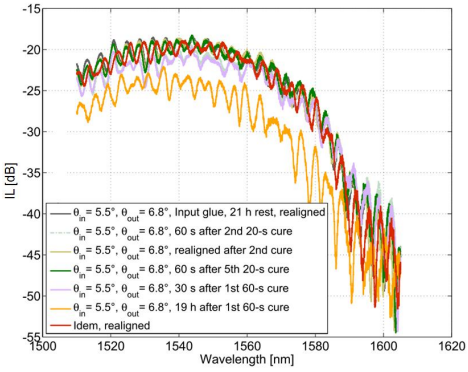

(b) Spectra after input GC curing

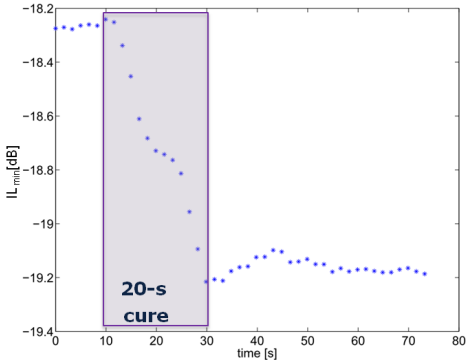

(c) Peak IL, first 20-s curing

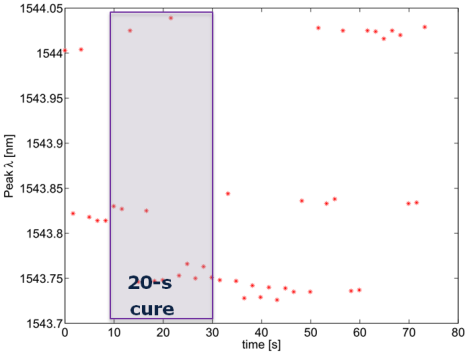

(d) Peak wavelength, first 20-s curing

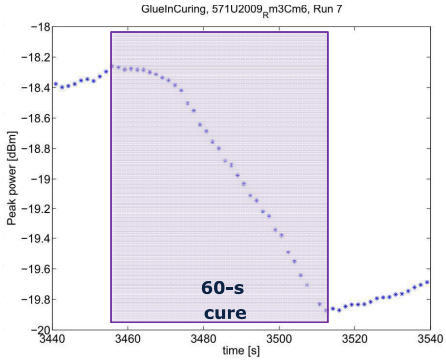

(e) Peak IL, second 60-s curing

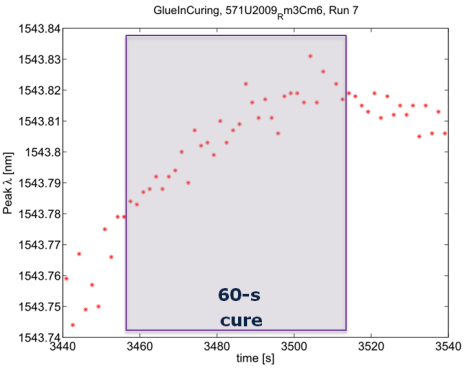

(f) Peak wavelength, second 60-s curing

Figure 3.29: Selected spectra and variations during curing on a glass-clad SMWG structure. Sample: Imec Glass cladding, R−3C−6.

3.3.5 Iteration Challenges and Conclusions

In this iteration, we designed resonators with a combination of SMWGs and MMWGs allowed for a reduction of the overall roundtrip loss. Our fabricated resonators showed Q factors ranging from 2×10^5 to 6×10^5, with an average $Q_{avg} \approx 3.4\times10^5$. Using equation 3.3 with $\lambda_0 = 1.55$ µm, and $n_g \approx 4$, the average field and power attenuation values are $\alpha_{avg} \approx 0.024$ mm^{-1} and $\alpha_p \approx 0.048$ mm^{-1}, respectively. Comparing to the resonators of the previous iteration, for a 6-mm length, the optical signal makes approximately 3.5 roundtrips before its intensity decreases by a factor of e. For the resonator described in Fig. 3.24, with $L = 7.4$ mm, the finesse is $F \approx 18$. This improvement by a factor of ~ 2 with respect to our previous iteration encouraged us to find ways to further reduce the roundtrip loss. This was achieved using rib MMWGs, and adiabatic strip SMWG bends, as will be shown in the next subsection.

Regarding layout creation, the use of scripts considerably accelerated the process in comparison to the manual drawing techniques used in previous iterations. The compatibility of CleWin$^{\text{TM}}$ with MATLAB$^{\text{TM}}$ allowed for flexibility and a relatively flat learning curve. However, issues such as broken waveguides or feature spacing violations had to be identified by visual inspection, as there is no embedded design rule checking (DRC) in CleWin$^{\text{TM}}$. To avoid these issues, the layout scripting was migrated to Mentor Graphics Pyxis$^{\text{TM}}$, which despite its complexity and steep learning curve, proved to be a much more robust layout tool with capabilities such as DRC and parametric cells, that allow for creation and modification of parametrized devices.

A turntable for testing SOI gyroscopes was built. Custom operation modes were implemented for characterizing the apparatus and the SOI devices. The turntable exhibited a bandwidth of 0.54 Hz, angular speeds ranging from 27 to 74.3 dps, angular acceleration values from 9.4 to 171.2 dps^2, and noise levels of 2 and 0.73 dps at its minimum and maximum speed, respectively. Static and dynamic tests were carried out on SOI gyroscope resonators fabricated using an air-clad e-beam process, showing an average

resonator Q of 3.4×10^5, and a resolution of 27 dps, as published in [55].

The variations in the measured signals of our gyroscopes were much larger than those expected due to the Sagnac effect, and were attributed to vibration and mechanical stress at the fibre-DUT bonds. Although some groups report performing rotational tests (e.g., [70]), they do not specify interrogation interface details, nor do they specify any measures to deal with vibrational noise. The construction of our turntable was a valuable experience. It helped to identify challenges and key parameters that needed to be addressed in subsequent iterations. The results of our tests suggested the need to reduce mechanical vibrations and to increase the angular speed range. An enclosure was also required in order to reduce the deleterious impact of ambient temperature variations. Thus, we acquired a turntable system within a temperature-controlled chamber and the necessary equipment to create a characterization setup within it.

During attachment experiments with 3D printed holders I observed that the optimum incidence angle changed after each facet re-polishing ($\theta_{\Delta p} \approx \pm\ 1^\circ$), suggesting variations due to polishing and fastening inaccuracies. I also noticed that occasionally the edge of the holder end face made contact with the sample before the fibre reached the surface, thus affecting the optimum holder angle and position. These issues occurred in spite of performing shallow-angle polishing on acute angle holders (e.g., 6.5° polishing on a 25° facet) to reduce the holder footprint.

Due to 3D printing dimension tolerances (e.g., $\sim$ 10% variations in 2.5-mm feature spacings) the distance variations between fibres precluded mounting more than one fibre per holder to form fibre arrays. Since the input and output GCs in these samples were separated by several millimetres, this required separate adhesive dispensing, manual alignment, and UV curing of the input and output fibres. Even though the fibre holders eliminated the fibre bending, observed when attaching unsupported bare fibres, the alignment of separate, bulky holders occasionally produced sample shifting and unintended fibre-sample separation. The manual fibre positioning still limited the position repeatability, which negatively impacted the IL level and overall device characterization. In order to solve these issues during the

following iteration, we used compact fibre arrays [126] instead of individual fibres, and replaced the manual positioning stages with computer-controlled micro-positioners.

3.4 Fourth Design Cycle

The Q factor increase achieved in our previous iteration as a result of using straight MMWGs motivated us to find ways to further reduce the overall rountrip loss of our resonators. As shown in Yap et al., rib waveguides have lower propagation losses than strip waveguides due to factors that depend on the etch depth [140]. Bogaerts et al. reported losses as low as 0.27 dB/cm using a combination straight rib MMWGs and strip SMWG adiabatic bends [15]. We decided to adopt a similar approach and submitted our designs for fabrication to the Institute of Microelectronics (IME), Singapore, where devices were fabricated using a CMOS-compatible SOI process with two etch depths: a 220-nm full etch for strip waveguides, and a 130-nm partial (shallow) etch for rib waveguides and GCs. This eventually allowed us to achieve Q factor values as high as $\sim 4.5 \times 10^6$, with an average value of $\sim 1.7 \times 10^6$, as shown in Subsection 3.4.3, and published in [56].

Compact arrays of four PM fibres with 127-µm-pitch and custom polish angles were acquired from PLC Connections, LLC (now PLCC2, LLC [3]), for simultaneous alignment of multiple input and output fibres. Thus, from this iteration onwards, all of our device GCs had the same orientation and a 127-µm-pitch. Unless explicitly stated otherwise, from this iteration onwards all samples had glass cladding, which contributed to waveguide protection, IL reduction, and smaller angular adjustments during fibre attachment.

A computer-controlled micro-positioning system was acquired for faster, more accurate positioning across the chips. In this new setup, the sample pedestal is translated in-plane, and the fibre array is translated only in the vertical direction. A graphical user interface (GUI) for instrument control and automatic alignment was developed by members of UBC and UW research groups using MATLAB$^{\text{TM}}$.

The setup is capable of automatically positioning the chip according

to pre-defined coordinates contained in the layout files, of performing automated fine alignments, and of measuring and recording spectra for various devices sequentially. In order to extend the angular speed range in comparison to that of our first rotary table, and also to reduce the exposure of our chips to ambient illumination and temperature variations, an Ideal Aerosmith 1291BL^{TM} single-axis automatic turntable system with a temperature-controlled chamber was acquired.

3.4.1 Layout Design

The GCs for each device were oriented in the same direction and spaced with a 127 µm pitch, so as to ensure compatibility with our fibre arrays. The resonator designs combine SMWGs and MMWGs, as done in the previous iteration. However, as previously mentioned, strip waveguides would be replaced with rib waveguides to the extent possible and used only for small-radius bends wherever required for space efficiency. To minimize the mode mismatch losses, the bends consisted of adiabatic Bézier bends with 5-µm equivalent radii [21], and 5-µm long strip SMWG stubs at both ends. 100-µm long linear tapers were used for conversion from strip SMWGs to rib MMWGs, and 50-µm long linear tapers were used to convert from strip SMWGs to rib SMWGs.

Gyroscope Devices and Propagation Loss Test Structures

On-chip splitting/merging was implemented in these designs as well. However, as shown in Figure 3.30, the splitting/combining coupler was modified for space efficiency, and the signal taps previously used were eliminated to decrease the excess loss. In the figure, the main I/O GC shows an arrow depicting the optical signal entering the device. Straight strip SMWGs (1) and strip SMWG Bézier bends (2) are used for short, space-efficient waveguide routing. The central Y-branch of our previous design was replaced by an adiabatic 50/50 splitter/merger, (labelled as 3 in Fig. 3.30) which uses a combination of strip waveguides (orange) and rib waveguides (drawn as blue strips with pink slabs) to evenly split the signal(s) injected to the input

strip SMWG(s) [145]. Straight rib waveguides and 20µm-radius rib SMWG bends (4 and 5 respectively, drawn as brown strips with pink slabs) were used to create a waveguide loop. A waveguide directional coupler (6) was incorporated in the loop and is regarded as a point coupler for modelling purposes. The directional coupler injects light into, and collects light from, the resonator (grayed out) in both propagation directions. Figure 3.31 shows the schematic of a gyroscope resonator with its splitting/merging coupler. Only GC_2 is used as an input and both GC_1 and GC_2 are used to detect the optical signals from the two outputs of the device. The output of GC_2 is interrogated via a PM circulator.

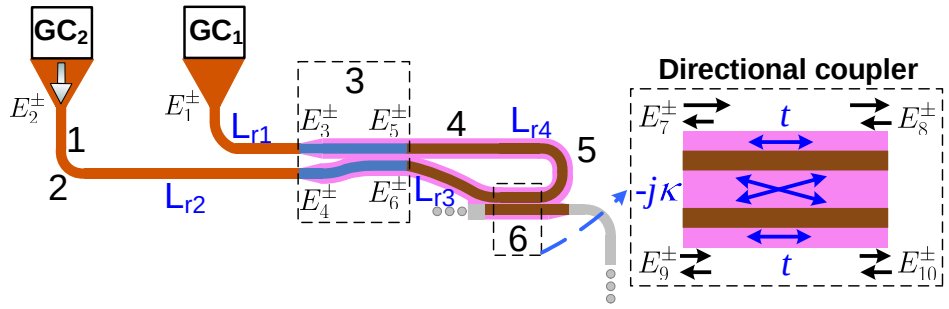

(a)

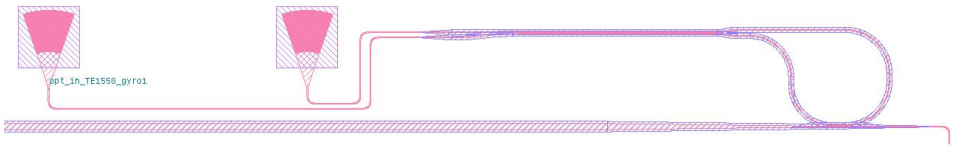

(b)

Figure 3.30: Splitting/merging coupler based on adiabatic splitter. **(a)** Schematic. 1- Straight strip SMWGs. 2- Strip SMWG bends. 3- Adiabatic 50/50 splitter/merger, input and output ports labelled in blue [145]. 4- Straight rib SMWGs. 5- Rib SMWG bends. **(b)** Layout schematic.

Figure 3.31 also shows, as an inset, the schematic of a test structure for MMWG propagation loss characterization. Each test structure consists of a fixed number of straight rib MMWG segments, Bézier bends, and waveguide tapers. Specifically, each test structure has forty 100-µm waveguide tapers,

forty 90° Bézier bends with 5µm equivalent radii [21], and twenty straight rib MMWG segments. Four different test structures were included in the layout design, with total MMWG length values of 2, 56, 86, and 116 mm, respectively. In principle, these length values allow one to observe an IL difference between the shortest and the longest test structure of ~ 0.35 dB in the best expected scenario ($\alpha_{\mathrm{dB}} \sim 0.03$ dB/cm [78]), and of ~ 11 dB in the worst expected scenario ($\alpha_{\mathrm{dB}} \sim 1$ dB/cm [78]). The experimental results obtained with these structures are described in Subsection 3.4.3.

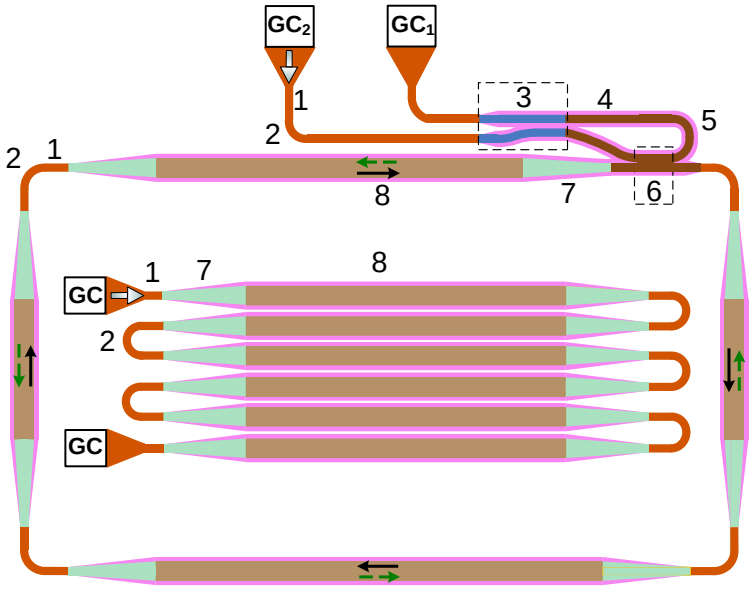

Figure 3.31: Large-area resonator, formed by straight SMWGs (1), strip SMWG adiabatic bends (2) [21], rib SMWG directional coupler (3), MMWGs (4), linear tapers (5) for SMWG to MMWG conversion, and adiabatic 50/50 splitter (6) [145]. GC: grating couplers [137]. Inset: Test structure for MMWG propagation loss characterization.

The matrix equations governing the electric fields on the way in (left to right) and on the way out of the adiabatic splitting/merging coupler shown

in Fig. 3.30 are, respectively:

$$\begin{bmatrix} E_5^+ \\ E_6^+ \end{bmatrix} = M \begin{bmatrix} E_3^+ \\ E_4^+ \end{bmatrix} \tag{3.11}$$

$$\begin{bmatrix} E_3^- \\ E_4^- \end{bmatrix} = M^{-1} \begin{bmatrix} E_5^- \\ E_6^- \end{bmatrix} \tag{3.12}$$

where:

$$M = \frac{1}{\sqrt{2}} \begin{bmatrix} 1 & 1 \\ -1 & 1 \end{bmatrix}. \tag{3.13}$$

Although during experiments only one input was excited at a time, the fields exiting the device will be described in terms of both possible input fields. For a CW rotation of the device depicted in Fig. 3.31, using Eqs. (3.35) through (3.13), we have:

$${E_3}^- = \frac{e^{j\Phi_{\text{ascl}}}}{2\sqrt{C_{\text{IL}}}} \left[-{E_3}^+ \left[T\left(\Phi_S\right) + T\left(-\Phi_S\right) \right] + {E_4}^+ \left[T\left(\Phi_S\right) - T\left(-\Phi_S\right) \right] \right] \tag{3.14}$$

$$E_4^- = \frac{e^{j\Phi_{\text{ascl}}}}{2\sqrt{C_{\text{IL}}}} \left[-E_3^+ \left[T\left(\Phi_S\right) - T\left(-\Phi_S\right) \right] + E_4^+ \left[T\left(\Phi_S\right) + T\left(-\Phi_S\right) \right] \right] \tag{3.15}$$

where $\Phi_{\text{ascl}} = j\alpha_{\text{scr}} L_{\text{ascl}} - \phi_{\text{ascl}}$, L_{ascl} is the path length of the rib SMWG loop (drawn as brown strips on pink slabs in Fig. 3.30(a)), α_{scr} is the rib SMWG propagation loss, ϕ_{ascl} is the phase shift produced by the rib SMWG loop, and $T\left(\Phi_S\right)$ is the phase-shifted ring transfer function defined in Eq. (3.6). The sum and difference of $T\left(\Phi_S\right)$ and $T\left(-\Phi_S\right)$ can be expanded as follows:

$$T\left(\Phi_S\right) + T\left(-\Phi_S\right) = 2 \cdot \frac{t\left(e^{j\Phi_{\text{ring}}} + e^{-j\Phi_{\text{ring}}}\right) - \left(t^2+1\right)\cos(\Phi_{\text{S}})}{e^{-j\Phi_{\text{ring}}} - 2t\cos(\Phi_{\text{S}}) + t^2 e^{j\Phi_{\text{ring}}}} \tag{3.16}$$

$$T\left(\Phi_S\right) - T\left(-\Phi_S\right) = 2 \cdot \frac{j\left(t^2-1\right)\sin\left(\Phi_{\text{S}}\right)}{e^{-j\Phi_{\text{ring}}} - 2t\cos(\Phi_{\text{S}}) + t^2 e^{j\Phi_{\text{ring}}}}. \tag{3.17}$$

Based on Eqs. (3.14) through (3.17), Fig. 3.32 shows the theoretical power spectra of the signals exiting the device, $P_1 = \left|E_1^-\right|^2$ and $P_2 = \left|E_2^-\right|^2$, when $E_1^+ = 0$ and $E_2^+ = 1$. Since theoretically $\left|E_1^-\right|^2 = 0$ at rest ($\Phi_S = 0$), an arbitrary noise floor of -70 dB, consistent with the noise floor of our current measurement system, has been added for plotting purposes.

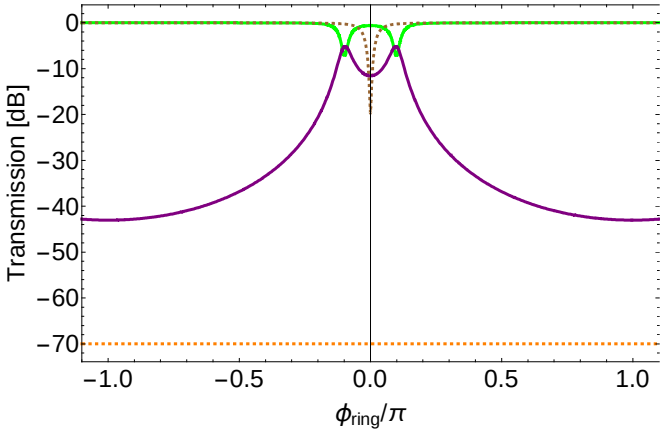

Figure 3.32: Comparison of theoretical output power levels P_1 and P_2 as functions of the ring normalized detuning, at rest and under CW rotation, for an all-pass resonator with length $L = 37$ mm, coupling $\kappa_a = 0.29$, average propagation loss $\alpha_{\text{dB}} = 0.085$ dB/cm, negligible IL and splitting loop losses ($IL_{\text{dB}} = 0$ dB, $\alpha_{\text{scr}} = 0$ m^{-1}), and $\Phi_S = 0.1\pi$ rad. Dashed brown curve: P_1 at rest. Solid green curve: P_1 under rotation. Orange dashed curve: P_2 at rest. Purple solid curve: P_2 under rotation.

Resonators with Thermally-Tuneable Coupling

Since fabrication imperfections can create discrepancies between the as-designed and the as-fabricated power coupling coefficients, we created a modified version of the splitting/merging coupler design (Fig. 3.30) to allow for thermally-tuneable coupling. The thermooptic effect is the phenomenon by which the refractive index of a medium changes as a result of a change in its temperature [75, 100]. By locally heating a waveguide, its optical length can be modified. This can be exploited in a Mach-Zehnder interferometer to produce a tuneable coupler as described below.

The splitting/merging coupler schematic is shown in Fig. 3.33. It consists of two sections. The first one is an adiabatic coupler, used for input signal splitting. The second section is the tuneable coupler. It consists of a thermally-tuneable Mach-Zehnder interferometer (T-MZI), formed by two adiabatic couplers and two arms consisting of straight rib SMWGs. A metal strip is deposited on top of one of the arms to act as a resistive heater, which modifies the optical phase difference between the T-MZI arms due to the thermooptic effect. Since this subcomponent is based on an MZI structure, rather than a resonator, and it occupies negligible area in comparison to that of the ring resonator (cf. ~ 0.034 mm^2 vs. ~ 90 mm^2), the effects of rotation on its behaviour are negligible.

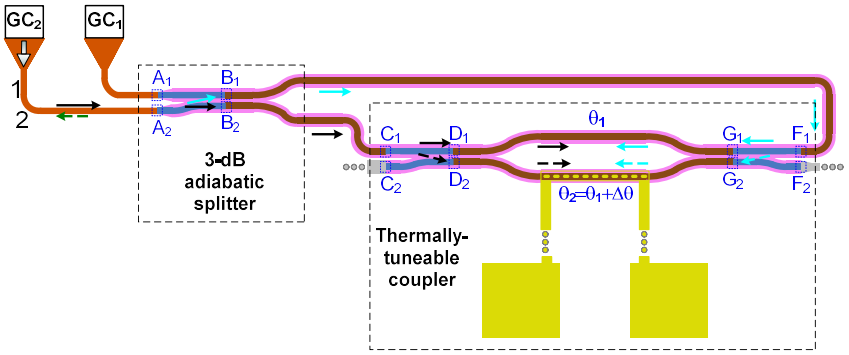

Figure 3.33: Schematic of a thermally-tuneable splitting/merging coupler for an IME resonator.

As derived in Appendix D, the matrix equation describing the relationship between the fields at the ports of a T-MZI with perfectly balanced adiabatic couplers is:

$$\begin{bmatrix} {F_1}^+ \\ {F_2}^+ \end{bmatrix} = e^{-j\frac{(\theta_1+\theta_2)}{2}} \begin{bmatrix} t(\Delta\theta) & j\kappa(\Delta\theta) \\ j\kappa(\Delta\theta) & t(\Delta\theta) \end{bmatrix} \cdot \begin{bmatrix} {C_1}^+ \\ {C_2}^+ \end{bmatrix}, \tag{3.18}$$

where θ_1 and θ_2 are, respectively, the optical phases of the top and bottom arms of the T-MZI, $\Delta\theta = \theta_2 - \theta_1$ is the arm phase imbalance, produced by the optical path difference between both arms, and the tuneable through-

and cross-coupling coefficients are defined, respectively, as:

$$t(\Delta\theta) = \cos(\Delta\theta/2) \tag{3.19}$$

$$\kappa(\Delta\theta) = \sin(\Delta\theta/2)\,. \tag{3.20}$$

Figure 3.34 shows the schematic of a T-MZI test structure, created to determine the phase shifter efficiency, η_θ, measured in units of power for a π phase shift. In this particular design only one input port is used, hence the tapered waveguide terminator at the unused input port. Our as-fabricated T-MZI couplers have an efficiency $\eta_\theta = 24$ mW/π, according to our experimental data (see Subsection 3.4.3).

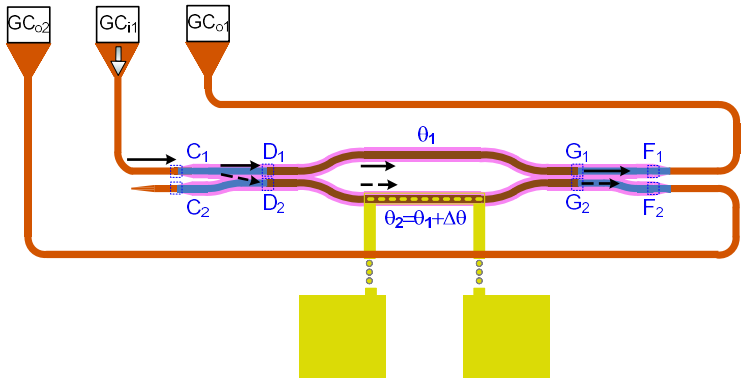

Figure 3.34: Thermally-tuneable coupler test structure. $L_{\mathrm{MZI}} = 200$ µm.

As fully derived in Appendix D, when the T-MZI coupler is connected to the resonator, as shown in Fig. 3.35, it is possible to express ${F_1}^+$ in terms of ${C_1}^+$ as:

$${F_1}^+ = T_{\mathrm{tc}}(\Phi_S){C_1}^+, \tag{3.21}$$

where

$$T_{\mathrm{tc}}(\Phi_S) = e^{-j\Phi(\theta)} \cdot \frac{t(\Delta\theta) - e^{-j(\Phi_{\mathrm{ring}}+\Phi(\theta)+\Phi_S)}}{1 - t(\Delta\theta)e^{-j(\Phi_{\mathrm{ring}}+\Phi(\theta)+\Phi_S)}} \tag{3.22}$$

and $\Phi(\theta) = (\theta_1 + \theta_2)/2$. By comparing Eqs. (3.22) and (3.6), one can see that the transfer functions for the resonators with tuneable and with

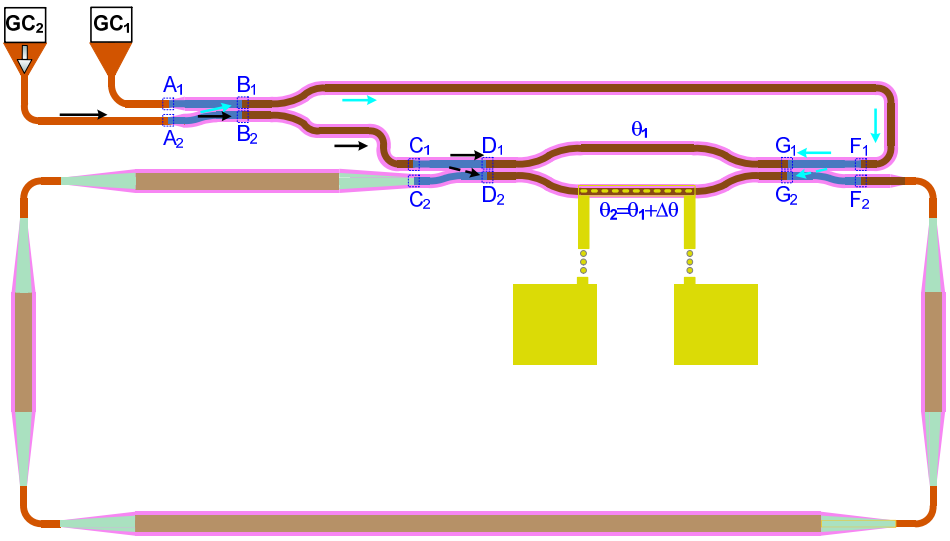

Figure 3.35: Resonator with thermally-tuneable coupler.

fixed couplers have similar structures. However, for the tuneable case, the through-coupling, cross-coupling, resonance wavelength, and extinction ratio vary as functions of the phase imbalance.

Figure 3.36 compares theoretical spectra for a 37 mm-long ring at various phase detuning conditions as a function of the power delivered to the thermal tuner. The optical signal is fed and interrogated through the same GC_1. A phase shifter efficiency of $\eta_\theta = 24$ mW/π was considered in the model, based on the experimental measurements shown in Section 3.4.3.

Figure 3.37 compares theoretical spectra at both ports for a gyroscope resonator with a tuneable splitting/merging coupler at rest and under rotation. The simulation parameters are: length $L = 37$ mm, phase imbalance $\Delta\theta = 0.1\pi$ produced by a thermal phase shifter power $P_\theta = 2.4$ mW, propagation loss $\alpha = 0.3$ m^{-1}, noise floor $N_\mathrm{f} = -70$ dB, and a Sagnac phase shift $\Phi_\mathrm{S} = 0.1\pi$ in the rotational simulation. As expected from Eq. (3.22), this plot is similar to Fig. 3.32, but with values of resonance shift and ER dependent on the phase imbalance.

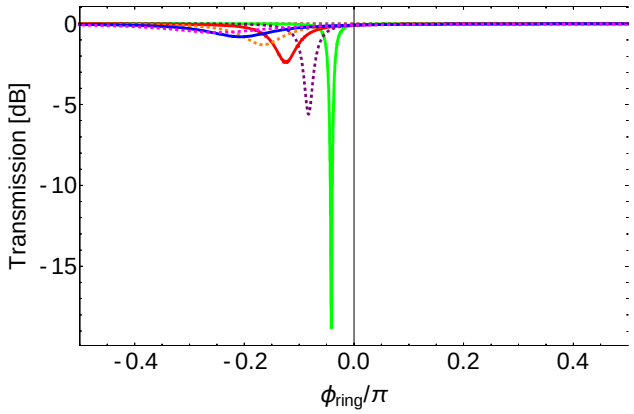

Figure 3.36: Spectral simulation for a resonator with a thermally-tuneable coupler at various MZI phase detuning conditions, fed and interrogated through GC_1. Parameters: $\eta_\theta = 24$ mW/π. $L = 37$ mm. $\Delta\theta = 0.1\pi$, $\alpha = 0.3$ m^{-1}. Thermal phase shifter power: $P_\theta = 0$ mW (brown dashed). $P_\theta = 2$ mW (green solid). $P_\theta = 4$ mW (purple dashed). $P_\theta = 6$ mW (red solid). $P_\theta = 8$ mW (orange dashed). $P_\theta = 10$ mW (blue solid). $P_\theta = 12$ mW (magenta dashed).

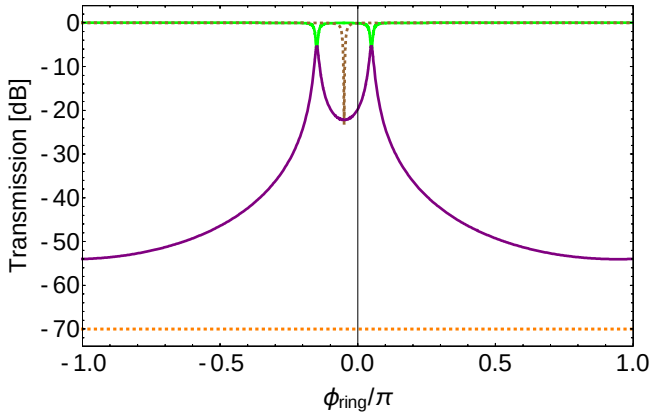

Figure 3.37: Simulations of the spectral response for a resonator with a thermally-tuneable coupler, at rest (dashed curves), and under rotation (solid curves, $\Phi_S = 0.1\pi$). The input signal is injected into GC_1, and the device is interrogated at both ports. Parameters: $L = 37$ mm, $\Delta\theta = 0.1\pi$ ($P_\theta = 2.4$ mW), $\alpha = 0.3$ m^{-1}.

Auto-Alignment Landmark Devices

For coordinate mapping purposes, from this iteration onwards, all layout design files were created with a layer dedicated for device name tags, located at the apex of the input GCs. The input GC tags must adhere to a specific syntax convention, in order to be recognized by a special script developed in Klayout^{TM} by group colleagues to create text files with device coordinates and names. These text files were used by the software interface for coordinate mapping and device data identification during automated measurements.

The coordinate mapping procedure requires a manual alignment upon, and recording of the location of, three unambiguous *landmark devices* on each chip. Recording the location of three different landmark devices across the chip (preferably near three chip corners) allows one to correlate the layout coordinates of these devices to the actual X and Y stage positions. The system is then able to carry out interpolations to the rest of the listed devices, perform automated translations to their locations, and record measurements made on them automatically. Figure 3.38 shows a typical landmark device set. Besides its coordinate mapping purpose, these devices proved quite useful as zero-length devices during propagation loss characterization (Subsection 3.4.3). The rationale for having more than one device, each with a different shape, is to unambiguously identify copies of the set across the chip. Specifically, for the set shown in Fig. 3.38, the device spectra observed moving from top to bottom should be a through-port ring response, a 50%-50% power-split loopback response, and a simple loopback response.

Waveguide Parameters

As previously mentioned, strip SMWGs were used for straight stubs and compact waveguide bends, whereas rib SMWGs were used in the WDC region, and rib MMWGs were used for the straight resonator segments (labelled 6 and 8 in Fig. 3.31, respectively). All rib waveguides had slab heights of 90 nm, and all waveguides had strip heights of 220 nm. Table 3.12 shows

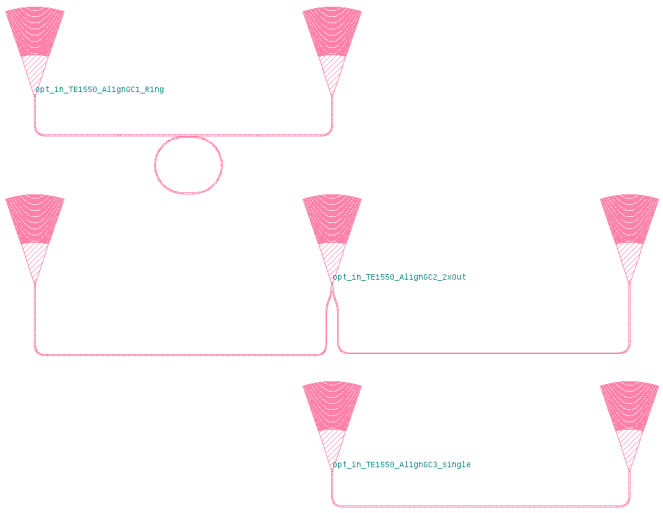

Figure 3.38: Landmark device set, for marking chip corners and correlating layout coordinates to motor coordinates. Input GC name tags (illegible due to layout snapshot settings) are shown only for illustration purposes.

the strip and slab widths of various waveguides used in these designs, as well as a-priori propagation loss ranges, based on experimental results reported in the literature [9, 15, 78].

Table 3.12: Parameter estimations for different glass-clad waveguides

Parameter \ WG	SM strip	SM rib	MM rib
Strip width (nm)	500	500	3000
Slab width (nm)	-	2600	5100
α_{dB} $\left(\frac{\mathrm{dB}}{\mathrm{cm}}\right)$ [9, 15, 78]	2.4 - 3	2.2 - 3.4	0.026 - 1

Table 3.13 shows the effective and group index values for various rib waveguide geometries used in the designs, obtained using MODE Solutions $^{\mathrm{TM}}$ eingenmode solver. The radius of the rib SMWG bends was chosen to be 20 µm to minimize bending and mode mismatch losses [29]. The mode mismatch loss was estimated to be -0.0065 dB, according to our simulations.

Table 3.13: Theoretical values for effective and group indices at $\lambda_0 = 1550$ nm, for rib waveguides of various geometries. In all cases the strip height is $H_{\text{strip}} = 220$ nm and the slab height is $H_{\text{slab}} = 90$ nm.

Strip width [nm]	Radius [µm]	Mode	n_{eff}	n_{g}
500	∞	TE-like	2.5660	3.8797
500	∞	TM-like	2.1144	3.1898
500	20	TE-like	2.5663	3.8790
500	20	TM-like	2.3072	3.3190
1750	∞	TE-like	2.8150	3.7273
1750	∞	TM-like	2.7215	3.8367
3000	∞	TE-like	2.8348	3.7049
3000	∞	TM-like	2.8017	3.7456

Figures 3.39(a) 3.39(b) show curve fits for the effective and group indices versus wavelength for rib waveguides consistent with the geometries described in Table 3.12. However, for simulation purposes, the rib waveguides were considered to have infinite slab widths. Each plot highlights the value of the effective and group indices at $\lambda_0 = 1550$ nm.

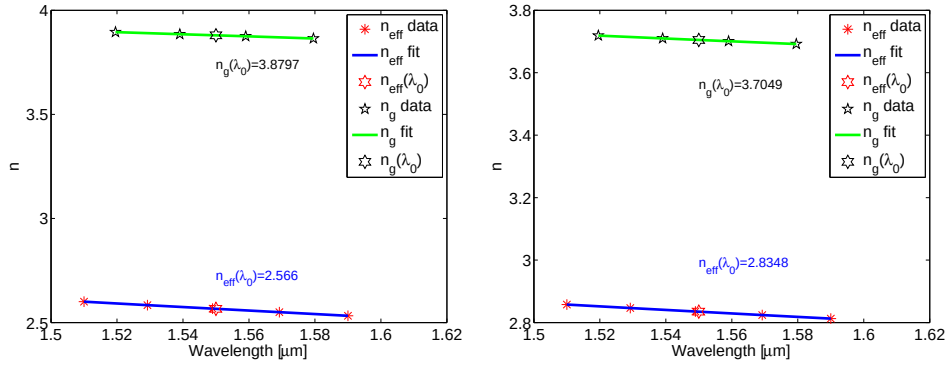

(a) Rib SMWG, W= 500 nm

(b) Rib MMWG, W= 3 µm

Figure 3.39: Curve-fitted effective index (green curves) and group index (blue curves) for glass-clad rib waveguides. **(a)** SMWG. **(b)** MMWG.

Figure 3.40(a) shows the cross-over length versus wavelength for rib

SMWG directional couplers with various gaps, and Fig. 3.40(b) shows the variation of the field-cross coupling, κ, as a function of wavelength, for couplers with various gaps but all of them with $\kappa = 1/\sqrt{2}$ at $\lambda_0 = 1550$ nm. Since smaller gaps produce less coupling variation versus wavelength, a 210-nm gap was used for the layout designs.

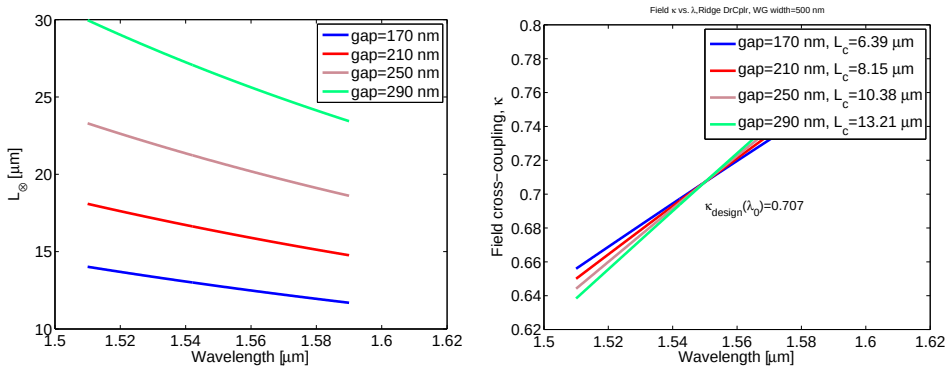

(a) (b)

Figure 3.40: **(a)** Cross-over length vs. wavelength for rib SMWG directional couplers with various gap values. **(b)** Variation of the field cross-coupling versus wavelength for rib SMWG directional couplers of various gaps, all designed for $\kappa = 1/\sqrt{2}$ at $\lambda_0 = 1550$ nm.

3.4.2 Setup Design

As previously mentioned, a new characterization stage was built to improve on the opto-mechanics and data acquisition. Initially, a benchtop version of this new stage was created, and, eventually, I built a compact version inside a turntable chamber. Figure 3.41 shows the block diagram of this setup. Major improvements included the use of a fibre array instead of individual fibres, computer-controlled positioners and a newer PXI controller for automated measurements, fast data recording using special drivers for faster spectral sweeps, a more powerful TEC controller, a larger TEC for a greater temperature range, and an improved vacuum chuck for holding the samples.

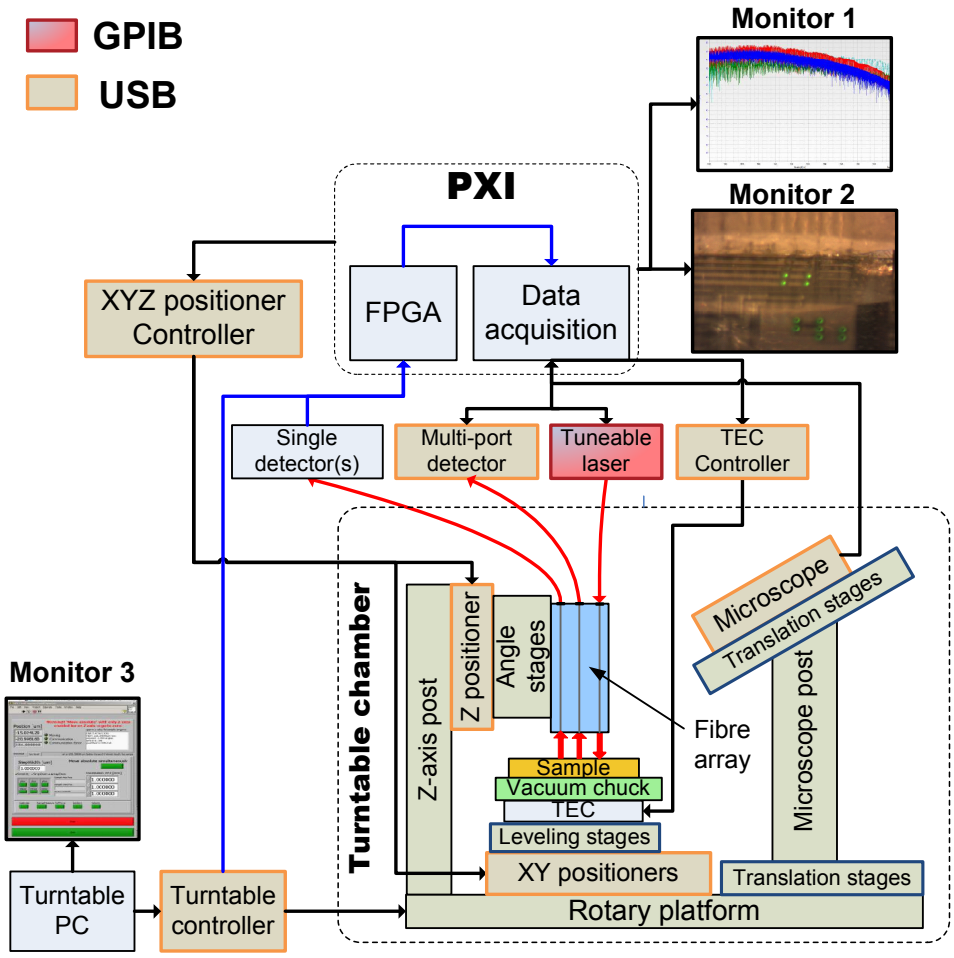

Figure 3.41: Block diagram of second rotary characterization setup.

Optomechanics Improvements

Figure 3.42(a) shows the benchtop configuration of the stage. The manual linear stages formerly used for fibre and sample positioning were substituted with a computer-controlled Micronix SMCorvus^{TM} positioning system. The X- and Y-axis stages were assembled together to control the in-plane position of a temperature-controlled sample vacuum chuck. The Z-axis stage was mounted in an independent post to control the height of the fibre array. A two-axis tilt stage was used to perform horizon-level adjustments after

loading each sample. Figure 3.42(b) shows our custom 127-µm pitch, 22° polish-angle, lidless fibre array on top of the sample vacuum chuck. This particular array has four equally-oriented polarization maintaining (PM) fibres, for proper excitation of the DUT's polarization-sensitive GCs. The same figure shows the aluminium sample pedestal, with a push-to-connect fitting for vacuum connection, and wires protruding from a perforation where a thermistor has been permanently attached. The perforations allow the thermistor to be approximately 2 mm away from the sample without affecting the vacuum.

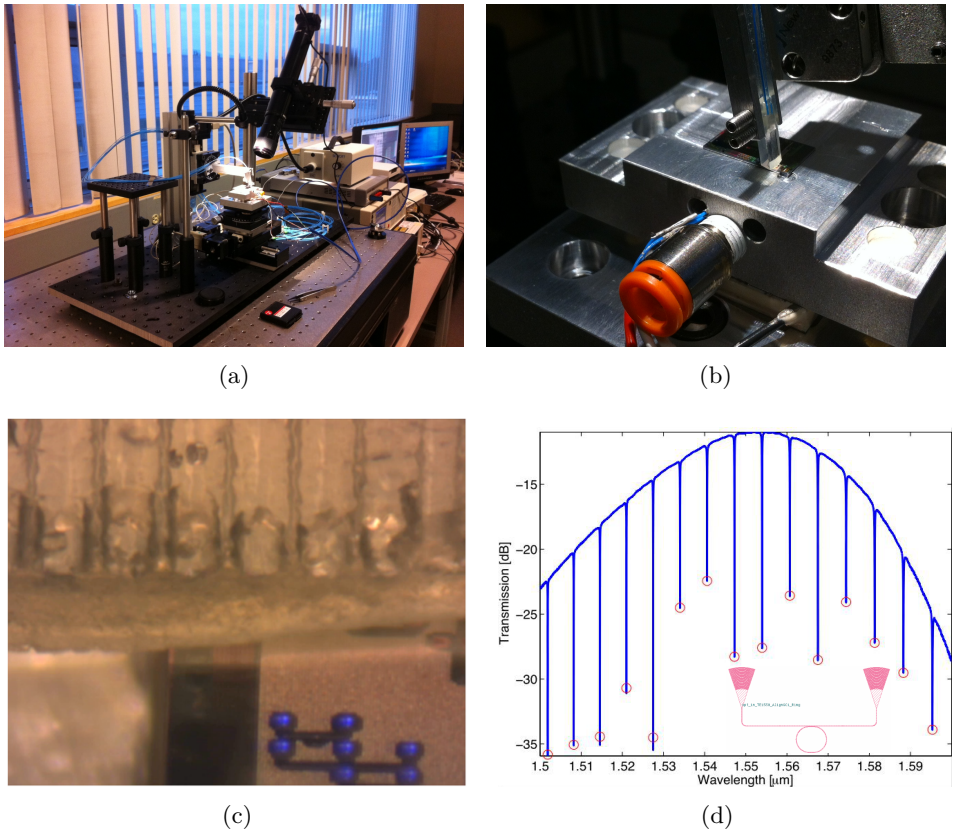

Figure 3.42: **(a)** Automated stage, bench-top configuration. **(b)** Sample pedestal and fibre array. **(c)** Microscope image of fibre array near chip alignment features. **(d)** Spectra of an 84 µm-long ring resonator alignment feature.

Figure 3.42(c) shows a microscope image of the fibre array tip on top of the GCs of the landmark device set shown in Fig. 3.38, and Fig. 3.42(d) shows the spectrum of the ring resonator landmark device, obtained using the automated measurement GUI. After successful automated alignment tests using the benchtop configuration, I re-assembled the characterization setup on a rotary platform within a temperature-controlled chamber. Given the dimension restrictions, elements such as the microscope tube, posts, and post holders were substituted with shorter elements, as shown in Fig. 3.43(a). I designed custom 3D-printed spacers shown in Fig. 3.43(b), to mount the fibre array on a set of two compact goniometres. These goniometres, in combination with a precision rotary platform, allowed for more repeatable and precise manual adjustment of the pitch, roll, and yaw angles than those obtained on the benchtop configuration. Since continuous rotation is not possible, due to the risk of fibre entanglement, fibres and cables within the chamber were laid down and clamped so as to allow for rotation in a sinusoidal pattern.

Instrument Improvements

A PXIe-1062Q chassis and a PXIe-8135 2.3GHz quad-core controller control the setup. The Agilent 81682A TLS used in the previous setup was now used with a four-channel Agilent N7744a photodetector, allowing for simultaneous measurements of up to four device ports. Eventually, an Agilent 81960a TLS and a 8163B mainframe were acquired, allowing for faster continuous sweep rates in a wider spectral range. However, the 81960a TLS does not have a low output power option ($P_{\text{in min}}$=6 dBm), and due to the lack of polarization-maintaining attenuators, the 81682A TLS was kept for tests with input power levels ranging from −13 to 6 dBm. A Stanford Research Systems TEC controller PTC10 [123] was acquired as to allow for a wider pedestal temperature range.

Software Improvements

Interfaces were created on various software platforms for open- and closed-loop sample positioning. Specifically, the Corvus^{TM} positioning system could be controlled using either MATLAB^{TM} or LabVIEW^{TM} for open-loop positioning, shifting each axis with user-defined displacements.

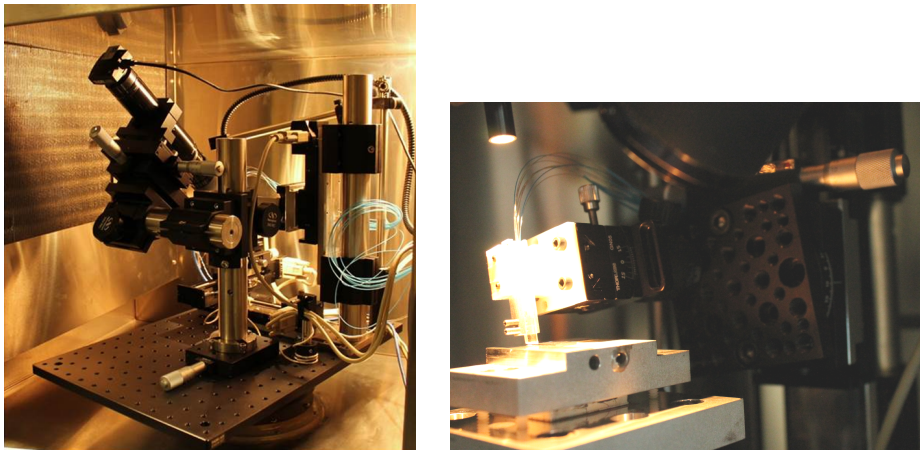

(a) (b)

Figure 3.43: **(a)** Compact configuration of the characterization setup, within turntable chamber. **(b)** Sample pedestal and improved fibre array holder.

The TLSs and the quad-port N7744a photodetector could be interfaced with either MATLAB^{TM} or LabVIEW. However, being explicitly intended for time-domain signal acquisition and control, of the two software environments, LabVIEW^{TM} proved more reliable and efficient at acquiring time-domain data. In contrast, the automatic alignment and spectral data recording algorithms had already been developed in the UBC-UW MATLAB^{TM} GUI. Attempts to embed the MATLAB^{TM} GUI within LabVIEW^{TM} as an alignment sub-routine proved futile. Due to timing and driver access issues, these two interfaces could not be open simultaneously.

In order to investigate resonance stability over time, I created continuous spectral sweep (CSS) algorithms using MATLAB^{TM} and Agilent's Fast Spectral Insertion Loss (FSIL) COM drivers. This allowed for spectrum

capturing and recording at rates between 0.5 to 5 seconds per sweep. The FSIL COM drivers were incompatible with the drivers used in the UBC-UW MATLAB^{TM} GUI, so these two elements could not be open simultaneously either. Therefore, the MATLAB^{TM} GUI was used for all fine alignments, and was closed prior to any CSS or LabVIEW^{TM} time-domain characterization. Once the time-domain or CSS characterization started, the LabVIEW^{TM} open-loop positioning VI could be used for any necessary manual adjustment without causing any conflict.

3.4.3 Measurements

After the preliminary automated alignment and measurement tests were carried out in the benchtop configuration (e.g., see Fig. 3.42(d)), I re-assembled the setup inside the turntable chamber and characterized the test structures to determine the propagation loss of MMWGs. This was followed by characterizing the large resonators.

MMWG Propagation Loss Characterization

As mentioned in Section 3.4.1, four MMWG test structures (MMWG TSs) with rib MMWG length values of 2, 56, 86, and 116 mm were created on the layout design. Neighbouring loopback and ring landmark structures were used as "zero-length" references. The MATLAB^{TM} GUI was used to perform sequential alignments upon the MMWG TSs and neighbouring landmark devices in various chips. At least twenty measurement cycles were recorded for each chip. I developed automated Matlab scripts to sort the data for each chip, obtain the average IL for each device, plot the average IL vs. MMWG TS length, and perform propagation loss curve fits.

Figure 3.44 shows the average IL as a function of wavelength for the MMWG TSs of a single chip, and the figure inset shows the corresponding linear fit. The average propagation losses ranged between 0.077 and 0.085 dB/cm across various chips. The excess loss caused by 40 adiabatic bends and tapers was estimated to be ~ 0.07 dB, by comparing the extrapolated zero-length loss of the MMWG test structures to that of a reference

loop-back device, also shown in the Figure.

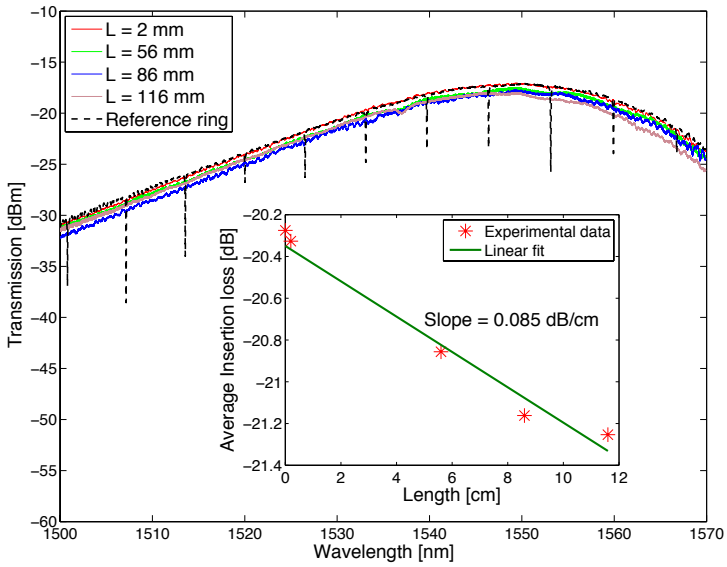

Figure 3.44: Spectra of test structures with various MMWG lengths, for an IME run. Also shown, spectrum of a reference loopback waveguide coupled to an 84-micrometer long racetrack resonator. **Inset:** Insertion loss versus length, showing an MMWG propagation loss of 0.085 dB/cm.

Resonator Characterization

Figure 3.45 shows the block diagram of the resonator characterization tests. Resonators with both fixed and thermally-tuneable couplers were characterized using this experimental configuration. Light was injected into the DUT via a PM circulator and two detectors were used to record the output power of the mixed-through port, $P_1 = \left|A_1^-\right|^2$ and the signal exiting through the input port, $P_2 = \left|A_2^-\right|^2$. These spectra were saved for each device, and automated codes were developed to obtain figures of merit (e.g., Q factor, ER, FSR, and group index) and to perform spectrum normalization and curve fitting for each resonance of the signal P_2. Figure 3.46 shows the spectra for a 37.6 mm-long tuneable-coupler resonator, with null bias current. The total wavelength span (not shown in the figure for clarity) ranged from 1548 to 1552 nm and encompassed over 200 resonances.

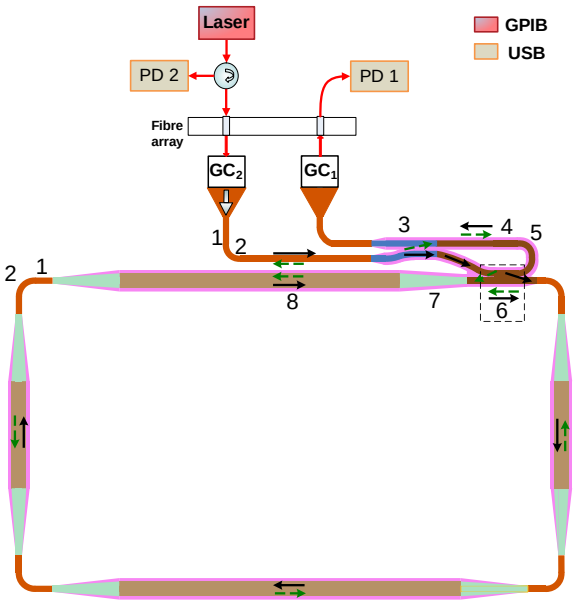

Figure 3.45: Experimental block diagram for characterization of resonators with splitting/merging couplers.

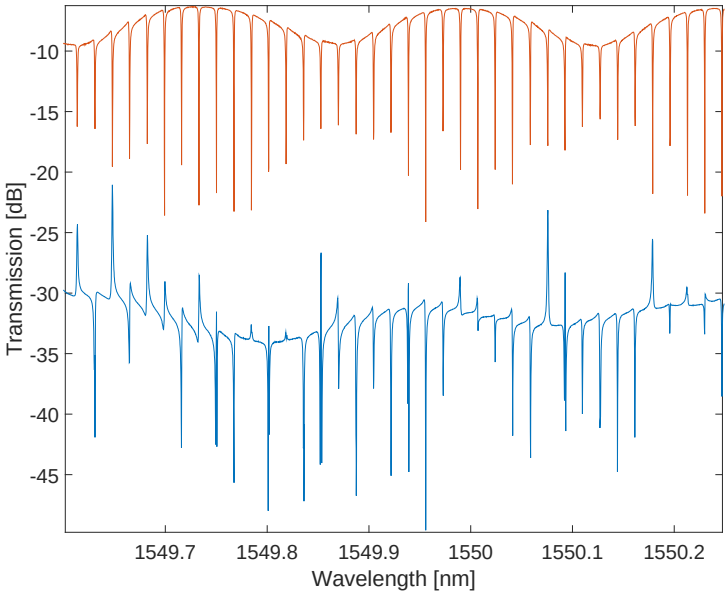

Figure 3.46: Spectra for a 37.6 mm-long ring resonator for the mixed through and the return signal ports, detected at PD1 and PD2 according to Fig. 3.45.

As one can see in Fig. 3.46, although the resonator was at rest, a signal was detected in the mixed-through port. One also can see in Fig. 3.48 that the values of Q, ER, and the curve fit parameters show considerable fluctuations. We initially associated this to non-idealities of the adiabatic splitters. However, as will be shown in Subsection 3.5.3, these fluctuations also appeared for rings with directional couplers without adiabatic splitters. A later study (see Subsection 3.5.4) showed that the peaks in the mixed-through port are consistent with the existence of backscattering in the ring [10]. The variations of the extinction ratio can be partially explained by the limited resolution of the wavelength sweep step of the laser. Figure 3.47 illustrates this effect by comparing simulated spectra with various wavelength step values. One can see that the variation of the ER increases as the wavelength step, $\Delta\lambda$, increases. This artifact, along with the backscattering effects, can explain the observed ER variations in our experimental spectra.

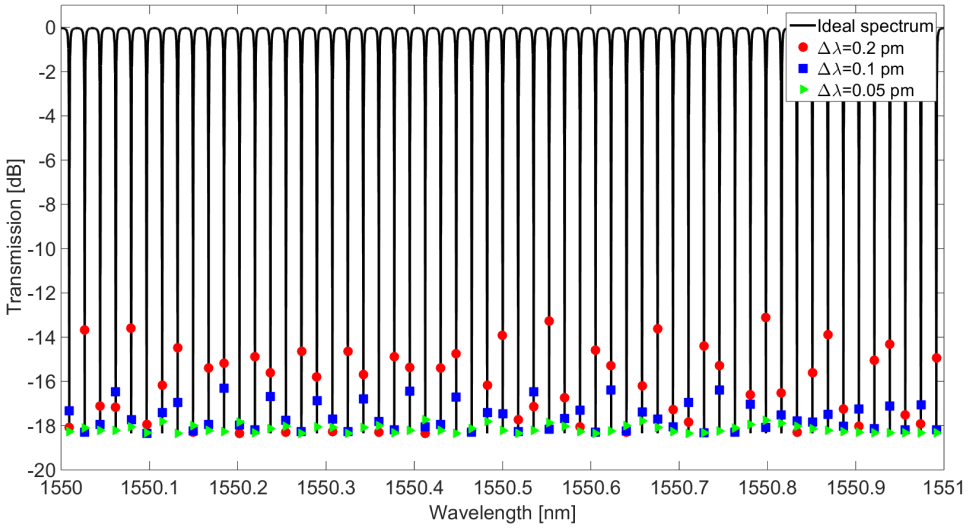

Figure 3.47: Spectra for a 37 mm-long resonator for various wavelength step values.

Figures 3.48(a), 3.48(b), 3.48(c), and 3.48(d) show, respectively, the Q, ER, FSR, and group index as functions of wavelength for this device. The wavelength sweep step was 0.2 pm. The Q factor in this experiments reached

values as high as $\sim 2 \times 10^6$, with an average $Q_{\text{avg}} \approx 1.7 \times 10^6$. Each spectral trough was curve-fitted to Eq. (2.24) in search for the round-trip loss, τ, the through transmission, t_a, and the insertion loss coefficient, C_{IL}. The detuning, ϕ was obtained as a function of wavelength based on the separation of adjacent resonances. Since these were all-pass resonators, $t_b = 1$, and neglecting losses in the directional couplers, $\gamma_a = 0$. Thus, Eq. (2.24) became:

$$|S_{21}|^2 = \frac{t_a^2 - 2t_a\tau\cos(\phi) + \tau^2}{C_{\text{IL}}\left[1 - 2t_a\tau\cos(\phi) + t_a^2\tau^2\right]} \tag{3.23}$$

Figure 3.48(e) shows the normalized spectrum for the aforementioned resonator and superimposed curve fits for each resonance obtained using Eq. (3.23). Figure 3.48(f) shows the fit values as functions of wavelength for t_a and τ. Due to the structure of Eq. (3.23), the round-trip loss τ and the coupling t_a are interchangeable parameters. In order to distinguish them, the idea was to observe the trends of the parameters as functions of wavelength, as τ should be fairly constant. However, it was difficult to find a trend versus wavelength due to the fluctuations in the fitted values.

However, since the T-MZI current was null, it was possible to associate the fitted values closer to 1 with the value of t_a. Thermal tuning experiments (see Subection 3.4.3) allowed us to confirm that for current values of 1 mA and 3.7 mA (equivalent to thermal phase shifter power values of 1.1 mW and 14.4 mW, respectively), the resonator was near critical coupling condition, and the ER was maximized.

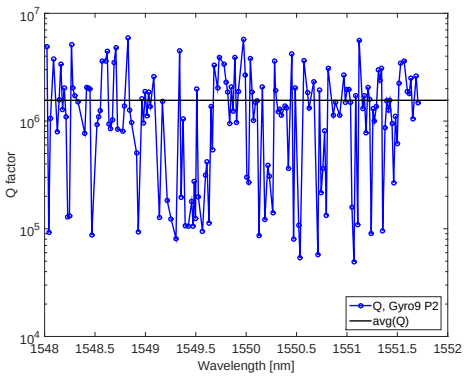

(a) Q factor

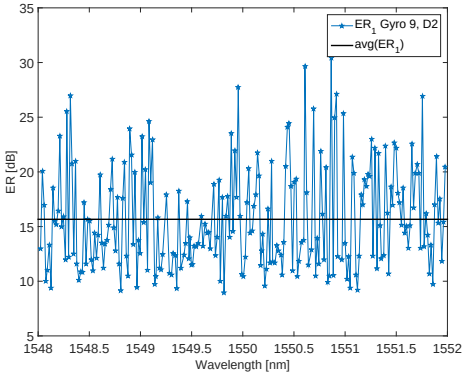

(b) ER

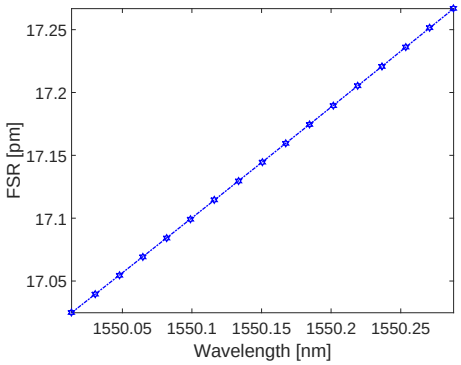

(c) FSR

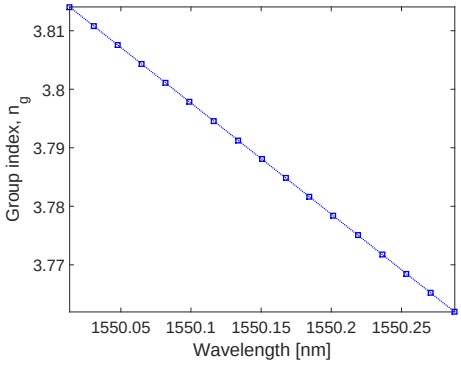

(d) Group index

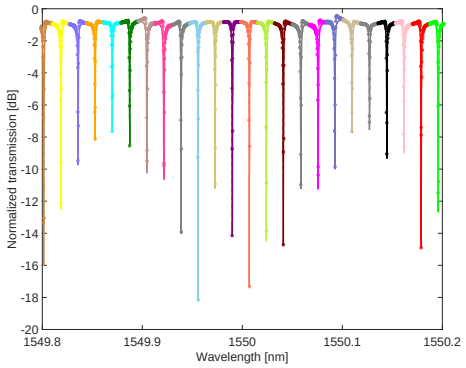

(e) Curve fits

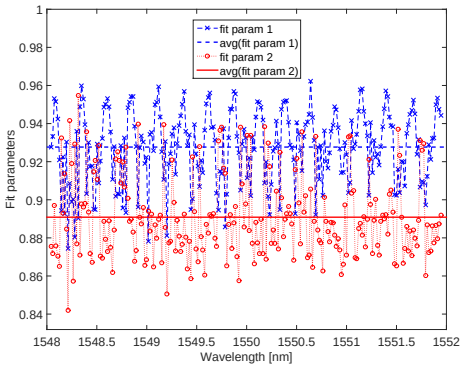

(f) Fit parameters

Figure 3.48: Figures of merit for a 37.6 mm-long resonator with unbiased tuneable coupler, in various wavelength ranges. **(a)** Q factor. **(b)** ER. **(c)** and **(d)** FSR and group index, respectively, extracted from full spectrum curve fit data. **(e)** Curve fits for each resonance trough. **(f)** Coupling and roundtrip loss curve fit parameters, for each resonance.

Tuneable Coupling Experiments

The samples with thermally-tuneable couplers were tested in an alternative characterization setup, as the electrical probes used during these experiments could not be accommodated within the turntable chamber without major modifications. Curves of voltage as a function of current (V-I curves) were obtained to determine the resistance of the 200 µm-long metallic thermal heaters. Their resistance ranged from 1070 Ω to 1200 Ω. Figure 3.49 shows experimental results obtained with a T-MZI test structure similar to that shown in Fig. 3.34. The electrical current of the metal heater was stepped, and the voltage and optical spectrum were recorded at each current value. During post-processing, the optical transmitted power at a single wavelength ($\lambda = 1530$ nm) was plotted as a function of the thermal phase shifter power, P_θ. Figure 3.49(a) shows the metal heater V-I curve, and Figure 3.49(b) shows the normalized optical power at the through and drop ports of the test structure as a function of P_θ. The metal heater resistance, insertion loss, and phase shifter efficiency for this device were, respectively, $R = 1106.5$ Ω, IL=16.3 dB, and $\eta_\theta = 24$ mW/π.

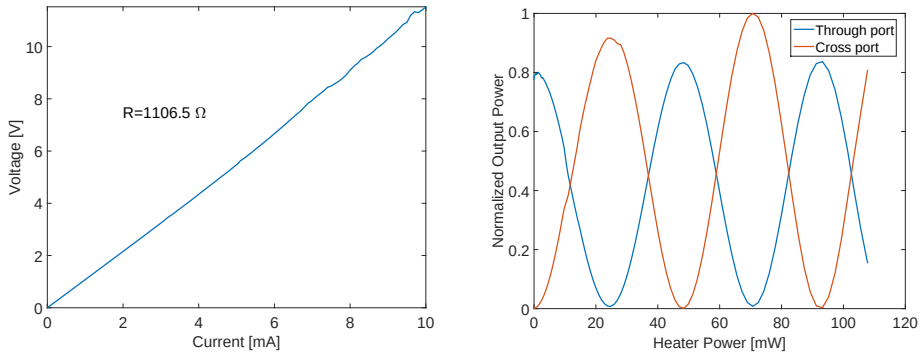

(a) (b)

Figure 3.49: T-MZI test structure experimental results. **(a)** V-I curve to determine metal heater resistance, R=1106.5 Ω. **(b)** Normalized optical output power vs. heater power, at $\lambda = 1530$ nm. Minimum IL: 16.3 dB.

Spectral sweeps over a 300-pm span were obtained for a 37 mm-long

resonator with tuneable coupler. The phase shifter currents ranged from 0 to 7.9 mA, in 0.1-mA steps. Figure 3.50 shows the spectra of the resonator's return signal via the PM circulator (dotted curves) and the mixed-through port signal (dashed curves) with the thermal phase shifter power, P_θ, as a parameter. For clarity, the plot range and has been restricted to 80 pm, and the values P_θ shown correspond to shifter currents ranging from 0 to 4 mA, in 0.5-mA steps. One can see changes in the return signal extinction ratio and the resonance wavelength as the current is increased. One can also see similar changes for the mixed-through signal, which is expected to be zero in the absence of rotation. Its appearance can be explained based on the backscattering model shown in Subsection 3.5.4.

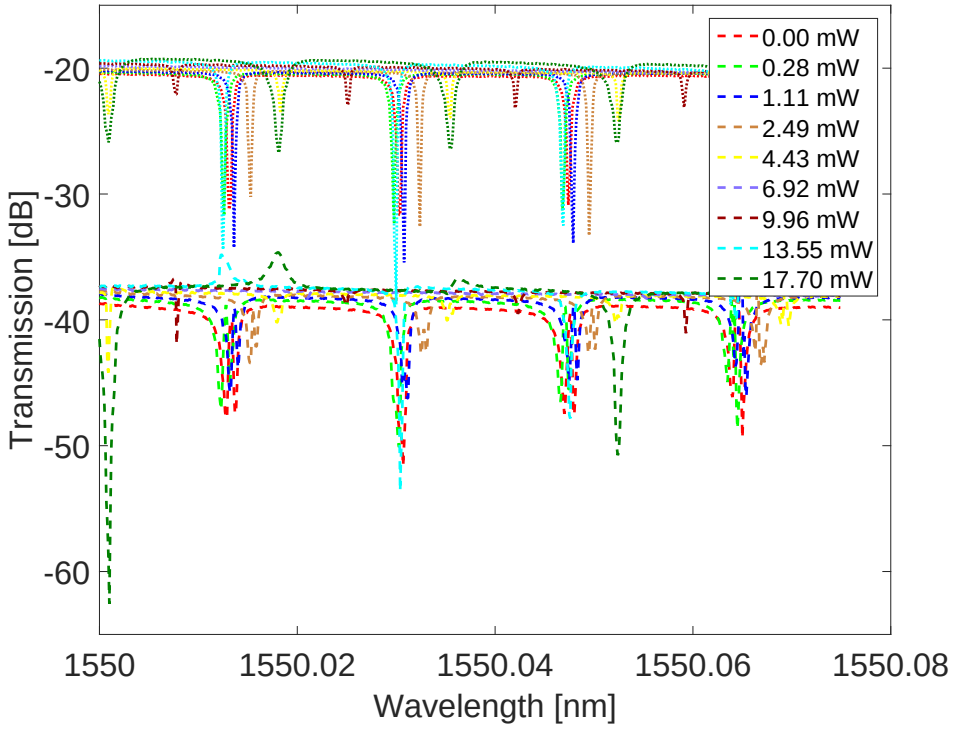

Figure 3.50: Resonator spectra during coupler thermal tuning, with thermal phase shifter power as a parameter. Heater resistance: 1100 Ω. Phase shifter current range: 0 to 4 mA, in 0.5 mA steps. Dotted curves: Return signal (on circulator's port 3). Dashed curves: Mixed-through port signal.

Figure 3.52 shows the evolution of the spectra and figures of merit of the return signal as the phase shifter power P_θ is varied. Figures 3.52(a) and 3.52(b) show, respectively, the spectra and ER versus wavelength for P_θ from 0 to 6.37 mW, corresponding to thermal phase shifter current (i_θ) values from 0 to 2.4 mA, with steps $\Delta i_\theta =$ 0.2 mA). One can see that the measurement for $P_\theta = 1.11$ mW is the closest to critical coupling condition, as the ER is maximum. The remaining subfigures of Fig. 3.52 show results for a wider P_θ range, from 0 to 27.7 mW, using a finer current step $\Delta i_\theta =$ 0.1 mA. For clarity, these subfigures show only average values of each figure of merit as functions of P_θ. Figs. 3.52(c), 3.52(d), 3.52(e), and 3.52(f) show, respectively, the average ER, average Q factor, average FSR, and the average curve fit parameters corresponding to the straight-through field transmission $t(\theta)$, and roundtrip loss τ, for P_θ ranging from 0 to 27.7 mW.

Based on Fig. 3.52(f) one can unambiguously discern between $t(\theta)$ and τ, as only $t(\theta)$ varies sinusoidally as P_θ is increased, whereas τ is fairly constant. The resonator is initially overcoupled, reaches its maximum ER at critical coupling, near $P_\theta = 1.1$ mW and $P_\theta = 13.6$ mW. The ring is undercoupled for 1.1 mW $< P_\theta <$ 13.6 mW, and overcoupled for 13.6 mW $<$ $P_\theta <$ 27.7 mW. The imperfect fits for $t(\theta)$ and τ near critical coupling are due to the fact that an infinite extinction ratio would be required to make both parameters identical. This is also true for non-fit-based parameter estimations, such as those described in [86].

To properly estimate the Q factor in heavily over- and under-coupled conditions, it is important to point out that for an all-pass resonator, the FWHM is located at half the depth of the spectral trough in a linear scale [14, 33], as shown in Fig. 3.51, rather than being fixed 3 dB below the maximum transmission value. Figure 3.51 depicts two cases: one slightly overcoupled (t=0.8, $\tau = 0.88$), and the other one, heavily overcoupled (t=0.42, $\tau = 0.88$). As one can see in the figure, the denomination of -3 dB linewidth can lead to erroneous estimations, as strictly, the FWHM can only be located at the -3 dB line for a critically coupled resonator. For high extinction ratio resonators (ER$\sim$ 1), the -3 dB approximation is valid. However, the separation between the two points intersected by a horizontal line at -3 dB

becomes narrower as the extinction ratio decreases. Thus, the FWHM and Q factor can be mistakenly under- and over-estimated, respectively. Taking into account the finite extinction ratio ER < 1, the normalized transmission at FWHM for an all-pass resonator is, in linear scale:

$$T(\phi_{\text{fwhm1,2}}) = 1 - 0.5 \cdot \text{ER}, \tag{3.24}$$

where $\phi_{\text{fwhm1,2}}$ are the two detuning values at FWHM, ER $= 1 - T(\phi_{res})$ is the extinction ratio (expressed in linear scale), and ϕ_{res} is the normalized power transmission at resonance. When processing experimental data, the FWHM is obtained as the difference of the wavelength values corresponding to $\phi_{\text{fwhm1,2}}$, and Q is obtained as $Q = \lambda_0/\text{FWHM}$. All Q factor estimations shown in Fig. 3.52(d) have been obtained using this procedure. The highest quality factors were $Q \approx 4.5 \times 10^6$, achieved in heavily undercoupled conditions.

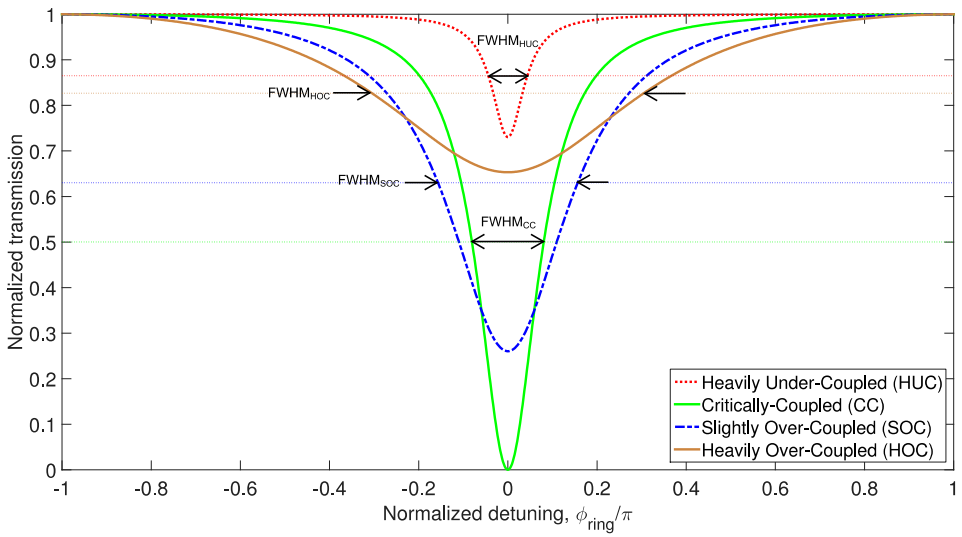

Figure 3.51: Comparison of FWHM values for rings with various coupling conditions.

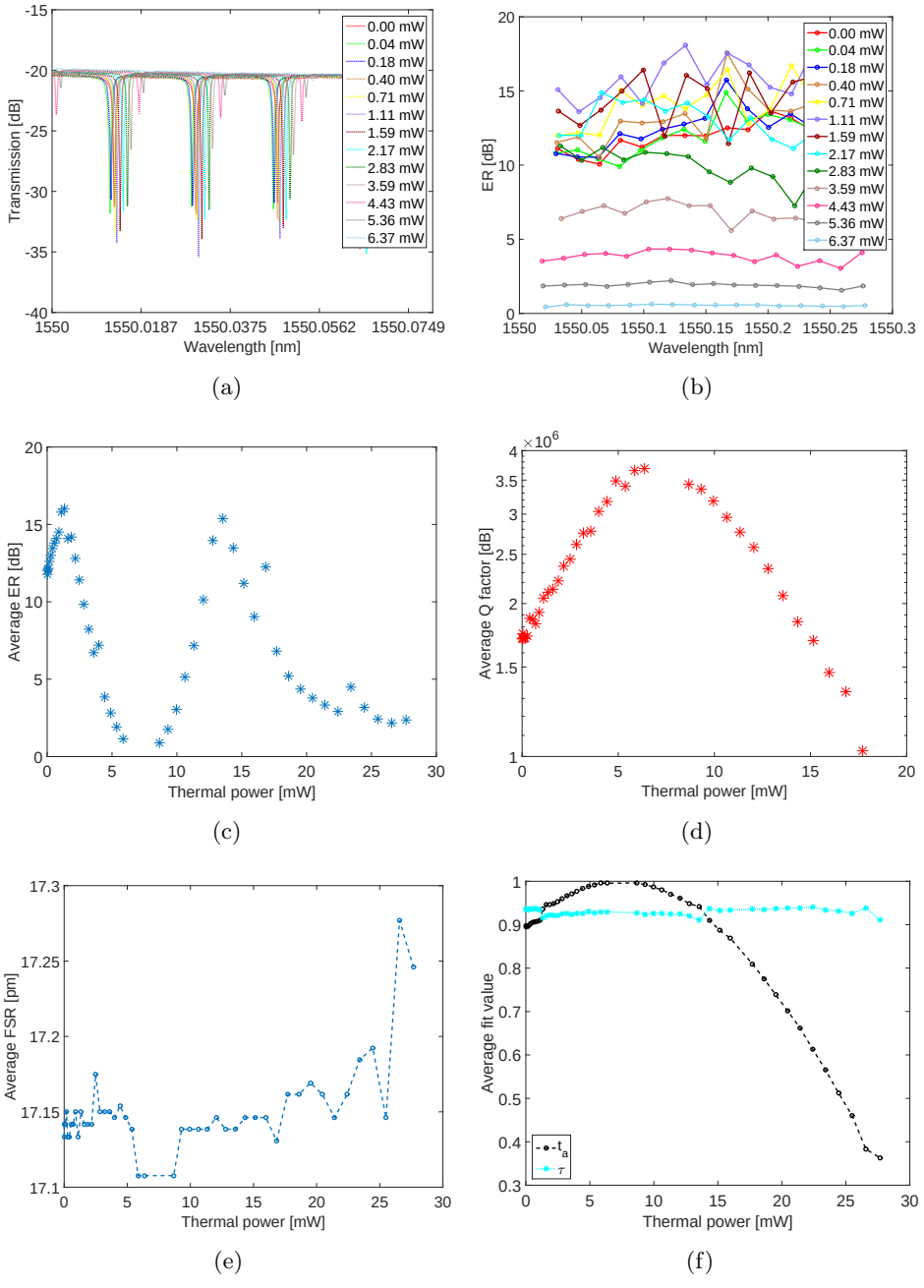

Figure 3.52: Selected spectra and figures of merit for a 37 mm-long resonator with thermally tuneable coupler. **(a)** Return signal spectra. **(b)** Extinction ratio (ER) vs. wavelength. **(c)** Average ER vs. thermal phase shifter power, P_θ. **(d)** Average Q-factor vs. P_θ. **(e)** Average FSR vs. P_θ. **(e)** Average straight-through field transmission, $t(\theta)$, and roundtrip loss, τ, vs. P_θ. 137

The average values of the the roundtrip loss and the group index were, respectively, $\tau_{\text{avg}} = 0.925$ and $n_{g\ \text{avg}} = 3.8$. Thus, $\alpha_{\text{avg}} = -\ln(\tau)/L = 2.118\ \text{m}^{-1}$, and:

$$Q_i = \frac{\pi n_g}{\alpha_{\text{avg}} \lambda_0} \approx 3.63 \times 10^6 \tag{3.25}$$

The coupling quality factor, Q_c, and $t(\theta)$ are related by [21, 68, 141]:

$$Q_c = \frac{-\pi n_g L}{\lambda_0 \ln(t(\theta))}, \tag{3.26}$$

and the total Q factor is:

$$Q = \frac{Q_i Q_c}{Q_i + Q_c}. \tag{3.27}$$

Fast Spectral Sweeps

As mentioned earlier, automated measurements were carried out sequentially for several devices on each chip. Any particular device was re-measured after a period that depended on the number of devices in the run. On a specific chip, we carried out repeated tests at various input power levels on multiple devices. Figure 3.53 shows the measurements carried out on a 38 mm long resonator at various input power levels. The measurements shown in this figure were taken over a time span of 1 hour. These measurements showed resonance shifts in spite of the fact that the sample pedestal was temperature-controlled. Similar resonance shifts were observed between measurements made on a single device at different times, even using a constant input power (0 dBm). If no translation was necessary, the MATLAB$^{\text{TM}}$ GUI measured a spectrum in approximately 60 to 90 seconds. In order to observe the resonant behaviour over time, measurements at faster sweep rates than those achievable with the MATLAB$^{\text{TM}}$ GUI were necessary.

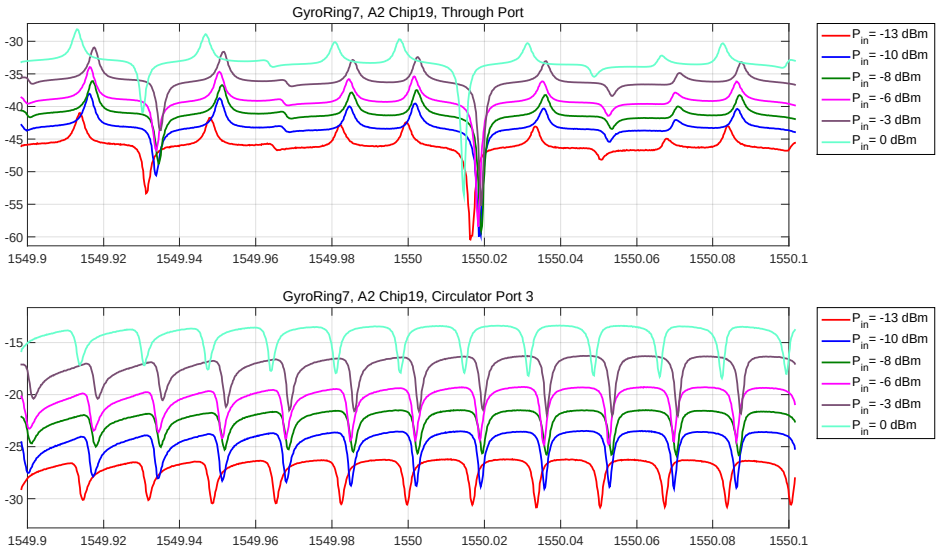

Figure 3.53: Resonances for a static, 38 mm-long ring at various input power levels, on a temperature-controlled pedestal, at 25°C.

Based on information provided by applications engineers from Keysight Technologies, Inc., I created scripts for fast sweeps and data recording at high repetition rates using proprietary COM drivers compatible with MATLAB^{TM}. The sweep rate for each run depended on its wavelength span, wavelength sweep step, and sweep speed. The recording rates ranged from 0.5 to 5 seconds per sweep.

To investigate whether the laser could be a source of noise, stability tests were carried out with a large ring resonator and an acetylene cell (C_2H_2), a gas with stable absorption lines in the C band [93]. These tests were carried out using a 0.1 pm wavelength step, the smallest possible with our TLSs.

Figure 3.54(a) shows the superimposed spectra for a 300-sweep test using the C_2H_2 cell. The input power was 6 dBm, and the sweep rate was 40 nm/s. The average sweep time was 0.7 s. During post-processing, two points were tracked in each spectrum to obtain statistical data. The resonance wavelength and its transmitted power were recorded for each spectrum. A fixed off-resonance wavelength value was chosen in the first spectrum, and the transmitted power at that wavelength was tracked in the remaining spec-

tra to assess the off-resonance power variation over time. Figure 3.54(b) compares the transmitted power vs. time for the selected wavelength values. Figure 3.54(c) shows the resonance wavelength value over time. The average resonance wavelength was $\overline{\lambda_0} = 1530.3651$ nm, and the standard deviation of the resonance wavelength was $\sigma(\lambda_0) = 0.239$ pm. The relative power fluctuation off-resonance, $\sigma(P_0)/\overline{P_0}$, was 3.44×10^{-4}. Fig. 3.54(d) shows a histogram for the resonance wavelength values.

Figure 3.55 shows plots for a similar test using a 37 mm-long ring resonator. The resonance wavelength average value was 1550.230 nm, the standard deviation of the resonance wavelength was 0.255 pm. The relative power fluctuation off-resonance for the resonator was 3.53×10^{-2}. Fig. 3.54(d) shows a histogram for the resonance wavelength values.

The resonance wavelength variation for the acetylene cell and the resonator were similar, suggesting that the variation was mainly caused by the laser wavelength accuracy rather than by an effect internal to the resonator. Furthermore, additional tests with the acetylene cell showed that the resonance wavelength fluctuation depended on the sweep speed of the laser. However, the off-resonance power fluctuations cannot be explained by the laser power stability, because the variations were much larger for the resonator than for the acetylene cell.

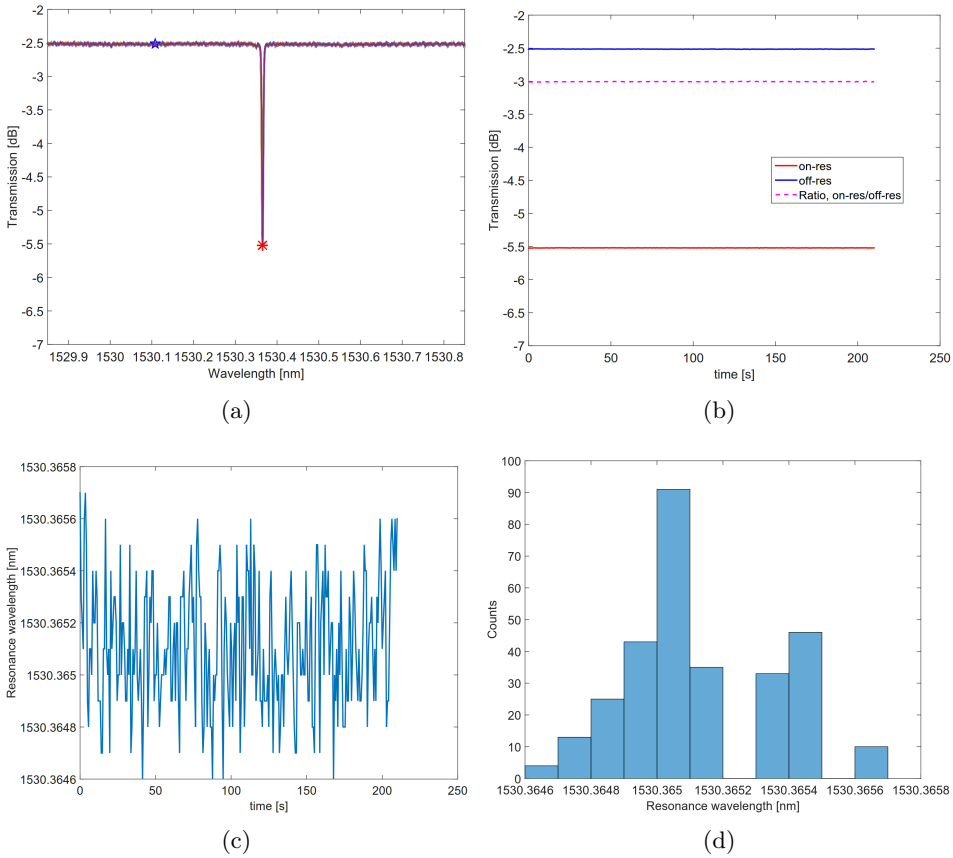

Figure 3.54: Resonance dip stability test for an acetylene (C_2H_2) cell. **(a)** 300 superimposed spectra, showing markers tracking transmitted power at resonance (red asterisks) and an arbitrary off-resonance wavelength (blue stars). **(b)** Comparison of transmitted power levels at selected wavelengths, and their ratio, over time. **(c)** Resonance wavelength over time. **(d)** Resonance wavelength histogram.

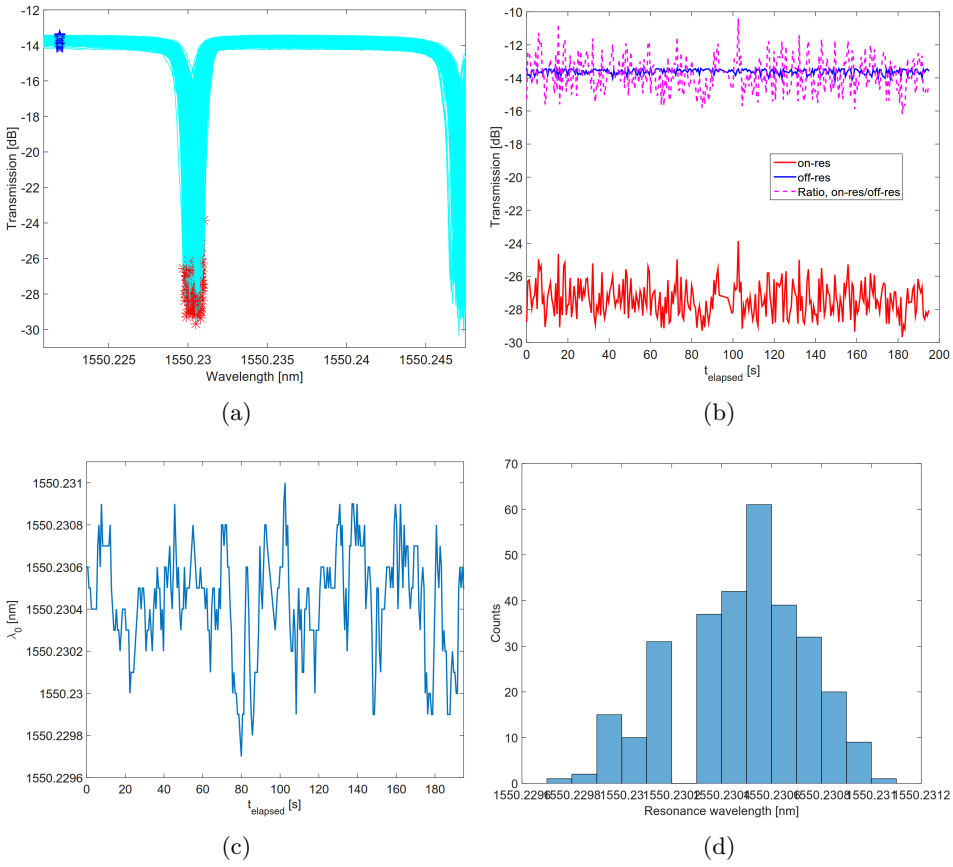

Figure 3.55: Resonance dip stability test for a 37 mm-long resonator. **(a)** 300 superimposed spectra, showing markers tracking transmitted power at resonance (red asterisks) and off-resonance (blue stars). **(b)** Comparison of transmitted power levels at selected wavelengths, and their ratio, over time. **(c)** Resonance wavelength over time. **(d)** Resonance wavelength histogram.

Time-Domain Measurements

Figure 3.56 shows the front panel of a LabVIEW^{TM} interface developed for monitoring and recording the power over time at a single wavelength for our Agilent N7744a quadruple photodetector. Statistical analysis features were also created to automatically calculate the mean, standard deviation, and SNR of linear scale power measurements. The experimental SNR values

were obtained as the ratio of the mean of the power divided by its standard deviation. For consistency, all measurements taken had an approximately equal number of data points.

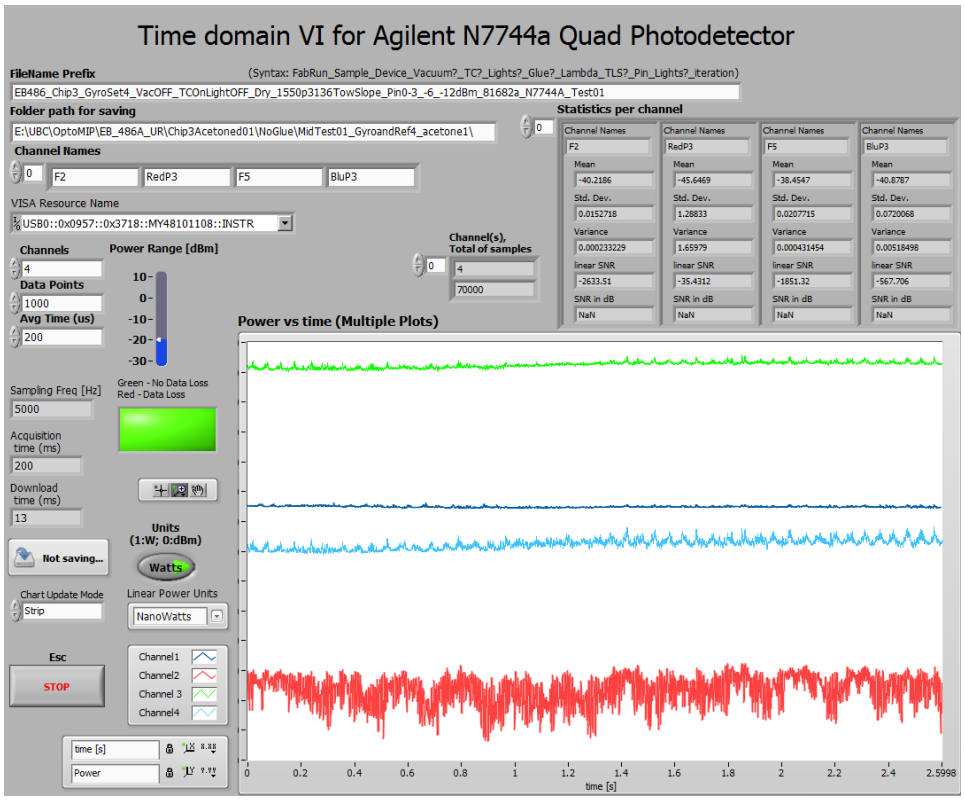

Figure 3.56: Front panel of the LabVIEW^{TM} VI for time-domain measurements with the N7744a photodetector.

The noise floor was estimated at each value of the photodetector power sensitivity, by connecting light dumps to its ports and carrying out 22000-point measurements using an integration time of 50 μs. Figure 3.57(a) shows the noise floor as a function of the photodetector sensitivity. Since the most commonly used sensitivity settings in our experiments were either -20 dBm or -10 dBm, our experimental noise floor value was considered to be -70 dBm.

The greatest achievable SNR at various input power levels was esti-

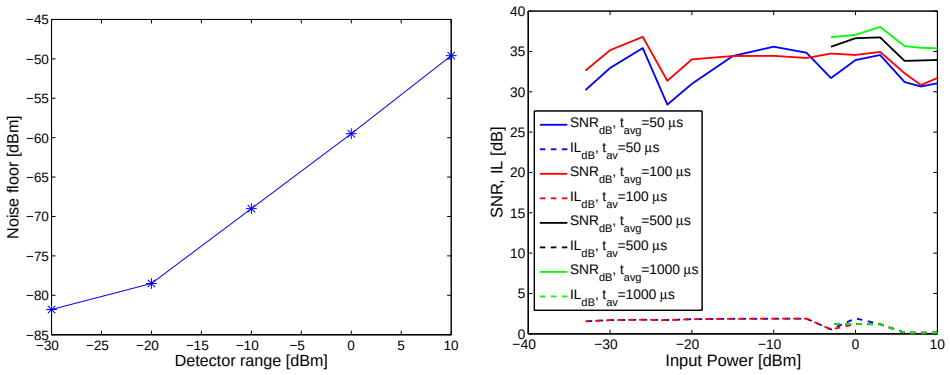

(a) Noise floor

(b) patch cord IL and SNR

Figure 3.57: **(a)** N7744a photodetector noise floor at various photodetector sensitivity values, for 22000 samples at a 50 μs averaging time (11 s measurements). **(b)** Insertion Loss and SNR as a function of input power for a 3 m long PM patch cord, for various integration times.

mated by connecting the laser to the photodetector using a connectorized polarization-maintaining (PM) patch cord. The patch cord length was 3 meters, similar to that of the PM fibre array. SNR and IL tests, with integration times ranging from 5 μs to 2 ms, were carried out for input power levels ranging from -30 to 10 dBm at a single wavelength ($\lambda = 1556$ nm), as shown in Fig. 3.57(b).

As expected, the IL was fairly constant, and the SNR was slightly improved for longer integration times. Considering the trade-off between SNR improvement and acquisition time, integration times in the range of 50 to 200 μs were deemed appropriate for subsequent experiments, and the remaining tests for $t_{avg} \geq 500$ μs were discontinued. Similar SNR tests were carried out with two PM circulators, showing that they did not significantly impact the achievable SNR. Details can be found in Appendix C.

Further time-domain tests were carried out with PM patch cords in order to determine the frequency content of the signals at the photodetectors. Measurements were recorded over a period of 2 minutes, using a constant input power and wavelength, with averaging times of 50 and 100 μs. During post-processing, the power spectral density (PSD) plots, normalized to unit

power, were obtained. Figure 3.58 compares PSD plots obtained in various experiments using the two aforementioned averaging times. The experiments were repeated several times to ensure consistency. Spurious signals are consistently observed at 120 Hz, due to the cavity vibration caused by the TLS wavelength tuning control. Similar tests were carried out on a loopback device to compare the PSDs of signals obtained with the pedestal vacuum pump on and off. The SNR values for the pump on and off are, respectively, 24.2 and 28.8 dB. Figure 3.59 shows the PSDs for each case. When the vacuum pump is on, the noise level is greater in the frequency range between $\sim$ 10 and $\sim$ 100 Hz. The time-domain plots in Fig. 3.60 shows a slight IL decrease when the vacuum is turned off. Thus, the vacuum pump should be turned off once the fibre array was properly attached to the samples.

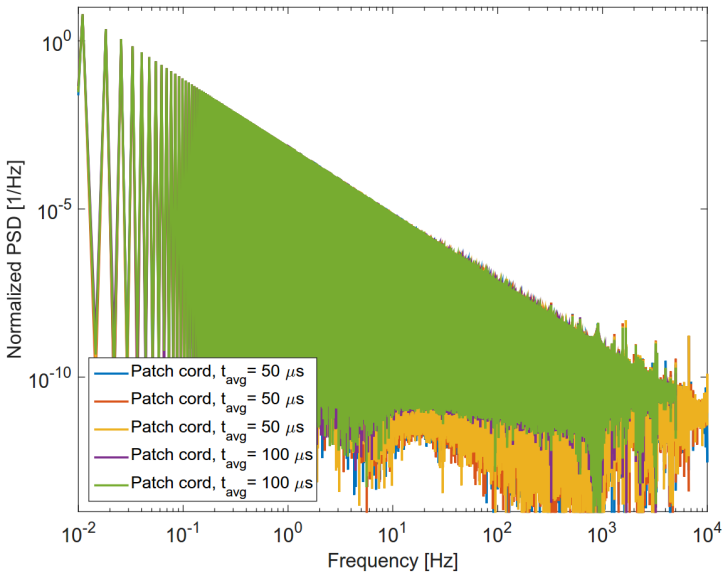

Figure 3.58: Comparison of noise PSD plots normalized to unit power, based on autocorrelations various time-domain tests for a 3 m-long patch cord. The legend shows the integration time for each run.

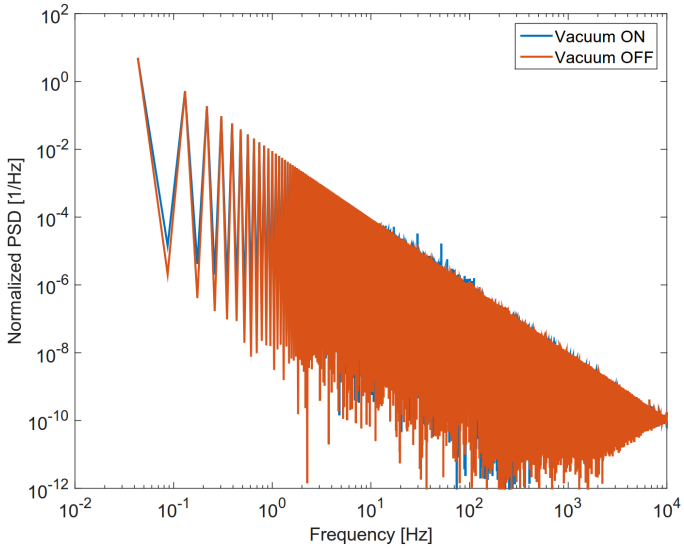

Figure 3.59: Comparison of noise PSD plots normalized to unit power, based on autocorrelations of time-domain tests for a loopback device, with the pedestal vacuum pump turned on and off. Integration time: 50 μs.

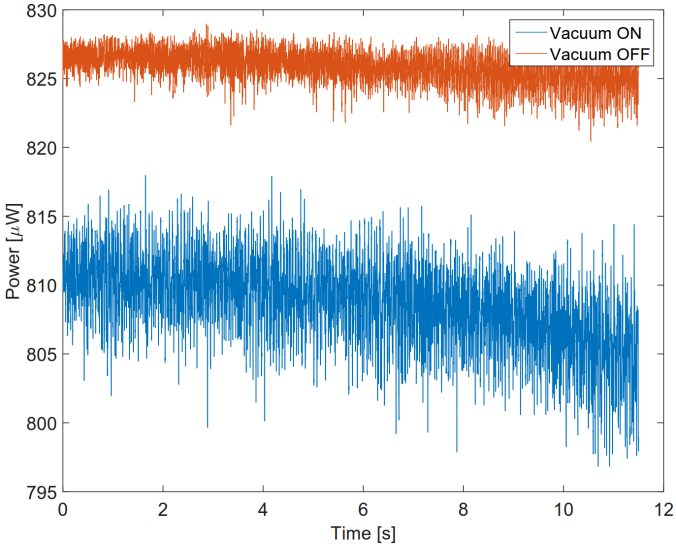

Figure 3.60: Comparison of time-domain signals for a loopback device with vacuum pump turned on and off. For both tests the integration time is 50 μs. IL: 10.9 dB with vacuum pump on, 10.8 dB with vacuum off.

3.4.4 Iteration Challenges and Conclusions

In this iteration, we designed resonators with a combination of strip SMWGs, rib SMWGs, and rib MMWGs. This allowed us to further reduce the propagation losses, as compared to our previous designs. The propagation losses of our rib MMWGs ranged from 0.077 to 0.085 dB/cm. Without thermal tuning of the coupling, our as-fabricated resonators show Q factors as high as $\sim 2 \times 10^6$, with an average $Q_{\text{avg}} \approx 1.7 \times 10^6$, as published in [56]. This is, to the best of our knowledge, the highest Q values reported to date for resonators fabricated using a standard CMOS-compatible process. Q factors as high as $\sim 4.5 \times 10^6$ were achieved by thermal tuning of the coupling.

Using equation (3.3) with $\lambda_0 = 1.55$ µm, and $n_g \approx 3.7$, the average field and power attenuation values are $\alpha_{avg} \approx 0.004$ mm^{-1} and $\alpha_p \approx 0.008$ mm^{-1}, respectively. As compared to the previous iteration's resonators, for a 6-mm length, the optical signal makes approximately 19 roundtrips before its intensity decreases by a factor of e. This was a significant improvement, by a factor of ~ 5, with respect to those previous resonators. For the resonator described in Fig. 3.46, with $L \approx 37.6$ mm, the optical signal makes approximately 3 roundtrips before its intensity decreases by a factor of e. The average finesse of these rings is 18.5 without thermal tuning.

Mathematical models were developed to describe the theoretical behaviour of devices designed for this run with fixed and with thermally tuneable splitting/merging couplers. Thermal tuning experiments allowed us to confirm the expected behaviour, as well as to compare figures of merit for resonators in over-coupled, under-coupled, and critically-coupled conditions. The Q factor estimations at critical coupling were in average $Q_{cc} \approx 1.9 \times 10^6$, with a finesse $F \approx 22.5$. For heavy under-coupling, the average Q value approached the estimated intrinsic Q value of the resonator, $Q_i \approx 3.7 \times 10^6$.

The use of computer controlled positioning allowed for automated measurements of several devices across each chip, and for obtaining the spectrum of each device in a period of 60 to 90 seconds. Continuous spectral sweep (CSS) algorithms were implemented in order to perform faster sweeps at

rates of 0.5 to 5 seconds per sweep, depending on the sweep parameters. This reduced the time required to measure devices across a chip from a few days to several hours.

The standard deviation of the resonance wavelength in the long-term continuous spectral sweep (CSS) tests ($\sigma(\lambda_0) \approx 0.44$ pm) was greater than what was expected according to the 0.2-mK standard deviation of the pedestal temperature (i.e., $\sigma_T(\lambda_0) \approx 0.014$ pm). The tests carried out with the acetylene absorption cell suggested that this variation was produced by the wavelength accuracy of the tuneable laser source. The variation of the transmitted power off-resonance for the large resonators suggested non-thermal sources of power variation, such as vibration and position drift.

A time-domain interface was developed using LabVIEW$^{\text{TM}}$. This interface was used to obtain the experimental SNR values for different system components and devices at constant values of power and wavelength. The best SNR value achieved with the experimental setup was $\sim$ 40 dB, obtained with connectorized PM patch cords. Power spectral density (PSD) plots were obtained for signals through the PM patch cords and SMWG loopback devices. The PSDs showed that over most of the frequency range, the laser noise is considerably smaller than that of the characterization stage. Thus, we concluded that the laser noise is not the main limitation for the system performance.

3.5 Fifth Design Cycle

During our experiments in the previous iteration, the resonators showed variations in the transmitted power that could not be attributed to the laser power stability. During this iteration, we designed devices consisting of two adjacent resonators with GCs laid out so as to allow for simultaneous measurements. Performing simultaneous measurements in both resonators could help us determine whether or not the transmitted power variations were correlated across different zones of the chip as well as help us eliminate undesirable common-mode signals.

During this iteration, we also developed a lumped-reflector backscatter-

ing model for the ring resonators, motivated by the non-zero signals detected at the mixed-through port of the devices from the previous iteration and by the backscattered signals detected in experiments carried out during this fifth cycle.

3.5.1 Layout Designs

Figure 3.61 shows the schematic of the resonator devices created during this iteration, combining SMWGs and MMWGs as previously done. Since the lengths and aspect ratios of the resonators could not be equal due to layout area constraints, we decided to maximize the enclosed area of the larger resonator to make them more sensitive to rotation, while the smaller resonators could be used as a reference to eliminate deleterious common-mode signals.

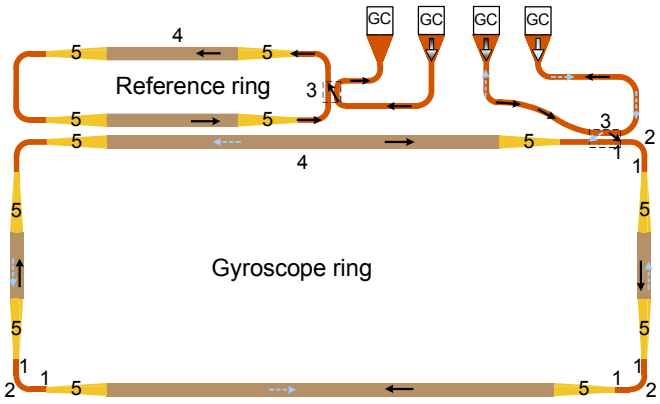

Figure 3.61: Dual resonator set. The smaller ring was created as a reference for tracking environment-related common-mode signals.

These designs had simple SMWG directional couplers to allow for estimations of the backscattering in our rings and also to investigate the feasibility of external phase modulation for backscattering noise reduction [120], which was not possible to assess with the splitting/merging couplers used in the previous design cycle. MMWG propagation loss test structures similar to those shown in the inset of Fig. 3.31 were created to assess the propagation

loss in samples fabricated using e-beam lithography.

3.5.2 Waveguide Parameters

Designs were submitted for fabrication to IME Singapore (IME) and the Nanofabrication Facility at University of Washington (UW). The designs submitted to IME used rib waveguides for the SMWG directional couplers and the MMWG straight segments. The designs submitted to UW were entirely strip-waveguide based. All chips were glass clad for waveguide protection and IL reduction.

Table 3.14 shows the values for effective and group indices for various strip waveguide geometries. Table 3.15 summarizes the propagation loss parameters for various types of waveguides used during this iteration. In the case of the rib MMWGs, the propagation loss estimation was based on the experimental results obtained in the previous iteration.

Table 3.14: Theoretical values of effective and group indices at $\lambda_0 = 1550$ nm, for strip waveguides of various geometries. In all cases the strip height is $H_{\text{strip}} = 220$ nm.

Strip width [nm]	Radius [µm]	Mode	n_{eff}	n_{g}
500	∞	TE-like	2.4435	4.1772
500	∞	TM-like	1.7703	3.7043
500	20	TE-like	2.4432	4.1769
500	20	TM-like	1.7708	3.7005
1750	∞	TE-like	2.8121	3.7343
1750	∞	TM-like	2.7087	3.8709
3000	∞	TE-like	2.8343	3.7064
3000	∞	TM-like	2.7993	3.7517

Table 3.15: Parameter estimations for different glass-clad waveguides

Parameter \ WG	SM strip	SM rib	MM rib	MM strip
Strip width (nm)	500	500	3000	3000
Slab width (nm)	-	2600	5100	-
α_{dB} $\left(\frac{\mathrm{dB}}{\mathrm{cm}}\right)$ [9, 15, 56, 78]	2.4 - 3	2.2 - 3.4	~ 0.085	0.1 - 1

3.5.3 Measurements

E-beam MMWG Propagation Losses

Following the same procedure described in Subsection 3.4.3, spectral sweeps were carried out for MMWG TSs on an e-beam sample. An average propagation loss of 0.55 dB/cm was estimated for the e-beam MMWGs. Figure 3.62 shows the spectra and the propagation loss for these devices.

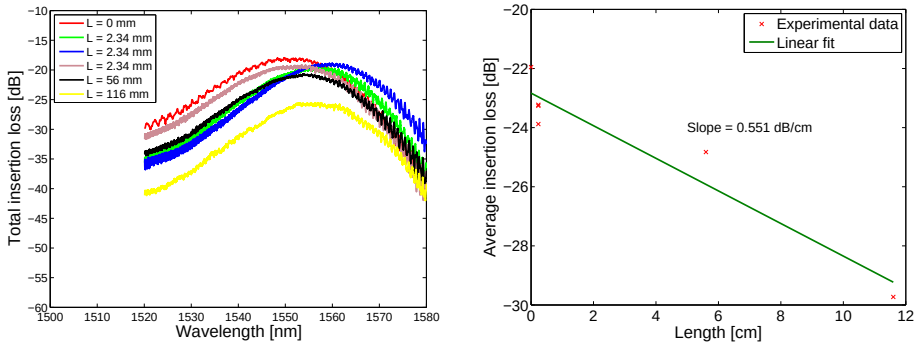

(a) (b)

Figure 3.62: Spectra of similar MMWG propagaqtion loss test structures, for e-beam samples, with a SMWG loopback as a zero-length reference. Insertion loss as a function of length, showing an MMWG propagation loss of 0.55 dB/cm.

Dual Resonator Device Characterization

Figure 3.63(a) schematically depicts an experiment for characterizing the dual ring devices. The input signal is split off-chip using a 50/50 PM splitter. Spectral sweeps were carried out for both rings simultaneously. After these spectral sweeps, the laser wavelength was tuned to fixed wavelength values to perform time-domain tests under various conditions. Figure 3.63(b) shows the spectra obtained at various sweep speeds for a dual resonator set. The gyro resonator has a length $L_1 = 32.8$ mm, and the reference resonator has a length $L_2 = 11.4$ mm. One can see that the sweep speed impacts the measurement noise in a counter-intuitive manner. Specifically, the slowest sweep speed, with the greatest integration time, produced the noisiest spectra. Figure 3.64 shows the Q, ER, FSR, and group index as functions of wavelength for this device, as well as resonance curve fits and fit parameters. The wavelength sweep step was 0.1 pm. Outlying Q factor values above 12×10^6 were discarded as they were considered to be unreliable estimations, due to the minimum wavelength resolution of the laser.

When compared to the resonators characterized in the previous iteration, one can notice that the Q factor values for these newer samples are smaller, and that the values of the FSR and the group index show greater variations, which impeded obtaining reliable fits of these two figures of merit as functions of wavelength. This could be due to greater levels of backscattering [10]. We conducted further experiments using one circulator per resonator to assess the backscattering in our devices, as per the block diagram in Fig. 3.65. Figure 3.66 shows the experimental spectra of the forward- and backward-propagated signals for a dual resonator set. For both resonators, the back-propagating signals are $\sim$ 15 dB weaker than the forward signals. This assessment was qualitative, as the GCs also contribute to backreflections on the order of ~ -16 dB [138]. Nevertheless, the evidence of backscattering and its impact on the figures of merit motivated us to develop the backscattering model described in Subsection 3.5.4. Based on the spectral sweep results, an appropriate wavelength value was chosen ($\lambda = 1550.3432$ nm) to record signals for both rings off-resonance in the time-

domain. A considerable improvement of the SNR in the forward-propagating signals was noticed when the microscope light was turned off, namely, from −0.4 dB to 19.25 dB. In contrast, the SNR for the back-propagating signals decreased slightly, from 2.21 to 2.05 dB.

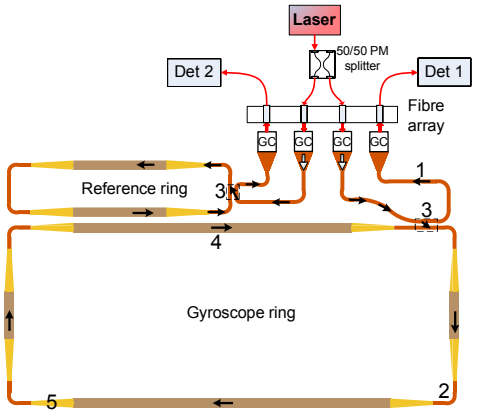

(a)

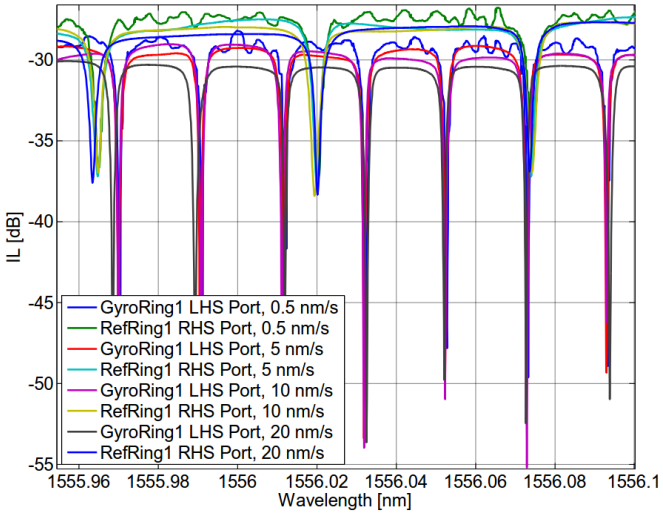

(b)

Figure 3.63: **(a)** Experimental block diagram, and **(b)** spectra at rest at various TLS sweep speeds, for a dual resonator system fabricated in e-beam technology. Gyro resonator length: $L_1 = 32.8$ mm. Reference resonator length: $L_2 = 11.4$ mm.

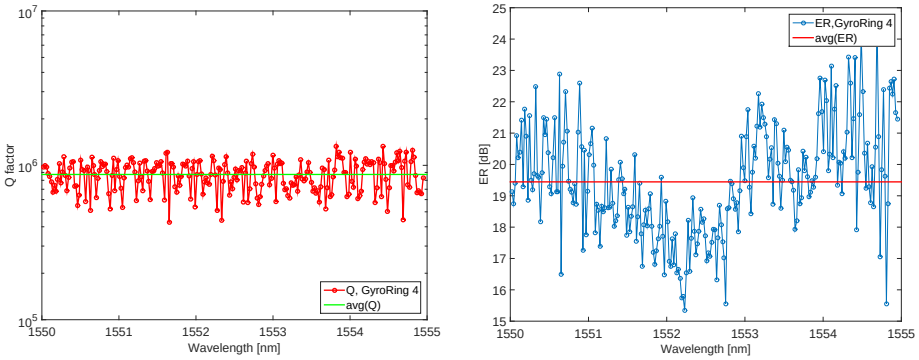

(a) Q factor

(b) ER

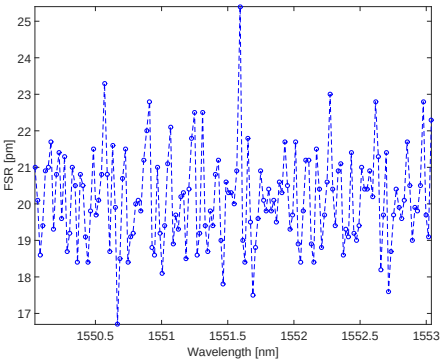

(c) FSR

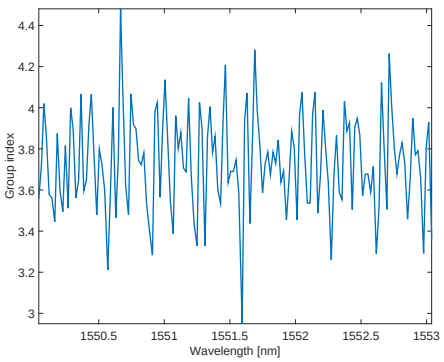

(d) Group index

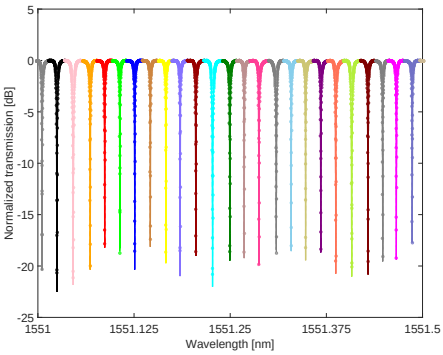

(e) Curve fits

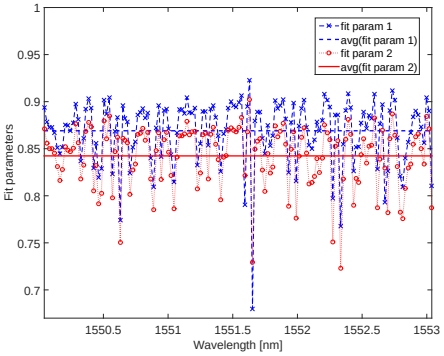

(f) Fit parameters

Figure 3.64: Figures of merit for a 32.1 mm-long resonator fabricated using e-beam lithography. **(a)** Q factor, **(b)** ER, **(c)** FSR, and **(d)** group index. **(e)** Curve fits for various resonance troughs. **(f)** Curve fit parameters.

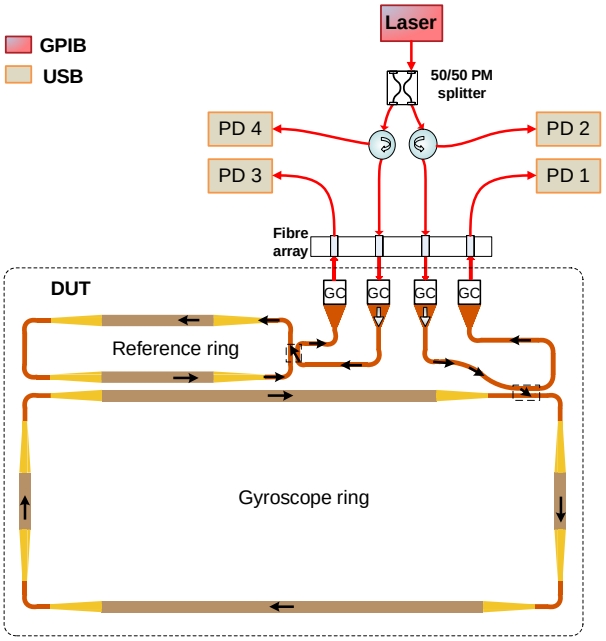

Figure 3.65: Experimental block diagram for a dual resonator system.

Figure 3.67 compares the PSD plots for time-domain signals recorded with the microscope light on and off, for the forward- and backward-propagating signals for the 32 mm-long gyro resonator. The trends shown by these plots are consistent with the SNR readings. Measurements for both rings off-resonance followed, to determine whether there was correlation between the signals of both rings. The cross-correlation of the forward-propagating signals for both resonators was 0.92 and 0.82, with the microscope light on and off, respectively. This indicated that the sources of noise for these rings were strongly correlated, and that the microscope light was a common-mode noise source, and should be turned off during experiments. The high cross-correlation also indicated that the use of a reference ring could help ameliorate the quality of the signal reading.

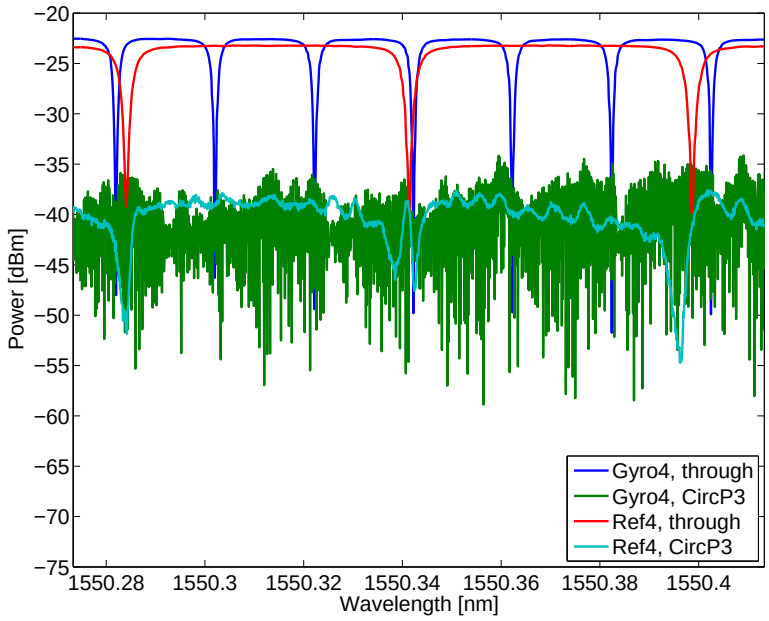

Figure 3.66: Spectra for the forward- and back-propagating signals of a dual resonator device. $L_1 \approx 32$ mm, $L_2 \approx 12$ mm. For both resonators, the back-propagating signals are ~ 15 dB weaker than the forward-propagating signals.

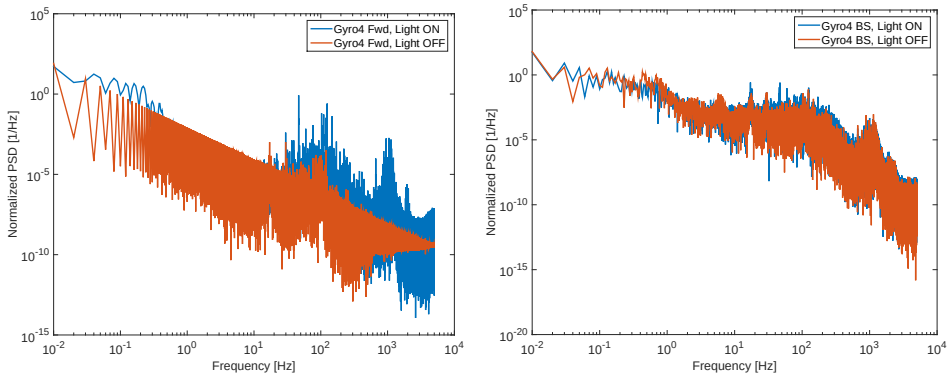

(a) Forward-propagating (b) Back-propagating

Figure 3.67: Normalized power spectral density comparison with microscope light on and off, for (a) forward-propagating and (b) back-propagating signals in a 32 mm-long gyro resonator.

Fibre Array Attachment and Dynamic Tests

Figure 3.68 shows the block diagram for the rotational experiments. A voltage signal proportional to the turntable speed was monitored via the FPGA FIFO. An external photodetector was also monitored via the FPGA FIFO to measure any backscattering from the main 50/50 splitter.

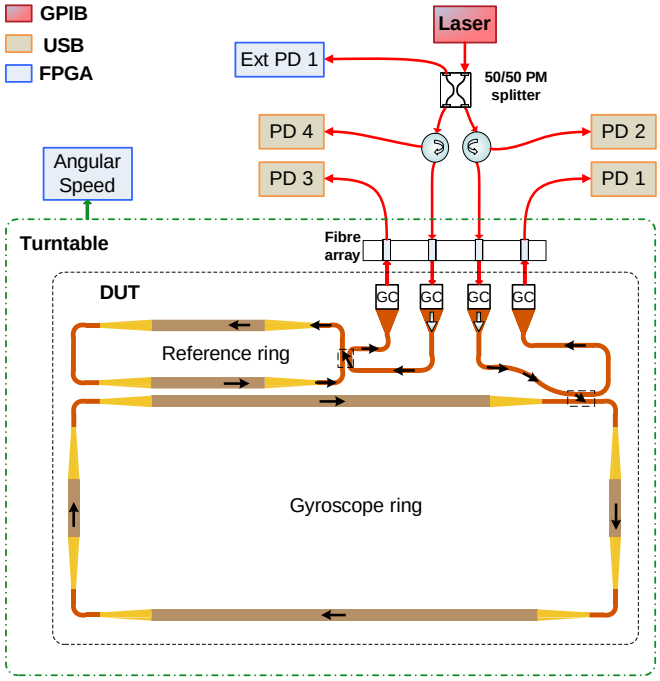

Figure 3.68: Experimental block diagram for rotational tests a dual resonator system.

The chip was held with vacuum, and optimal alignment coordinates were recorded using the LabVIEW^{TM} positioning VI. The fibre array was raised so as to allow for deposition of low shrinkage UV-curable adhesive (Dymax 4-20418 [41]), then returned to its original optimal position. The adhesive was cured in various cycles of progressive duration, as previously described in Subsection 3.3.4. The vacuum pump was turned off after curing. Figure 3.69 shows spectra for forward- and backward-propagating signals before and after fibre array attachment. An increase in the power of the backward-

propagating signals was observed (cf. IL ≈ -35 dB without adhesive to IL ≈ -25 dB with cured adhesive).

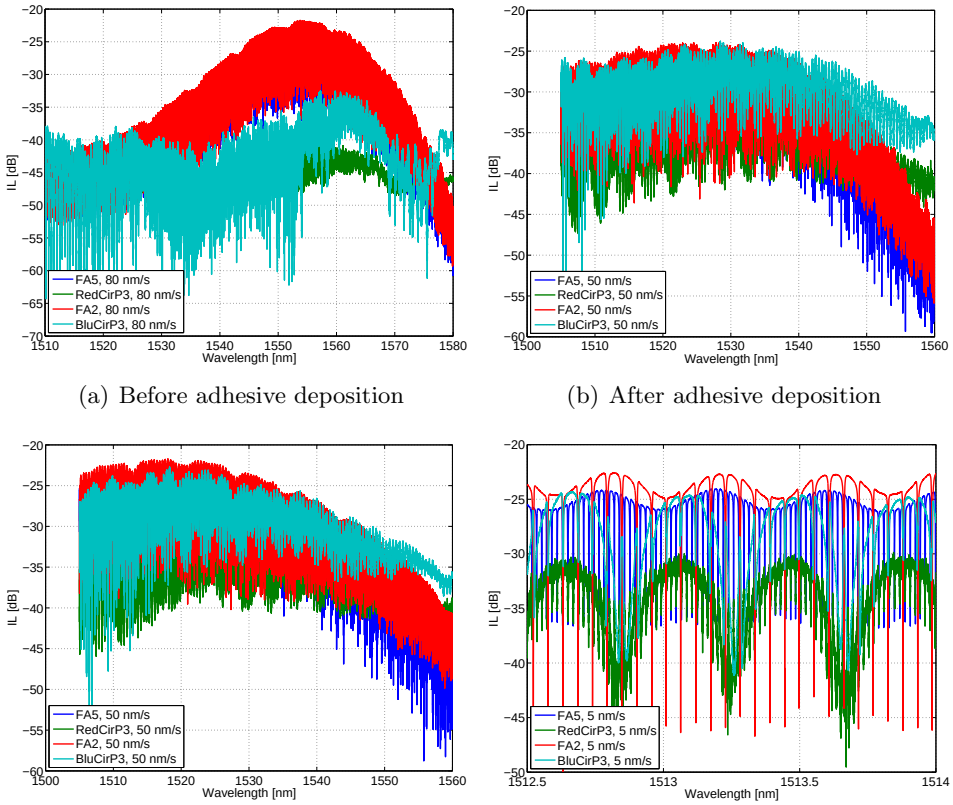

(a) Before adhesive deposition

(b) After adhesive deposition

(c) After curing

(d) After curing, zoom-in

Figure 3.69: Gyro and reference resonator spectra of forward- and back-propagating signals. **(a)** Before adhesive deposition. **(b)** After adhesive deposition, before curing. **(c)** After adhesive curing. **(d)** Narrow-range sweep after adhesive curing.

In this iteration I decided not to re-adjust the pitch angle, to ensure optimal alignment when lowering the array back to its original position. This produced a blue shift in the working wavelenths, (cf. Figs. 3.69(a) and 3.69(b)). One can see that the power of the back-propagating signals became comparable to those of the forward-propagating signals after adhesive deposition. Figures 3.69(c) and 3.69(d) show, respectively, wide- and narrow-

range spectra after adhesive curing. The IL of the forward-propagating signals is approximately the same before and after fibre attachment.

Subsequent spectral sweeps after fibre attachment showed no variation of the spectra at input power levels between −13 dBm and 3 dBm, as shown in Fig. 3.70(a). Figure 3.70(b) shows a narrow spectral sweep at rest, with $P_{\text{in}} = 0$ dBm, for wavelength selection prior to a rotational test. For clarity, only the forward-propagating signal of each resonator is shown.

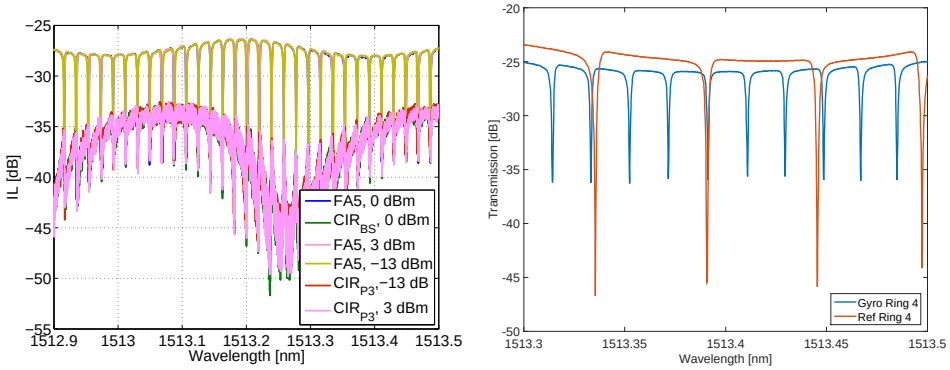

(a) (b)

Figure 3.70: **(a)** Spectra for the forward- and backward-propagating signals of a 32 mm-long gyro resonator at various input power levels, after fibre attachment. **(b)** Narrow spectral sweep of the forward-propagating signals for the same gyro resonator, and its reference ring.

The TLS was tuned to a wavelength $\lambda = 1513.3805$ nm with $P_{\text{in}} = 0$ dBm. The SNR at rest for the forward- and backward-propagating signals of the gyro resonator were, respectively, 8.68 dB and 6.54 dB. The turntable was rotated sinusoidally with a maximum angular speed $\Omega = 20$ dps at a frequency $f_{\text{in}} = 0.5$ Hz. Figure 3.71(a) compares the normalized turntable angular speed to the unfiltered normalized optical signal of the gyro resonator. A delay of ~ 1 s between the signals is due to the asynchronous acquisition times of the FPGA FIFO and the photodetector LabVIEW$^{\text{TM}}$ VIs. Fig. 3.71(b) shows the PSDs of these two normalized signals, where one can see the optical signal has considerable high-frequency noise. Based on these PSDs, we chose to use a low-pass filtering scheme to eliminate noise in

the optical signal at frequencies above the dominant frequency components of the turntable signal. A 6th order Butterworth low-pass filter (LPF) with a 5 Hz cutoff frequency was implemented for this purpose.

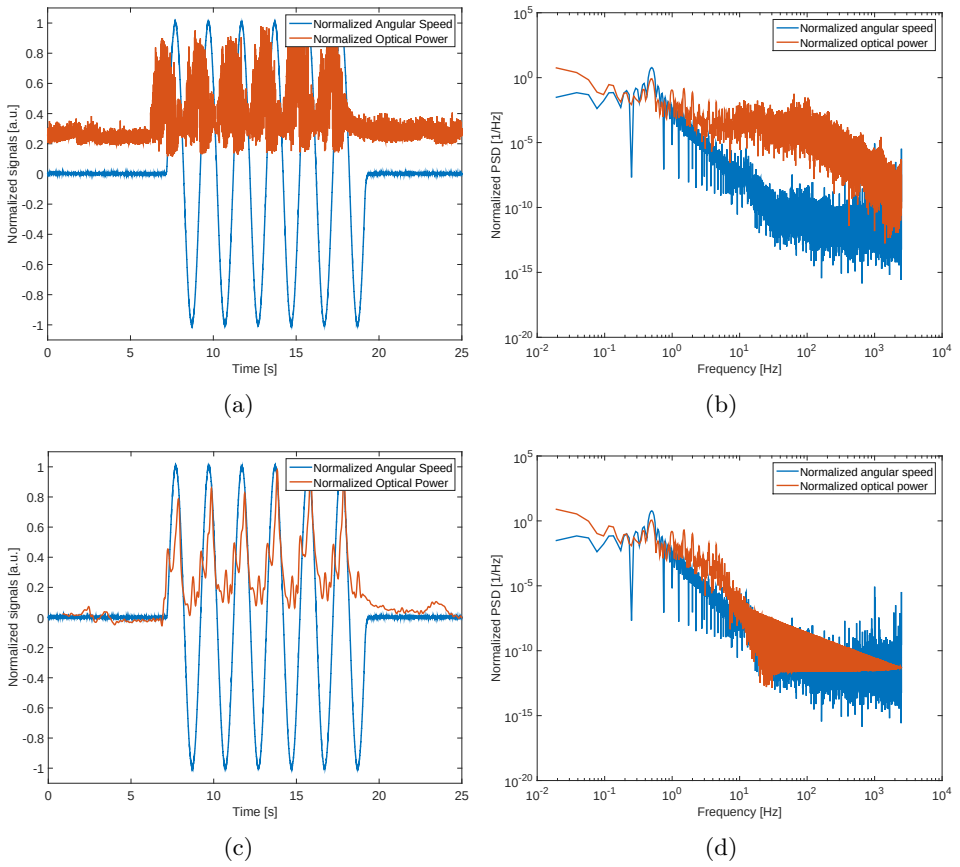

Figure 3.71: Comparison of normalized time-domain signals and their PSD plots. Time-domain plots **(a)** and PSDs **(b)** for the angular speed and the unfiltered optical power signal. Time-domain plots **(c)** and PSDs **(d)** for the angular speed and the filtered and shifted optical power signal.

The cross-correlation of the time-domain signals was obtained to determine the time delay between them ($\Delta t = 0.9$ s), and shift the filtered signals accordingly in Fig. 3.71(c). Figure 3.71(d) compares the PSDs of the turntable and the filtered optical signal. According to our theoretical

calculations (2.4.5), the optical signal variation is too large to be due solely to a Sagnac phase shift. Therefore, vibration and stress have a significant influence on the optical amplitude variation, despite the fibre array attachment.

3.5.4 Effects of Backscattering

As exemplified in Figs. 3.48 and 3.64, in our measurements we observed that the Q factor and the ER of our device spectra changed considerably as the wavelength was varied. As shown in Fig. 3.72, for devices with splitting/merging couplers, we observed that the mixed-through port had a non-zero transmission at rest, which exhibited resonances coinciding with those of the return signal at the input port. As shown in Fig. 3.73, the return signal in these devices also showed considerable variation in its Q factor and ER. This motivated us to develop a distributed backscattering model for our resonators.

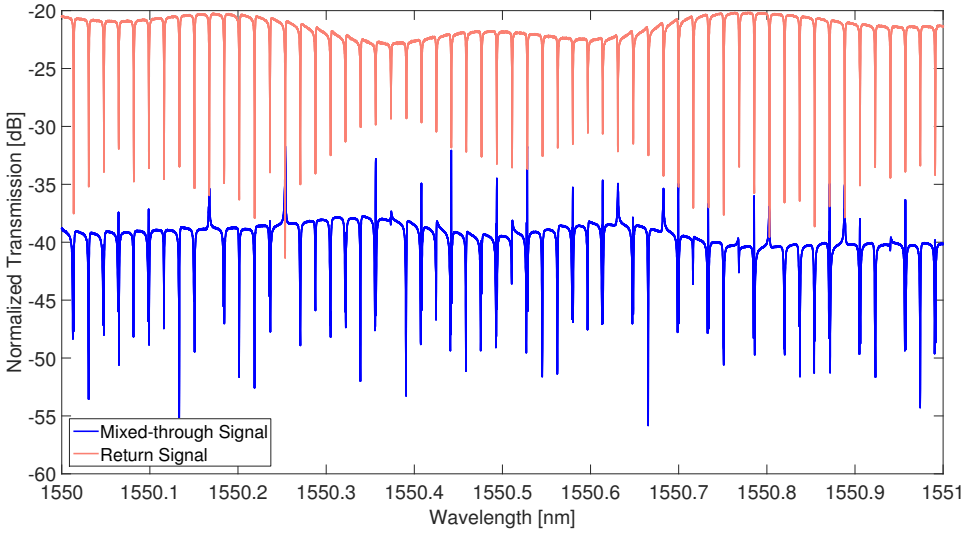

Figure 3.72: Measured wavelength spectra for the return signal (top, pink) and mixed-through signal (bottom, blue) of a device with a 37 mm-long resonator.

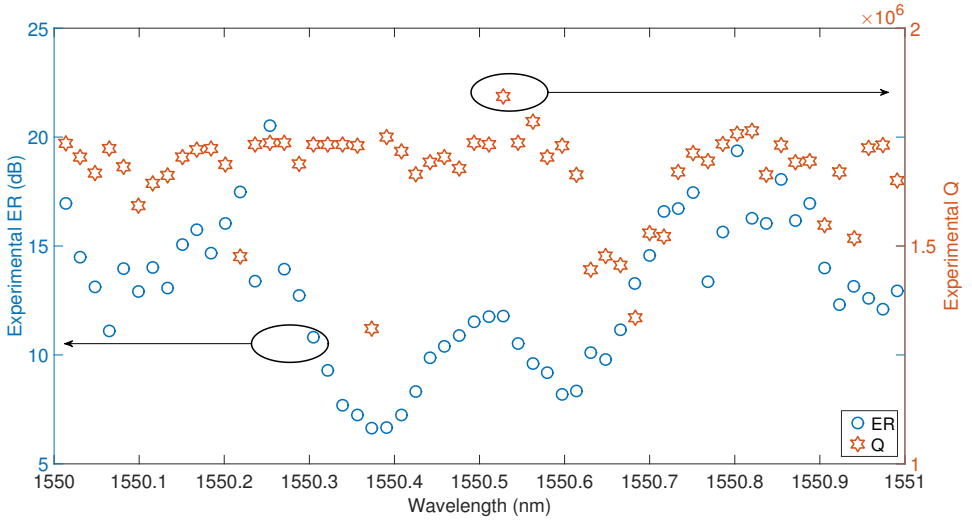

Figure 3.73: Q factor and ER as functions of wavelength for the return signal spectrum of Fig. 3.72.

Figure 3.74 shows a schematic of the reflection that occurs in a waveguide segment of length Δz with a backscattering per unit length b and forward transmission $f = \sqrt{1-(b\Delta z)^2}$. The backscattering coefficient at each point is considered to be a random complex number, $b = \widetilde{b}(z)e^{j\widetilde{\theta}(z)}$, with amplitude $\widetilde{b}(z)$ normally distributed with mean 0 and root mean square magnitude $\sigma_{\widetilde{b}}(z)$, and with a phase $\widetilde{\theta}(z)$ equal to 0 or π with equal probability. In our model, we estimate that the backscattering coefficient ratio between SMWGs and MMWGs is the same as their propagation loss ratio, since both arise from scattering. Based on this model, the electric fields shown in Fig. 3.74 are related by the matrix equation:

$$\begin{bmatrix} E^+(z+\Delta z) \\ E^-(z) \end{bmatrix} = B \begin{bmatrix} E^+(z) \\ E^-(z+\Delta z) \end{bmatrix}, \tag{3.28}$$

where the matrix B is defined by:

$$B = \begin{bmatrix} fe^{-jk^+\Delta z} & b\Delta z e^{-j(\frac{k^+ + k^-}{2})\Delta z} \\ -b^*\Delta z e^{-j(\frac{k^+ + k^-}{2})\Delta z} & f^* e^{-jk^-\Delta z} \end{bmatrix}, \tag{3.29}$$

where $k^{\pm} = 2\pi n_{\text{eff}}(\lambda, z)/\lambda - j\alpha(z) \pm \Phi_S/L$, $n_{\text{eff}}(\lambda, z)$ is the effective index, and $\alpha(z)$ is the field loss coefficient. At rest, $k^+ = k^- = k = 2\pi n_{\text{eff}}(\lambda, z)/\lambda - j\alpha(z)$. By re-arranging Eq. (3.28) and taking the limit as Δz goes to zero, we have:

$$\frac{\partial}{\partial z}\begin{bmatrix} E^+(z) \\ E^-(z) \end{bmatrix} = P(z)\begin{bmatrix} E^+(z) \\ E^-(z) \end{bmatrix}, \tag{3.30}$$

where the propagation matrix, $P(z)$, is given by:

$$P(z) = -j\begin{bmatrix} k^+ & jb \\ jb^* & -k^- \end{bmatrix}\begin{bmatrix} E^+(z) \\ E^-(z) \end{bmatrix}. \tag{3.31}$$

For a z range starting at z_0 over which $P(z)$ is constant, the solution to Eq. (3.30) is given by:

$$\begin{bmatrix} E^+(z) \\ E^-(z) \end{bmatrix} = e^{(z-z_0)\cdot P(z)}\begin{bmatrix} E^+(z_0) \\ E^-(z_0) \end{bmatrix}. \tag{3.32}$$

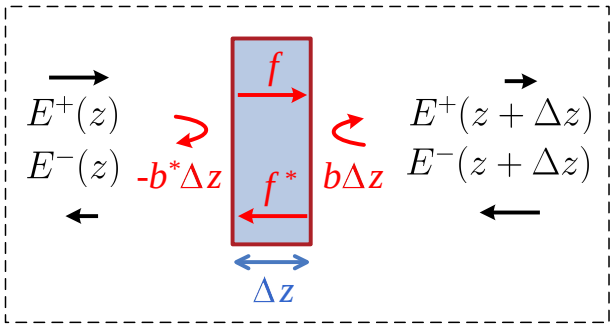

Figure 3.74: Backscattering model schematic.

By dividing the resonator of length L shown in Fig. 3.75 into N segments and letting $N \to \infty$ so that each segment is considered to have a constant propagation matrix, using Eq. (3.32) we have:

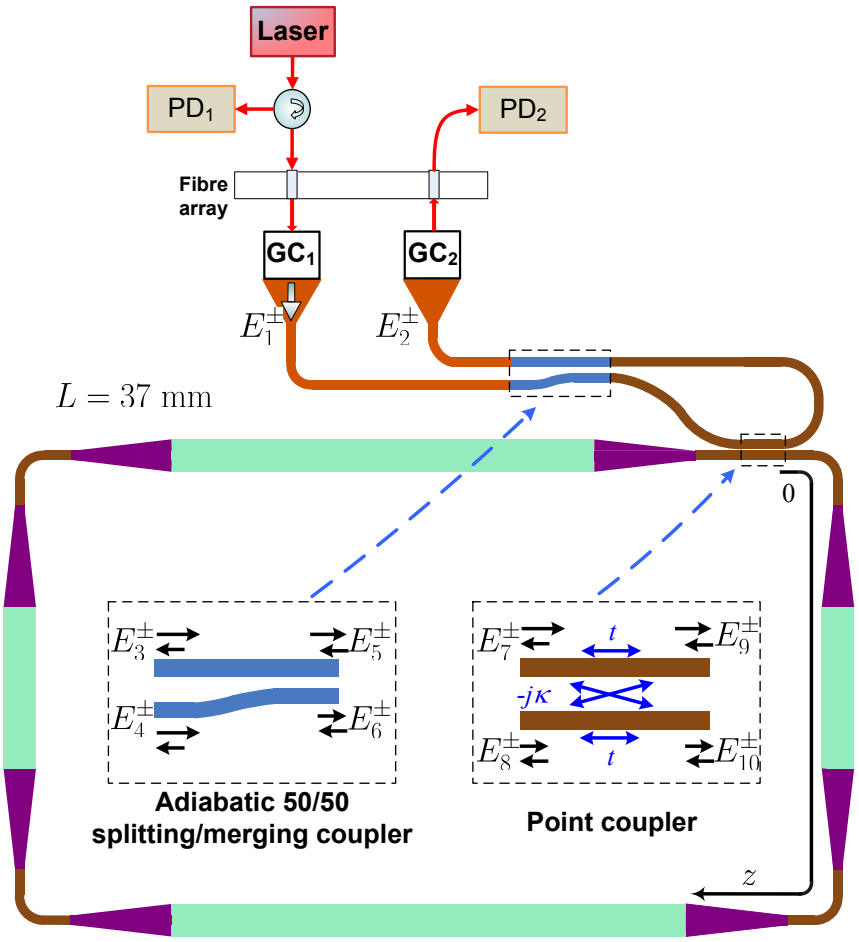

Figure 3.75: Schematic of resonator formed by rib SMWGs (brown), rib MMWGs (cyan), and linear SM to MM converters (purple). The total resonator length is 37 mm. The variable z denotes the position along the length of the ring, starting at the point coupler. Left inset: Adiabatic splitting/merging coupler, formed by strip (orange) and rib (blue) waveguides. Right inset: Point coupler model.

$$\begin{bmatrix} E_8^+ \\ E_8^- \end{bmatrix} = X \begin{bmatrix} E_{10}^+ \\ E_{10}^- \end{bmatrix}, \tag{3.33}$$

where the matrix X is given by:

$$X = \lim_{N\to\infty}\left[\prod_{m=0}^{N-1}\exp\left\{\frac{L}{N}\cdot P\left(\frac{mL}{N}\right)\right\}\right] \tag{3.34}$$

In Eq. 3.34 $P(\frac{mL}{N})$ is the propagation matrix of the m^{th} segment and the product of matrix exponentials is evaluated from right to left with increasing m. For computational simplicity, the horizontal and vertical MMWGs were divided into 3500 and 4900 segments, respectively. The SMWGs and their tapers were divided into 700 segments. The number of segments was chosen using convergence testing.

The matrix equations governing the electric fields on the way in and on the way out of an ideal adiabatic splitting/merging coupler are, as referred to the insets of Fig. 3.75:

$$\begin{bmatrix}E_5^+\\E_6^+\end{bmatrix} = \frac{1}{\sqrt{2}}\begin{bmatrix}1 & 1\\-1 & 1\end{bmatrix}\begin{bmatrix}E_3^+\\E_4^+\end{bmatrix} = M\begin{bmatrix}E_3^+\\E_4^+\end{bmatrix} \tag{3.35}$$

$$\begin{bmatrix}E_3^-\\E_4^-\end{bmatrix} = \frac{1}{\sqrt{2}}\begin{bmatrix}1 & -1\\1 & 1\end{bmatrix}\begin{bmatrix}E_5^-\\E_6^-\end{bmatrix} = M^{-1}\begin{bmatrix}E_5^-\\E_6^-\end{bmatrix} \tag{3.36}$$

The fields at the point coupler are related by:

$$\begin{bmatrix}E_7^-\\E_8^-\end{bmatrix} = \begin{bmatrix}t & -j\kappa\\-j\kappa & t\end{bmatrix}\begin{bmatrix}E_9^-\\E_{10}^-\end{bmatrix} = K\begin{bmatrix}E_9^-\\E_{10}^-\end{bmatrix} \tag{3.37}$$

$$\begin{bmatrix}E_9^+\\E_{10}^+\end{bmatrix} = K\begin{bmatrix}E_7^+\\E_8^+\end{bmatrix}, \tag{3.38}$$

where t and κ are real numbers and represent, respectively, the magnitudes of the field through-coupling and the field cross-coupling. Assuming that the coupler is lossless, $\kappa^2 + t^2 = 1$.

Based on Eqs. (3.28) through (3.38), E_7 and E_9 are related by:

$$\begin{bmatrix} E_7^- \\ E_9^+ \end{bmatrix} = A \begin{bmatrix} E_7^+ \\ E_9^- \end{bmatrix} \tag{3.39}$$

where:

$$A = \begin{bmatrix} -\kappa^2(W_{21}^{-1}X_{11} + W_{22}^{-1}X_{21}) & t + \kappa^2 W_{22}^{-1} \\ t - \kappa^2\left(W_{11}^{-1}X_{11} + W_{12}^{-1}X_{21}\right) & \kappa^2 W_{12}^{-1} \end{bmatrix} \tag{3.40}$$

The fields entering and leaving the device are thus related by:

$$\begin{bmatrix} E_1^- \\ E_2^- \end{bmatrix} = \Phi_{\text{str}} M^{-1} \Phi_{\text{rib}} A \Phi_{\text{rib}} M \Phi_{\text{str}} \begin{bmatrix} E_1^+ \\ E_2^+ \end{bmatrix}. \tag{3.41}$$

where Φ_{str} and Φ_{rib} are matrices that represent, respectively, the phase shifts undergone by travelling through the strip and rib routing waveguides of the splitting/merging coupler (see Fig. 3.30(a)), and are given by:

$$\Phi_{\text{str,rib}} = \begin{bmatrix} e^{-jk_{\text{str,rib}}L_{r1,r4}} & 0 \\ 0 & e^{-jk_{\text{str,rib}}L_{r2,r3}} \end{bmatrix}, \tag{3.42}$$

where $k_{\text{str}} = 2\pi n_{\text{eff str}}/\lambda - j\alpha_{\text{str}}$ and $k_{\text{rib}} = 2\pi n_{\text{eff rib}}/\lambda - j\alpha_{\text{rib}}$ are, respectively, the strip and rib SMWG propagation constants, L_{r1} and L_{r2} are, respectively, the lengths of the strip SMWGs routing the grating couplers GC_1 and GC_2 to the adiabatic coupler, and L_{r3} and L_{r4} are the lengths of the bottom and top segments of the rib SMWG loop.

As described in Subsection 3.4.1, theoretical estimations of the effective indices of the SMWGs and MMWGs of these devices were carried out using MODE Solutions$^{\text{TM}}$ eigenmode solver. The field propagation loss values used in our model for the SMWGs and the MMWGs were, respectively, $\alpha_{\text{SM}} = 34.5\ \text{m}^{-1}$ and $\alpha_{\text{MM}} = 1\ \text{m}^{-1}$, in agreement with previously reported experimental results [9, 15, 56, 78].

For our initial simulations, we used a SMWG backscattering value of $\sigma_{\widetilde{b}_{\text{SM}}} = 5.8\ \text{mm}^{-1}$, estimated based on [89, 92]. However, as shown in Fig. 3.80, our simulation results showed a greater agreement with the measured

spectra for $\sigma_{\widetilde{b}_{\mathrm{SM}}} = 18\ \mathrm{mm}^{-1}$ and $\sigma_{\widetilde{b}_{\mathrm{MM}}} = 0.522\ \mathrm{mm}^{-1}$. The values of $n_{\mathrm{eff}}(\lambda, z)$, $\alpha(z)$, and $\sigma_{\widetilde{b}}(z)$ for the waveguide tapers were obtained by linearly interpolating between the SMWG and the MMWG values.

Unbalanced Adiabatic Couplers

As shown in Fig. 3.79, the simulated spectra obtained assuming an ideal 50%/50% power splitting ratio at the adiabatic coupler showed non-zero signals in the mixed-through port due to backscattering, but did not resemble the measured spectra. Thus, we investigated the effects of non-ideal power splitting ratio values in the adiabatic coupler, by generalizing its matrix as:

$$M(T_{\mathrm{ac}}) = \begin{bmatrix} \sqrt{T_{\mathrm{ac}}} & \sqrt{1-T_{\mathrm{ac}}} \\ -\sqrt{1-T_{\mathrm{ac}}} & \sqrt{T_{\mathrm{ac}}} \end{bmatrix}, \tag{3.43}$$

where $T_{\mathrm{ac}}/(1-T_{\mathrm{ac}})$ is the power splitting ratio. At this stage in the model, the phase relationships between the ports of the adiabatic coupler are still considered ideal.

Directional Coupler Imperfections

Figure 3.76 shows the schematic of a waveguide directional coupler with reflections. For clarity, Fig. 3.76 only depicts the propagation directions and corresponding S parameter coefficients for the case $E_7^+ = 1$. After algebraic manipulation, the equation governing this subcomponent is, according to the transfer matrix (T-matrix) formalism [51]:

$$\begin{bmatrix} E_7^- \\ E_9^+ \\ E_8^- \\ E_{10}^+ \end{bmatrix} = \begin{bmatrix} \epsilon & -j\gamma & t & -j\kappa \\ t & -j\kappa & \epsilon & -j\gamma \\ -j\gamma & \epsilon & -j\kappa & t \\ -j\kappa & t & -j\gamma & \epsilon \end{bmatrix} \begin{bmatrix} E_7^+ \\ E_8^+ \\ E_9^- \\ E_{10}^- \end{bmatrix} = D \begin{bmatrix} E_7^+ \\ E_8^+ \\ E_9^- \\ E_{10}^- \end{bmatrix} \tag{3.44}$$

In order to ensure this point coupler is passive and power-conserving, D must be unitary. Thus, assuming real values for t and κ, the following restrictions

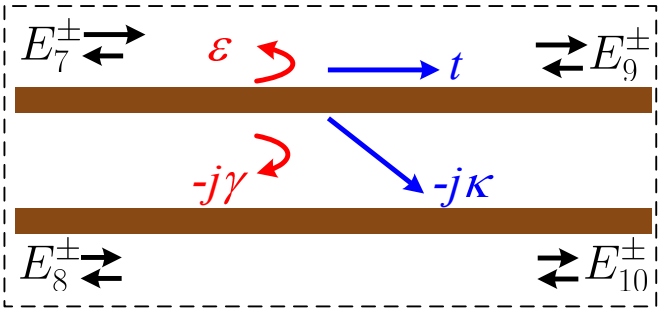

Figure 3.76: Point coupler with straight through transmission t, cross-coupling κ, back-reflection ϵ, and contra-directional coupling γ.

apply:

$$t, \kappa, \gamma, \epsilon \in \mathbb{R} \tag{3.45}$$

$$t^2 + \kappa^2 + \gamma^2 + \epsilon^2 = 1 \tag{3.46}$$

$$\kappa = \sqrt{\frac{1 - \gamma^2 - t^2}{1 + (\gamma/t)^2}} \tag{3.47}$$

$$\epsilon = \kappa\gamma/t \tag{3.48}$$

In order to determine the theoretical values of the return loss (RL) and the contra-directional coupling S parameters in various WDCs, finite-difference, time-domain simulations were carried out using FDTD Solutions$^{\text{TM}}$. According to our simulations, as-designed directional couplers with 7 µm-long parallel waveguides show theoretical RL values on the order of −48 dB. In contrast, the measured RL levels are on the order of −20 dB. However, one must note that the experimental results also include the grating coupler RL, which cannot be separated from the directional coupler RL. After S parameter obtention, the WDC phase shift contribution was neglected in the rest of the model (i.e., the WDCs were treated as point couplers).

Measurements vs. Simulations

For all the simulation results shown in this section, $E_1^+ = 1$ and $E_2^+ = 0$, and all of the results shown will be referred to a device consistent with that shown in Fig. 3.75, with a 37 mm-long resonator, unless explicitly stated otherwise. Figure 3.77 shows normalized measured spectra for the mixed-through and the return port for the DUT. The data used to generate this plot is the same used to create Fig. 3.72. However, the wavelength range has been restricted to clearly show some features of the mixed-through port spectrum, such as lobe skew and near-resonance spikes.

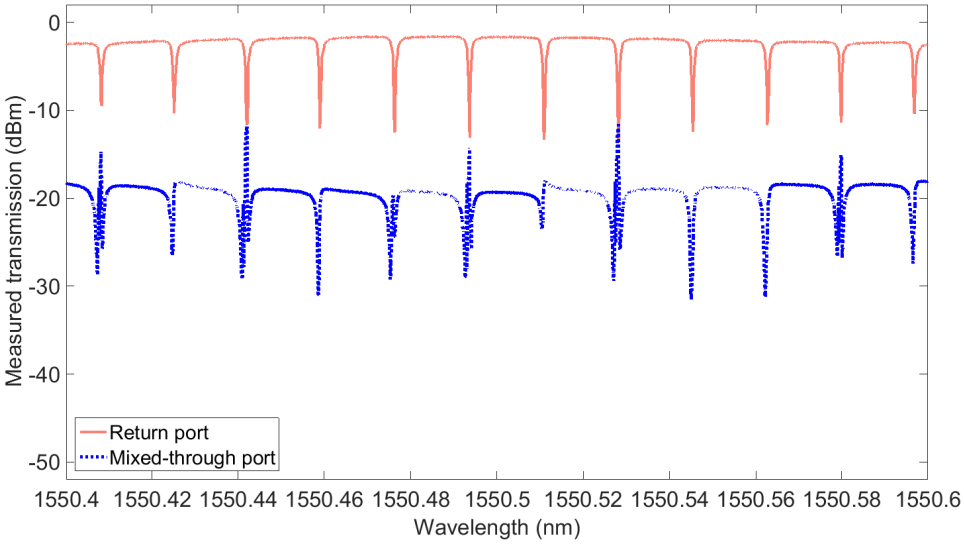

Figure 3.77: Normalized measured spectra for the DUT.

Figure 3.78 shows the theoretical spectra for a DUT with $t = 0.938$, $\Delta\lambda = 0.1$ pm, perfect adiabatic and point couplers, and a backscatter-free ring, i.e., $T_{\text{ac}} = 0.5$, $\sigma_{\tilde{b}_{\text{SM}}} = \sigma_{\tilde{b}_{\text{MM}}} = 0\,\text{mm}^{-1}$, $\gamma = 0$. The slight ER variations are due to the minimum wavelength step of our laser, $\Delta\lambda = 0.1$ pm.

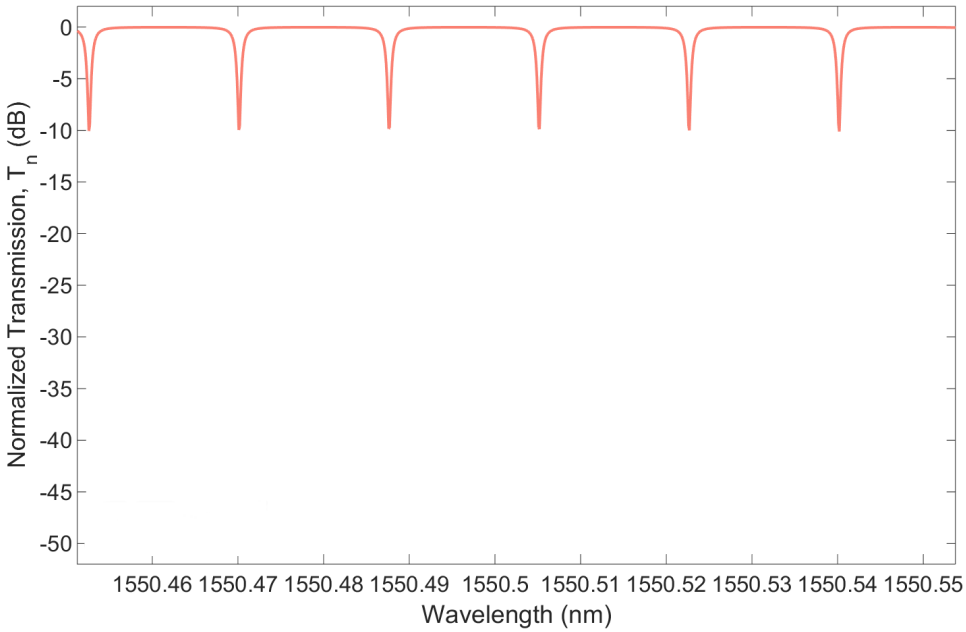

Figure 3.78: Simulated spectra with $\Delta\lambda = 0.1$ pm for a DUT with a backscatter-free ring and a perfect adiabatic coupler.

Figure 3.79 shows simulation results for a DUT with $T_{\text{ac}} = 0.5$, $t = 0.905$, $\sigma_{\tilde{b}_{\text{SM}}} = 5.8$ mm^{-1}, $\gamma = 0$, and $\Delta\lambda = 0.2$ pm. The noticeable ER variations in the return signal are in this case due to both backscattering and the non-zero value of $\Delta\lambda$. A non-zero mixed-through signal is observed due to backscattering. However, there is no resemblance of the simulated signal to its experimental counterpart. Therefore, simulations for adiabatic couplers with various non-ideal splitting ratios were investigated until a close match between the experimental and theoretical spectral baselines was found. Several simulations with various levels of backscattering were performed until the spectral features of our simulations resembled the phenomena observed in our measurements. The variations of Q and ER in our model are greater for higher backscattering levels. Since each backscattering profile is random, it is practically impossible to perfectly recreate all the spectral features of our measurements in one simulation. Rather, phenomenological resemblances can be observed in each of many simulations created using the same

parameters. Several simulations were performed and showed resemblances to the measured spectra, such as skewed lobes and resonance spikes instead of troughs. However, for the sake of briefness, only selected plots have been included in the document. Simulations to investigate the impact of greater reflections at the point coupler were performed. According to our simulations, γ should not exceed $\gamma_{\max} = 0.3$, to ensure that the Q and ER value ranges of the simulations resemble those of our experiments.

Figure 3.80 shows simulation results for a 57%/43% splitting ratio, $\sigma_{\widetilde{b}_{\mathrm{SM}}} = 18\ \mathrm{mm}^{-1}$, $t = 0.905$, and $\gamma = 0$. Figure 3.81 shows simulation results for the same parameters, except for $t = 0.932$, and $\gamma = 0.1$, whereas Fig. 3.82 shows simulation results for the same parameters, except for $t = 0.938$, and $\gamma = 0.1$. One can see resemblances between the baseline ratios and near-resonance spikes when comparing the measured spectra to each simulation. Figure 3.83(a) compares the forward- and backward-propagating output signals for the same ring backscattering profile used to create Fig. 3.82, i.e., it compares the signals exiting the ring for $E_7^+ = 1,\ E_9^- = 0$ and for $E_7^+ = 0,\ E_9^- = 1$ (see Eq. (3.39)). Figure 3.83(b) shows the output spectra in the CW and the CCW directions for the same ring, for a unit-magnitude input evenly split and simultaneously injected in both directions of the ring (hence the -3 dB baselines). Although the effects of $\gamma \neq 0$ are very noticeable when comparing the output spectra for CW- and CCW-propagating signals in the resonator alone (Fig. 3.83(a)), according to our simulations the impact of this parameter is not as significant on the spectrum of the full device, except for the need to adjust the value of t to match port baseline levels and to ensure sensible values of Q and ER. Figures 3.84(a) and 3.84(b) compare the measured values of Q and ER with those obtained in various simulations with different parameter values and random backscattering patterns.

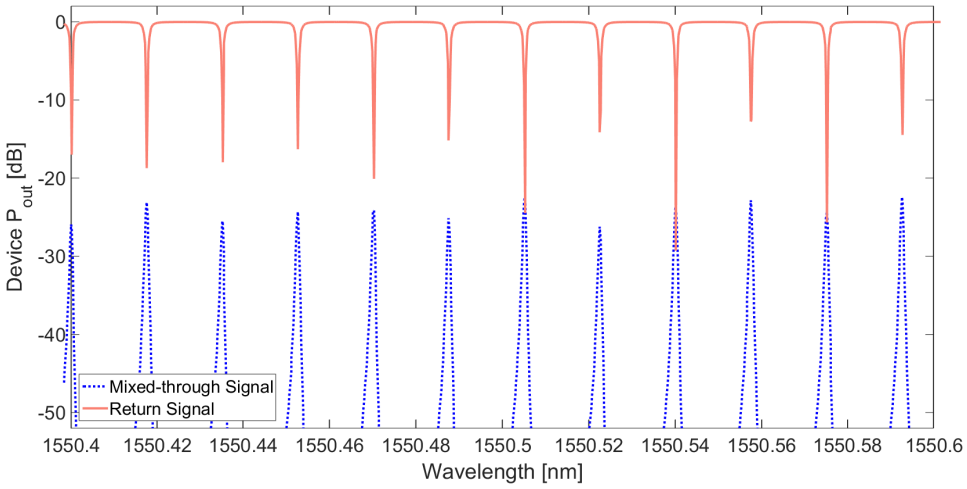

Figure 3.79: Theoretical spectra for a DUT with $T_{\text{ac}} = 0.5$, $t = 0.905$, $\sigma_{\tilde{b}_{\text{SM}}} = 5.8$ mm^{-1}, $\sigma_{\tilde{b}_{\text{MM}}} = 0.084$ mm^{-1}, $\gamma = 0$, and $\Delta\lambda = 0.2$ pm.

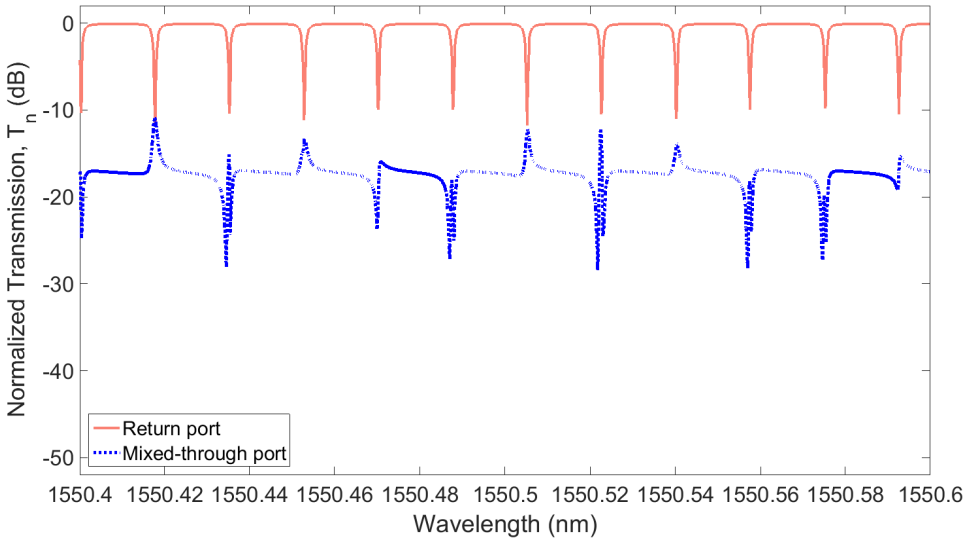

Figure 3.80: Theoretical spectra for a DUT with $T_{\text{ac}} = 0.57$, $t = 0.905$, $\sigma_{\tilde{b}_{\text{SM}}} = 18$ mm^{-1}, $\sigma_{\tilde{b}_{\text{MM}}} = 0.522$ mm^{-1}, $\gamma = 0$, and $\Delta\lambda = 0.1$ pm.

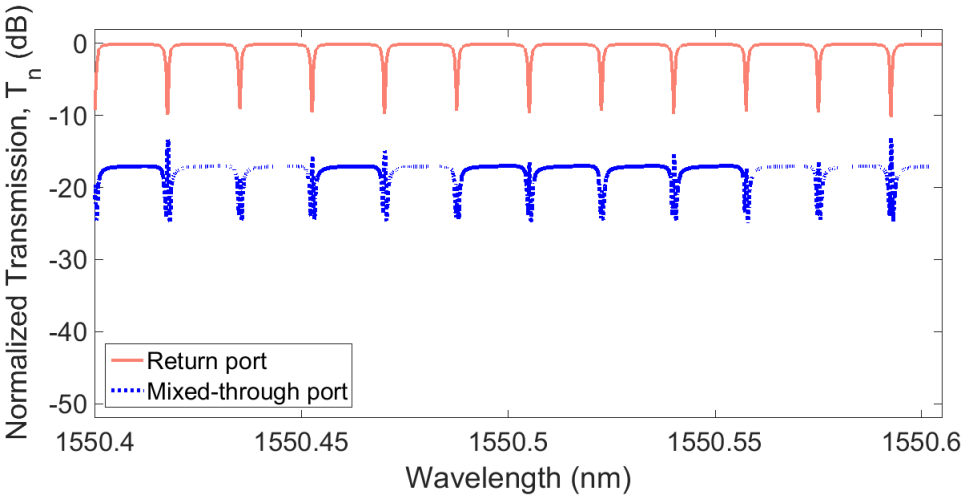

Figure 3.81: Theoretical spectra for a DUT with $T_{\text{ac}} = 0.57$, $t = 0.932$, $\sigma_{\widetilde{b}_{\text{SM}}} = 18$ mm^{-1}, $\sigma_{\widetilde{b}_{\text{MM}}} = 0.522$ mm^{-1}, $\gamma = 0.1$, and $\Delta\lambda = 0.1$ pm.

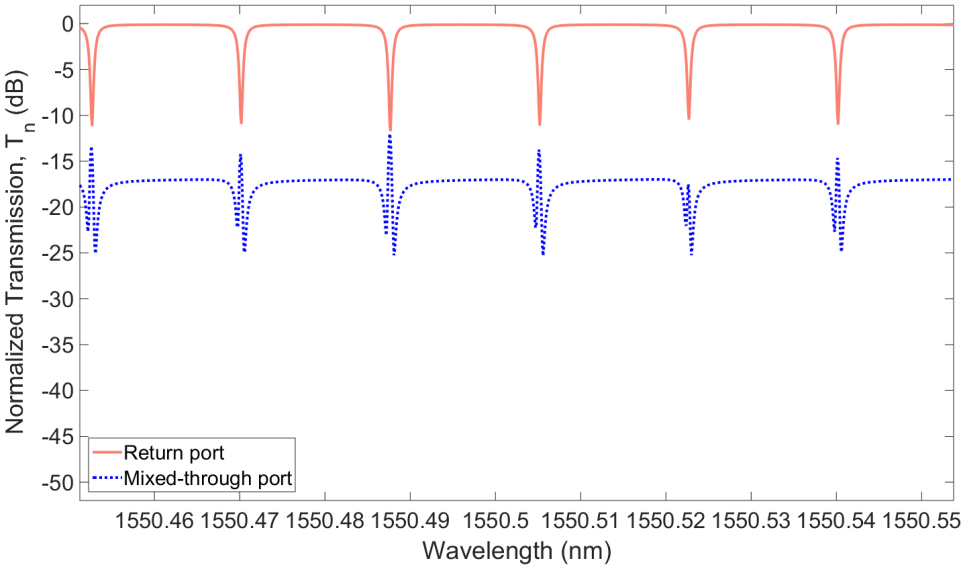

Figure 3.82: Simulated spectra for a DUT with $T_{\text{ac}} = 0.57$, $t = 0.938$, $\sigma_{\widetilde{b}\,\text{SM}}(z) = 18$ mm^{-1}, $\sigma_{\widetilde{b}\,\text{MM}}(z) = 0.522$ mm^{-1}, $\gamma = 0.1$, and $\Delta\lambda = 0.1$ pm.

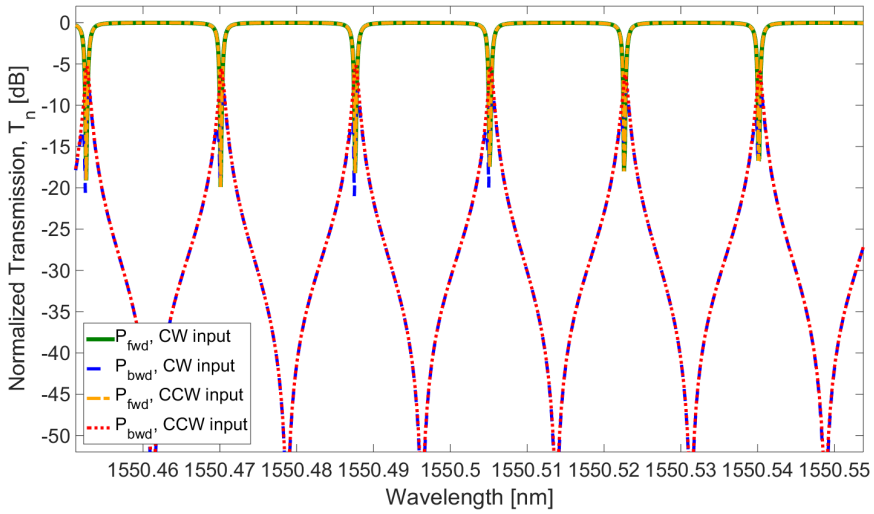

(a)

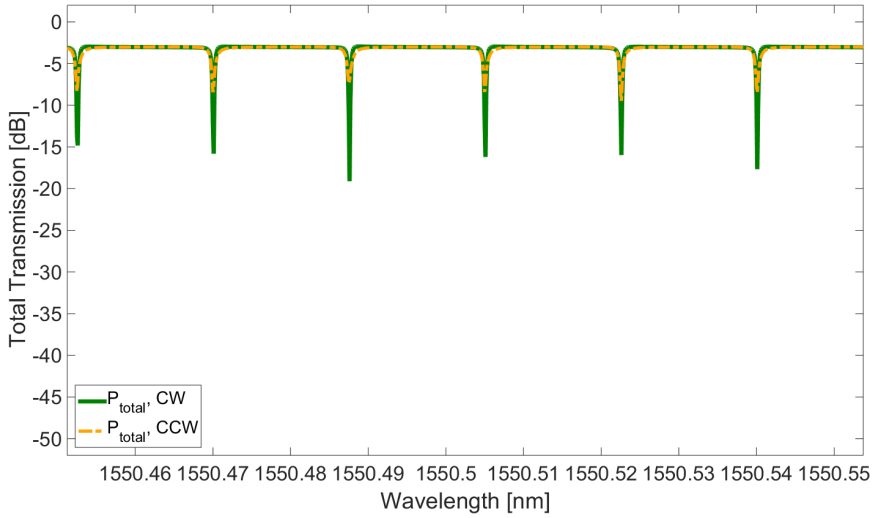

(b)

Figure 3.83: Theoretical spectra for a 37 mm-long ring resonator with $t = 0.938$, $\sigma_{\tilde{b}\,\mathrm{SM}}(z) = 18\ \mathrm{mm}^{-1}$, $\sigma_{\tilde{b}\,\mathrm{MM}}(z) = 0.522\ \mathrm{mm}^{-1}$, $\gamma = 0.1$, and $\Delta\lambda = 0.1$ pm. **(a)** Normalized transmitted power in forward- and backward-propagating directions for CW- and CCW-direction input beams. **(b)** Total output spectra in CW and CCW directions for simultaneous counter-propagation excitation. The power is referred to the total input power.

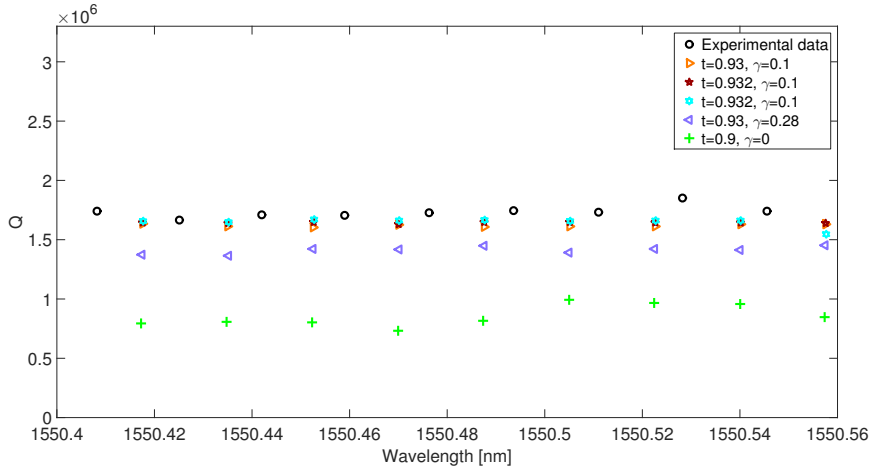

(a)

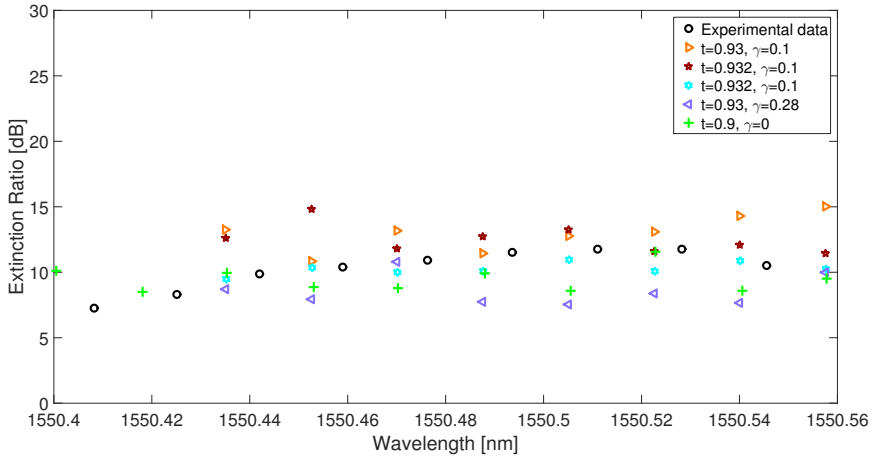

(b)

Figure 3.84: Comparison of measured values of **(a)** Q factor, and **(b)** ER with those obtained in various simulations. In all cases, $T_{\text{ac}} = 0.57$, $\sigma_{\widetilde{b}\,\text{SM}}(z) = 18\ \text{mm}^{-1}$, $\sigma_{\widetilde{b}\,\text{MM}}(z) = 0.522\ \text{mm}^{-1}$, and $\Delta\lambda = 0.1$ pm.

3.5.5 Iteration Challenges and Conclusions

The devices studied in this iteration consisted of two adjacent resonators. Both resonators combined SMWGs and MMWGs. Devices were fabricated at two facilities: IME and UW, using two-etch and single-etch fabrication

methods, respectively. Device spectra were obtained for devices from both fabrication batches. The devices fabricated at IME showed higher propagation losses due to fabrication-related issues. The devices with the best figures of merit belonged to the e-beam lithography batch. These devices were used for the remainder of the static and dynamic tests. The average ER and Q of these resonators were, respectively, ER $\sim$ 19 dB and $Q \sim 1 \times 10^6$. The estimation of the propagation loss for the strip MMWGs was $\alpha_{\mathrm{dB}} \sim 0.55$ dB/cm. Using Eq. (3.3) with $n_g \approx$ 3.8 at $\lambda_0 = 1.55$ µm, the average field and power attenuation values are $\alpha_{avg} \approx$ 0.0077 mm^{-1} and $\alpha_p \approx 0.0154$ mm^{-1}, respectively. As expected due to the use of e-beam lithography, the propagation losses are higher than in the previous iteration. Nevertheless, it was possible to achieve high quality factor values.

For the gyro devices fabricated during this iteration, the power of the backward-propagating signals increased approximately 10 dB after adhesive deposition and curing. Rotational tests were performed, and the normalized angular speed and optical signals were compared in the time- and frequency-domains. A filtering scheme (6th order Butterworth low-pass filter with a 5 Hz cutoff frequency) was implemented to eliminate high frequency noise.

Despite the significant improvements as regards mechanical actuation and fibre attachment (in comparison to our first rotary setup), the amplitude variations of the optical signals are still dominated by vibration and stress. These variations are still considerably greater than those due to the Sagnac effect.

In order to improve the readout and reduce backscattering effects [67, 71, 82], significant efforts were made to implement frequency tracking using the phase modulation techniques described in Section 2.5. Unfortunately, the available signal generators were unable to simultaneously produce ramp signals with the necessary amplitude and frequency values. Specifically, for our latest resonators, $Q \approx 1 \times 10^6$, thus FWHM$\approx$ 200 MHz. In order to produce the necessary frequency excursion $\Delta f \approx 100$ MHz between points B and C in Fig. 2.25, ramp signals must be generated with frequencies $f_1 \approx 100$ MHz and $2f_1 \approx 200$ MHz. The V_π voltage of the Thorlabs$^{\mathrm{TM}}$ LN65s-FC phase modulators intended for this purpose is $V_\pi = 4\ V$ [128].

Therefore, the required peak-to-peak ramp amplitude is $V_{\mathrm{pp}} = 8\ V$, i.e., the sawtooth root-mean-square (RMS) voltage is $V_{\mathrm{RMS}} = 4/\sqrt{3}$ V ≈ 2.3 V. Since the input impedance of these modulators is $R_{\mathrm{L}} = 50\ \Omega$, the driving power required is:

$$P_{\mathrm{dBm}} = 10 \log \left(\frac{V_{\mathrm{RMS}}^2 / R_{\mathrm{L}}}{1 \times 10^{-3}[W]} \right) = 20.3 \text{ dBm} \tag{3.49}$$

The fastest arbitrary waveform generator (AWG) available to me was a Fluke$^{\mathrm{TM}}$ 294. Although this instrument can generate signals with sufficient amplitudes, its maximum linear ramp frequency is 500 kHz [26], i.e., 400 times lower than the required maximum frequency. To overcome the power and bandwidth limitations faced when trying to implement serrodyne phase modulation techniques used in previous work [62, 118], sinusoidal modulation schemes are envisioned as part of future work.

A backscattering model has been developed to explain the non-zero signals detected at the output ports of our devices. Our simulations indicate that the appearance of signals at the mixed-through port is not only due to waveguide backscattering, but it is also due to an imperfect splitting ratio at the as-fabricated adiabatic couplers. Suitable value ranges for key parameters of various DUT subcomponents have been found, in order to phenomenologically match the simulations and the experimental data. Due to the stochastic nature of the backscattering profile distribution, each simulation run provides a unique case in which a combination of various spectral behaviours can be found. Our model shows that the variations of Q and ER are coupling-, backscattering-level-, and backscattering-profile-dependent, and that these variations are greater for increasing values of backscattering.

Chapter 4

Summary, Conclusions, and Suggestions for Future Work

4.1 Summary

In this thesis, we have reviewed the state of the art of passive optical gyroscopes, developed analytical models for design parameter optimization, and iteratively designed and improved both SOI gyroscopic devices and characterization setups.

We introduced the concept of optical gyroscopes and described the state of the art in Chapter 1. In Chapter 2 we presented a theoretical study with a thorough device-level optimization. Based on this study, we concluded that the most crucial design parameter for the gyroscope resonators is the propagation loss, α. This parameter dictates the optimal values for the resonator length, L_{opt}, the field coupling, κ_{opt}, and the detuning, ϕ_{opt}. Our study showed that for each resonator configuration, the product αL_{opt} is a constant. For lengths above L_{opt}, the resolution deteriorates at a noticeably faster rate than for decreasing length values, below L_{opt}.

Taking into account the resonator size constraints imposed by the fabrication technology, we obtained optimized coupling and detuning for $L < L_{\text{opt}}$, with α and L as parameters. In all cases, the best resonator design is an under-coupled, all-pass configuration. In order to assess the design robustness, normalized parameter bandwidths for the length, the coupling, and the detuning of all-pass and drop-port resonators were obtained. For each port configuration, these bandwidths were identical for all values of α. However, when these parameters are denormalized, lower values of α allow for

wider tuning ranges. On the system level, the impact of insertion loss and signal-to-noise ratio on resolution are described. Based on our theoretical study, large-area resonators were designed and fabricated on SOI wafers, as part of MPW runs.

Complex mechano-opto-electrical characterization setups were created to test the fabricated devices, and both the resonator designs and the characterization setups were improved during the five design iterations described in Chapter 3. Our initial experiments motivated us to combine SMWG directional couplers and SMWG resonator corners with straight MMWG segments, in order to reduce the resonator round-trip loss. Figure 4.1 shows the average propagation loss and average Q value for each design cycle. Based on our prior theoretical study and on the experience gained through various fabrication iterations, we were able to design large-area resonators with Q factors as high as 4.5×10^6 and 2×10^6, with and without thermally-tuned coupling, respectively. The latter have been published in [56]. To the best of our knowledge, these are the highest Q factor values reported to date for SOI resonators fabricated using standard CMOS-compatible processes. Our resonators met or exceeded the specifications for Q factor and propagation loss of resonant structures reported in the literature, fabricated in other materials (e.g., InP [23, 28]) and also intended for gyroscopic applications.

Regarding the characterization apparatus, LabVIEW$^{\text{TM}}$ FPGA interfaces were created to control the rotation speed and patterns of a first rotational setup. Preliminary gyroscopic measurements were carried out, allowing for identification of limitations regarding alignment repeatability, speed range, environmental noise, mechanical vibration, and stress. In order to address these limitations, I built a second rotational setup with support of CMC Microsystems. Its main features consisted of an enclosure that reduced air motion and ambient light, auto-alignment capability, lower vibration, and improved rotational speed control. Continuous spectral sweeps were implemented in order to observe the behaviour of resonance over time.

The initial LabVIEW$^{\text{TM}}$ FPGA interfaces were improved so as to allow for observation and recording of time-domain signals from up to six

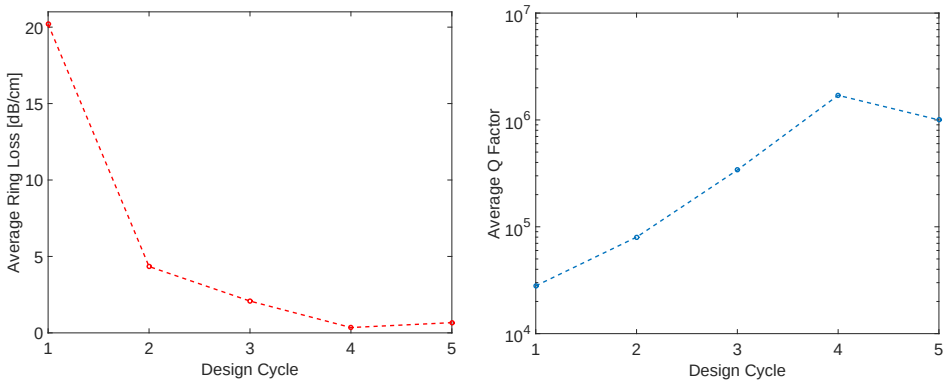

(a) (b)

Figure 4.1: **(a)** Average ring propagation loss, and **(b)** average ring Q factor vs. design cycle.

different photodetector channels and from the turntable's angular speed encoder. Fast Fourier Transform plots and power spectral density plots were also obtained automatically upon measurement completion. Based on the spectral characterization results, filtering schemes were implemented. This work resulted in the creation of the Microsystem Integration Platform for Silicon-Photonics (Si-P MIP). This characterization platform is, to the best of our knowledge, the only characterization platform of its kind available in Canada, and is now being commercialized by CMC Microsystems for academic and industrial applications.

We have performed repeatable, amplitude-based tests for angular speeds above 20 dps. However, despite the mechano-opto-electrical improvements, the detected signals were still dominated by effects of system vibration and stress at the bond between the chip and the array during rotation. Efforts to achieve better resolution by implementing frequency tracking schemes were explored, however, their implementations were hindered by signal distortions in the amplification stage. RF amplifiers with gain values between 27 and 30 dB were indispensable to achieve the required 2π phase shift per ramp cycle in the phase modulators. High frequency ramp signals require at least 100 harmonics to ensure acceptable sharp features. Thus, a flat 30-dB gain

across a full bandwidth from DC to 20 GHz would be required to properly amplify the 200 MHz ramp signals required to track a resonance with a 100-MHz linewidth (consistent $Q \approx 2 \times 10^6$). As none of the the available RF amplifiers had such high, flat gain over such a wide frequency range, all high-frequency ramp signals were unavoidably distorted. An alternative scheme, based on sinusoidal signals, is proposed and analyzed in detail in Section 4.3, as part of future work suggestions.

A backscattering model has been developed to explain the non-zero signals detected at the output ports of our devices. Our simulations indicate that the appearance of signals at the mixed-through port is not only due to waveguide backscattering, but it is also due to an imperfect splitting ratio at the as-fabricated adiabatic couplers. Suitable value ranges for key parameters of various DUT subcomponents have been found, in order to phenomenologically match the simulations and the experimental data. Due to the stochastic nature of the backscattering profile distribution, each simulation run provides a unique case in which a combination of various spectral behaviours can be found. Our model shows that the variations of Q and ER are coupling-, backscattering-level-, and backscattering-profile-dependent, and that these variations are greater for increasing values of backscattering.

A distributed backscattering model has been developed for our large area resonators. The phase asymmetries between the CW and CCW signals in the resonators create differences in their spectra. The non-zero output signals at rest at the mixed-through port of our devices with adiabatic couplers are due to waveguide backscattering and also due to imperfect splitting ratios at the as-fabricated adiabatic couplers. Due to the stochastic backscattering profile distribution, each simulation run provides a unique case, in which a combination of various experimental spectral behaviours can be found. Due to the resonator lengths and coupling values used in our devices, the impact of directional coupler reflections is negligible in comparison to those of backscattering and imperfect splitting ratios. At its present form, our backscattering model uses a combination of S parameters for the point coupler and T-matrix formalisms, assuming ideal phase relationships between the adiabatic coupler ports. Further steps to add complexity to the

model include the incorporation of S parameters for the adiabatic couplers, followed by modelling of DUTs with thermally tuneable couplers.

4.2 Conclusions

We have developed models for the optimization and robustness analysis of the design parameters of ring resonator gyroscopes. We have achieved the necessary Q factor values for making SOI gyroscopes feasible, and implemented thermal tuning methods to compensate for fabrication-related coupling variations. We have also created mechano-opto-electrical platforms for frequency- and time-domain characterization of SOI gyroscopes, both at rest and under rotation.

During time-domain tests, with the TLS directly connected to the detectors using PM patch cords, the SNR improved marginally for longer averaging times, and it was approximately constant as the input power was varied. This suggested that the measurements at rest were limited by laser noise. This qualitatively agrees with our initial theoretical study (see Fig. 2.9), considering that for our TLSs, the RIN=-145 dB/Hz [72]. However, theoretically the SNR = 67 dB, whereas experimentally the SNR $\approx$ 30 dB. As mentioned in Subsection 2.4.5, the SNR has a significant impact on the resolution.

Considering the vibration-related amplitude fluctuations, the experimental SNR values ($SNR \approx 30$ dB), resonator length, aspect ratio, propagation losses, laser RIN, and lack of frequency tracking readout, the potential performance of the system in its present state is approximately $|\delta\Omega| > 920$ °/s, according to estimations based on the equations developed in Chapter 2. Rotating the system at these angular rates is impractical, as both the setup and the DUTs would unavoidably be damaged or destroyed. Moreover, higher angular speeds cannot guarantee that the Sagnac-related signals will overcome vibration- or stress-related ones, as the latter will also increase in the present setup configuration.

In order to avoid the difficulties associated with amplitude variations, frequency tracking readout schemes are indispensable. Since the resonance

linewidth values of our resonators are on the order of 100 MHz, the implementation of a sinusoidal frequency-tracking readout scheme is necessary, in order to avoid the distortion of the RF modulation signals observed during our experiments.

Based on my findings, I conclude that with the implementation of sinusoidal frequency tracking techniques (further discussed in Section 4.3 below), and provided that the mechanical stress and vibration are reduced (e.g., by releasing the fibre array from its metallic holder after curing the UV adhesive), tactical-grade resolutions (for gyroscope resolution grades see Table 1.1) on the order of $\delta\Omega \approx 3 \times 10^{-3}$ °/s should be feasible for square-shaped SOI resonators with lengths on the order of 70 mm and $Q \approx 2 \times 10^6$. This is consistent with resolution predictions based on high-quality resonant structures fabricated in other technologies [22].

Although other materials such as glass or SiN offer lower propagation losses, the benefits of SOI technology lie on the lower fabrication costs as well as its its compatibility with CMOS fabrication processes, which allow for both larger production volumes and for easier integration with readout electronics and other on-chip functionalities. For instance, in order to reduce the resonance wavelength shifts due to ambient temperature variations, we have developed wavelength tuning and stabilization schemes of microrings to track the input signal wavelength using photoconductive heaters [69]. Similar schemes can be implemented in the large-area gyro resonators to compensate for variations associated with temperature fluctuations. On-chip phase modulation schemes can also be implemented, as long as the lengths available for the phase modulators ensure that $V_\pi < 4$ V and that their modulation bandwidth is of at least 100 MHz.

Besides the implementation of frequency tracking readout techniques, the most important obstacles to overcome are the amplitude variations associated with mechanical vibration and stress in the bond between the fibre array and the DUT during rotation, as well as the low SNR values of our currently laser-noise limited system.

Despite the use of sturdy optomechanics, compact fibre arrays, and UV-curable adhesives, these amplitude variations remain considerably larger

than any Sagnac-related variation. This results in any Sagnac-related amplitude variation being buried in the aforementioned vibration-related signals. As previously mentioned, due to the mass and shape of the optomechanics (e.g., the 40 cm-tall, 3.8 cm-wide solid aluminium post that currently holds the fibre array in place), as well as the use of optical fibres, continuous rotation and high angular speeds are impractical in our characterization setup.

The SNR value could be improved with the use of low Spontaneous Source Emission (low SSE) laser sources, e.g., the Keysight^{TM} 81600B [73]. According to our theoretical study, a RIN ≈ -160 dB/Hz is required in order to achieve shot-noise limit. Thus, the use of low-RIN laser sources (e.g., see [16, 47]) is advised.

In order to achieve better resolution, the optical interface for device interrogation must be improved further. Device packaging will very likely help, as it will in principle reduce the vibration- and stress-related amplitude fluctuations. Tests should be performed before and during packaging in order to ensure that the adhesives used for permanent fibre attachment do not produce significant reflections due to refractive index mismatch. Care must also be taken to ensure that the packaging itself does not produce significant time-varying nor temperature-dependent stress on the chip, as this would negatively impact the device performance. This, in combination with the aforementioned on-chip functionalities of resonance stabilization, phase modulation, and gyro signal readout, would significantly increase the SNR and reduce the sensitivity to environmental fluctuations.

The IL and backreflection levels must also be reduced. Due to the small size of the SOI waveguides, edge coupling tolerances are more stringent than those of GC alignments. Therefore, GC schemes with reduced backreflection are advisable. GC designs with backreflections as low as -40 dB have been proposed [132], and GC designs with -30 dB backreflection have been designed and experimentally demonstrated for TE [7] and TM [59] polarization. Novel space-efficient approaches, such as lateral fibre coupling [3, 77], could also be explored.

Other areas of potential improvement pertain to reduction of bend loss

and propagation loss. Euler bends with effective radii of 100 µm and losses of 0.005 dB/bend have been reported by the VTT Technical Research Centre of Finland, where very-low loss SMWGs and custom electrical/optical packaging options are available [134].

4.3 Suggestions for Future Work

4.3.1 Sinusoidal Phase Modulation

My principal suggestion for future work is the implementation of suppressed-carrier sinusoidal phase modulation for both frequency tracking and for reduction of backscattering-induced noise [36, 63, 82, 121]. Although the use of serrodyne and triangular wave phase modulation is considered to be more advantageous than sinusoidal phase modulation [144], the driving frequency and signal bandwidth requirements of sinusoidal phase modulation are considerably less stringent than those imposed by serrodyne and triangular phase modulation schemes [62, 118, 125]. In this scheme, the sinusoidal signals driving the phase modulators for the CW and CCW beams are, respectively:

$$s_{\mathrm{cw}} = V_1 \sin(2\pi f_1 t) \tag{4.1}$$

$$s_{\mathrm{ccw}} = V_2 \sin(2\pi f_2 t), \tag{4.2}$$

where V_1 and V_2 are the peak voltages and f_1 and f_2 are the modulation frequencies for the CW and CCW beam, respectively. The electric fields of the phase modulated beams entering the resonator in the CW and CCW directions are:

$$E_{\mathrm{cw}} = \frac{E_{\mathrm{in}}}{\sqrt{2C_{\mathrm{IL}}}} \exp\left[-j\left(2\pi\nu_1 t + \frac{\pi}{V_\pi}\cdot s_{\mathrm{cw}}\right)\right] \tag{4.3}$$

$$E_{\mathrm{ccw}} = \frac{E_{\mathrm{in}}}{\sqrt{2C_{\mathrm{IL}}}} \exp\left[-j\left(2\pi\nu_2 t + \frac{\pi}{V_\pi}\cdot s_{\mathrm{ccw}}\right)\right], \tag{4.4}$$

where E_{in} is the amplitude of the TLS optical input field, the factor C_{IL} represents the insertion loss, ν_1 and ν_2 are the central frequencies of the phase

modulated beams travelling in the CW and CCW direction, respectively, and V_π is the half-wave voltage of the phase modulators. Assuming that $V_1 = V_2 = V_s$, the input fields can be expressed in terms of Bessel functions as follows [142]:

$$E_{\text{in cw}} = \frac{E_{\text{in}}}{\sqrt{2C_{\text{IL}}}} e^{-j2\pi\nu_1 t} \sum_{u=-\infty}^{\infty} J_u(m) \cdot e^{-j2\pi u f_1 t} \tag{4.5}$$

$$E_{\text{in ccw}} = \frac{E_{\text{in}}}{\sqrt{2C_{\text{IL}}}} e^{-j2\pi\nu_2 t} \sum_{u=-\infty}^{\infty} J_u(m) \cdot e^{-j2\pi u f_2 t}, \tag{4.6}$$

where $J_u(m)$ is the u^{th}-order Bessel function of the first kind, and m is the modulation index of the phase modulators, given by:

$$m = \frac{\pi V_s}{V_\pi}. \tag{4.7}$$

In order to suppress the carrier, $J_0(m)$ must be zero, i.e., a modulation index $m = 2.405$ is required [142]. In our particular case, $V_\pi = 4$ V, so $V_s \approx 3.062$ V, and $V_{\text{RMS}} = 2.165$ V. Thus, based on Eq. (3.49), the required signal power is $P_{\text{dBm}} = 19.72$ dBm. Although this power level is similar to what was required for the serrodyne implementation, in this case the driving signal has (ideally) only one spectral component, which eases the implementation. We have been able to generate sinusoidal signals of $P_{\text{dBm}} = 20$ dBm with a quad-channel Fluke$^{\text{TM}}$ 294 signal generator [26], up to frequencies of 300 MHz without distortion and without requiring additional amplification. For $m = 2.405$, the amplitudes of $J_k(m)$ for $|k| \geq 4$ are considered negligible. Therefore, the fields of the beams exiting the all-pass resonator are:

$$E_{\text{out cw}} = \frac{E_{\text{in}}}{\sqrt{2C_{\text{IL}}}} e^{-j2\pi\nu_1 t} \sum_{u=-3}^{3} J_u(m) \cdot e^{-j2\pi u f_1 t} \cdot S_{\text{cw}}(\nu_1 + k f_1) \tag{4.8}$$

$$E_{\text{out ccw}} = \frac{E_{\text{in}}}{\sqrt{2C_{\text{IL}}}} e^{-j2\pi\nu_2 t} \sum_{u=-3}^{3} J_u(m) \cdot e^{-j2\pi u f_2 t} \cdot S_{\text{ccw}}(\nu_2 + k f_2), \tag{4.9}$$

where S_{cw} and S_{ccw} are the Lorentzian spectral responses of the resonator in the CW and CCW directions, centred at ν_{cw} and ν_{ccw}, respectively, and defined based on Eqs. (2.19),(2.20), and (2.21). Considering the 6 relevant spectral components for each beam, at the photodetectors we have the following voltage signals [36]:

$$V_{\text{pd1}} \propto |E_{\text{out cw}}|^2 = \sum_{u=0}^{6} A_{1u} \cdot \cos(2\pi \cdot u f_1 \cdot t) \tag{4.10}$$

$$V_{\text{pd2}} \propto |E_{\text{out ccw}}|^2 = \sum_{u=0}^{6} A_{2u} \cdot \cos(2\pi \cdot u f_2 \cdot t), \tag{4.11}$$

where A_{1u} and A_{2u} are the amplitudes of the spectral components of the signals at the photodetectors Det_1 and Det_2. Two LIAs, with reference signals of frequencies f_1 and f_2, respectively, must be used to demodulate the signals V_{pd1} and V_{pd2}. The output signal of LIA_1 will be proportional to the component of V_{pd1} at f_1. Similarly, the output signal of LIA_2 will be proportional to the component of V_{pd2} at f_2, with amplitudes A_{11} and A_{21}, respectively.

Figure 4.2 shows the LIA output as a function of the frequency deviation from resonance due to the Sagnac effect, for several modulation frequencies. As shown in the figure, the slope and extension of the linear regime near zero deviation varies with the modulation frequency. Figure 4.3 shows the LIA output signal slope as a function of the modulation frequency, for a 40 mm-long resonator with a $Q \approx 1 \times 10^6$, consistent with our latest designs. As shown in the figure, the optimum sinusoidal modulation frequency is $f_1 \approx 35$ MHz, which is feasible with our currently available equipment. The output signal of LIA_1 is used as an error signal in a feedback loop to either tune the laser frequency or to impart a thermal phase shift to the ring resonator. The output signal of LIA_2 is used as an error signal that is minimized by adjusting the value of f_2. The rotation-induced frequency shift Δf_{Sagnac} is then proportional to f_2.

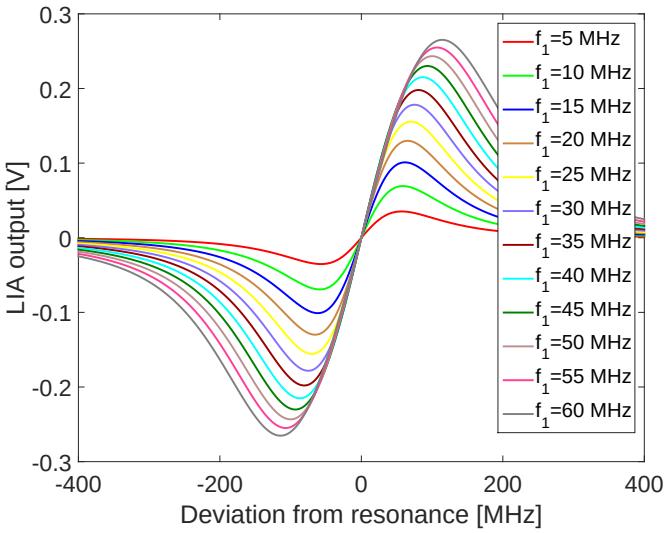

Figure 4.2: Lock-in amplifier output vs. resonance frequency detuning, with modulation signal frequency as a parameter.

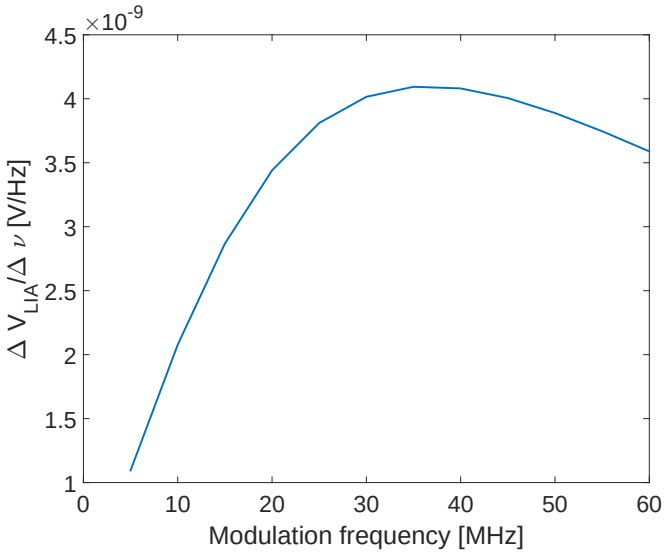

Figure 4.3: Lock-in amplifier output slope vs. modulation signal frequency.

Bibliography

[1] *Honeywell GG5300 MEMS gyro*. 2011.

[2] Melexis MEMS angular rate sensor, 2011.

[3] PLC Connections, LLC, 2015.

[4] Don C. Abeysinghe and Joseph T. Boyd. Micromachining Techniques and MEMS Structures in Optical Interferometric Sensors. In *MEMS/NEMS*, pages 1587–1630. Springer, 2006.

[5] V. Annovazzi-Lodi, M. Benedetti, S. Merlo, and M. Norgia. Optical detection of multiple modes on resonant micromachined structures. *IEEE Photonics Technology Letters*, 16(7):1703–1705, July 2004.

[6] V. Annovazzi-Lodi, S. Merlo, and M. Norgia. Measurements on a micromachined silicon gyroscope by feedback interferometry. *IEEE/ASME Transactions on Mechatronics*, 6(1):1–6, March 2001.

[7] Mikael Antelius, Kristinn B. Gylfason, and Hnas Sohlstrm. An apodized SOI waveguide-to-fiber surface grating coupler for single lithography silicon photonics. *Optics Express*, 19(4):3592, February 2011.

[8] H. J. Arditty and H. C. Lefevre. Sagnac effect in fiber gyroscopes. *Opt. Lett.*, 6(8):401–403, August 1981.

[9] Tom Baehr-Jones, Ran Ding, Ali Ayazi, Thierry Pinguet, Matt Streshinsky, Nick Harris, Jing Li, Li He, Mike Gould, Yi Zhang, Andy Eu-Jin Lim, Tsung-Yang Liow, Selin Hwee-Gee Teo, Guo-Qiang

Lo, and Michael Hochberg. A 25 Gb/s Silicon Photonics Platform. *arXiv:1203.0767 [physics]*, March 2012. arXiv: 1203.0767.

[10] G. C. Ballesteros, J. Matres, J. Mart, and C. J. Oton. Characterizing and modeling backscattering in silicon microring resonators. *Opt. Express*, 19(25):24980–24985, December 2011.

[11] N. Barbour and G. Schmidt. Inertial sensor technology trends. *IEEE Sensors Journal*, 1(4):332–339, December 2001.

[12] Jared Bauters, Martijn Heck, Demis D. John, Ming-Chun Tien, Wenzao Li, Jon S. Barton, Daniel J. Blumenthal, John Bowers, Arne Leinse, and Rene G. Heideman. Ultra-low-loss Single-mode Silicon Nitride Waveguides with 0.7 dB/m Propagation Loss. In *37th European Conference and Exposition on Optical Communications*, OSA Technical Digest (CD), page Th.12.LeSaleve.3. Optical Society of America, September 2011.

[13] W. Bogaerts, R. Baets, P. Dumon, V. Wiaux, S. Beckx, D. Taillaert, B. Luyssaert, J. Van Campenhout, P. Bienstman, and D. Van Thourhout. Nanophotonic waveguides in silicon-on-insulator fabricated with CMOS technology. *Lightwave Technology, Journal of*, 23(1):401–412, 2005.

[14] W. Bogaerts, P. De Heyn, T. Van Vaerenbergh, K. De Vos, S. Kumar Selvaraja, T. Claes, P. Dumon, P. Bienstman, D. Van Thourhout, and R. Baets. Silicon microring resonators. *Laser & Photon. Rev.*, 6(1):47–73, January 2012.

[15] W. Bogaerts and S.K. Selvaraja. Compact Single-Mode Silicon Hybrid Rib/Strip Waveguide With Adiabatic Bends. *IEEE Photonics Journal*, 3(3):422–432, June 2011.

[16] J.-R. Burie, G. Beuchet, M. Mimoun, P. Pagnod-Rossiaux, B. Ligat, J. C. Bertreux, J.-M. Rousselet, J. Dufour, P. Rougeolle, and F. Laruelle. Ultra high power, ultra low RIN up to 20 GHz 1.55 m DFB

AlGaInAsP laser for analog applications. pages 76160Y–76160Y–10, February 2010.

[17] Jaime Cardenas, Carl B. Poitras, Jacob T. Robinson, Kyle Preston, Long Chen, and Michal Lipson. Low loss etchless silicon photonic waveguides. *Opt. Express*, 17(6):4752–4757, March 2009.

[18] C. F. Carlborg, K. B. Gylfason, A. Kamierczak, F. Dortu, M. J. Bauls Polo, A. Maquieira Catala, G. M. Kresbach, H. Sohlstrm, T. Moh, L. Vivien, J. Popplewell, G. Ronan, C. A. Barrios, G. Stemme, and W. van der Wijngaart. A packaged optical slot-waveguide ring resonator sensor array for multiplex label-free assays in labs-on-chips. *Lab Chip*, 10(3):281, 2010.

[19] J.T.A Carriere, J.A Frantz, S. Honkanen, R.K. Kostuk, B.R. Youmans, and E.AJ. Vikjaer. An integrated optic gyroscope using ion-exchanged waveguides. In *The 16th Annual Meeting of the IEEE Lasers and Electro-Optics Society, 2003. LEOS 2003*, volume 1, pages 99–100 vol.1, October 2003.

[20] Oguz Celikel. Construction and characterization of interferometric fiber optic gyroscope (IFOG) with erbium doped fiber amplifier (EDFA). *Optical and Quantum Electronics*, 39(2):147–156, January 2007.

[21] Lukas Chrostowski and Michael Hochberg. *Silicon Photonics Design*. Cambridge University Press, 2015.

[22] Caterina Ciminelli, Francesco Dell'Olio, Mario N. Armenise, Francisco M. Soares, and Wolfgang Passenberg. High performance InP ring resonator for new generation monolithically integrated optical gyroscopes. *Opt. Express*, 21(1):556–564, January 2013.

[23] Caterina Ciminelli, Vittorio M. N. Passaro, Francesco Dell'Olio, and Mario N. Armenise. Quality factor and finesse optimization in buried InGaAsP/InP ring resonators. *Journal of the European Optical Society: Rapid Publications*, 4, June 2009.

[24] Larry A. Coldren. *Diode Lasers and Photonic Integrated Circuits*. 1995.

[25] S. Cole, R. L. Fork, D. Lamb, and P. Reardon. Multi-turn all-reflective optical gyroscope. *Opt Express*, 7(8):285–291, October 2000.

[26] Fluke Corporation. Fluke 294 Arbitrary Waveform Generator, 2014.

[27] C. C. Cutler, S. A. Newton, and H. J. Shaw. Limitation of rotation sensing by scattering. *Opt. Lett.*, 5(11):488–490, November 1980.

[28] D. D'Agostino, G. Carnicella, C. Ciminelli, H.P.M.M. Ambrosius, and M.K. Smit. Design of a compact high-performance InP ring resonator. In *Photonics Conference, 2014 Third Mediterranean*, pages 1–3, May 2014.

[29] Daoxin Dai and Sailing He. Analysis of characteristics of bent rib waveguides. *J. Opt. Soc. Am. A*, 21(1):113–121, January 2004.

[30] J. L. Davis and S. Ezekiel. Techniques for Shot-Noise-Limited Inertial Rotation Measurement Using a Multiturn Fiber Sagnac Interferometer. volume 0157, pages 131–136, 1978.

[31] J. L. Davis and S. Ezekiel. Closed-loop, low-noise fiber-optic rotation sensor. *Opt. Lett.*, 6(10):505–507, October 1981.

[32] T. De Fazio, K.L. Belsley, R.H. Smith, Jr. Shank, G.B., and W.H. Culver. Development issues for automating quadrupole-pattern optical-fiber coil-winding for fiber-optic gyro manufacture. In *, 1994 IEEE International Conference on Robotics and Automation, 1994. Proceedings*, pages 202–207 vol.1, May 1994.

[33] Peter de Heyn. *Receivers Based on Silicon Ring Resonators for Multi-Wavelength Optical Interconnects*. PhD thesis, Ghent University, Ghent, Belgium, 2014.

[34] F. Dell'Olio, A. Di Nisio, F. Indiveri, P. Lino, C. Ciminelli, and M.N. Armenise. Backscattering noise control in the readout circuit of innovative optoelectronic resonant gyroscopes. In *2014 Fotonica AEIT Italian Conference on Photonics Technologies*, pages 1–3, May 2014.

[35] F. Dell'Olio, T. Tatoli, C. Ciminelli, and M. N. Armenise. Recent advances in miniaturized optical gyroscopes. *Journal of the European Optical Society - Rapid publications*, 9(0), March 2014.

[36] Francesco DellOlio, Fabrizio Indiveri, Filomena Innone, Pasquale Dello Russo, Caterina Ciminelli, and Mario N. Armenise. System test of an optoelectronic gyroscope based on a high Q-factor InP ring resonator. *Opt. Eng*, 53(12):127104–127104, 2014.

[37] Analog Devices. *Analog Devices ADIS16355 3-axis Inertial Sensor Datasheet*. 2009.

[38] P. Dumon, W. Bogaerts, V. Wiaux, J. Wouters, S. Beckx, J. Van Campenhout, D. Taillaert, B. Luyssaert, P. Bienstman, D. Van Thourhout, and R. Baets. Low-loss SOI photonic wires and ring resonators fabricated with deep UV lithography. *IEEE Photonics Technology Letters*, 16(5):1328–1330, May 2004.

[39] Pieter Dumon. *Ultra-Compact Integrated Optical Filters in Silicon-on-insulator by Means of Wafer-Scale Technology*. Ph.D. Thesis, Gent University, Belgium, 2007.

[40] Dymax. Light Weld Optically Clear Structural Bonding Glass Adhesive 429, 2014.

[41] Dymax. Ultra Light-Weld 4-20418 Low-Stress Glass and Plastic Bonder Data Sheet, 2014.

[42] Professor Dr Karl Joachim Ebeling. Directional Couplers. In *Integrated Optoelectronics*, pages 143–173. Springer Berlin Heidelberg, January 1993.

[43] David F. Edwards. Silicon (Si)*. In Edward D. Palik, editor, *Handbook of Optical Constants of Solids*, pages 547–569. Academic Press, Burlington, 1997.

[44] S. Ezekiel and H. J. Arditty. Fiber-Optic Rotation Sensors. In *Fiber-Optic Rotation Sensors and Related Technologies*, pages 3–27. Springer Verlag, Berlin, 1982.

[45] S. Ezekiel and S. R. Balsamo. Passive ring resonator laser gyroscope. *Applied Physics Letters*, 30(9):478–480, May 1977.

[46] S. Ezekiel, J. A. Cole, J. Harrison, and G. Sanders. Passive Cavity Optical Rotation Sensor. volume 0157, pages 68–72, 1978.

[47] M. Faugeron, M. Tran, F. Lelarge, M. Chtioui, Y. Robert, E. Vinet, A. Enard, J. Jacquet, and F. Van Dijk. High-Power, Low RIN 1.55- Directly Modulated DFB Lasers for Analog Signal Transmission. *IEEE Photonics Technology Letters*, 24(2):116–118, January 2012.

[48] Lishuang Feng, Junjie Wang, Yinzhou Zhi, Yichuang Tang, Qiwei Wang, Haicheng Li, and Wei Wang. Transmissive resonator optic gyro based on silica waveguide ring resonator. *Opt. Express*, 22(22):27565–27575, November 2014.

[49] W.R. Finley, M.M. Hodowanec, and W.G. Holter. An analytical approach to solving motor vibration problems. In *Petroleum and Chemical Industry Conference, 1999. Industry Applications Society 46th Annual*, pages 217–232, 1999.

[50] C. Ford, R. Ramberg, K. Johnson, W. Berglund, B. Ellerbusch, R. Schermer, and A. Gopinath. Cavity element for resonant micro optical gyroscope. In *Position Location and Navigation Symposium, IEEE 2000*, pages 285–290, 2000.

[51] J. Frei, Xiao-Ding Cai, and S. Muller. Multiport -Parameter and -Parameter Conversion With Symmetry Extension. *IEEE Transactions*

on Microwave Theory and Techniques, 56(11):2493–2504, November 2008.

[52] Eric Lee Goldner and Daniel Eugene Auerbach. Integrated optic gyroscope and method of fabrication, July 2003. U.S. Classification 356/465; International Classification G01C19/72; Cooperative Classification G01C19/722; European Classification G01C19/72D2.

[53] Alexander Gondarenko, Jacob S. Levy, and Michal Lipson. High confinement micron-scale silicon nitride high Q ring resonator. *Opt. Express*, 17(14):11366–11370, July 2009.

[54] M.A Guillen-Torres, E. Cretu, N. A F Jaeger, and L. Chrostowski. Ring Resonator Optical Gyroscopes - Parameter Optimization and Robustness Analysis. *Journal of Lightwave Technology*, 30(12):1802–1817, June 2012.

[55] Miguel Á. Guillén-Torres, Maan Almarghalani, Elie H. Sarraf, Michael Caverley, Nicolas A. F. Jaeger, Edmond Cretu, and Lukas Chrostowski. Silicon photonics characterization platform for gyroscopic devices. In *Proceedings of SPIE*, volume 9288, pages 92880U–92880U–8, Montral, Canada, 2014. SPIE.

[56] Miguel Ángel Guillén-Torres, Michael Caverley, Edmond Cretu, Nicolas A. F. Jaeger, and Lukas Chrostowski. Large-Area, High-Q SOI Ring Resonators. San Diego, California, USA, October 2014. IEEE.

[57] Lijun Guo, Bangren Shi, Meng Zhao, Chen Chen, and Rong Zhang. Direct-Coupled Large-Diameter Silica on Silicon Waveguide Ring Resonator Used in Microoptic Gyro. *International Journal of Optomechatronics*, 5(1):30–50, March 2011.

[58] Wei Guo, Huilian Ma, Zhonghe Jin, Yanzhe Tang, and Yuelin Wang. Novel structure of passive ring waveguide resonator on silicon substrate. In *MEMS/MOEMS Technologies and Applications*, volume 4928, pages 297–300, Shanghai, China, 2002. SPIE.

[59] R. Halir, P. Cheben, J. H. Schmid, R. Ma, D. Bedard, S. Janz, D.-X. Xu, A. Densmore, J. Lapointe, and . Molina-Fernndez. Continuously apodized fiber-to-chip surface grating coupler with refractive index engineered subwavelength structure. *Optics Letters*, 35(19):3243, October 2010.

[60] John Heebner, Rohit Grover, and Tarek Ibrahim. *Optical Microresonators*. Springer, 2008.

[61] Henkel North America. Loctite 3492 Light Cure Acrylic Adhesive, 2011.

[62] K. Hotate and M. Harumoto. Resonator fiber optic gyro using digital serrodyne modulation. *Journal of Lightwave Technology*, 15(3):466–473, March 1997.

[63] K. Hotate, K. Takiguchi, and A. Hirose. Adjustment-free method to eliminate the noise induced by the backscattering in an optical passive ring-resonator gyro. *IEEE Photonics Technology Letters*, 2(1):75–77, January 1990.

[64] J.Y. Hung and H. Van White. Precision winding of fiber optic filament. I. Winding characteristics. *IEEE Transactions on Industrial Electronics*, 39(3):258–267, June 1992.

[65] National Instruments. PXI-7852r FPGA Module Specifications, 2014.

[66] National Instruments. PXIe-1062q Chassis Specifications, 2014.

[67] K. Iwatsuki, K. Hotate, and M. Higashiguchi. Effect of Rayleigh backscattering in an optical passive ring-resonator gyro. *Appl. Opt.*, 23(21):3916–3924, November 1984.

[68] Nicolas A. F. Jaeger. Optical Resonators. In *Optical Fibers and Devices Course Notes, UBC EECE 582*. University of British Columbia, 2013.

[69] Hasitha Jayatilleka, Kyle Murray, Miguel Ángel Guillén-Torres, Michael Caverley, Ricky Hu, Nicolas A. F. Jaeger, Lukas Chrostowski, and Sudip Shekhar. Wavelength tuning and stabilization of microring-based filters using silicon in-resonator photoconductive heaters. *arXiv:1507.00686 [physics]*, July 2015. arXiv: 1507.00686.

[70] Zhonghe Jin, Guhong Zhang, Hui Mao, and Huilian Ma. Resonator micro optic gyro with double phase modulation technique using an FPGA-based digital processor. *Optics Communications*, 285(5):645–649, March 2012.

[71] Todd J. Kaiser, Dan Cardarelli, and Joseph G. Walsh. Experimental developments in the RFOG. volume 1367, pages 121–126, 1991.

[72] Keysight. Agilent 81682a User's Guide, 2001.

[73] Keysight. 81600b Tunable Laser Source Family | Keysight (Agilent), 2015.

[74] K. Killian. Pointing grade fiber optic gyroscope. In *, IEEE Position Location and Navigation Symposium, 1994*, pages 165–169, April 1994.

[75] J. Komma, C. Schwarz, G. Hofmann, D. Heinert, and R. Nawrodt. Thermo-optic coefficient of silicon at 1550 nm and cryogenic temperatures. *Applied Physics Letters*, 101(4):041905, July 2012.

[76] Franois Ladouceur and Leon Poladian. Surface roughness and backscattering. *Optics Letters*, 21(22):1833, November 1996.

[77] Chao Li, Koh Sing Chee, Jifang Tao, Huijuan Zhang, Mingbin Yu, and G. Q. Lo. Silicon photonics packaging with lateral fiber coupling to apodized grating coupler embedded circuit. *Opt Express*, 22(20):24235–24240, October 2014.

[78] Guoliang Li, Jin Yao, Hiren Thacker, Attila Mekis, Xuezhe Zheng, Ivan Shubin, Ying Luo, Jin-hyoung Lee, Kannan Raj, John E. Cunningham, and Ashok V. Krishnamoorthy. Ultralow-loss, high-density

SOI optical waveguide routing for macrochip interconnects. *Opt. Express*, 20(11):12035–12039, May 2012.

[79] S. Lidgate. *Advanced Finite Difference-Beam Propagation Method Analysis of Complex Components*. PhD thesis, U. Nottingham, 2004.

[80] B.E. Little, S.T. Chu, H.A. Haus, J. Foresi, and J.-P. Laine. Microring resonator channel dropping filters. *Lightwave Technology, Journal of*, 15(6):998–1005, 1997.

[81] Kai Liu, Weiping Zhang, Wenyuan Chen, Kai Li, Fuyan Dai, Feng Cui, Xiaosheng Wu, Gaoyin Ma, and Qijun Xiao. The development of micro-gyroscope technology. *J. Micromech. Microeng.*, 19(11):113001, November 2009.

[82] Huilian Ma, Zuyuan He, and Kazuo Hotate. Reduction of Backscattering Induced Noise by Carrier Suppression in Waveguide-Type Optical Ring Resonator Gyro. *Lightwave Technology, Journal of*, 29(1):85–90, 2011.

[83] Huilian Ma, Xulin Zhang, Zhonghe Jin, and Chun Ding. Waveguide-type optical passive ring resonator gyro using phase modulation spectroscopy technique. *Opt. Eng*, 45(8):080506–080506–3, 2006.

[84] Hui Mao, Huilian Ma, and Zhonghe Jin. Polarization maintaining silica waveguide resonator optic gyro using double phase modulation technique. *Opt. Express*, 19(5):4632–4643, February 2011.

[85] D. Marcuse. *Theory of Dielectric Optical Waveguides*. Academic Press, 1974.

[86] W. R. McKinnon, D. X. Xu, C. Storey, E. Post, A. Densmore, A. Delge, P. Waldron, J. H. Schmid, and S. Janz. Extracting coupling and loss coefficientsfrom a ring resonator. *Opt. Express*, 17(21):18971–18982, October 2009.

[87] A. Mekis, S. Gloeckner, G. Masini, A. Narasimha, T. Pinguet, S. Sahni, and P. De Dobbelaere. A Grating-Coupler-Enabled CMOS Photonics Platform. *IEEE Journal of Selected Topics in Quantum Electronics*, 17(3):597–608, June 2011.

[88] F. Mohr. Thermooptically induced bias drift in fiber optical Sagnac interferometers. *Journal of Lightwave Technology*, 14(1):27–41, January 1996.

[89] F. Morichetti, A. Canciamilla, C. Ferrari, M. Martinelli, and A. Melloni. Backscattering in silicon photonic waveguides and circuits. volume 7943, pages 79430J–79430J–8, 2011.

[90] F. Morichetti, A. Canciamilla, M. Martinelli, A. Samarelli, R. M. De La Rue, M. Sorel, and A. Melloni. Coherent backscattering in optical microring resonators. *Applied Physics Letters*, 96(8):081112, February 2010.

[91] F. Morichetti, A. Melloni, M. Martinelli, R.G. Heideman, A. Leinse, D.H. Geuzebroek, and A. Borreman. Box-Shaped Dielectric Waveguides: A New Concept in Integrated Optics? *Lightwave Technology, Journal of*, 25(9):2579–2589, 2007.

[92] Francesco Morichetti, Antonio Canciamilla, Carlo Ferrari, Matteo Torregiani, Andrea Melloni, and Mario Martinelli. Roughness Induced Backscattering in Optical Silicon Waveguides. *Phys. Rev. Lett.*, 104(3):033902, January 2010.

[93] K. Nakagawa, M. de Labachelerie, Y. Awaji, and M. Kourogi. Accurate optical frequency atlas of the 1.5-um bands of acetylene. *J. Opt. Soc. Am. B*, 13(12):2708–2714, December 1996.

[94] T. Niesel and A. Dietzel. 120 silicon double mirrors for use in a micro-optical gyroscope. volume 8977, pages 897712–897712–7, 2014.

[95] M. Norgia and S. Donati. Hybrid opto-mechanical gyroscope with

injection-interferometer readout. *Electronics Letters*, 37(12):756–758, June 2001.

[96] Y. Ohtsuka. Analysis of a fiber-optic passive loop-resonator gyroscope: Dependence on resonator parameters and light-source coherence. *Journal of Lightwave Technology*, 3(2):378–384, April 1985.

[97] Yoshihiro Ohtsuka. Optical coherence effects on a fiber-sensing Fabry-Perot interferometer. *Appl. Opt.*, 21(23):4316–4320, December 1982.

[98] F. P. Payne and J. P. R. Lacey. A theoretical analysis of scattering loss from planar optical waveguides. *Opt Quant Electron*, 26(10):977–986, October 1994.

[99] Peyton Z Peebles. *Probability, Random Variables, and Random Signal Principles*. McGraw-Hill series in electrical and computer engineering. McGraw Hill, New York, NY, 4th ed edition, 2001.

[100] Milos Popovic. *Theory and design of high-index-contrast microphotonic circuits*. Thesis, Massachusetts Institute of Technology, 2008.

[101] E. J. Post. Sagnac Effect. *Rev. Mod. Phys.*, 39(2):475, April 1967. Copyright (C) 2008 The American Physical Society; Please report any problems to prola@aps.org.

[102] Yang Ren, Zhong-he Jin, Yan Chen, and Hui-lian Ma. Optimization of the resonant frequency servo loop technique in the resonator micro optic gyro. *Journal of Zhejiang University*, 12(11):942–950, 2011.

[103] Robert Resnick, David Halliday, and Kenneth S. Krane. *Physics*. Wiley, 2002.

[104] G. Sagnac. Effet tourbillonnaire optique. La circulation de léther lumineux dans un interférographe tournant. *Journal de Physique Théorique et Appliquée*, 4(1):177–195, 1914.

[105] A. Sakai, T. Fukazawa, and B. Toshihiko. Low Loss Ultra-Small Branches in a Silicon Photonic Wire Waveguide. *IEICE Trans. Electron.*, E85-C(4):1033–1038, 2002.

[106] B. A. E. Saleh and M. C. Teich. *Fundamentals of Photonics*. Wiley Interscience, 2 edition, 2007.

[107] G. A. Sanders, M. G. Prentiss, and S. Ezekiel. Passive ring resonator method for sensitive inertial rotation measurements in geophysics and relativity. *Opt. Lett.*, 6(11):569–571, November 1981.

[108] S.J. Sanders, L.K. Strandjord, and D. Mead. Fiber optic gyro technology trends - a Honeywell perspective. In *Optical Fiber Sensors Conference Technical Digest, 2002. OFS 2002, 15th*, pages 5–8 vol.1, 2002.

[109] Jacob Scheuer and Amnon Yariv. Sagnac Effect in Coupled-Resonator Slow-Light Waveguide Structures. *Phys. Rev. Lett.*, 96(5):053901–4, February 2006.

[110] G. Schmidt. INS/GPS Technology Trends. In *Research and Technology Organisation Educational Notes*, volume 064 of *SET*, pages 1–16, London, UK, 2004. North Atlantic Treaty Organisation.

[111] S. D. Senturia. *Microsystems Design*. Springer, USA, 2005.

[112] Wei Shi, Raha Vafaei, Miguel Ángel Guillén-Torres, Nicolas A. F. Jaeger, and Lukas Chrostowski. Design and characterization of microring reflectors with a waveguide crossing. *Opt. Lett.*, 35(17):2901–2903, September 2010.

[113] Christopher Sorrentino, John R. E. Toland, and Christopher P. Search. Ultra-sensitive chip scale Sagnac gyroscope based on periodically modulated coupling of a coupled resonator optical waveguide. *Opt. Express*, 20(1):354–363, January 2012.

[114] D.K. Sparacin, S.J. Spector, and L.C. Kimerling. Silicon waveguide sidewall smoothing by wet chemical oxidation. *Journal of Lightwave Technology*, 23(8):2455–2461, August 2005.

[115] Steven Spector, Michael W. Geis, Donna Lennon, Richard C. Williamson, and Theodore M. Lyszczarz. Hybrid multi-mode/single-mode waveguides for low loss. In *Optical Amplifiers and Their Applications/Integrated Photonics Research*, Technical Digest (CD), page IThE5. Optical Society of America, June 2004.

[116] Sudharsanan Srinivasan, Renan Moreira, Daniel Blumenthal, and John E. Bowers. Design of integrated hybrid silicon waveguide optical gyroscope. *Optics Express*, 22(21):24988, October 2014.

[117] STMicroelectronics. Triple Axis Gyro LYPR540ah Specifications, 2014.

[118] Lee K. Strandjord and Glen A. Sanders. Effects of imperfect serrodyne phase modulation in resonator fiber optic gyroscopes. volume 2292, pages 272–282, 1994.

[119] Jeremy P. Stringer. The Air Force Institute of Technology (AFIT) Micro Electro-Mechanical Systems (MEMS) Interferometric Gyroscope (MiG). Technical report, March 2000.

[120] K. Suzuki, K. Takiguchi, and K. Hotate. Reduction of backscattering-induced noise by ternary phase shift keying in resonator micro-optic gyro integrated on silica planar lightwave circuit. *Electronics Letters*, 35(13):1076–1077, June 1999.

[121] K. Suzuki, K. Takiguchi, and K. Hotate. Monolithically integrated resonator microoptic gyro on silica planar lightwave circuit. *Journal of Lightwave Technology*, 18(1):66–72, January 2000.

[122] Stanford Research Systems. LDC500 Series Laser Diode Controller Manual, July 2007.

[123] Stanford Research Systems. PTC10 Programmable Temperature Controller Manual, November 2013.

[124] Kazumasa Takada. Calculation of Rayleigh backscattering noise in fiber-optic gyroscopes. *J. Opt. Soc. Am. A*, 2(6):872–877, June 1985.

[125] Yichuang Tang, Huilan Liu, Yinzhou Zhi, Lishuang Feng, and Junjie Wang. Closed-loop experiment of resonator integrated optic gyro with triangular wave phase modulation. volume 9270, pages 92700P–92700P–7, 2014.

[126] T. Tekin, H. Schroder, L. Zimmermann, P. Dumon, and W. Bogaerts. Fibre-array optical interconnection for silicon photonics. In *34th European Conference on Optical Communication, 2008. ECOC 2008*, pages 1–2, September 2008.

[127] M. Terrel, M.J.F. Digonnet, and S. Fan. Performance comparison of slow-light coupled-resonator optical gyroscopes. *Laser & Photon. Rev.*, 3(5):452–465, September 2009.

[128] Thorlabs. Thorlabs LN65s-FC - 10 GHz Phase Modulator with Polarizer, 2014.

[129] Frank Trager. *Springer Handbook of Lasers and Optics*. Springer Science & Business Media, May 2012.

[130] V. Vali and R. W. Shorthill. Fiber ring interferometer. *Appl. Opt.*, 15(5):1099–1100, May 1976.

[131] V. Vali, R. W. Shorthill, and M. F. Berg. Fresnel-Fizeau effect in a rotating optical fiber ring interferometer. *Appl. Opt.*, 16(10):2605–2607, October 1977.

[132] D. Vermeulen, Y. De Koninck, Y. Li, E. Lambert, W. Bogaerts, R. Baets, and G. Roelkens. Reflectionless grating couplers for Silicon-on-Insulator photonic integrated circuits. *Optics Express*, 20(20):22278, September 2012.

[133] A. Vorckel, M. Monster, Wolfgang Henschel, P.H. Bolivar, and H. Kurz. Asymmetrically coupled silicon-on-insulator microring resonators for compact add-drop multiplexers. *IEEE Photonics Technology Letters*, 15(7):921–923, July 2003.

[134] Technical Research Centre of Finland VTT. VTT Silicon Photonics Technology, 2015. http://www.epixfab.eu/technologies/vttsip.

[135] R. G. Walker, C. D. W. Wilkinson, and J. A. H. Wilkinson. Integrated optical waveguiding structures made by silver ion-exchange in glass. 1: The propagation characteristics of stripe ion-exchanged waveguides; a theoretical and experimental investigation. *Appl. Opt.*, 22(12):1923–1928, June 1983.

[136] Yun Wang. *Grating coupler design based on silicon-on-insulator*. Master of Applied Science, University of British Columbia, Vancouver, Canada, 2013.

[137] Yun Wang, Jonas Flueckiger, Charlie Lin, and Lukas Chrostowski. Universal grating coupler design. page 89150Y, October 2013.

[138] Yun Wang, Xu Wang, Jonas Flueckiger, Han Yun, Wei Shi, Richard Bojko, Nicolas A. F. Jaeger, and Lukas Chrostowski. Focusing subwavelength grating couplers with low back reflections for rapid prototyping of silicon photonic circuits. *Opt. Express*, 22(17):20652–20662, August 2014.

[139] Oliver Woodman. An introduction to inertial navigation. Cambridge Computer Lab Technical Report on Inertial Navigation, University of Cambridge, Cambridge Computer Lab, 2007.

[140] Kuan Pei Yap, A. Delage, J. Lapointe, B. Lamontagne, J.H. Schmid, P. Waldron, B.A. Syrett, and S. Janz. Correlation of Scattering Loss, Sidewall Roughness and Waveguide Width in Silicon-on-Insulator (SOI) Ridge Waveguides. *Journal of Lightwave Technology*, 27(18):3999–4008, September 2009.

[141] A. Yariv and P. Yeh. *Photonics*. Oxford University Press, USA, 2007.

[142] R. K. Rao Yarlagadda. Analog Modulation. In *Analog and Digital Signals and Systems*, pages 429–487. Springer US, 2010.

[143] N. Yazdi, F. Ayazi, and K. Najafi. Micromachined inertial sensors. *Proceedings of the IEEE*, 86(8):1640–1659, August 1998.

[144] Diqing Ying, Huilian Ma, and Zhonghe Jin. Resonator fiber optic gyro using the triangle wave phase modulation technique. *Optics Communications*, 281(4):580–586, February 2008.

[145] Han Yun, Wei Shi, Yun Wang, Lukas Chrostowski, and Nicolas A. F. Jaeger. 22 adiabatic 3-dB coupler on silicon-on-insulator rib waveguides. volume 8915, page 89150V. SPIE, October 2013.

[146] Yundong Zhang, Nan Wang, He Tian, Hao Wang, Wei Qiu, Jinfang Wang, and Ping Yuan. A high sensitivity optical gyroscope based on slow light in coupled-resonator-induced transparency. *Physics Letters A*, 372(36):5848–5852, September 2008.

Appendix A

Other Publications

A.1 Journal Publications

1. H. Jayatilleka, K. Murray, M. A. Guillén-Torres, M. Caverley, N. A. F. Jaeger, L. Chrostowski, and S. Shekhar, "Automated wavelength stabilization of microring filters using intra-ring photoconductive heaters", Submitted to *Optics Express*, July 2015

2. W. Shi, R. Vafaei, M. A. Guillen-Torres, N. A. F. Jaeger, and L. Chrostowski, "Design and Characterization of Microring Reflectors with a Waveguide Crossing," *Opt. Letters*, vol. 35, no. 17, pp. 2901-2903, 2010

A.2 Conference Proceedings

1. W. Shi, R. Vafaei, M. A. Guillen-Torres, N. A. F. Jaeger, and L. Chrostowski, "Ring-resonator reflector with a waveguide crossing," in *IEEE International Conference on Optical MEMS and Nanophotonics 2010*, Sapporo, Japan, pp. 1-2, Aug. 2010

A.3 Conference Presentations

1. M. A. Guillen-Torres, H. Yun, S. Grist, X. Wang, W. Shi, R. Boeck, C. Li, J. Yu, N. A. F. Jaeger, L. Chrostowski, "SOI Nanophotonics Fabrication Course", Pacific Centre for Advanced Materials and Microstructures (PCAMM) Annual Meeting, 2010

2. M. A. Guillen-Torres, N. Rouger, R. Vafaei, S. M. Amin, R. Boeck, B. Faraji, B. Francis, A. Kulpa, J. M. Michan, L. Chrostowski, N. A. F. Jaeger, and D. Deptuck, "SOI Nanophotonics Devices Analysis and Fabrication", Pacific Centre for Advanced Materials and Microstructures (PCAMM) Annual Meeting, 2008

3. M. A. Guillen-Torres, M. Sharma, K. Parsa, Y. Zeng, L. Chrostowski, and E. Cretu, "Optical Readout for In-Plane Micro Displacements", Pacific Northwest Microsystems and Nanotechnology Meeting, Friday Harbor, USA, 2008

Appendix B

Frequency-Stepped Sinusoidal Patterns

The PWM duty cycle of the first turntable motor control is kept constant during an integer number M of PWM signal cycles, in order to achieve a gradual speed change. Thus, the sinusoid sample number, n_s, and the PWM cycle number, n_{pwm}, are related by $n_{pwm} = M \cdot n_s$. The input duty cycle resembles a sinusoid quantized at a sampling interval T_s, which is a multiple of the PWM signal period, T_{pwm}, i.e., $T_s = M \cdot T_{pwm}$. The quantized sinusoid, with K samples per period, is depicted in Fig. B.1(a), and has the form:

$$S_n(n_s) = p_{max} \cdot \sin\left(\frac{2\pi}{K} \cdot n_s\right), \tag{B.1}$$

where S_n is the normalized angular speed and p_{max} is the maximum duty cycle value. The sinusoid has a period $T = KT_s = KMT_{pwm}$. The condition $\text{mod}\,(K, 4) = 0$ is required to ensure proper sampling of the sinusoid extrema and zeros. At any given time, the sign of Eq. (B.1) defines the rotation direction. The frequency of this sinusoid is:

$$f = \frac{1}{T} = \frac{1}{KMT_{pwm}} = \frac{f_{pwm}}{KM}, \tag{B.2}$$

where $f_{pwm} = 1/T_{pwm}$ is the PWM signal frequency. Figure B.1(b) shows the ideal PWM duty cycle (red curve), the rotation direction signal (black curve), and the experimental PWM duty cycle (blue curve). For easier interpretation, the duty cycle values are signed according to the rotation direction.

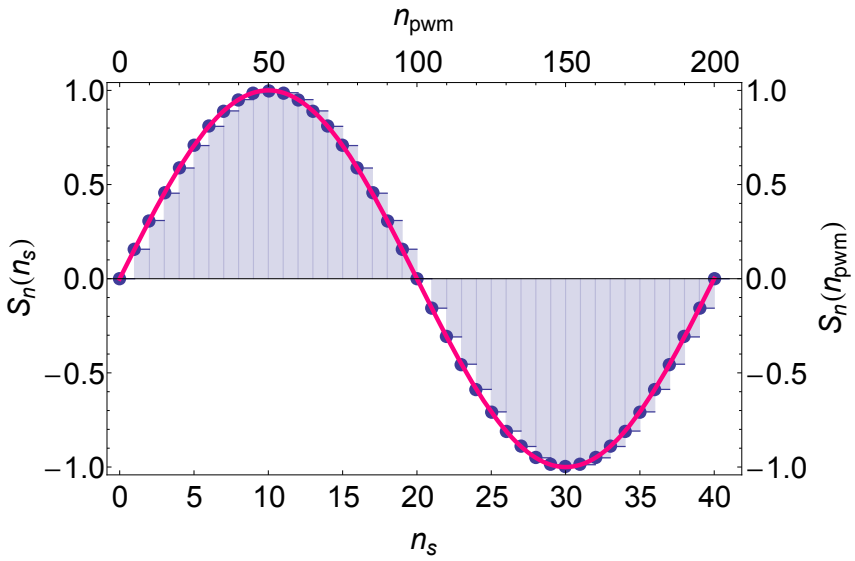

(a)

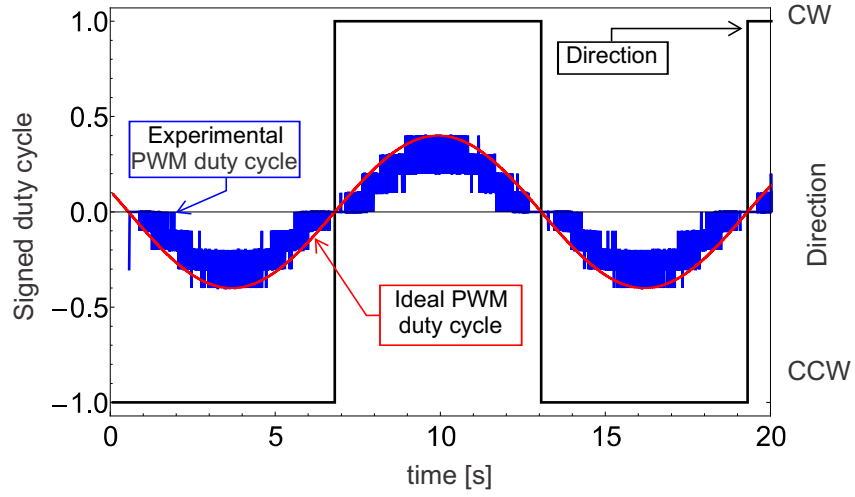

(b)

Figure B.1: **(a)** Normalized angular speed, S_n, as a function of sample number, n_s (bottom axis), and PWM cycle number, n_{pwm} (top axis), for $p_{max} = 1$, $M = 5$, and $K = 40$. **(b)** Comparison of input and output signals for a sinusoid of frequency $f_{in} = 0.083$ Hz. The red curve is the ideal PWM duty cycle, the black curve is the rotation direction signal, and the blue curve is the experimental PWM duty cycle.

In order to characterize the turntable frequency response, the sinusoid frequency was stepped and the inputs and output signals for each frequency value were recorded as a function of time. The input sinusoid was modelled as:

$$x(t) = S_{n_{max}} \sin[2\pi f_{in}(t - t_{0in})], \tag{B.3}$$

where $S_{n_{max}}$ is the maximum normalized angular speed, f_{in} is the input frequency, and t_{0in} is the input time delay. The reference gyroscope output was curve-fitted to:

$$y(t) = A_{fit} \sin[2\pi f_{fit}(t - t_{0fit})], \tag{B.4}$$

where A_{fit}, f_{fit}, and t_{0fit} are the fitted magnitude, frequency, and time delay, respectively. The fit parameters are then compared to their input signal counterparts. In all cases, f_{fit} and f_{in} were identical. The turntable frequency response was then obtained using the following expressions:

$$|H(f_{in})|^2 = 20 \log_{10} \left[\frac{|A_{fit}(f_{in})|}{S_{n_{max}}} \right] \tag{B.5}$$

$$\measuredangle H(f_{in}) = 2\pi f_{in}(t_{0fit} - t_{0in}), \tag{B.6}$$

where $|H(f_{in})|^2$, in dB, is the magnitude response, and $\measuredangle H(f_{in})$ is the phase shift.

Appendix C

Time-Domain Measurements in Selected Components

Two polarization-maintaining circulators were used throughout our experiments. They are referred to as red and blue, according to their fibre jacket colours. Both circulators were tested injecting light in their port 1 and measuring the output power at their ports 2 and 3. The optical output power at port 2 for these devices showed insertion losses of ~ 0.01 dB and ~ 0.04 dB, respectively. The SNR values measured at port 2 were ~ 40 dB and 34 dB, respectively. During this test, the output power at port 3 was below the noise floor for both circulators. Figure C.1 shows the time-domain output power signals measured at port 2 of these circulators, and the corresponding Fast Fourier Transforms (FFTs). The rationale behind the obtention of the FFTs was to identify the frequency range of deleterious signals producing noise or drift.

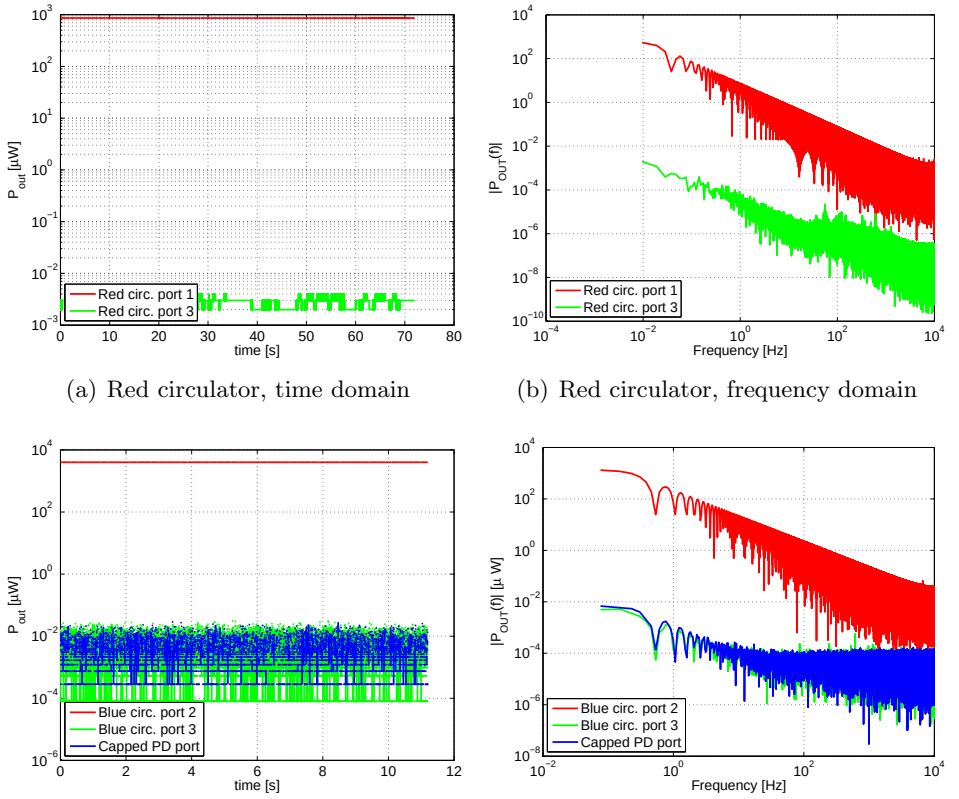

(a) Red circulator, time domain

(b) Red circulator, frequency domain

(c) Blue circulator, time domain

(d) Blue circulator, frequency domain

Figure C.1: Linear power vs. time and FFT spectra for two PM circulators. **(a, b)** Red (first) circulator. **(c, d)** Blue (second) circulator.

Appendix D

Transfer Functions of Resonators with Thermally-Tuneable Couplers

To obtain the tuneable coupler transfer matrix of the device shown in Fig. 3.33, K_{tc}, we will assume that the input signal enters through port C_1 and propagates towards ports F_1 and F_2. The matrices describing the propagation through the adiabatic coupler regions and the arms are described, respectively, by equations Eqs. (3.13) and by:

$$N = \begin{bmatrix} e^{-j\theta_1} & 0 \\ 0 & e^{-j\theta_2} \end{bmatrix}, \tag{D.1}$$

where θ_1 and θ_2 are, respectively, the phase shifts undergone after propagation through the top and the bottom T-MZI arms. These quantities are given by:

$$\theta_1 = \frac{2\pi L_{\mathrm{MZ}} \cdot n_{\mathrm{eff1}}}{\lambda} \tag{D.2}$$

$$\theta_2 = \frac{2\pi L_{\mathrm{MZ}} \cdot n_{\mathrm{eff2}}}{\lambda} = \frac{2\pi L_{\mathrm{MZ}} \cdot (n_{\mathrm{eff1}} + \Delta n_{\mathrm{thermal}})}{\lambda} = \theta_1 + \Delta\theta, \tag{D.3}$$

where n_{eff1} and n_{eff2} are, respectively, the effective indices of the top and bottom arm waveguides, L_{MZ} is the length of both T-MZI arms, $\Delta n_{\mathrm{thermal}}$ is the refractive index change due to the thermooptic effect, and $\Delta\theta$ is the arm phase imbalance, produced by the optical path difference between both

arms. Thus, we have:

$$\begin{aligned} D^+ &= MC^+ \\ G^+ &= ND^+ \\ F^+ &= M^{-1}G^+ \\ \therefore F^+ &= K_{\mathrm{tc}}C^+ = M^{-1}NMC^+ \end{aligned} \tag{D.4}$$

Explicitly,

$$\begin{bmatrix} {F_1}^+ \\ {F_2}^+ \end{bmatrix} = \frac{e^{-j\frac{(\theta_1+\theta_2)}{2}}}{2} \begin{bmatrix} e^{-j\frac{\Delta\theta}{2}} + e^{j\frac{\Delta\theta}{2}} & e^{-j\frac{\Delta\theta}{2}} - e^{j\frac{\Delta\theta}{2}} \\ e^{-j\frac{\Delta\theta}{2}} - e^{j\frac{\Delta\theta}{2}} & e^{-j\frac{\Delta\theta}{2}} + e^{j\frac{\Delta\theta}{2}} \end{bmatrix} \cdot \begin{bmatrix} {C_1}^+ \\ {C_2}^+ \end{bmatrix}, \tag{D.5}$$

This equation can be simplified to:

$$\begin{bmatrix} {F_1}^+ \\ {F_2}^+ \end{bmatrix} = e^{-j\frac{(\theta_1+\theta_2)}{2}} \begin{bmatrix} t(\Delta\theta) & j\kappa(\Delta\theta) \\ j\kappa(\Delta\theta) & t(\Delta\theta) \end{bmatrix} \cdot \begin{bmatrix} {C_1}^+ \\ {C_2}^+ \end{bmatrix}, \tag{D.6}$$

where the tuneable through- and cross-coupling coefficients are defined, respectively, as:

$$t(\Delta\theta) = \cos\left(\Delta\theta/2\right) \tag{D.7}$$

$$\kappa(\Delta\theta) = \sin\left(\Delta\theta/2\right). \tag{D.8}$$

For simplicity, in this particular model $\Delta\theta$ has been considered wavelength-independent, as the length of the MZI ($\sim$ 200 µm) is considerably smaller than that of the resonator ($L \sim 40$ mm), and therefore, for a wavelength span equivalent to one FSR ($\sim$ 20 pm), we have:

$$\phi_{R2} - \phi_{R1} = 2\pi = \delta k \cdot n_{\mathrm{eff}} L \tag{D.9}$$

$$\Rightarrow \delta k = 2\pi/(n_{\mathrm{eff}} L) \tag{D.10}$$

$$\delta(\Delta\theta) = \delta k \cdot \Delta n_{\mathrm{thermal}} L_{\mathrm{MZ}} \tag{D.11}$$

$$\Rightarrow \delta(\Delta\theta) = 2\pi \frac{\Delta n_{\text{thermal}} L_{\text{MZ}}}{n_{\text{eff}} L} \ll 2\pi, \tag{D.12}$$

where ϕ_{R1} and ϕ_{R2} are the phase values of two adjacent resonances, and δ indicates the change of a quantity over one period of the resonator.

When the tuneable coupler is connected to the resonator, as shown in Fig. 3.35, the field ${C_2}^+$ can be expressed in terms of the field ${F_2}^+$ as:

$${C_2}^+ = e^{-j\phi_{\text{ring}}} {F_2}^+ \tag{D.13}$$

Thus, using Eqs. (D.6) through (D.13):

$${F_2}^+ = e^{-j\frac{(\theta_1+\theta_2)}{2}} \left[-j\kappa(\Delta\theta){C_1}^+ + t(\Delta\theta){C_2}^+\right] = e^{j\phi_{\text{ring}}} {C_2}^+ \tag{D.14}$$

$$\Rightarrow {C_2}^+ = \frac{-j\kappa(\Delta\theta)e^{-j\phi_{\text{ring}}}}{e^{j(\theta_1+\theta_2)/2} - t(\Delta\theta)e^{-j\phi_{\text{ring}}}} \cdot {C_1}^+ \tag{D.15}$$

We can then express ${F_1}^+$ exclusively in terms of ${C_1}^+$ as:

$${F_1}^+ = e^{-j\frac{(\theta_1+\theta_2)}{2}} \left[t(\Delta\theta) - \frac{\kappa(\Delta\theta)^2 e^{-j\phi_{\text{ring}}}}{e^{j\frac{(\theta_1+\theta_2)}{2}} - t(\Delta\theta)e^{-j\phi_{\text{ring}}}}\right] {C_1}^+ \tag{D.16}$$

$${F_1}^+ = e^{-j\frac{(\theta_1+\theta_2)}{2}} \left[\frac{t(\Delta\theta)e^{j\frac{(\theta_1+\theta_2)}{2}} - t^2(\theta)e^{-j\phi_{\text{ring}}} - \kappa^2(\theta)e^{-j\phi_{\text{ring}}}}{e^{j\frac{(\theta_1+\theta_2)}{2}} - t(\Delta\theta)e^{-j\phi_{\text{ring}}}}\right] {C_1}^+ \tag{D.17}$$

Since $\kappa^2(\theta) + t^2(\theta) = 1$, and by defining $\Phi(\theta) = (\theta_1 + \theta_2)/2$, Eq. (D.17) can be rearranged as follows:

$$\frac{{F_1}^+}{{C_1}^+} = T_{\text{tc}}(\Phi_S) = e^{-j\Phi(\theta)} \cdot \frac{t(\Delta\theta) - e^{-j(\Phi_{\text{ring}}+\Phi(\theta)+\Phi_S)}}{1 - t(\Delta\theta)e^{-j(\Phi_{\text{ring}}+\Phi(\theta)+\Phi_S)}} \tag{D.18}$$

Equation D.4 can be generalized for a T-MZI with imperfect adiabatic

couplers of power splitting ratios $T_{\mathrm{ac1}}/(1-T_{\mathrm{ac1}})$ and $T_{\mathrm{ac2}}/(1-T_{\mathrm{ac2}})$. In this case, the matrix describing the adiabatic couplers is:

$$M(T_{\mathrm{ac1,2}}) = \begin{bmatrix} \sqrt{T_{\mathrm{ac1,2}}} & \sqrt{1-T_{\mathrm{ac1,2}}} \\ -\sqrt{1-T_{\mathrm{ac1,2}}} & \sqrt{T_{\mathrm{ac1,2}}} \end{bmatrix}, \tag{D.19}$$

The generalized elements of matrix K_{tc} are given by:

$$K_{\mathrm{tc11}} = e^{-j\Theta}\left(e^{-j\frac{\Delta\theta}{2}}\sqrt{(1-T_{\mathrm{ac1}})(1-T_{\mathrm{ac2}})} + e^{j\frac{\Delta\theta}{2}}\sqrt{T_{\mathrm{ac1}}T_{\mathrm{ac2}}}\right) \tag{D.20}$$

$$K_{\mathrm{tc12}} = e^{-j\Theta}\left(-e^{-j\frac{\Delta\theta}{2}}\sqrt{T_{\mathrm{ac1}}(1-T_{\mathrm{ac2}})} + e^{j\frac{\Delta\theta}{2}}\sqrt{(1-T_{\mathrm{ac1}})T_{\mathrm{ac2}}}\right) \tag{D.21}$$

$$K_{\mathrm{tc21}} = e^{-j\Theta}\left(-e^{-j\frac{\Delta\theta}{2}}\sqrt{(1-T_{\mathrm{ac1}})T_{\mathrm{ac2}}} + e^{j\frac{\Delta\theta}{2}}\sqrt{T_{\mathrm{ac1}}(1-T_{\mathrm{ac2}})}\right) \tag{D.22}$$

$$K_{\mathrm{tc22}} = e^{-j\Theta}\left(e^{-j\frac{\Delta\theta}{2}}\sqrt{T_{\mathrm{ac1}}T_{\mathrm{ac2}}} + e^{j\frac{\Delta\theta}{2}}\sqrt{(1-T_{\mathrm{ac1}})(1-T_{\mathrm{ac2}})}\right), \tag{D.23}$$

where $\Theta = \left(\frac{\theta_1+\theta_2}{2}\right)$.